Finite Element Modelling of Fracture & Damage in Austenitic Stainless Steel in Nuclear Power Plant

A thesis submitted to the University of Manchester

for the degree of

Doctor of Philosophy (PhD)

in the Faculty of Engineering and Physical Sciences

2015

SUTHAM ARUN

School of Mechanical, Aerospace and Civil Engineering

TABLE OF CONTENTS

Word Count: 30,513

LIST OF FIGURES

CHAPTER 7 PREDICTION OF DAMAGE IN A LARGE SCALE BENDING TEST USING ROUSSELIER MODEL

LIST OF TABLES

ABSTRACT

Name of the University: The University of Manchester
Submitted by: Sutham Arun
Degree Title: Doctor of Philosophy
Thesis Title: Finite Element Modelling of Fracture & Damage in Austenitic Stainless Steel in Nuclear Power Plant
Date: 26-06-2015

The level of residual stresses in welded components is known to have a significant influence on their failure behaviour. It is, therefore, necessary to understand the combined effect of mechanical loading and residual stresses on the ductile fracture behaviour of these structures in order to provide the accurate structural safety assessment. Recently, STYLE (Structural integrity for lifetime management-non-RPV component) performed a large scale bending test on a welded steel pipe containing a circumferential through-thickness crack (the MU2 test). The purpose of this test is to study the impact of high magnitude weld residual stresses on the initiation and growth of cracks in austenitic stainless steels.

This research presents the simulation part of the STYLE project which aims to develop the finite element model of MU2 test in ABAQUS to enhance the understanding and ability to predict the combined influence of mechanical loading and residual stresses on the ductile fracture behaviour of nuclear pressure vessel steels. This research employs both fracture mechanics principles (global approach) and Rousselier damage model (local approach) to study this behaviour including crack initiation and growth.

In this research, the Rousselier model was implemented into ABAQUS via the user defined subroutines for ABAQUS/Standard and ABAQUS/Explicit modules, i.e. UMAT and VUMAT. The subroutines were developed based on the integration algorithm proposed by Aravas and Zhang. The validation of these subroutines was checked by comparing the FE results obtained from the implementation of these subroutines with the analytical and other benchmark solutions. This process showed that UMAT and VUMAT provide accurate results. However, the UMAT developed in this work shows convergence problems when the elements start to fail. Hence, only VUMAT was used in the construction of the finite element model of the MU2 test.

As mentioned above, the results obtained from both fracture mechanics approach and Rousselier model are compared with the experimental data to validate the accuracy of the model. The results shows that both fracture mechanics approach and the Rousselier model predict similar final crack shapes which correspond closely to the test results in south direction. The other conclusions about the influence of residual stress on ductile fracture obtained from this work are also summarized in this thesis.

DECLARATION

I hereby declare that no portion of the work referred to in the thesis has been submitted in support of an application for another degree or qualification of this or any other university or other institute of learning.

Sutham Arun

June 2015

COPYRIGHT STATEMENT

(i) The author of this thesis (including any appendices and/or schedules to this thesis) owns certain copyright or related rights in it (the "Copyright") and s/he has given The University of Manchester certain rights to use such Copyright, including for administrative purposes.

(ii) Copies of this thesis, either in full or in extracts and whether in hard or electronic copy, may be made only in accordance with the Copyright, Designs and Patents Act 1988 (as amended) and regulations issued under it or, where appropriate, in accordance with licensing agreements which the University has from time to time. This page must form part of any such copies made.

(iii) The ownership of certain Copyright, patents, designs, trade marks and other intellectual property (the "Intellectual Property") and any reproductions of copyright works in the thesis, for example graphs and tables ("Reproductions"), which may be described in this thesis, may not be owned by the author and may be owned by third parties. Such Intellectual Property and Reproductions cannot and must not be made available for use without the prior written permission of the owner(s) of the relevant Intellectual Property and/or Reproductions.

(iv) Further information on the conditions under which disclosure, publication and commercialisation of this thesis, the Copyright and any Intellectual Property and/or Reproductions described in it may take place is available in the University IP Policy (see http://documents.manchester.ac.uk/DocuInfo.aspx?DocID=487), in any relevant Thesis restriction declarations deposited in the University Library, The University Library's regulations (see http://www.manchester.ac.uk/library/aboutus/regulations) and in The University's policy on Presentation of Theses.

Acknowledgements

First and foremost, I would like to express my sincerest gratitude to my supervisors, Dr.Mohammad Sheikh and Professor Andrew Sherry, who have supported me throughout my PhD programme with their patience and knowledge whilst allowing me the room to work in my own way. Without their kind supervision and encouragement, the completion of this thesis would not have been possible.

Additionally, I would also like to thank Professor Mike C. Smith who has devoted his time in reviewing my modelling and sharing his knowledge on fracture that has formed much of the basis of the work conducted here. Besides, I would also like to thank Dr.Michael Keavey for his invaluable technical discussion on finite element analysis and the numerical integration algorithm used in this thesis. Moreover, I am also thankful to Dr.Graham Wardle for giving me the technical knowledge of fracture toughness test and also devoting his time to review some part of my thesis. My special thanks also go to Dr.Peter James and Mike Ford from AMEC for their assistance in the finite element modelling and fracture tests respectively.

I would also give very special gratitude to my parents who have worked very hard through their life to bring me the aspiration to this level. I wish to thank my aunt for her love and support to both myself and my sister. I am also thankful to my sister who has taken good care of my parents on my behalf while I am studying here. I would like to give very special thanks to Miss.Tanyathip Jaimulwong for her unconditional love and support. I couldn't have done this work without her.

I would like to thank the EU-STYLE project (Structural integrity for lifetime management – non-RPV component) for supporting all data used in the thesis and the Royal Thai Government for giving me an opportunity to study at The University of Manchester.

NOMENCLATURES

a	crack length
C^e_{ijkl}	the forth order elastic tensor
D	Rousselier model's parameter
$d\epsilon_p, d\epsilon_q$	intermediate variables corresponding to volumetric and deviatoric strain increment.
E	Young's moduli
f	void volume fraction, the volume fraction of cavities
f_0	initial void volume fraction
G	shear modulus.
H^i	internal variable vector.
J	*J*-integral
K	bulk modulus.
K_I	mode I stress intensity factor
L_c	The characteristic length or the mesh size
n_{ij}	unit vector in the deviatoric space normal to the yield surface.
p	pressure.
q, σ_{eq}	von Mises equivalent stress.
S_{ij}	deviatoric stress tensor
β	damage parameter
δ_{ij}	Kronecker delta

ε_{eq}	equivalent plastic strain
$\epsilon_{ij}, \epsilon_{ij}^{e}, \epsilon_{ij}^{p}$	total, elastic and plastic strain tensor.
λ	positive scalar factor.
ν	Poisson's ratio
ρ	mass density, relative density
σ_{ij}	Cauchy stress tensor.
σ_{ij}^{tr}	trial stress tensor, elastic predictor
σ_m	mean Stress
σ_1	Rousselier model's parameter
ϕ, F	yield function or plastic potential

CHAPTER 1

INTRODUCTION

1.1 INTRODUCTION

The level of residual stresses in welded components is known to have a significant influence on their failure behaviour. Over the last decade, there has been an increased interest in understanding the effect of residual stresses on fracture behaviour. For example, Anisworth et al. [1] has shown that residual stress can reduce the load carrying capacity of a defective structure under elastic conditions. However, this effect decreases when the material becomes plastic. Liu et al.[2] have studied the combined effect of the applied load and residual stresses on crack-tip constraint. Their results show that the residual stress can induce an additional crack-tip constraint which is defined by a parameter *R*. The study carried out by Ren et al. [3] confirms that the residual stress can significantly elevate the crack-tip constraint which results in an increase of the probability of cleavage fracture. The residual stress also plays an important role on ductile crack growth resistance. The tensile residual stress can significantly reduce the ductile crack growth resistance when the crack growth is small, but this effect decreased with the increase of crack growth [4]. It is, therefore, necessary to study the effect of residual stress on various aspects of failure, and these effects need to be included in the practical assessment of defect behaviour in engineering components.

The assessment of defect behaviour in engineering components can be performed by two main approaches. The first approach is referred to as the global approach, based on the continuum fracture mechanics theory. In this approach the behaviour of defects in components is assessed by comparing the driving force for crack propagation with the resistance to fracture of the material defined in terms of fracture mechanics parameters. The global approach is appropriate for failure analysis of bodies with pre-existing cracks. It cannot be used for crack initiation and propagation.

The second approach is called the local approach, which attempts to incorporate microstructure information and physical mechanisms of damage and failure. In this approach, the damage can be represented in the bulk using the continuum damage mechanics (CDM) models or on the surface using *cohesive zone models*. The effect of displacement discontinuities (microvoids or microcracks) is modelled within the framework of continuum mechanics.

In practical, both global and local approaches are usually employed to assess the behaviour of defects in mechanical components via finite element analysis. The residual stress can be introduced into the analysis via two main methods. The first method is to introduce the residual stress via plastic deformation which requires the knowledge of the history of prior deformation in the structure. Another method is to specify the residual stress directly at the integration points in the model as initial stress. This method only requires the formation of stress fields in the current condition of the structure.

The main aim of this research is to develop a new understanding of the combined influence of mechanical loading and residual stresses on the ductile fracture behaviour of a repair welded pipe containing a circumferential through-thickness crack. To achieve this, an ABAQUS user defined subroutine for micro-mechanical model of failure was developed and employed to predict the fracture behaviour, crack initiation and growth, of a pipe specimen under combined loading using a three dimensional finite element model. The material and the model parameters were derived from standard fracture mechanics tests performed within EU STYLE project. The predictions from the developed model were compared with the experimental data of a large-scale four point bending test performed by CAE as part of STYLE project [5].

1.2 BACKGROUND AND MOTIVATION

STYLE, or “Structural integrity for lifetime management-non-RPV component” is a EURATOM Framework 7 project which aims to improve and unify methods of structural integrity assessment in the aging and lifetime management of reactor coolant pressure boundary (RCPB) components [6]. This project ran from January

2010 to December 2013, and was undertaken by 20 organisations from 11 EU member states including universities, research and engineering institutes, manufacturers, plant operators and industrial companies. STYLE was built around a series of large-scale tests on mock-ups of RCPB components.

One of the focus areas of STYLE project is to study the impact of high magnitude weld residual stresses on the initiation and growth of cracks in austenitic stainless steels. This is because the welds made from austenitic stainless steels are not normally post-weld heat treated before entering service. Therefore, they contain weld residual stresses of yield magnitude which lead to a number of ageing-related instances of in-service cracking in operating nuclear plants. In addition, the presence of weld repairs worsen these problems because the residual stresses in a weld repair are higher than in plain girth weld in both longitudinal and transverse directions. Hence, the studying of effects of the weld residual stresses on the fracture behaviour in STYLE project is focused on repair-welded area.

The STYLE project can be divided into two main parts, i.e. the experimental part and the simulation part. The experimental part involves a series of the tests which comprise of large-scale bending test, standard tensile tests and fracture mechanics tests. The large-scale bending test was performed on a welded steel pipe containing a circumferential through-thickness crack. The test specimen is referred to as Mock-up 2 (MU2) and was manufactured from two Esshete 1250 stainless steel pipes joined by a girth weld containing a deep repair. A through-thickness circumferential pre-crack was introduced in the centre of the repair prior to testing in four-point bend. This large scale test was supported by a set of standard tensile and ductile fracture tests performed in order to provide the material data necessary to undertake a full structural integrity assessment. The simulation part involves finite element analysis of MU2 test. In this part, the fracture mechanics principles and micro-mechanical models were employed to study the defect behaviour, i.e. crack initiation and growth, of MU-2 test piece via the commercial finite element code, ABAQUS.

This thesis presents in the simulation part of STYLE project which aims to analyse the fracture behaviour of MU2 test under combined loading. The thesis presents details of all the FE models employed in this study. The Rousselier damage model

was chosen as the micro-mechanical model to describe the ductile fracture of MU2 test. The numerical algorithm of ABAQUS user defined subroutine for the this model are also given in the thesis.

1.3 SPECIFIC OBJECTIVES

The main aim of this research is to enhance the understanding and ability to predict the combined influence of mechanical loading and residual stresses on the ductile fracture behaviour of engineering components. The particular focus is on a large scale bending test undertaken as part of STYLE EU Framework 7 project. The specifics objective of this work can be summarised as follows :

1. To develop and validate a modelling approach to simulate the combined influence of primary and residual stresses on ductile crack initiation and growth.
2. To use the modelling approach to simulate and predict the ductile fracture behaviour of a structural components using fracture mechanics and damage mechanics approaches.
3. To compare the results of the two approaches with experimental data to provide new insight into the influence of residual stresses on ductile fracture.
4. To establish new guidance on the prediction of ductile fracture under combined loading.

1.4 THESIS STRUCTURE

CHAPTER 2 LITERATURE REVIEW

Chapter 2 gives a brief review of knowledge base employed in the STYLE project. It starts with the principles of fracture mechanics and micro-mechanical models of failure and their implementation in structural integrity assessment procedures. This is followed by the material properties used in reactor systems, focussing in detail on austenitic stainless steels. The origin of residual stress in the welding process and residual stress measurement technique used in STYLE project are also described in this chapter.

CHAPTER 3 NUMERICAL INTEGRATION FOR PRESSURE DEPENDENT MODEL

Chapter 3 reviews the basic concepts of elastoplastic constitutive relations. The mathematical formulation and the integration method for pressure dependent elastoplasticity model are discussed. This chapter also presents the formulation of consistent tangent moduli which is required to determine the solutions in standard displacement finite element analysis.

CHAPTER 4 AN IMPLEMENTATION OF THE ROUSSELIER DAMAGE MODEL IN ABAQUS

Chapter 4 presents the background of Rousselier damage model and the implementation of this model via ABAQUS user defined subroutines, such as UMAT and VUMAT. Finally, the validation of these subroutines is illustrated by comparing FE results with the analytical solutions and the solutions available in the literature.

CHAPTER 5 GLOBAL APPROACH FOR LARGE SCALE BENDING TEST

Chapter 5 presents the results of a structural integrity assessment of MU2 test. The method used in the assessment is based on fracture mechanics approaches. The details of FE models, with and without the weld residual stresses, are given and the results from FE model and experiments are discussed.

CHAPTER 6 DETERMINATION OF ROUSSELIER MODEL PARAMETERS FOR ESSHETE WELD MATERIAL

Chapter 6 focuses on the numerical calibration of Rousselier model parameters for Esshete weld material. This calibration was performed via the FE models of standard tensile and fracture mechanics tests. Details of the FE models which include the implementation of the ABAQUS user defined subroutine for Rousselier damage model are presented. The main conclusions from this work are drawn in this chapter.

CHAPTER 7 LOCAL APPROACH FOR LARGE SCALE BENDING TEST

Chapter 7 focuses on the prediction of the fracture behaviour of MU2 test using Rousselier model. The analysis was performed by employing the Rousselier model parameters for Esshete weld material calibrated in chapter 6. The results obtained

from this analysis were compared with the results obtained by following fracture mechanics approach presented in chapter 5 in order to confirm the validation of the analysis. Details of finite element analysis and the conclusions from this work are described in this chapter.

CHAPTER 8 CONCLUSIONS AND RECOMMENDATION FOR FUTURE WORK

Chapter 8 draws the conclusions from the results obtained from this research. The contributions of the structural integrity assessment on MU2 test are summarised. Recommendations for possible future work to improve the accuracy of the subroutines and the finite element models employed in this research are also addressed.

CHAPTER 2

LITERATURE REVIEW

2.1 INTRODUCTION

This chapter first gives a brief review of the principles of fracture mechanics and micro-mechanical models employed in structural integrity assessment procedures. The latter part of this chapter is concerned with the STYLE project. It starts with the material properties used in the reactor systems, focussing in detail on austenitic stainless steels. The origin of residual stress in the welding process and the residual stress measurement techniques used in this project are then described.

2.2 THE GLOBAL APPROACH TO FRACTURE

The behaviour of defects in engineering component is conventionally assessed using the principles of fracture mechanics that can be classified into three types depending on the material behaviour near the crack tip. The first type is Linear Elastic Fracture Mechanics (LEFM). It is based on the theory of elasticity and is used as long as nonlinear deformation is limited to a small region surrounding the crack tip. LEFM is suitable for brittle materials, such as glass, ceramics and high strength steels. The second approach is Elastic-plastic Fracture Mechanics (EPFM) which can be applied to materials exhibiting non-linear behaviour, e.g. medium strength steels. EPFM is based on concepts which assume that the stress-strain curve of the material is non-linear. One other fracture mechanics type is Time-Dependent Fracture Mechanics (TDFM). It is applied when the deformation behaviour is time dependent such as in creep.

Each type of fracture mechanics provides certain parameters, e.g. K and J, which represent the driving force for crack propagation and the crack initiation is predicted to occur when the value of these parameters exceeds the resistance of the material to fracture. This section introduces the principles of LEFM and EPFM, focusing on these two parameters K and J, and shows how to employ these parameters for predicting failure in engineering structures and components.

2.2.1 Linear Elastic Fracture Mechanics (LEFM)

Based on isotropic linear elasticity theories, when an elastic cracked body is subjected to external forces, the stress field in the vicinity of a crack tip can be expressed as an infinite power series [7-9]:

$$\sigma_{ij}(r,\theta) = \frac{k}{\sqrt{r}} f_{ij}(\theta) + A_0 g_{ij}^0(\theta) + \sum_{m=1}^{\infty} A_m r^{m/2} g_{ij}^m(\theta) \qquad (2.1)$$

where σ_{ij} is the stress tensor, r is the distance from the crack tip, k and A are constants which are proportional to the remotely applied load, and the functions f_{ij} and g_{ij} are dimensionless functions of θ at a point defined with respect to a polar axes set located at crack tip, as shown in Figure 2.1.

The second term on the right hand side of Eq.(2.1) is known as T-stress. It is the constant tensile or compressive stress acting parallel to the crack plane. The T-stress value depends on the geometry, crack size and the traction parallel to crack plane and has an effect on plastic zone size and crack tip opening displacement [10]. The negative (compressive) T-stress causes a reduction in crack-tip constraint and increases the apparent fracture toughness [11-13].

However, as $r \to 0$, the first term on the right hand side of Eq.(2.1) exhibits a $1/\sqrt{r}$ singularity and approaches infinity. Hence, the rest of the terms of Eq.(2.1) can be neglected. Consequently, Eq.(2.1) can be reduced to

$$\sigma_{ij}(r,\theta) = \frac{K}{\sqrt{2\pi r}} f_{ij}(\theta) \qquad (2.2)$$

The regions surrounding the crack tip where the difference of results in stress between Eqs.(2.1) and (2.2) is less than 10%, is called the singularity–dominated zone [14].

Parameter K in Eq.(2.2) is known as the stress intensity factor. It defines the amplitude of crack tip singularity and provides fundamental information on how the crack is going to propagate. Generally, there are three basic types (modes) of loading that a crack can experience (Figure 2.2). Any component can be subjected to any one of these modes or a combination of two or even three modes. However, for many practical cases, cracks generally grow in accordance with the largest opening loads,

so that mode I is usually considered as the predominant mode. The solution of mode I stress intensity factor, K_I for a crack in a finite body is often written in the following form.

$$K_I = Y\sigma\sqrt{\pi a} \tag{2.3}$$

where Y is a dimensionless parameter depending on the geometry of the specimen and the crack, σ is the (remotely) applied stress, and a is the crack length. The values of K_I for common cracks and specimen geometries are widely available in handbooks [15-17].

In an elastic cracked body, the stress intensity factor K is used to describe the fracture behaviour. Crack extension occurs when the value of stress intensity factor exceeds a critical value, $K \geq K_c$, defined as fracture toughness. K_c can be determined experimentally for any material by inserting a crack of known length into a piece of the same material and loading it until fast fracture occurs [18]. For mode I loading, at a particular temperature, the value of K_c decreases with increasing specimen thickness but remains stable beyond a certain thickness when the specimen is predominantly in plane strain, as shown in the experimentally derived data of Figure 2.3 [19]. The stable (lowest) value of K_c is called the plane strain fracture toughness, defined by K_{Ic}, and is considered as a material property.

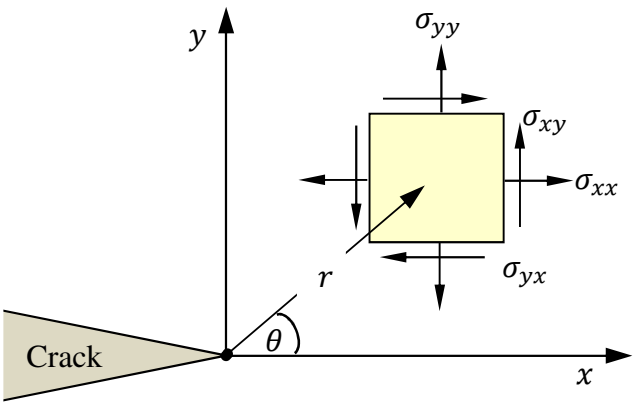

Figure 2.1 Stress distribution at the tip of crack in an elastic material.

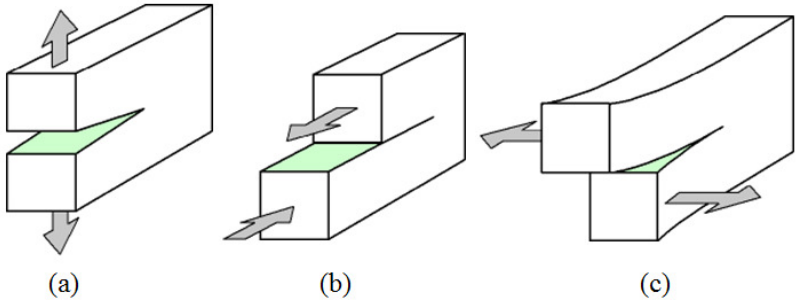

Figure 2.2 The three modes of loading that can be applied to crack :
(a) Mode I (opening mode), (b) Mode II (sliding mode) and
(c) Mode III (tearing mode).

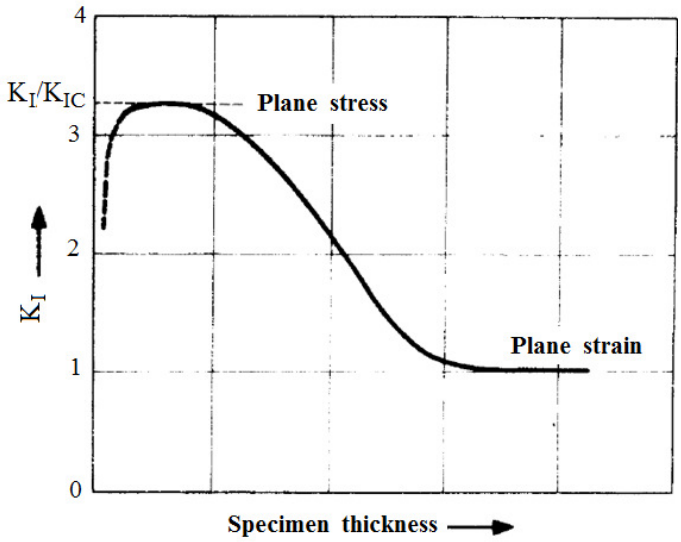

Figure 2.3 Variation of critical stress intensity factor versus specimen thickness [19].

2.2.2 Elastic –Plastic Fracture Mechanics (EPFM)

There are many cases where the crack tip plastic zone is too large to permit the description of failure behaviour by LEFM. For these cases, another method, namely Elastic–Plastic Fracture Mechanics (EPFM), is required. This topic focuses on one of the most important elastic–plastic parameters, called *J*-integral. This parameter can be considered as both an energy and stress intensity factor. It is employed to describe crack–tip conditions and can be used as fracture criterion for both elastic and elastic–plastic materials.

- **The *J*-integral (*J*)**

The *J*-contour integral is used as a fracture characterizing parameter for nonlinear materials. The concept of this parameter was first introduced by Rice [20]. He defined *J* as a path-independent line integral with a value equal to the energy release rate in non-linear elastic body that contains the crack. Consider an arbitrary counter clockwise path (Γ) around the tip, as in Figure 2.4, the *J*-integral is given by :

$$J = \int_{\Gamma} \left(w dy - T_i \frac{\partial u_i}{\partial x} d\Gamma \right) \tag{2.4}$$

where w is strain energy density which is defined as $w = \int_0^{\epsilon_{ij}} \sigma_{ij} \epsilon_{ij}$

$T_i = \sigma_{ij} n_j$ are components of the traction vector

u_i = displacement vector components

$d\Gamma$ = length increment along the contour Γ

For linear elastic case, *J* is related to *K* by

$$J = \frac{K^2}{E'} \tag{2.5}$$

where $E' = E$ for plane stress and $E' = E/(1-\nu^2)$ for plane strain. E and ν are Young's modulus and Poisson's ratio respectively.

Hutchinson, Rice and Rosengren have examined Eq.(2.4) and shown that for materials which deform according to the Ramberg-Osgood equation [21], the magnitude of crack tip stresses and strains can expressed in term of *J* as [22, 23] :

$$\sigma_{ij} = \sigma_0 \left(\frac{E\,J}{\alpha \sigma_0^2 I_n r} \right)^{n/(1+n)} \tilde{\sigma}_{ij}(n, \theta) \tag{2.6a}$$

$$\varepsilon_{ij} = \frac{\alpha \sigma_0}{E} \left(\frac{EJ}{\alpha \sigma_0^2 I_n r} \right)^{n/(1+n)} \tilde{\varepsilon}_{ij}(n, \theta) \tag{2.6b}$$

where α is a dimensionless constant, σ_0 is a reference stress value that is usually equal to yield stress and n is the strain hardening exponent. I_n is an integration constant which depends on n and $\tilde{\sigma}_{ij}$ and $\tilde{\varepsilon}_{ij}$ are dimensionless functions of n and θ.

Eq.(2.6) is known as the HRR singularity. It illustrates that the stress/strain field in the direct vicinity of a crack tip is completely characterized by *J*. The specimens with different geometry can be expected to have the same stress and strain fields near

the crack tip, if the values of J are identical. This confirms that J can be considered as a fracture mechanics parameter. For linear elastic materials (n = 1), Eq.(2.6) shows a $1/\sqrt{r}$ singularity which is consistent with *LEFM*. On the other hand, for ideal plasticity behaviour ($n = \infty$), the solution of Eq.(2.6) is equal to the so-called Prandtl slip-line field solution [24].

In fracture assessment using J, crack extension is postulated to take place when J reaches a critical value. In mode I loading, the critical value of J for plane strain conditions denoted by J_{Ic}, is also considered as the material property, since it is independent of the size of plastic zone [25]. Under elastic condition, J_{Ic} may be related to the fracture toughness K_{Ic} by Eq.(2.5).

Normally, J_{Ic} is often evaluated from testing specimens exhibiting significant plasticity. The tests include the multiple specimen method in which a number of specimen are loaded to give small but different amounts of crack extension, and the single specimen method which uses a technique for measuring the current crack extension during a test. The details of these two methods are explained in ASTM standard for fracture toughness measurement [26].

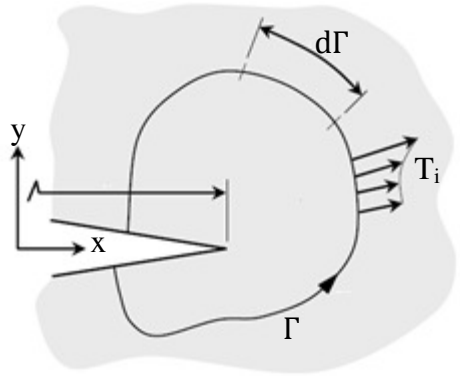

Figure 2.4 An arbitrary J-integral contour around a crack.

- **The material *J-R* curves**

When a structural component containing a crack is loaded, it is represented by a certain value of *J*-integral which can be considered as 'crack resistance'. This idea leads to the assessment of crack extension in the component by using crack-growth resistance curve (*R*-curve). Figure 2.5 is an example of a ductile material *R*-curve that represents the relation between the crack resistance in terms of *J*-integral and crack extension, the so called *J-R* curve. In small-scale yielding condition, the *J-R* curve is a material property, since the value of *J* depends of crack extension only [27].

The methodologies to establish material *J-R* curves are given in standard handbooks, such as ESIS P2-92 and ASTM E1820 [28, 29]. One of the frequently used techniques is the elastic unloading compliance method which provides the procedure to obtain a *J-R* curve with a single specimen. This technique starts by loading the specimen until a small amount of crack extension occurs. After that, the load is partially removed and subsequently reapplied, resulting in the load-displacement diagram shown in Figure 2.6. From this diagram, the instantaneous crack length which leads to the values of crack extension (Δa), and the *J*-values at each unloading point are calculated from the resulting elastic compliance and the area under the curve by using formulae given in the standards. A *J-R* curve is then obtained as *J*-integral plotted against crack extension, which exhibits an increasing fracture toughness as the crack grows.

The test specimens recommended to establish *J-R* curve are fracture mechanics specimens with high geometry constraint, i.e. single edge-notched bend (SENB), compact tension (CT), and disk-shaped compact tension (DCT) specimens. However, some experimental data shows that *J-R* curves vary with the level of constraint [30, 31]. Figure 2.7 shows that the values of *J*-integral on *J-R* curve for a high constraint specimen are lower than those for a low constraint specimen. In other words, the slope of *J-R* curves after crack initiation steadily decreases with increasing crack-tip constraint [32]. Therefore, the constraint effect due to geometry must be corrected so that the *J-R* curves determined in laboratory test can be applied to real cracked structures. From this, three methods have been developed in order to

quantify crack-tip constraint. These methods are the *J-T* approach [33], *J-Q* theory [34, 35] and *J-A*$_2$ method [36]. The *J-Q* theory and *J-A*$_2$ method are quite popular approaches for characterizing the constraint effects under large scale yielding [37], whereas the *J-T* approach has limited use in elastic-plastic fracture because it is based on the theory of elasticity.

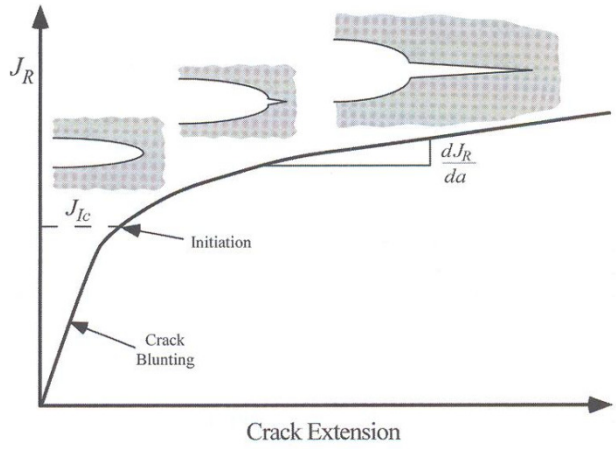

Figure 2.5 Schematic *J* resistance curve for a ductile material [27].

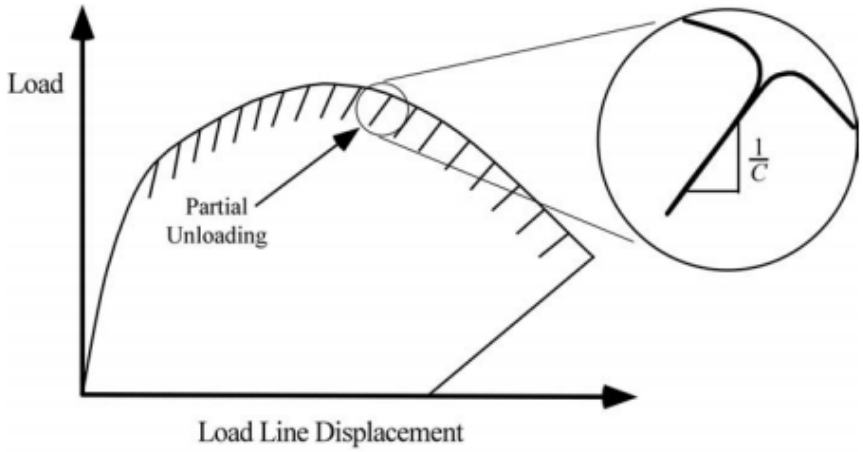

Figure 2.6 The unloading compliance method for monitoring crack growth [27].

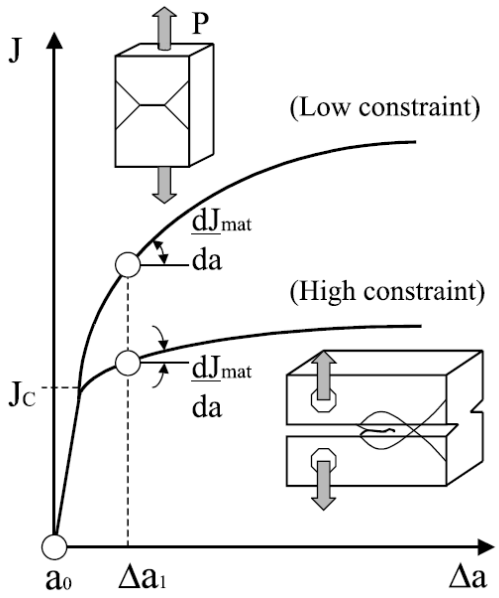

Figure 2.7 Variation of *J-R* curves with the level of crack-tip constraint [32].

2.2.3 Failure Assessment Diagram (FAD) approach

The failure assessment of cracked structural components cannot only use fracture mechanics concepts, but should also consider the effects of plastic deformation. In 1975, Dowling and Townley [38] proposed the two-criteria approach to study defects in structures. This approach assumes that failure occurs when the applied load reaches the lower of either a load to cause brittle failure or a load to cause ultimate plastic collapse of the structure. The concept of this approach has led to the introduction of failure assessment diagram (FAD) to describe the mechanical integrity of flawed components.

- **Brief introduction of FAD [17, 39, 40]**

In FAD methodology, the safety of a cracked component is assessed via the failure assessment curve (FAC) which is established from the relationship between crack-tip loading describing the fracture conditions and a limit-load solution describing plastic collapse of the remaining crack ligament. The FAC is defined by the following function:

$$K_r = f_i(L_r) \tag{2.7}$$

The subscript i = 1, 2, 3 is used to demonstrate different levels of failure assessment. K_r and L_r are the fracture and load ratios respectively that are calculated using the applied loads, material properties, and specimen geometry including defect size and shape.

$$K_r = \frac{K_I(a,P)}{K_{mat}} \tag{2.8a}$$

$$L_r = \frac{P}{P_L(a,\sigma_y)} \tag{2.8b}$$

Here, K_I is the mode I stress intensity factor at load P, P_L is the value of P corresponding to plastic collapse of the cracked component. a is the crack size, K_{mat} is material's fracture toughness and σ_y is the yield strength of material. The parameter L_r can be defined in terms of a reference stress (σ_{ref}) defining the plastic collapse load solution of the remaining crack ligament as [41] :

$$L_r = \frac{\sigma_{ref}}{\sigma_y} \tag{2.9}$$

When FAD is used to assess the safety of a structure containing defects, the integrity of structures are judged through the relative position of the assessment point (L_r, K_r) on FAD. The structure is simply considered to be safe if the assessment point lies within the safe area bounded by the failure line and the (L_r, K_r) axes (Figure 2.8).

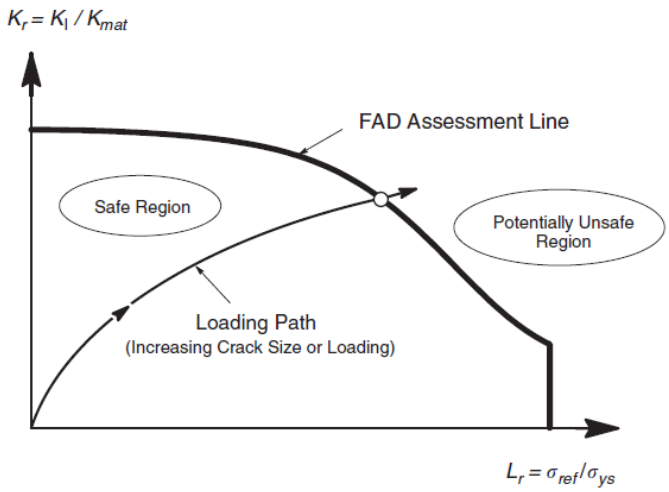

Figure 2.8 Schematic illustration of the FAD methodology [41].

- **Failure assessment curve [17, 39, 40]**

In R6 procedure, three options are given to evaluate the FAC's functions given by Eq.(2.7). The choice of option depends on the material involved, the available input data, and the level of conservatism required. Higher options are expected to lead to reduce conservatism or increase accuracy in an assessment, but they require more data and analysis.

The simplest choice is option 1. It can be employed for general applications when information on material properties is limited. The FAC function for option 1 is :

$$f_1(L_r) = (1 - 0.14L_r^2)\{0.3 + 0.7\ exp(-0.65\ L_r^6)\} \tag{2.10}$$

The above function needs no material data apart from σ_y and the ultimate stress, σ_u, which are used to define the plastic collapse cut-off :

$$L_r = L_r^{max} = \frac{\sigma_y + \sigma_u}{2\sigma_y} \tag{2.11}$$

For materials which exhibit a discontinuous yield point in the stress-strain curve, either a cut-off value for $L_r \leq 1$ or option 2 FAC should be used.

Option 2 is a more sophisticated approach. It requires more information in the form of stress-strain data for material assessment. The FAC for this option is described by the following equation :

$$f_2(L_r) = \left(\frac{E\ \varepsilon_{ref}}{\sigma_{ref}} + \frac{L_r^3\ \sigma_y}{2\ E\ \varepsilon_{ref}}\right)^{-1/2} \tag{2.12}$$

where σ_{ref} is the reference stress defined in Eq.(2.9), ε_{ref} is the true strain obtained from the uniaxial tensile stress-strain curve at a true stress level σ_{ref}. Option 2 is suitable for all types of materials regardless of their geometry and generally gives more accurate results than option 1.

Option 3 is an advanced procedure which is appropriate for ductile materials that exhibit stable tearing, e.g. austenitic steels and ferritic steels. In this option, a FAC specific to a material and geometry is obtained by determining the *J*-integral using elastic and elastic-plastic analysis of the flawed structure with the loads of interest. The FAC for this option is :

$$f_3(L_r) = \sqrt{\frac{J_e}{J}} \tag{2.13}$$

where J_e and J are J-integral values obtained from elastic and elastic-plastic analyses with the same load respectively. The fracture ratio for this option is defined by :

$$K_r = \sqrt{\frac{J_e}{J_{mat}}} \tag{2.14}$$

where J_{mat} is the material toughness measured by J-methods.

By combining Eqs.(2.13) and (2.14), it can be seen that the assessment is based on criterion $J \leq J_{mat}$ [24]. The advantage for using option 3's FAC lies in the fact that once this curve is established for the geometry and material under consideration, the actual assessment is based on J_e, for which only an elastic calculation needs to be performed. Although option 3 FAC requires a J analysis of the cracked structure, it has the potential for greater accuracy than FAC from options 1 and 2.

- **Treatment of combined primary and secondary stresses**

The stresses acting on structures are classified into primary stresses and secondary stresses. Primary stresses arise from loads which actually contribute to plastic collapse, such as pressure, while secondary stresses are self-equilibrating stresses originated from a range of sources, such as thermal and residual stress due to welding.

In FAD methodology, L_r and FAC depend only on primary stresses, but K_r must include both primary and secondary stress contributions. In the elastic range, the stress intensity caused by secondary stress, K_I^s, can be simply added to the stress intensity factor caused by primary stresses, K_I^p. However, due to crack tip plasticity, this superposition will be an underestimate when stress levels become higher. In order to account for this interaction of primary and secondary stresses, an additive interaction parameter, ρ is applied to the definition of K_r :

$$K_r = \frac{K^p + K^s}{K_{mat}} + \rho \tag{2.15}$$

The value of ρ depends on the magnitude of both primary and secondary stresses. Different routes for evaluating ρ based on elastic or inelastic analysis have been provided in Appendix 4 of R6.

2.3 THE LOCAL APPROACH TO FRACTURE

The local approach is an alternative method which can be used to simulate the failure behaviour of steel structures without the use of fracture mechanics parameters. This approach has been developed in recent years and used to predict the fracture behaviour of both ferritic and austenitic steel structures for a range of geometries under combinations of primary and secondary loads [42-47].

"The local approach is based on the application of micro-mechanical models of failure in which the stress, strain and 'damage' local to a crack tip or stress concentrator are related to the critical conditions required for fracture. Normally, these models involve parameters which need to be calibrated using a combination of reference test data, quantitative metallography and finite element (FE) analysis. Once these parameters have been derived for a particular material, they can be assumed to be independent of geometry and loading mode, and are transferred to the assessment of any structure fabricated from the same material [40]". The local approach has been developed for both ductile and brittle (cleavage) fracture processes. Since the failure type occurred in the experimental part of STYLE project is the ductile fracture, only on the local approach for ductile fracture is discussed in this section.

The micromechanical models of local approach for ductile fracture are usually based on the common process of ductile fracture which can be divided into the following 3 stages.

(i) Microscopic void nucleation
(ii) The growth of void
(iii) Coalescence of the growing void with adjacent voids.

There are a number of mathematical models which try to explain the ductile fracture process. The three widely referenced models are presented as follows :

2.3.1 Rice and Tracy model (RT model)

Rice and Tracy [48] studied the growth of a spherical cavity in an infinite solid under a remote normal stress. They found that the void growth in all cases could be approximated by the following expression :

$$ln(R/R_0) = 0.283 \int exp\left(1.5\ \sigma_m/\sigma_{eq}\right) d\varepsilon_{eq} \tag{2.16}$$

where R_0 is the radius of the initial spherical void, R is the average radial displacement of ellipsoidal void, $d\varepsilon_{eq}$ is the increment of equivalent plastic strain and σ_m/σ_{eq} is the stress triaxiality. This integration is taken over the history of plastic strain and the crack initiation is predicted when the parameter $ln(R/R_0)$ reaches a critical value. Hence, this model is characterized by a unique parameter : critical void growth ratio $(R/R_0)_c$.

The determination of $(R/R_0)_c$, corresponding to crack initiation requires both experimental measurements from tensile tests on notched or cracked specimen and FE analysis of the same specimen [49, 50]. In FE analysis, the values of R/R_0 in the element in front of the crack tip are calculated at each load increment by Eq.(2.18) which is rewritten in numerical form as follows [51, 52] :

$$(R/R_0)_{n+1} = (R/R_0)_n\left\{1 + 0.283\ \Delta\varepsilon_{eq}\ exp\left(1.5\ \sigma_m/\sigma_{eq}\right)\right\} \tag{2.17}$$

where $(R/R_0)_n$ and $(R/R_0)_{n+1}$ are the cavity growth rates at steps n and $n+1$ respectively. These calculations provide the relationship between the evolution of void growth ratio and the values of *J*-integral. The value of (R/R_0) which corresponds to J_{Ic} is defined as $(R/R_0)_c$, as shown in Figure 2.9. Once the value of $(R/R_0)_c$ is defined, it can be used to predict the initiation of ductile tearing in cracked structure by FE analysis.

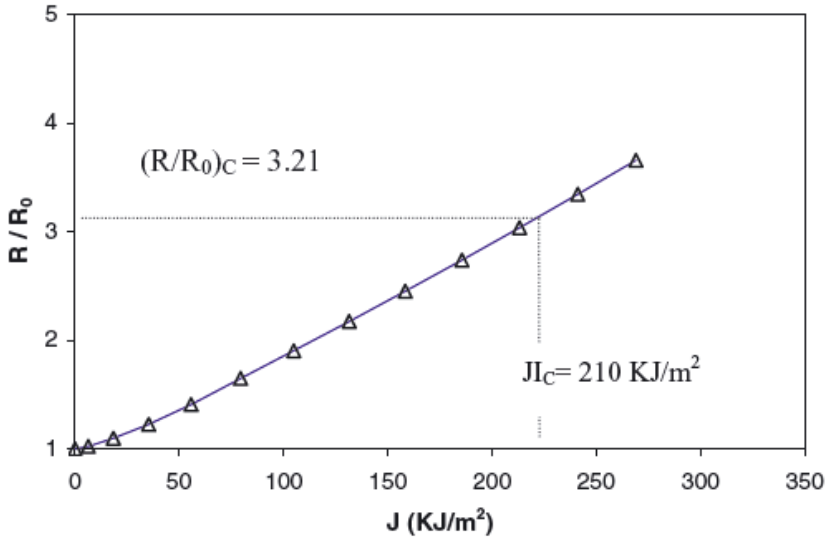

Figure 2.9 The relationship between R/R_0 and *J*-Integral [50].

2.3.2 Damage models

2.3.2.1 Gurson model

Based on the work by the Rice and Tracy, Gurson further studied the plastic flow of a void containing material. He provided a yield function that includes the softening effect due to the initial void [53]:

$$\phi = \left(\frac{\sigma_{eq}}{\bar{\sigma}}\right)^2 + 2q_1 f \cosh\left(\frac{3\, q_2 \sigma_m}{2\bar{\sigma}}\right) - 1 - (q_1 f)^2 = 0 \qquad (2.18)$$

where σ_{eq} is the macroscopic von Mises stress, σ_m is the macroscopic mean stress, $\bar{\sigma}$ is the flow stress for the matrix material of the cell and f is the current void volume fraction. Parameters q_1 and q_2 are constants which were later introduced by Tvergaard [54, 55]. During progressive straining, the void growth rate has the following form [56] :

$$\dot{f} = (1-f)\dot{\epsilon}^p_{kk} + \Lambda \dot{\epsilon}^p_{eq} \qquad (2.19)$$

The first term in Eq.(2.19) defines the growth rate of the pre-existing voids and the second term quantifies the contribution of the new voids that are nucleated with plastic strain. The scaling coefficient Λ is given by:

$$\Lambda = \frac{f_N}{S_N\sqrt{2\pi}} exp\left[-\frac{1}{2}\left(\frac{\epsilon_{eq}^{p}-\epsilon_N}{S_N}\right)^2\right] \tag{2.20}$$

The above expression indicates that the plastic strain range at nucleation of a new void follows a normal distribution with a mean value ϵ_N, a standard deviation S_N, and a volume fraction of void nucleating particle f_N.

However, Eq.(2.18) alone cannot predict the necking instability between voids, since this equation does not consider discrete voids. To overcome this problem, Tvergaard and Needleman [57] modelled the void coalescence by replacing f with an effective void volume fraction f^*

$$f^* = \begin{cases} f & for \quad f \leq f_c \\ f_c - K(f - f_c) & for \quad f > f_c \end{cases} \tag{2.21}$$

where

$$K = \frac{f_u^* - f_c}{f_F - f_c} \tag{2.22}$$

where f_c is the critical void volume fraction at which voids coalesce. f_F is the final void volume fraction where the material fails and $f_u^* = 1/q_1$. This equation simply implies that before void coalescence, the relationship between void volume fraction and the decrease of load will follow the Gurson model. After the void coalescence has started, the void volume fraction will be amplified to present the sudden loss of load carrying capacity.

As mentioned above, the Gurson model requires a number of parameters that need to be determined for the material under investigation, i.e. $q_1, q_2, f_0, f_c, f_f, f_n, S_N$ and ε_n. Zhang [58, 59] improved this model by using the plastic limit load criterion proposed by Thomason to determine the critical state when voids coalesce [60-62]. From this modification, void coalescence can be automatically determined and material failure is directly linked to the void nucleation parameters (i.e. no need to determine f_c). In addition, Zhang also suggested that the value of the final void volume fraction can be estimated by the following relation.

$$f_f = 0.15 + 2\, f_0 \tag{2.23}$$

Since there is no need to determine f_c and the value of f_f can be estimated by Eq.(2.23), only 4 parameters (f_0, f_n, S_N and ε_N) need to be determined.

2.3.2.2 The Rousselier continuum damage model

Rousslier model [63, 64] is based on the thermodynamical concept of generalized standard media. The yield function of this model is close to Gurson model and has the form :

$$\phi = \frac{\sigma_{eq}}{\rho} - R(p) + B(\beta)Dexp\left(\frac{\sigma_m}{\sigma_1}\right) \tag{2.24}$$

where D and σ_1 are constants, ρ is relative density and β is the damage variable. The second term $R(p)$ is the material hardening parameter which is determined from the stress-strain hardening curve in a standard tensile test. $B(\beta)$ is a function that present the softening of the material due to damage. This function is calculated from the knowledge of initial void volume fraction and β by :

$$B(\beta) = \frac{\sigma_1 f_0 \, exp(\beta)}{1 - f_0 + f_0 exp(\beta)} = \sigma_1 f \tag{2.25}$$

where f_0 is a constant representing the initial volume fraction of cavities, and f is the actual volume fraction of cavities.

According to Eq.(2.24), the Rousselier damage model defines the softening of the material by a damage parameter (β) and fracture proceeds from the competition between hardening and damage. Therefore, it is not necessary to introduce a critical value of the damage variable. In addition, the number of parameters in the model which need to be defined is less than the Gurson model.

2.3.2.3 Application of Gurson and Rousselier models to cracked structures

The applications of Gurson and Rousselier models to predict structural behaviour are described in literature [42, 65, 66]. The process starts by determining the model parameters of the material of interest by calibrating FE calculation with experimental data. This step requires both experimental testing and FE analysis. After all the parameters are obtained, they are used to model the large scale structure. The steps in using Gurson and Rousselier models are summarized in Figure 2.10 [40].

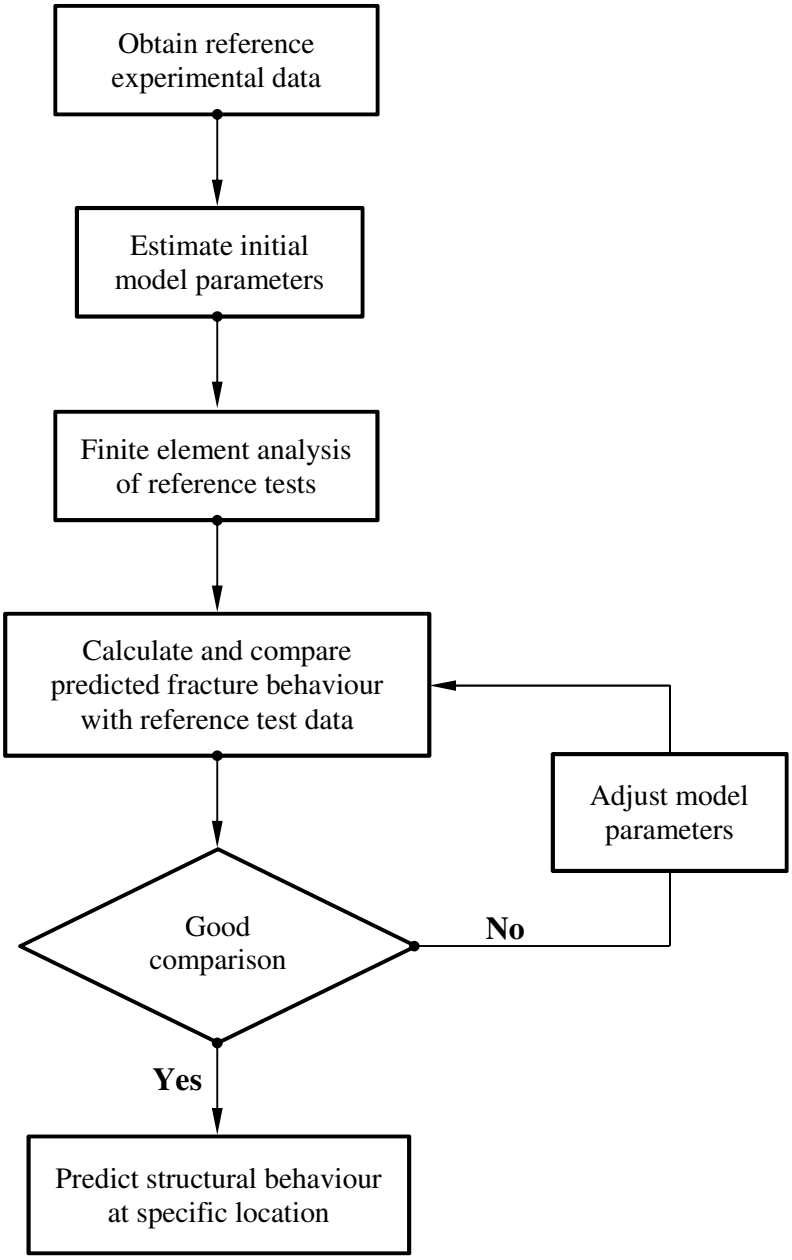

Figure 2.10 Schematic illustrating the steps involved in using Gurson and Rousselier damage models [50].

2.4 FINITE ELEMENT APPROACH FOR FRACTURE ANALYSIS

The finite element method (FEM) has become an indispensable tool to undertake fracture analysis. It is employed to evaluate fracture mechanics parameters, i.e. *J*-integral, in cracked structures having complicated geometries or subjected to complex loads or boundary conditions. Nowadays, additional numerical techniques, such as the extended finite element method (XFEM) or cohesive zone model (CZM), were added into the conventional FEM. These techniques have the ability to analyse the moving discontinuous problems, such as crack propagation, without remeshing or the rearranging of nodal points. A description regarding the method commonly used for the determination of *J*-integral using finite element analysis is provided in the first part of this section. Background and theory of the XFEM and CZM are also given afterwards.

2.4.1 Evaluation of *J*-integral by finite element approach

Shih et al. [67] provided a convenient method for evaluating *J* within a finite element framework. From this, the domain integral expression of Eq.(2.4) is obtained by introducing a smooth function, q, which take the value of unity at the crack tip nodes and zero on the contour Γ and then applying the divergence theorem to give

$$J = \int_{A^*} \left\{ \left(\sigma_{ij} \frac{\partial u_j}{\partial x_1} - w\delta_{1i} \right) \frac{\partial q}{\partial x_i} \right\} dA \tag{2.26}$$

where A^* is the area that is enclosed by $\Gamma^* = \Gamma_1 + \Gamma_+ + \Gamma_- - \Gamma_0$ as illustrated in Figure 2.11.

In finite element analysis, the q function must be specified at all nodes within the area of integration. The variation of q within an element can be written as follows

$$q = \sum_{I=1}^{n} N_I Q_I \tag{2.27}$$

where n is the number of node per element, N_I is the element shape function and Q_I are the nodal values for the I^{th} node. The special derivative of q is given by

$$\frac{\partial q}{\partial x_i} = \sum_{I=1}^{n} \sum_{k=1}^{2 \; or \; 3} \frac{\partial N_I}{\partial \xi_k} \frac{\partial \xi_k}{\partial x_j} Q_I \tag{2.28}$$

where ξ_k represents the local coordinates (ξ_1, ξ_2) and $\frac{\partial \xi_k}{\partial x_j}$ is the inverse Jacobian matrix of the transformation. With 2×2 Gaussian integration, the domain integral expression of *J*-integral in Eq.(2.26) for the plane problem is then

$$\mathrm{J} = \sum_{\substack{all\ elements \\ in\ A^*}} \sum_{P=1}^{m} \left\{ \left[\left(\sigma_{ij} \frac{\partial u_j}{\partial x_1} - w\delta_{1i} \right) \frac{\partial q}{\partial x_i} \right] det \left(\frac{\partial x_j}{\partial \xi_k} \right) \right\}_P w_P \qquad (2.29)$$

where m is the number of gauss points per element, and w_P is weighting factors. The quantities within $\{\ \ \}_P$ are evaluated at all gauss points in an element. Note that the integration over the crack faces is necessary only when there are non–zero tractions.

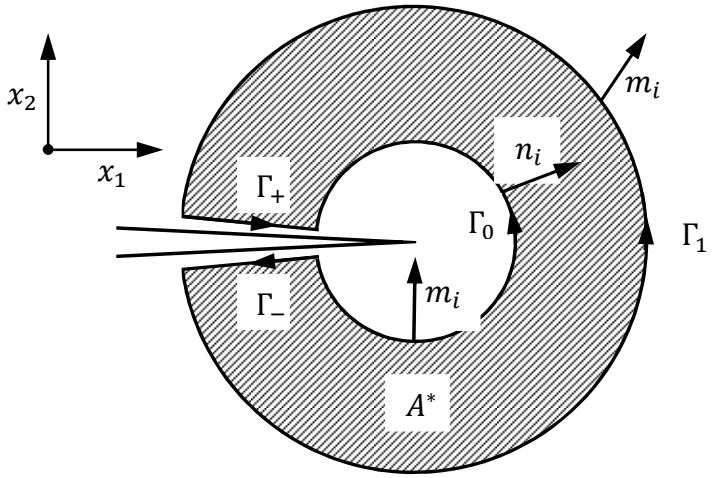

Figure 2.11 Inner and outer contours, which form a closed contour around the crack tip when connected by Γ_+ and Γ_-.

2.4.2 Extended Finite Element Method (XFEM)

The method of XFEM was originally proposed by Belytschko and Black [68]. They introduced a method to develop the finite element approximation by adding discontinuous enrichment functions into the displacement fields near the crack tip. This method allowed the crack to be arbitrarily aligned within the mesh and the crack growth problems could be solved with minimal re-meshing. Based on this concept, Dolbow et al. [69] provided a more sophisticated technique by adapting an enrichment that included the asymptotic near-tip field and a Heaviside function *H(x)*. This technique was successfully applied to fracture mechanics problems, in which

crack discontinuities were represented using both a jump function and the asymptotic near-tip fields. Therefore, the modelling of crack or crack growth problem could be performed without remeshing. The concept of this technique is summarized as follows :

Considering the domain Ω bounded by Γ with an internal boundary Γ_c as shown in Figure 2.12a. Without the model of the discontinuity, the general discrete approximation u^h to the function u_I for the uniform mesh of N nodes (Figure 2.12b) takes the form

$$u^h(x) = \sum_I N_I(x) u_I \tag{2.30}$$

where N_I is the standard finite element shape function for node I and u_I is the vector of nodal degree of freedom. In order to incorporate the discontinuity in the field along Γ_c without a change of mesh such that it conforms to the line of discontinuity (Figure 2.12c), the standard approximation in Eq.(2.30) is modified using the partition of unity concept as [70]

$$u^h(x) = \sum_{I=1}^{n} N_I(x)\left\{u_I + \sum_{l=1}^{ne(I)} a_{Il} G_l(x)\right\} \tag{2.31}$$

where $G_l(x)$ are the enrichment functions, and a_{Il} are additional nodal degree of freedom for node I. In the above, $ne(I)$ is the total number of enriched degrees of freedom for a node. If the enrichment functions G_l are discontinuous along the boundary Γ_c, then the finite element mesh does not need to model the discontinuity. For example, the uniform mesh in Figure 2.12d is capable of modelling a jump in u when the circled nodes are enriched with the function which are discontinuous across Γ_c. The change in form of the approximation from Eq.(2.30) to Eq.(2.31) is only made locally in the vicinity of a feature of interest, such as a discontinuity.

The precise form of the enrichment functions used to model discontinuous fields in crack or crack growth problems can be determined by dividing the crack geometry to be three distinct regions [69]. These are the crack interior and the two near-tip regions as shown in Figure 2.13. From this, three different nodal sets which correspond to each of these regions are distinguished. The set J is taken to be the set of nodes enriched for the crack interior, and the set K_1 and K_2 are those nodes

enriched for the first and second crack tips, respectively. From this the enriched approximation takes the form

$$u^h(x) = \sum_I N_I u_I + \sum_J N_J b_J H(x)$$
$$- \sum_{K \in K1} N_K \{\sum_{l=1}^{4} c_{Kl}^1 F_l^1(x)\} + \sum_{K \in K2} N_K \{\sum_{l=1}^{4} c_{Kl}^2 F_l^2(x)\} \quad (2.32)$$

where b_J and c_{Kl}^1, c_{Kl}^2 are nodal degree of freedom corresponding to the enrichment functions $H(x)$, $F_l^1(x)$ and $F_l^2(x)$ respectively.

The function $H(x)$ is a discontinuous function across the crack line and is constant on each side of crack : +1 on one side and -1 on the other. The set $F_l^1(x)$ and $F_l^2(x)$ consist of those functions which span the near-tip asymptotic fields. For two-dimensional elasticity, these are given by

$$\{F_l(r,\theta)\}_{j=1}^{4}$$
$$= \left\{\sqrt{r}\, sin\left(\frac{\theta}{2}\right),\ \sqrt{r}\, cos\left(\frac{\theta}{2}\right),\ \sqrt{r}\, sin\left(\frac{\theta}{2}\right) sin(\theta),\ \sqrt{r}\, cos\left(\frac{\theta}{2}\right) sin(\theta)\right\} \quad (2.33)$$

where (r,θ) are the local polar coordinate for the crack tip.

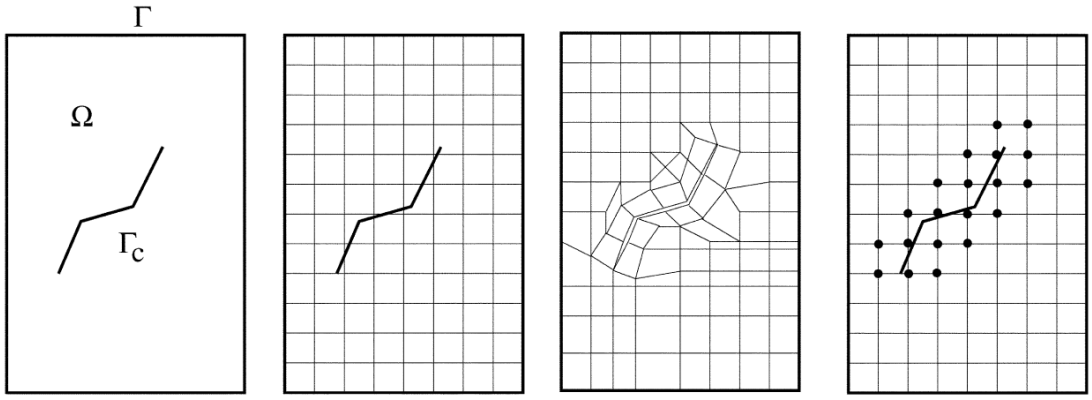

(a) (b) (c) (d)

Figure 2.12 Various discretizations for (a) a domain with an internal boundary Γ_c. (b) A mesh which does not model the internal boundary. (c) A mesh which conforms to the geometry of Γ_c. (d) A uniform mesh in which the circled nodes have additional degrees of freedom and enrichment functions [69].

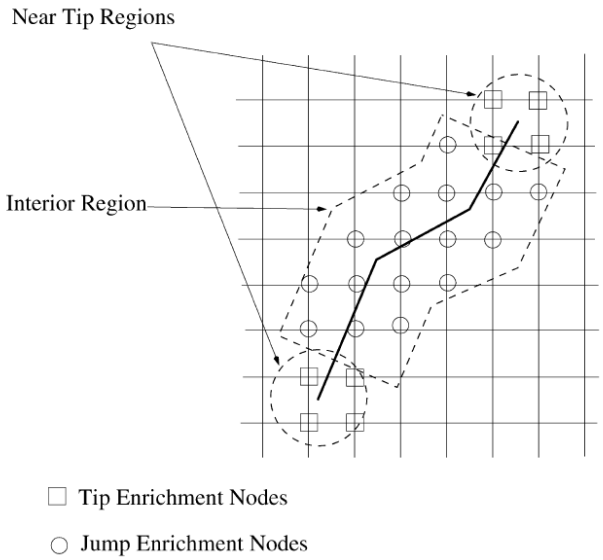

Figure 2.13 Regions of a crack for enrichment. The circled nodes are enriched with a discontinuous function, while the squared nodes are enriched with near-tip functions [69].

2.4.3 Cohesive zone model (CZM)

The cohesive zone model (CZM) is an alternative approach to model crack propagation problems. This model considers fracture as " a gradual phenomenon in which separation takes place across an extended crack 'tip', or cohesive zone, and is resisted by cohesive tractions [71]". With this concept, the CZM is able to predict the behaviour of uncrack structures, including those with blunt notches, not only the responds the bodies with cracks which is the usual drawback of most fracture models [72].

The application of CZM to FEM can be shown schematically by Figure 2.14. From this Figure, the fracture process zone (FPZ) is represented by the cohesive zone elements. These elements are inserted between continuum (bulk) elements either by sharing common nodes or through a tie constraint. As the cohesive surfaces separate, the traction across the cohesive zone elements first increases until a maximum is reached, and subsequently decreases to zero, which results in complete (local) separation. Therefore, the limitation of this approach is that the FPZ must be known in advance, either from experimental evidence or from the structure of the material

(such as in laminated composites). The crack cannot develop in any location, but only along the pre-established lines where the cohesive elements have been inserted.

The cohesive zone elements do not represent any physical properties of material, but describe the cohesive forces occurring when material elements are being pulled apart. This traction-separation relation is used to define the constitutive behaviour of CZMs. Various CZMs have been proposed in literature [73], but all models exhibit the similar global behaviour which starts by increasing traction across cohesive zone elements as the crack surfaces increase up to the maximum value, T_0 and then reducing the traction to zero at critical separation δ_c (Figure 2.15).

Although all CZMs have the same global behaviour, but they have a number of different factors which play an important role in the resulting failure behaviour. For example, the area under the traction separation curve corresponds to the energy needed for separation. The initial stiffness of the cohesive zone model has a large influence on the overall elastic deformation and should be very high in order to obtain realistic results. It has been shown by Chandra et al. [73] that the form of the traction-separation relations plays an important role in the macroscopic mechanical response of the system.

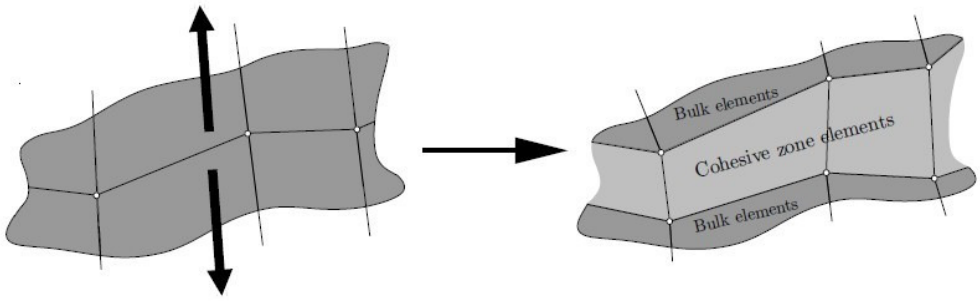

Figure 2.14 Application of cohesive zone element along the bulk element boundaries [74].

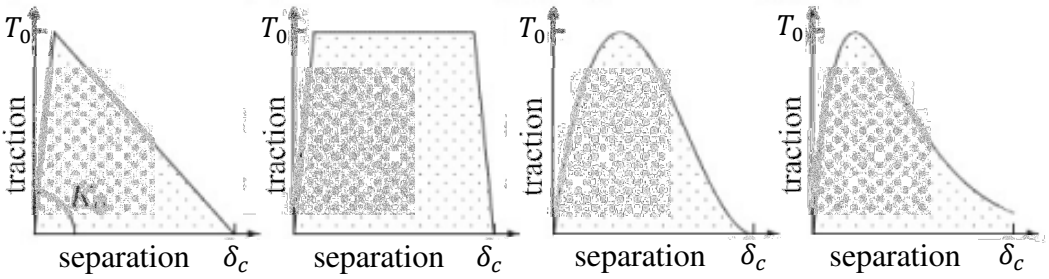

Figure 2.15 Traction-separation relations used in cohesive zone modelling : (a) bilinear, (b) trapezoidal, (c) polynomial and (d) exponential.

2.5 STYLE PROJECT

STYLE, or "Structural integrity for lifetime management-non-RPV component" is a EURATOM Framework 7 project which aimed to improve and unify methods of structural integrity assessment in the aging and lifetime management of reactor coolant pressure boundary (RCPB) components. One of the focus areas of STYLE project is to study the impact of high magnitude weld residual stresses on the initiation and growth of cracks in austenitic stainless steel. This is because the welds made from austenitic stainless steels are not normally post-weld heat treated before entering service, so they will contain weld residual stresses of yield magnitude. The presence of high residual stresses lead to a number of ageing-related instances of in-service cracking in operating nuclear plants. In addition, the presence of weld repairs worsen these problems, because the residual stresses in a weld repair are higher than in plain girth weld in both longitudinal and transverse directions.

The following sections review the details about the material and the residual stress measurement technique employed in the STYLE project.

2.6 AUSTENITIC STAINLESS STEELS

AGR reactors are the main nuclear plants currently operated in UK. At full power the reactor coolant gas temperature is higher than 500^{o}C as it enters the boilers. Consequently, the service life times of boiler components are affected by creep deformation [75]. Therefore, the materials used for the boiler components must have alloying elements, such as Niobium, Titanium and Vanadium [76], to provide high creep resistance at high temperature. Apart from high-temperature creep resistance, the boiler materials used in reactor systems must meet the requirements below [77]:

- Dimensional stability under irradiation.
- An acceptable level of mechanical properties with aging.
- Good performance and integrity withstanding neutron irradiation and corrosion.
- Acceptable cost to construction and fabrication.
- Good weldability.

These requirements have to be met under normal operating conditions, and in incidental or accidental conditions. One of candidate boiler materials recommended to use in reactor environment is austenitic stainless steel.

2.6.1 General properties [78-81]

Austenitic stainless steels are used in a large number of plants in the UK, USA and France. In addition to excellent formability and good corrosion resistance in most environments, these steels also have very good ductility and remain ductile within a large range of temperature, because they have no transition temperature. Austenitic stainless steels have strength equivalent to that of mild steels with minimum yield strength of approximately 210 MPa at room temperature and are not transformation hardenable. They cannot harden by heat treatment but can be strengthened and hardened significantly by cold working. In addition, these steels are non-magnetic and are considered to be weldable. Austenitic steels are often used in applications requiring good atmospheric or elevated temperature corrosion resistance.

2.6.2 The chemical composition

Austenitic steels have Chromium and Nickel as their major alloying elements. Additional elements are added to these steels to improve their properties and make them suitable for many critical applications involving high temperature as well as corrosion resistance. Table 2.1 gives the composition range of standard austenitic stainless steels.

The roles of the alloying elements given in Table 2.1 are listed below [78, 79]:

- Chromium (Cr) is a ferrite stabilising element added primarily to improve the resistance to corrosion and typical rusting (oxidation) which occurs with unprotected carbon steel.
- Nickel (Ni) is an alternative austenite stabilising element added also to improve the hardenability. It also makes the material non-magnetic.
- Manganese (Mn) is introduced to replace Ni to reduce cost. The solubility of nitrogen in austenite is also increased with manganese.
- Molybdenum (Mo), a ferrite stabiliser, plays a role in the solid solution hardening to improve creep resistance. It also helps to resist the detrimental effects of chlorides.
- Niobium (Nb) and Titanium (Ti) act as stabilising elements to improve creep strength with fine transgranular precipitated carbides. Precipitate strengthening is maximised by the optimal ratio of the elements to carbon.
- Carbon (C) works together with Nb, Ti and V in precipitate strengthening.
- Nitrogen (N) is added to enhance strength, mainly at room and cryogenic temperatures. It is also added to promote chromium diffusion and reduce the rate of chromium carbides precipitation ($M_{23}C_6$).
- Silicon (Si) is usually added to austenitic stainless steels containing Mo to improve corrosion resistance due to sulphuric acid. Silicon also improves oxidation resistance and is a ferrite stabilizer.

Table 2.1 The composition range of standard austenitic stainless steel in wt% [79].

	C	Si	Mn	Cr	Mo	Ni	N	Ti&Nb
Max.	0.08	3	2	25	2	20	0.15	0.2
Min.	0.02	0.5	1	16	-	8	-	-

2.6.3 Applications

Although, austenitic stainless steels are expensive due to high alloy content, they offer distinct engineering advantages, especially good formability and weldability that can reduce the overall cost compared to other groups of stainless steels. Among a wide variety of austenitic steels, the 300 series alloys are most commonly used [82]. Most of these alloys are based on 18Cr-8Ni system, with additional alloying elements or modification to provide unique or enhanced properties.

For nuclear applications, Types 316 and 304 are very important [80]. They are used for the manufacturing of piping systems and boilers. Type 304 is the most common of austenitic grades, containing approximately 18% chromium and 8% nickel, whereas type 316 contains 16-18% chromium and 11% to 14% nickel. Type 316 also has molybdenum which is used to improve pitting corrosion resistance.

2.6.4 Esshete 1250

Another advanced austenitic stainless steel used in nuclear section is Esshete 1250. It was first developed by the former United Steel Company Ltd in 1960s [83]. Esshete 1250 contains Vanadium and Niobium to provide additional creep resistance and are typically used for applications in temperature range between 550^{o}C and 675^{o}C, for example as high-temperature superheater materials [84]. Figure 2.16 shows that the proof strength of this steel at 600^{o}C is 40% higher than Type 316. This enables the use of thinner tubing in Esshete 1250 compared to other austenitic steels which results in a considerable cost saving. Esshete 1250 also has good weldability and can be readily welded with either inert gas or metal arc welding, as it incorporates approximately 6% manganese in alloy composition [82]. This material is used as a superheater boiler tube material in UK power stations, especially in plants operated by EDF Energy [6]. The specification for Esshete 1250 is summarized in Table 2.2.

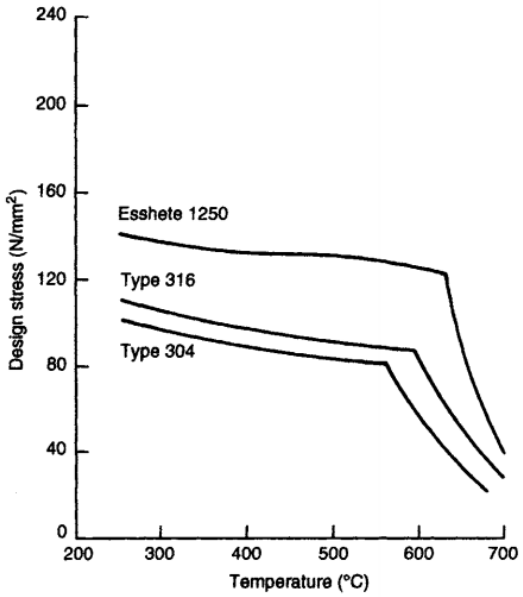

Figure 2.16 Design stress values for austenitic stainless steels according to BS 113:1992 (Design and manufacture of water tube steam generating plant) [83].

Table 2.2 The composition of Esshete 1250 in wt% [85].

	C	Si	Mn	P	S	Cr	Mo	Ni	B	N	V
Max.	0.06	0.2	5.5	-	-	14	0.8	9	0.003	0.75	0.15
Min.	0.15	1	7	0.035	0.015	16	1.2	11	0.009	1.25	0.4

2.7 WELD RESIDUAL STRESS

Welds made from austenitic stainless steel are not normally post-weld heat treated before engineering service, as this leads to unnecessary material degradation, such as low fracture toughness [6, 86]. This leads to the presence of high tensile residual stress in the structure which has an undesirable effect on life, because the residual stress alone can initiate cracking even before a component is subjected to service loads [87, 88]. In addition, tensile residual stresses can combine with stresses due to service loads to increases the potential for crack initiation and the higher rate of growth of defects [89]. Therefore, the characterisation of the magnitude and profile of residual stress and understanding its effects on the fracture behaviour is necessary in order to perform accurate and reliable structural integrity assessments.

2.7.1 Causes of residual stresses in weldments

"Welding residual stresses are a consequence of the fluctuating inhomogeneous temperature distribution arising in the course of different welding processes in and around the weld seam. Heating and the cooling periods are of the importance [90]". Some aspects that contribute to the amount and distribution of welding residual stresses are as follows:

- **Residual stresses due to shrinking processes [90, 91]**

A major cause of welding residual stress comes from the impeded shrinkage process, which occurs when heated and cooled regions are in the neighbourhood. In the beginning of welding process, the stress in the region below the arc and the weld pool is almost zero, as the molten metal cannot support any load. During the cooling process, molten metal is cooled down and becomes solid. In this state, the weld metal tries to shrink but it is restrained by the cold metal surrounding it. This results in the development of tensile residual stress in the weld seam at the end of the cooling process. If the amount of shrinkage is high enough, the tensile residual stress in this zone may reach the yield strength of weld seam material.

- **Residual stresses due to quenching process [90]**

The residual stresses from quenching process occur particularly in case of thick plates. The considerable temperature difference between the outer surface and the core layer of the plate during the cooling process generates these thermal residual stresses. If the residual stresses exceed the yield strength of the material, it results in plastic deformations which leads to residual stress after cooling.

- **Residual stresses due to phase transformations**

In the case of steels, transformation from austenite to martensite or ferrite during cooling has a significant influence on the residual stress and distortion. Martensite is formed by inheriting carbon atom from parent austenite which increase material volume [92]. This results in the development of compressive residual stresses in transformed volumes and balance tensile residual stress in adjacent volumes [93].

2.7.2 Measurement of residual stresses in weldments

Measuring residual stress is very important not only for performing an accurate safety assessment but also for validating the analytical and numerical models. In fact, there are many techniques available for measuring residual stress in metals. These techniques are generally classified into non-destructive, semi-destructive and totally destructive methods, as shown in Figure 2.17.

The non-destructive methods usually measure some physical or crystallographic parameter and relate it to the stress inside the material [94]. These methods are cheap and have short measuring time comparing with the other two methods, as the preparation of the part prior to the test is not time-consuming. These techniques are suitable for any structure that needs to be inspected periodically to prevent failure, e.g. bridges, aircraft structures or offshore platforms.

The destructive and semi-destructive methods are based on the measurement of deformations due to the release of residual stresses which occur due to material removal. The difference between these two methods is that semi-destructive methods still remain some part of the weld section, whereas with destructive methods, there are no further measurements that can be taken on the welded section after the residual stresses measurement [95].

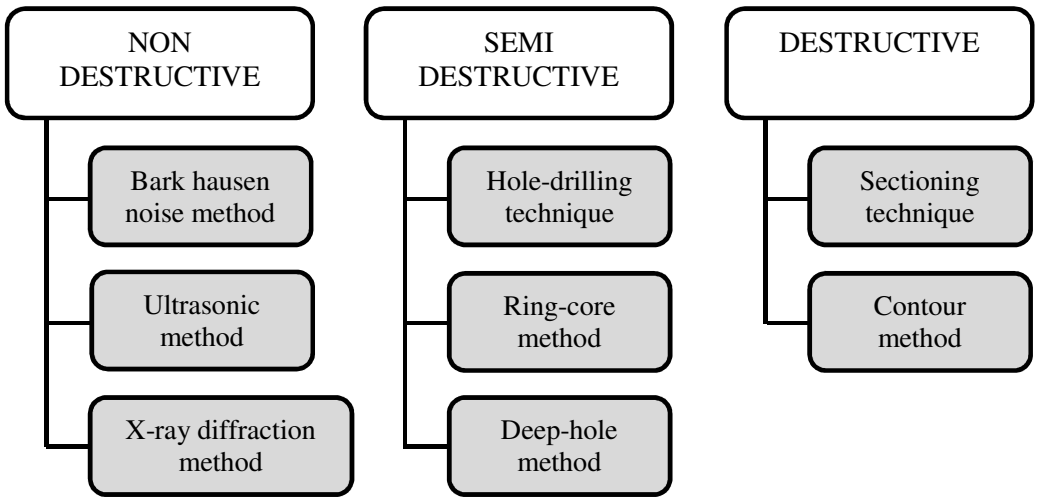

Figure 2.17 Residual stress measuring techniques [94].

2.7.3 Deep hole drilling technique

The Deep Hole Drilling (DHD) technique was first developed in the UK for nuclear industry in 1974 by Beany, Zhdanov and Gonchar [96, 97]. This technique was later reviewed and further developed by David Smith and his team at University of Bristol [95, 98-100]. DHD is one of the most popular semi-destructive methods, since this method is relatively simple and quick in terms of data collection and can be applied to many groups of materials. This technique has the ability to measure residual stresses at depths of up to 450 mm away from the free surface [101]. In addition, the apparatus required to perform DHD is portable and relatively inexpensive.

The procedure of the DHD technique can be explained by using a schematic diagram in Figure 2.18 [98, 102]. The process starts by attaching the reference bushes on the outer surfaces of a component used to measure the residual stress. The bushes have to be positioned at the start and end points of a reference hole which is later drilled through the specimen with a gun drill, as shown in Figure 2.18a.

After that, the initial diameter of the reference hole is measured through the entire thickness of component using an air probe (Figure 2.18b). Since this step is quite sensitive, it is necessary to recalibrate the air pressure gauge every few hours in order to maintain its accuracy.

The next step is to trepan a core of material around the reference hole using electro-discharge machining (EDM), as shown in Figure 2.18c. This step make the stress contained in material between the hole and the core to relax which causes the change of reference hole diameter. The final diameter of reference hole is re-measured and the change in diameter is then used to calculate the original residual stresses presented as a function of depth.

Although the DHD method has now become a standard technique for the measurement of residual stress in the material, it still has some accuracy problems. One of the reasons is that the traditional formulae employed in stress calculations are derived from plane stress condition. The second reason is that the effect of plastic deformation produced in the drilling process is ignored. Kitano et al. [102] have modified the stress evaluation formula for plane strain conditions. This formula has

been proven to measure the residual stress fields in thick objects better than the traditional formula. In addition, Kitano also proposed a new procedure which can evaluate the effect of plastic deformation occurring in the drilling process. Another development in DHD technique was made by Bateman et al. [103]. They improved this method to allow the measurement of residual stresses in orthotropic materials such as laminated composite components.

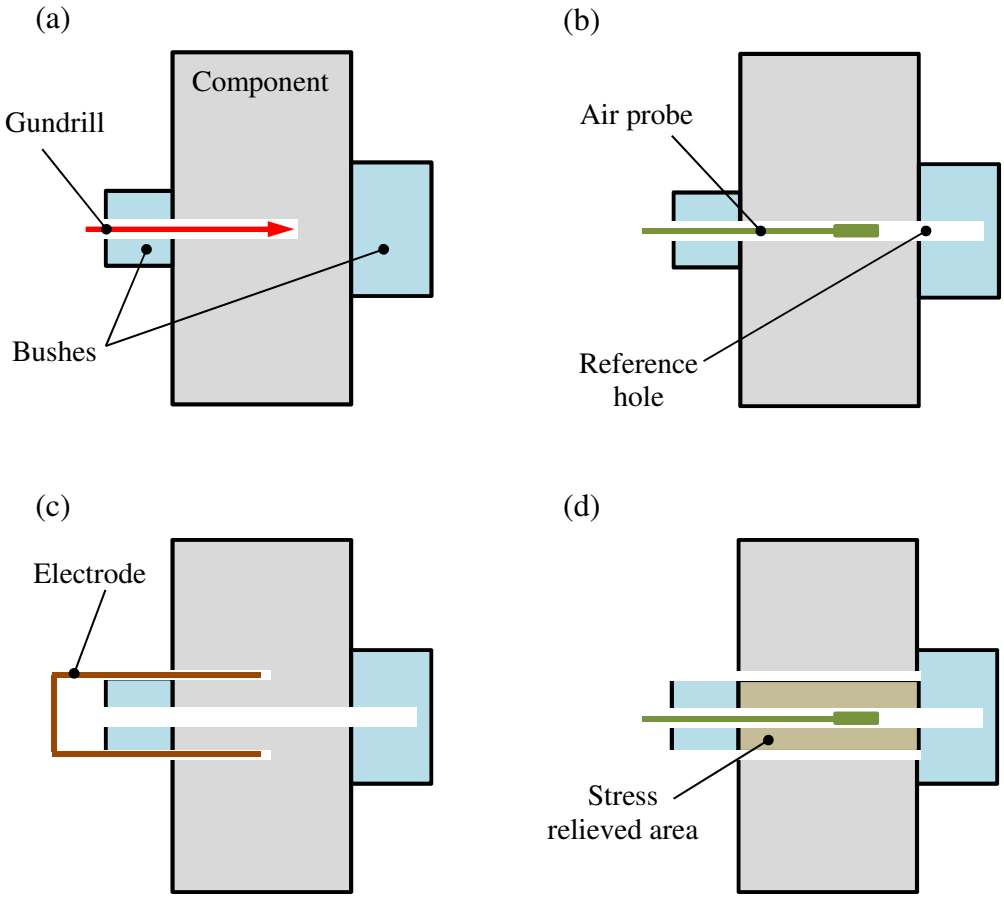

Figure 2.18 The stages of the DHD technique : a) gundrilling of the reference hole, b) measurement of reference hole diameter, c) trepanning and d) re-measurement of the reference hole [98].

CHAPTER 3

FINITE ELEMENT ANALYSIS FOR A PRESSURE-DEPENDENT PLASTICITY MODEL

3.1 INTRODUCTION

The heart of the implementation of plasticity models in FE analysis is the integration of the constitutive equations which are usually given in rate form. Several methods for the integration of elastoplastic constitutive equations have been proposed in literature. Earlier integrating schemes were based on the methods which were equivalent to Forward Euler but used different schemes for solving non-linear equilibrium equations to move the calculations forward, such as initial stress method and tangent modulus method [104-107]. However, these approaches still had conditional stability and required a small load step in the calculation.

In order to achieve unconditional stability, the concepts of predictor-corrector methods were developed. In 1964 Wilkins [108] proposed the well-known radial return algorithm which is a particular case of elastic predictor-plastic corrector algorithms. This algorithm has become the most widely used integration procedure for elastoplasticity and involves two main parts; elastic predictor part, and plastic corrector part. In the predictor part, an elastic predictor or 'trial stress' tensor is simply calculated from the given strain increment tensor by the application of Hooke's law. This trial stress tensor is then substituted into the yield function to check the behaviour of the material. If the value of yield function is still less than zero, then the material behaviour is elastic. For this case, the trial stress will become the required stress at the end of the time increment and no corrector step is necessary. However, if the stress point is outside the yield surface which means that the material behaviour is plastic, the corrector iteration performs the function to bring the stress point back on to the yield surface. This process must be performed under the satisfaction of the consistency condition. This procedure is shown schematically in Figure 3.1.

Based on the concept above, various return mapping algorithms for the plastic corrector part have been established. The purpose of these correctors is to create the precise route for taking stress point back on to the yield surface in the stress space. For example, Ortiz and Popov [109] presented two important return mapping algorithms which were derived by adopting the generalised versions of the classical trapezoidal and midpoint rules. They also assessed the accuracy and stability of both algorithms and found that the choice of the algorithmic parameter $\alpha = 0.5$ provides the best accuracy for small strain increments but in the presence of large strain increments larger values of α may result in improved accuracy. In addition, the stability properties of the generalized trapezoidal rule are very sensitive to the degree of distortion of the loading surface, whereas the generalized midpoint rule is unconditionally stable for $\alpha \geq 0.5$, regardless of the choice of loading surface.

Aravas [110] extended the idea within the framework of the radial return algorithm by including the first invariant for the hydrostatic stress into the corrector part. This algorithm is very popular and widely used for a class of the pressure-dependent elastoplasticity models, such as Gurson and Rousselier models. He also provided the formulation for calculating the consistent tangent moduli which is consistent with this algorithm. However, the consistent tangent moduli formulation provided by Aravas is very complicated and sometimes impossible to implement, as it requires matrix inversion during the computation.

In order to solve Aravas's problem, Zhange [111] developed an explicit expression for the linearization moduli which is consistent with a closest point return mapping algorithm. The significant advantage of this methodology is that no matrix inversion is required in the consistent tangent moduli expression. In addition, Zhange [112, 113] also studied the accuracies of the return mapping algorithm using iso-error map by formulating a class of generalized mid-point algorithm for the Gurson-Tvergaard model. This algorithm was later modified in order to derive the seven-constant formula for explicitly calculating the tangent muduli consistent with the generalized mid-point algorithm [114].

Another return mapping algorithm which needs to be mentioned here is a canonical form algorithm presented by Keavey [115, 116]. Unlike other approaches, the

process of this algorithm is essentially numerical and does not involve the difficult algebraic manipulations. In this approach, consistent tangent moduli can be automatically obtained by a two-stage process of partial elimination.

In this chapter, a mathematical model of elastoplastic constitutive relation and the concept of the radial return method are reviewed. The numerical scheme proposed by Aravas and Zhang are studied in more detail. Their algorithms are derived again in the tensorial form for the integration of Rousselier damage model described in chapter 4.

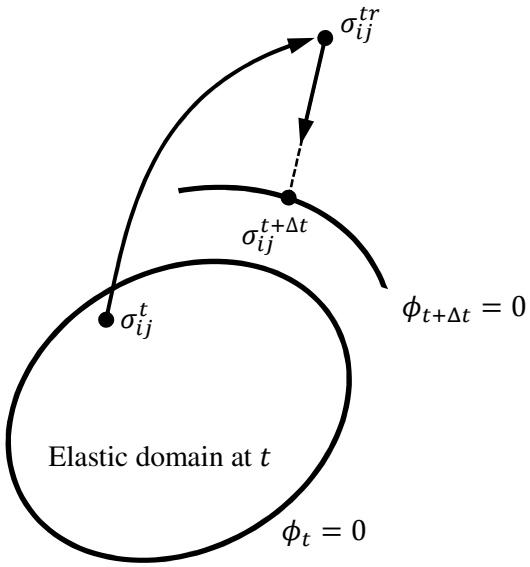

Figure 3.1 The geometric illustration of the concept of radial return method [117].

3.2 ELASTOPLASTIC CONSTITUTIVE RELATIONS [110, 118, 119]

According to the small deformation theory of plasticity, the strain rate decomposition is

$$d\epsilon_{ij} = d\epsilon_{ij}^{e} + d\epsilon_{ij}^{p} \tag{3.1}$$

where $d\epsilon_{ij}$, $d\epsilon_{ij}^{e}$, and $d\epsilon_{ij}^{p}$ denote the differential change in the total, elastic and plastic strain tensors respectively.

Assuming small elastic strains, we can write

$$\sigma_{ij} = \frac{\partial W}{\partial \epsilon_{ij}^e} \tag{3.2}$$

where σ_{ij} is the Cauchy stress tensor, and $W = W\left(\epsilon_{ij}^e\right)$ is the elastic strain energy potential. For the case of isotropic elasticity, Eq. (3.2) becomes

$$\sigma_{ij} = C_{ijkl}^e \epsilon_{kl}^e \tag{3.3}$$

where $C_{ijkl}^e = 2G\delta_{ik}\delta_{jl} + \left(K - \frac{2}{3}G\right)\delta_{ij}\delta_{kl}$ is the fourth order elasticity tensor. G and K are the elastic shear and bulk moduli.

The stress tensor in Eq.(3.3) can be decomposed into deviatoric component, S_{ij}, and spherical (mean) component, σ_m, as :

$$\sigma_{ij} = \sigma_m \delta_{ij} + S_{ij} \tag{3.4}$$

where $\sigma_m = \frac{1}{3}\sigma_{kk}$ and δ_{ij} is the Kronecker-Delta or second order identity tensor.

Normally, the elastic limit of material under combined state of stress can be defined by yield function which involves the first and second invariants of the stress tensor. The yield function can be expressed as :

$$\phi\left(p, q, H^i\right) = 0 \tag{3.5}$$

where p and q are hydrostatic pressure and von Mises equivalent stress respectively which are defined as :

$$p = -\sigma_m \tag{3.6}$$

$$q = \sqrt{\frac{3}{2}S_{ij}S_{ij}} \tag{3.7}$$

$H^i, i = 1, 2, \ldots$ is the internal state variable such as hardening. From Eq.(3.5), the yield criterion is given by

$\phi < 0$: Elastic deformation

$\phi = 0$: Plastic deformation

In case of associated flow rule, the increment in the plastic strain tensor is in a direction which is normal to the tangent to the yield surface at the load point as shown in Figure 3.2, and may be written in term of the yield function, ϕ as,

$$d\epsilon_{ij}^{p} = d\lambda \frac{\partial \phi}{\partial \sigma_{ij}} \tag{3.8}$$

where $d\lambda$ is a positive scalar factor of proportionality, which is non-zero only when plastic deformation occurs.

Using Eqs. (3.6) and (3.7), Eq. (3.4) becomes

$$\sigma_{ij} = -p\delta_{ij} + \frac{2}{3} q n_{ij} \tag{3.9}$$

where n_{ij} is the unit vector in the deviatoric space normal to the yield surface. It is defined by using Eq. (3.7)

$$n_{ij} = \frac{\partial q}{\partial S_{ij}} = \frac{3}{2} \frac{S_{ij}}{q} \tag{3.10}$$

Like the stress tensor, the plastic strain increment in Eq.(3.8) can be decoupled into volumetric $\left(d\epsilon_{ij}^{p}\right)_{V}$ and deviatoric $\left(d\epsilon_{ij}^{p}\right)_{D}$ parts by,

$$\begin{aligned} d\epsilon_{ij}^{p} &= \left(d\epsilon_{ij}^{p}\right)_{V} + \left(d\epsilon_{ij}^{p}\right)_{D} \\ &= d\lambda \left(\frac{\partial \phi}{\partial p} \frac{\partial p}{\partial \sigma_{ij}} + \frac{\partial \phi}{\partial q} \frac{\partial q}{\partial \sigma_{ij}} \right) \\ &= -\frac{1}{3} d\lambda \frac{\partial \phi}{\partial p} \delta_{ij} + d\lambda \frac{\partial \phi}{\partial q} n_{ij} \end{aligned}$$

$$d\epsilon_{ij}^{p} = \frac{1}{3} d\epsilon_{p} \delta_{ij} + d\epsilon_{q} n_{ij} \tag{3.11}$$

where $d\epsilon_{p}$ and $d\epsilon_{q}$ are the variables corresponding to volumetric and deviatoric strain increments. They are defined by:

$$d\epsilon_{p} = -d\lambda \frac{\partial \phi}{\partial p} \tag{3.12a}$$

$$d\epsilon_{q} = d\lambda \frac{\partial \phi}{\partial q} \tag{3.12b}$$

For classical plasticity model (pressure independent model), $d\epsilon_q$ becomes zero as there is no volumetric component of plastic strain tensor. By eliminating $d\lambda$ from the above two equations, one obtains

$$d\epsilon_p \left(\frac{\partial \phi}{\partial q}\right) + d\epsilon_q \left(\frac{\partial \phi}{\partial p}\right) = 0 \tag{3.13}$$

The final ingredient in the plasticity model is a set of evolution equations for state variable, H^{α}, such as equivalent plastic strain or damage parameters. The evolution of these variables are given by

$$dH^{\alpha} = h^{\alpha}\left(d\epsilon_{ij}^{p}, \sigma_{ij}, H^{\beta}\right) \tag{3.14}$$

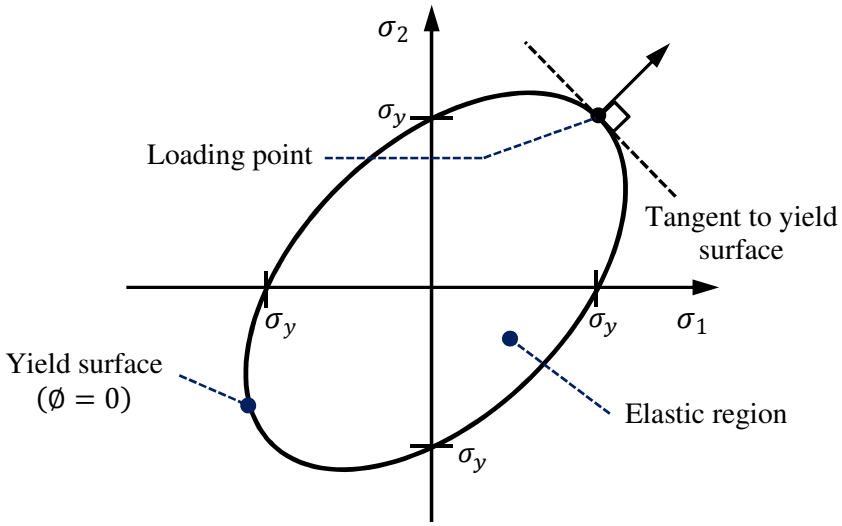

Figure 3.2 Graphical representation of associated flow rule [119].

3.3 A RETURN MAPPING ALGORITHM FOR PRESSURE-DEPENDENT ELASTOPLASTICITY MODEL

In FE analysis, the integration of constitutive equations is carried out at the Gaussian integration points. The analysis is carried out incrementally and the solution is assumed to be known at the start of each increment. Given a strain increment $\Delta\epsilon_{ij}$, one needs to calculate the stress and state variables at the end of each increment.

The integration procedure which is discussed here is known as a "*radial return method*". In this method, a step forward in time takes the updated stress, σ_{ij}^{tr} outside the yield surface. This stress is called trial stress or elastic predictor. The trial stress is then updated with plastic correction to bring it back onto the yield surface at $t + \Delta t$ (Figure 3.1). Although the mathematical basis of the return mapping method for the pressure-dependent plasticity model has been well established [110-112], the details of this method are reviewed again in this section in order to maintain consistency of this thesis.

3.3.1 The radial return method

In what follows, the time at which a variable is evaluated will be indicated by a superscript. For the current time step $t + \Delta t$, the superscript will be omitted. We first start with the algorithm for the total strain tensor :

$$\epsilon_{ij} = \epsilon_{ij}^{t} + \Delta\epsilon_{ij} \tag{3.15}$$

where $\Delta\epsilon_{ij}$ is the total strain increment tensor.

The idealized stress-strain behaviour can be explained by using Figure 3.3. From this Figure, the stress tensor achieved at a strain of ϵ_{ij} can be obtained by using Eqs. (3.1) and (3.3) :

$$\begin{aligned}\sigma_{ij} &= C_{ijkl}^{e}\epsilon_{kl}^{e} = C_{ijkl}^{e}\left(\epsilon_{kl} - \epsilon_{kl}^{p}\right)\\ &= C_{ijkl}^{e}\left[\epsilon_{kl}^{t} + \Delta\epsilon_{kl} - \left(\epsilon_{kl}^{p}\right)^{t} - \Delta\epsilon_{kl}^{p}\right]\\ \sigma_{ij} &= \sigma_{ij}^{tr} - C_{ijkl}^{e}\left(\Delta\epsilon_{kl}^{p}\right)\end{aligned} \tag{3.16}$$

where $\sigma_{ij}^{tr} = C_{ijkl}^{e}\left[(\epsilon_{kl}^{e})^{t} + \Delta\epsilon_{ij}\right]$ is the trial stress or elastic predictor and $(\epsilon_{kl}^{e})^{t}$ is the elastic strain tensor at time step t.

Considering the second term of right hand side of Eq. (3.16)

$$\begin{aligned}C_{ijkl}^{e}\left(\Delta\epsilon_{kl}^{p}\right) &= \left[2G\delta_{ik}\delta_{jl} + \left(K - \frac{2}{3}G\right)\delta_{ij}\delta_{kl}\right]\Delta\epsilon_{kl}^{p}\\ &= 2G\Delta\epsilon_{ij}^{p} + K\Delta\epsilon_{kk}^{p}\delta_{ij} - \frac{2}{3}G\Delta\epsilon_{kk}^{p}\delta_{ij}\end{aligned} \tag{3.17}$$

Substituting Eq. (3.11) into (3.17),

$$C^e_{ijkl}\left(\Delta\epsilon^p_{kl}\right) = 2G\Delta\epsilon_q n_{ij} + K\Delta\epsilon_p\delta_{ij} \tag{3.18}$$

Hence, Eq. (3.16) can now be rewritten as :

$$\sigma_{ij} = \sigma^{tr}_{ij} - 2G\Delta\epsilon_q n_{ij} - K\Delta\epsilon_p\delta_{ij}$$

Using Eq.(3.9), this becomes

$$-p\delta_{ij} + \frac{2}{3}qn_{ij} = -p^{tr}\delta_{ij} + \frac{2}{3}q^{tr}n^{tr}_{ij} - 2G\Delta\epsilon_q n_{ij} - K\Delta\epsilon_p\delta_{ij} \tag{3.19}$$

The above equation shows that in the deviatoric stress plane, return to the yield surface is along n_{ij}. This means that S^{tr}_{ij} and S_{ij} are co-axial, and n_{ij} can be simply determined by [110, 120] :

$$n_{ij} = n^{tr}_{ij} = \frac{3}{2}\frac{S^{tr}_{ij}}{q^{tr}} \tag{3.20}$$

Applying this relation to Eq. (3.19),

$$p = p^{tr} + K\Delta\epsilon_p \tag{3.21a}$$

$$q = q^{tr} - 3G\Delta\epsilon_q \tag{3.21b}$$

Eq.(3.21) is the correction equation for the hydrostatic pressure and von Mises equivalent stress at $t + \Delta t$.

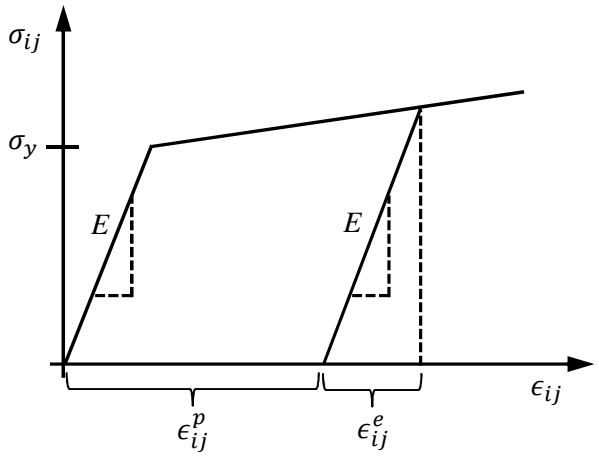

Figure 3.3 Classical decomposition of strain into elastic and plastic parts.

3.3.2 The solution method

From the previous sections, the increment of stress tensor and the evolution of the internal variables for pressure-dependent plasticity model can be obtained by solving the following set of non-linear equations:

$$\Delta\epsilon_p\left(\frac{\partial\Phi}{\partial q}\right)+\Delta\epsilon_q\left(\frac{\partial\Phi}{\partial p}\right)=0 \tag{3.22}$$

$$\Phi(p,q,H^\alpha)=0 \tag{3.23}$$

$$p=p^{tr}+K\Delta\epsilon_p \tag{3.24}$$

$$q=q^{tr}-3G\Delta\epsilon_q \tag{3.25}$$

$$\Delta H^\alpha=h^\alpha\left(\Delta\epsilon_p,\Delta\epsilon_q,p,q,H^\beta\right) \tag{3.26}$$

Aravas [110] suggested to solve this set of non-linear equations by Newton-Raphson method based on Taylor series expansion. According to this, $\Delta\epsilon_p$ and $\Delta\epsilon_q$ are chosen as the primary unknowns, and Eqs.(3.22) and (3.23) are treated as the basic equations in which p, q and ΔH^α are defined by Eqs.(3.24)-(3.26). Details of the solution method are given as follows:

By ignoring the higher order terms, and assuming that only 2 internal variables, $\Delta\epsilon_p$ and $\Delta\epsilon_q$, are involved with the model, the application of the Taylor series method to Eqs.(3.22) and (3.23) gives,

$$\begin{aligned}&\Delta\epsilon_p P+\Delta\epsilon_q Q\\&+d\Delta\epsilon_p\left\{P+\Delta\epsilon_p\frac{\partial P}{\partial\Delta\epsilon_p}+\Delta\epsilon_q\frac{\partial Q}{\partial\Delta\epsilon_p}\right\}+d\Delta\epsilon_q\left\{Q+\Delta\epsilon_p\frac{\partial P}{\partial\Delta\epsilon_q}+\Delta\epsilon_q\frac{\partial Q}{\partial\Delta\epsilon_q}\right\}\\&+dH^1\left\{\Delta\epsilon_p\frac{\partial P}{\partial H^1}+\Delta\epsilon_q\frac{\partial Q}{\partial H^1}\right\}+dH^2\left\{\Delta\epsilon_p\frac{\partial P}{\partial H^2}+\Delta\epsilon_q\frac{\partial Q}{\partial H^2}\right\}=0\end{aligned} \tag{3.27a}$$

$$\begin{aligned}&\Phi+\left(\frac{\partial\Phi}{\partial p}\frac{\partial p}{\partial\Delta\epsilon_p}+\frac{\partial\Phi}{\partial q}\frac{\partial q}{\partial\Delta\epsilon_p}\right)d\Delta\epsilon_p+\left(\frac{\partial\Phi}{\partial p}\frac{\partial p}{\partial\Delta\epsilon_q}+\frac{\partial\Phi}{\partial q}\frac{\partial q}{\partial\Delta\epsilon_q}\right)d\Delta\epsilon_q\\&+\frac{\partial\Phi}{\partial H^1}dH^1+\frac{\partial\Phi}{\partial H^2}dH^2=0\end{aligned} \tag{3.27b}$$

where $P = \frac{\partial \Phi}{\partial q}$, $Q = \frac{\partial \Phi}{\partial p}$. $d\Delta\epsilon_p$ and $\mathrm{d}\Delta\epsilon_q$ are defined as the correction values for $\Delta\epsilon_p$ and $\Delta\epsilon_q$ respectively.

The values of dH^1 and dH^2 in Eq.(3.27) can be determined as functions of $d\Delta\epsilon_p$ and $d\Delta\epsilon_q$ from implicit differential equation as follows:

$$dH^1 = \frac{-1}{\Omega}\left\{\left(\frac{\partial G^2}{\partial H^2}\frac{\partial G^1}{\partial \Delta\epsilon_p} - \frac{\partial G^1}{\partial H^2}\frac{\partial G^2}{\partial \Delta\epsilon_p}\right) d\Delta\epsilon_p + \left(\frac{\partial G^2}{\partial H^2}\frac{\partial G^1}{\partial \Delta\epsilon_q} - \frac{\partial G^1}{\partial H^2}\frac{\partial G^2}{\partial \Delta\epsilon_q}\right) d\Delta\epsilon_q\right\}$$

$$-\frac{1}{\Omega}\left\{\left(\frac{\partial G^2}{\partial H^2}\frac{\partial G^1}{\partial p} - \frac{\partial G^1}{\partial H^2}\frac{\partial G^2}{\partial p}\right)\frac{\partial p}{\partial \Delta\epsilon_p} d\Delta\epsilon_p + \left(\frac{\partial G^2}{\partial H^2}\frac{\partial G^1}{\partial q} - \frac{\partial G^1}{\partial H^2}\frac{\partial G^2}{\partial q}\right)\frac{\partial q}{\partial \Delta\epsilon_q} d\Delta\epsilon_q\right\} \quad (3.28a)$$

$$dH^2 = \frac{-1}{\Omega}\left\{\left(-\frac{\partial G^2}{\partial H^1}\frac{\partial G^1}{\partial \Delta\epsilon_p} + \frac{\partial G^1}{\partial H^1}\frac{\partial G^2}{\partial \Delta\epsilon_p}\right) d\Delta\epsilon_p + \left(-\frac{\partial G^2}{\partial H^1}\frac{\partial G^1}{\partial \Delta\epsilon_q} + \frac{\partial G^1}{\partial H^1}\frac{\partial G^2}{\partial \Delta\epsilon_q}\right) d\Delta\epsilon_q\right\}$$

$$-\frac{1}{\Omega}\left\{\left(-\frac{\partial G^2}{\partial H^1}\frac{\partial G^1}{\partial p} + \frac{\partial G^1}{\partial H^1}\frac{\partial G^2}{\partial p}\right)\frac{\partial p}{\partial \Delta\epsilon_p} d\Delta\epsilon_p + \left(-\frac{\partial G^2}{\partial H^1}\frac{\partial G^1}{\partial q} + \frac{\partial G^1}{\partial H^1}\frac{\partial G^2}{\partial q}\right)\frac{\partial q}{\partial \Delta\epsilon_q} d\Delta\epsilon_q\right\} \quad (3.28b)$$

where

$$\Omega = \left(\frac{\partial G^1}{\partial H^1}\right)\left(\frac{\partial G^2}{\partial H^2}\right) - \left(\frac{\partial G^2}{\partial H^1}\right)\left(\frac{\partial G^1}{\partial H^2}\right) \quad (3.29)$$

G^1 and G^2 are the functions made by regrouping the implicit function in Eq.(3.26).

$$G^1 = \Delta H^1 - h^1\left(\Delta\epsilon_p, \Delta\epsilon_q, p, q, H^1, H^2\right) \quad (3.30a)$$

$$G^2 = \Delta H^2 - h^2\left(\Delta\epsilon_p, \Delta\epsilon_q, p, q, H^1, H^2\right) \quad (3.30b)$$

Introducing Eq.(3.28) into Eq.(3.27) and replacing $d\Delta\epsilon_p$ and $d\Delta\epsilon_q$ by c_p and c_q, leads to the reduced form of the Newton-Raphson equations as follows,

$$A_{11}c_p + A_{12}c_q = b_1 \quad (3.31a)$$

$$A_{21}c_p + A_{22}c_q = b_2 \quad (3.31b)$$

where A_{ij} and b_i are given in Appendix I. Eq.(3.31) is solved for c_p and c_q, and the values of $\Delta\epsilon_p$ and $\Delta\epsilon_q$ are then updated by

$$\Delta\epsilon_p = \Delta\epsilon_p + c_p \quad (3.32a)$$

$$\Delta\epsilon_q = \Delta\epsilon_q + c_q \quad (3.32b)$$

The values of p and q are then updated using Eqs.(3.24) and (3.25) and the increment of the state variables, ΔH^1 and ΔH^2, are updated by solving Eq.(3.26). This iterative loop has to be continued until the values of $\Delta\epsilon_p$ and $\Delta\epsilon_q$ converge.

Finally, the stress and strain tensors are updated by Eqs.(3.9), (3.11) and (3.15), to give equations below :

$$\sigma_{ij} = -p\delta_{ij} + q\left(\frac{S_{ij}^{tr}}{q^{tr}}\right) \tag{3.33}$$

$$\Delta\epsilon_{ij}^{p} = \frac{1}{3}\Delta\epsilon_p\delta_{ij} + \frac{3}{2}\left(\frac{S_{ij}^{tr}}{q^{tr}}\right)\Delta\epsilon_q \tag{3.34}$$

$$\epsilon_{ij}^{e} = \left(\epsilon_{ij}^{e}\right)^{t} + \Delta\epsilon_{ij} - \Delta\epsilon_{ij}^{P} \tag{3.35}$$

The difficulty with Aravas's method is that in each iteration of Newton's method for calculating the values of $\Delta\epsilon_p$ and $\Delta\epsilon_q$, the values of H^α are required to be updated. The method employed to update H^α is again the Newton's method. This means that many iterations are required to obtain the solution. For example, if 10 iterations are required to solve Eqs.(3.22) and (3.23), then in each iteration another 10 iterations are required to solve Eq.(3.26). Thus, the total number of iterations required to solve this problem is 100. Small increments may be taken to ensure that the solution by this method converges. Beardsmore et al. [121] presented a new approach based on a hybrid solution method and a trust region method. This method utilises iterative corrections and a trust region surrounding the current estimation solution. In the early stages of the iteration, the steepest descent method is used to improve the solution when the estimated solution is far from the true solution. Once the estimated solutions are in the acceptable region, Newton's method is then used to obtain the solutions for the final stages.

3.4 THE SOLUTION METHODS FOR FINITE ELEMENT ANALYSIS

At present, the FE method is one of the most popular tools used to obtain solutions required in both research and industrial design. Several algorithms with different associated computational costs are implemented in FE codes for solving problem in various fields. In the field of solid mechanics, especially for non-linear quasi-static

problems, the FE solution algorithms can be classified into implicit or explicit methods.

The implicit method refers to the procedure that the solution at time $t + \Delta t$ is determined based on the information at time $t + \Delta t$, whereas the explicit method solves for solution at time $t + \Delta t$ using the information at time t. In the implicit method, a set of FE equations are formulated from static equilibrium, and solutions are determined by the iteration method which is performed until a convergence criterion is satisfied for each increment. On the other hand, the finite element equations in the explicit approach are established based on the dynamic equilibrium equation which can be solved directly to obtain the solution at the end of increment without iteration.

The comparison between implicit and explicit methods for different nonlinear problems has been reported in literature [122-125]. The main advantage of implicit method is that the equilibrium conditions are checked at the end of each time or load step in order to minimize the residual force vector which is specified as tolerance [125]. This makes implicit method to be unconditionally stable which can use larger time steps to solve problems. However, the unconditionally stable implicit method may encounter some difficulties which are summarized as follows [123, 125]:

- Requiring a material Jacobian Matrix which is difficult to evaluate for complex constitutive laws.
- High computation times and high memory requirement.
- Local instabilities cause force equilibrium difficult to achieve which often leads to convergence problems.
- Difficulties in dealing with complex non-linear contact and tribological boundary conditions.

As mentioned above, the explicit method does not involve the iterative technique, so it requires much less disk space and memory than the implicit method for the same simulation. This method is more robust and efficient when it is used to solve the more complicated contact problems. However, the explicit method is conditionally stable for which the maximum time increment must be less than a critical value of

the smallest transition time for dilational wave to cross any element in the mesh [123]. Another limitation is that the nature of the explicit method is more suitable for transient problems. Hence, when this method is used for quasi-static problem, the inertia effects must be small enough to be neglected. In order to achieve this condition, the ratio of the kinetic energy to the internal energy must be less than 5% [124, 126].

The implicit and explicit methods have been usually implemented into several FE codes, such as ABAQUS. Learning and understanding the procedures of these two methods enable the user to feel more confident when using these methods. This section presents details of implicit and explicit solution procedures.

3.4.1 Static implicit method [112, 114]

In static implicit FE method, the virtual work principle is usually employed to explain the equilibrium at the end of an increment. This results in a set of non-linear equations for the nodal unknowns which must be solved by an iterative method.

Considering a material continuum body having volume V and bounding surface S which is subjected to surface traction t_i and distributed body force per unit volume f_i, the equilibrium equation for this body can be written as :

$$\int_S t_i \, dS + \int_V f_i \, dV = 0 \tag{3.36}$$

The true or Cauchy stress matrix σ_{ij} at a point on *S* is defined by $t_i = \sigma_{ji} n_j$ where n_j is the unit vector outward normal to *S* at the point. Using this definition together with divergence theorem of Gauss, the above equation reduce to :

$$\frac{\partial \sigma_{ji}}{\partial x_j} + f_i = 0 \tag{3.37}$$

Multiplying Eq.(3.37) by a 'virtual displacement δu_i' to obtain a single scalar equation applicable to all points of the continuum body,

$$\left(\frac{\partial \sigma_{ji}}{\partial x_j} + f_i\right) \delta u_i = 0 \tag{3.38}$$

Integrating Eq.(3.38) over the whole volume and then applying the chain rule and the divergence theorem gives,

$$\int_V \sigma_{ji} \frac{\partial \delta u_i}{\partial x_j} dV - \int_S t_i \delta u_i \, dS - \int_V f_i \delta u_i \, dV = 0 \tag{3.39}$$

The term $\frac{\partial \delta u_i}{\partial x_j}$ is the unit relative virtual displacement which can be decomposed into the virtual strain tensor and virtual rotation tensor. In case of small strain, Eq.(3.39) can be written as follows :

$$G(u_i) = \int_V \sigma_{ij} \, \delta \epsilon_{ij} dV - \int_S t_i \delta u_i \, dS - \int_V f_i \delta u_i \, dV \tag{3.40}$$

where σ_{ij} and ϵ_{ij} are any conjugate pairing of material stress and strain measures.

If Newton-Raphson method is used to determine a set of solutions of Eq.(3.40), the estimation of the root of Eq.(3.40) can be written as :

$$\Delta u_i^{n+1} = u_i^{n+1} - u_i^n = -\left\{\frac{\partial G(u_i^n)}{\partial u_i}\right\}^{-1} G(u_i^n) \tag{3.41}$$

The superscript n in Eq.(3.41) represents the number of iteration. This equation can be solved iteratively until the values of Δu_i^{n+1} are close to zero. $\frac{\partial G(u_i^n)}{\partial u_i}$ in Eq.(3.41) is known as the jacobian matrix of the governing equations and can be referred to as the global stiffness matrix. The derivation and the closed from of the complete jacobian matrix is presented in ABAQUS theory manual [127] :

$$\frac{\partial G(u_i^n)}{\partial u_i} = K_{MN} = \int_{V^0} B_{ij,M} D_{ijkl} B_{ij,N} \, dV^0 + J_{MN} \tag{3.42}$$

$B_{ij,M}$ and $B_{ij,N}$ matrices depend on the current position of the material point being to considered. This matrix defines the strain variation in terms of the variation of the kinematic variables. J_{MN} represents part of the global jacobian matrix which is explained in [127]. D_{ijkl} is the so-called consistent tangent moduli (CTM) of material. It is defined as :

$$D_{ijkl} = \frac{\partial \sigma_{ij}}{\partial \epsilon_{kl}} = \frac{\partial \Delta \sigma_{ij}}{\partial \Delta \epsilon_{kl}} \tag{3.43}$$

The convergence of Eq.(3.41) is controlled by the choice of CTM. In order to achieve the quadratic rate of asymptotic convergence, Simo and Taylor [120] proposed to derive the CTM by consistent linearization of the response functions used for updating the state variables.

3.4.2 Dynamic explicit method

The explicit method was originally developed and primarily used to solve dynamic problems involving deformable bodies. This procedure is based on the implementation of an explicit integration rule together with the use of diagonal or "lumped" element mass matrices, M_{ij} [127]. Considering the equations of motion for the body, the acceleration vector, $\ddot{u}_j$ can be computed at the start of increment n by:

$$\ddot{u}_i^{(n)} = M_{ij}^{-1}\left(F_j^n - I_j^n\right) \tag{3.44}$$

F_i^n and I_i^n are the applied load vector and the internal force vector respectively. Using the central difference integration scheme, $\ddot{u}_i$ can be written in terms of displacement vector, u_i, as follows:

$$\ddot{u}_i^{(n)} = \frac{u_i^{(n+1)} - 2u_i^{(n)} + u_i^{(n-1)}}{\Delta t^2} \tag{3.45}$$

Substituting Eq.(3.45) into (3.44), the explicit formulation for the displacement vector is :

$$u_i^{(n+1)} = 2u_i^{(n)} - u_i^{(n-1)} + \Delta t^2 M_{ij}^{-1}\left(F_j^n - I_j^n\right) \tag{3.46}$$

Based on above, the value of u_i at time $n+1$ is easy to obtain as only information at time n is needed. In addition, M_{ij} is diagonalised and it is a trivial process to invert it. However, the dynamic explicit procedure is conditionally stable. Its stability depends on the size of the time increment which must satisfy

$$\Delta t \leq \frac{2}{\omega_{max}} \tag{3.47}$$

where ω_{max} is the maximum element eigenvalue. A conservative estimate of the stable time increment is given by the minimum value for all elements in the model. The above stability limit can be written as :

$$\Delta t = min\left(\frac{L_e}{c^d}\right) \tag{3.48}$$

where L_e is the characteristic element dimension and c^d is the dilatational wave speed of the material.

Eq.(3.48) implies that the stable time increment in explicit analysis depends on the size of elements. "Although the incremental solution is easy to obtain using the explicit method, it is not unusual for the analysis to take 100,000 increments to produce a solution. In order to maintain the efficiency of the analysis, it is important to ensure that the sizes of the elements are as regular as possible [124]".

3.5 THE DERIVATION OF CTM WITH THE RADIAL RETURN METHOD [111, 112, 114]

According to section 3.5.1, the CTM defined in Eq.(3.43) needs to be consistent with the stress update procedure in order to achieve convergence for the analyses. For pressure-dependent elastoplasticity model, Zhang developed an explicit CTM formula which is consistent with a return mapping algorithm. This formula was derived in terms of hydrostatic and deviatoric components separately. Details of the derivation of this CTM are given below :

The deviatoric component of stress tensor presented in Eq.(3.16) is,

$$\begin{aligned} S_{ij} &= 2G\left\{\left(\epsilon_{ij}^{e}\right)_D^t + \left(\Delta\epsilon_{ij}\right)_D - \left(\Delta\epsilon_{ij}^{p}\right)_D\right\} \\ &= 2G\left(\epsilon_{ij}\right)_D^{tr} - 2G\left(\Delta\epsilon_{ij}^{p}\right)_D \\ S_{ij} &= S_{ij}^{tr} - 2G\left(\Delta\epsilon_{ij}^{p}\right)_D \end{aligned} \tag{3.54}$$

where $\left(\epsilon_{ij}\right)_D^{tr} = \left(\epsilon_{ij}^{e}\right)_D^t + \left(\Delta\epsilon_{ij}\right)_D$, $\left(\epsilon_{ij}^{e}\right)_D^t$ is the deviatoric component of the total elastic strain tensor at time step t, $\left(\Delta\epsilon_{ij}\right)_D$ and $\left(\Delta\epsilon_{ij}^{p}\right)_D$ are the deviatoric components of total and plastic strain increment, and $S_{ij}^{tr} = 2G\left(\epsilon_{ij}\right)_D^{tr}$ is the deviatoric component of the trial stress tensor,

Using relation $\left(\Delta\epsilon_{ij}^{p}\right)_D = \Delta\epsilon_q n_{ij}$ and Eq.(3.10), Eq.(3.49) becomes

$$S_{ij}^{tr} = \left[1 + \left(\frac{3G}{q}\right)\Delta\epsilon_q\right] S_{ij} = 2G\left(\epsilon_{ij}\right)_D^{tr} \tag{3.50}$$

Taking variation of Eq.(3.50) with respect to all quantities,

$$\left[1 + \left(\frac{3G}{q}\right)\Delta\epsilon_q\right]\partial S_{ij} + S_{ij}\partial\left[1 + \left(\frac{3G}{q}\right)\Delta\epsilon_q\right] = 2G\ \partial\left(\epsilon_{ij}\right)_D^{tr}$$

$$\left(1 + \frac{3G}{q}\Delta\epsilon_q\right)\partial S_{ij} + S_{ij}\frac{3G}{q}\left(\partial\Delta\epsilon_q - \frac{\Delta\epsilon_q}{q}\partial q\right) = 2G\ \partial\left(\epsilon_{ij}\right)_D^{tr} \tag{3.51}$$

With the relation given in Eq.(3.21b), Eq.(3.51) can be written as :

$$\frac{q^{tr}}{q}\partial S_{ij} + S_{ij}\frac{3G}{q}\left(\partial\Delta\epsilon_q - \frac{\Delta\epsilon_q}{q}\partial q\right) = 2G\ \partial\left(\epsilon_{ij}\right)_D^{tr}$$

$$\partial S_{ij} = 2G\frac{q}{q^{tr}}\partial\left(\epsilon_{ij}\right)_D^{tr} - S_{ij}\frac{3G}{q^{tr}}\partial\Delta\epsilon_q + S_{ij}\frac{3G}{q\,q^{tr}}\Delta\epsilon_q\partial q \tag{3.52}$$

∂q in Eq.(3.52) can be determined from Eq.(3.50). By taking the inner product of Eq.(3.50) with itself gives,

$$\left[1 + \left(\frac{3G}{q}\right)\Delta\epsilon_q\right]\sqrt{\frac{3}{2}S_{ij}S_{ij}} = 2G\sqrt{\frac{3}{2}\left(\epsilon_{ij}\right)_D^{tr}\left(\epsilon_{ij}\right)_D^{tr}}$$

$$q + 3G\Delta\epsilon_q = 2G\bar{\epsilon}_D^{tr} = q^{tr} \tag{3.53}$$

where $\bar{\epsilon}_D^{tr} = \sqrt{\frac{3}{2}\left(\epsilon_{ij}\right)_D^{tr}\left(\epsilon_{ij}\right)_D^{tr}}$

Differentiation of Eq.(3.53) yields

$$\partial q = \partial q^{tr} - 3G\partial\Delta\epsilon_q = 2G\partial\bar{\epsilon}_D^{tr} - 3G\partial\Delta\epsilon_q$$

$$\partial q = 3G\left[\frac{S_{ij}^{tr}}{q^{tr}}\partial\left(\epsilon_{ij}\right)_D^{tr} - \partial\Delta\epsilon_q\right] \tag{3.54}$$

Substituting Eq.(3.54) into Eq.(3.52) and rearranging,

$$\partial S_{ij} = 2G\frac{q}{q^{tr}}\partial\left(\epsilon_{ij}\right)_D^{tr} - S_{ij}\frac{3G}{q^{tr}}\partial\Delta\epsilon_q + S_{ij}\frac{3G}{qq^{tr}}\Delta\epsilon_q 3G\left[\frac{S_{ij}^{tr}}{q^{tr}}\partial\left(\epsilon_{ij}\right)_D^{tr} - \partial\Delta\epsilon_q\right]$$

$$\partial S_{ij} = 2G\frac{q}{q^{tr}}\partial\left(\epsilon_{ij}\right)_D^{tr} + \frac{9G^2}{q(q^{tr})^2}\Delta\epsilon_q S_{ij}S_{kl}^{tr}\ \partial\left(\epsilon_{ij}\right)_D^{tr} - \frac{3G}{q}\ S_{ij}\partial\Delta\epsilon_q \tag{3.55}$$

Alternatively, Eq.(3.55) can be written as :

$$\partial S_{ij} = 2G\frac{q}{q^{tr}}\left(\delta_{ik}\delta_{jl}\right)\partial\left(\epsilon_{ij}\right)_D^{tr} + \frac{4G^2}{q^{tr}}\Delta\epsilon_q\left(\frac{3S_{ij}}{2q}\right)\left(\frac{3S_{kl}^{tr}}{2q^{tr}}\right)\partial\left(\epsilon_{ij}\right)_D^{tr} - 2G\left(\frac{3S_{ij}}{2q}\right)\partial\Delta\epsilon_q$$

$$\partial S_{ij} = \left\{2G\frac{q}{q^{tr}}J_{ijkl} + \frac{4G^2}{q^{tr}}\Delta\epsilon_q n_{ij}n_{kl}^{tr}\right\}\partial\left(\epsilon_{ij}\right)_D^{tr} - 2G\, n_{ij}\partial\Delta\epsilon_q \tag{3.56}$$

where $J_{ijkl} = \delta_{ik}\delta_{jl}$ is the fourth order unit tensor.

For all cases in which three direct strains are defined by a kinematic solution,

$$\partial\left(\epsilon_{ij}\right)_D^{tr} = \partial\left(\Delta\epsilon_{ij}\right)_D = \left(J_{ijkl} - \frac{1}{3}\delta_{ij}\delta_{kl}\right)\partial\epsilon_{kl} \tag{3.57}$$

and

$$\partial p = -K\delta_{pq}\partial\epsilon_{pq} + K\partial\Delta\epsilon_p \tag{3.58a}$$

$$\partial\sigma_m = K\delta_{ij}\delta_{pq}\partial\epsilon_{pq} - K\delta_{ij}\partial\Delta\epsilon_p \tag{3.58b}$$

Differentiation Eq.(3.4) and using Eqs.(3.58b) and (3.56) gives,

$$\partial\sigma_{ij} = K\delta_{ij}\delta_{pq}\partial\epsilon_{pq} - K\delta_{ij}\partial\Delta\epsilon_p$$
$$+\left\{2G\frac{q}{q^{tr}}J_{ijkl} + \frac{4G^2}{q^{tr}}\Delta\epsilon_q n_{ij}n_{kl}^{tr}\right\}\partial(\epsilon_{kl}^{tr})_D - 2G\, n_{ij}\partial\Delta\epsilon_q \tag{3.59}$$

Substituting Eq.(3.57) into Eq.(3.59),

$$\partial\sigma_{ij} = Z_{ijmn}\partial\epsilon_{mn} - K\delta_{ij}\partial\Delta\epsilon_p - 2G\, n_{ij}\partial\Delta\epsilon_q \tag{3.60}$$

where

$$Z_{ijmn} = \left(K - \frac{2}{3}G\frac{q}{q^{tr}}\right)\delta_{ij}\delta_{mn} + 2G\frac{q}{q^{tr}}J_{ijmn} + \frac{4G^2}{q^{tr}}\Delta\epsilon_q n_{ij}n_{mn} \tag{3.61}$$

The expressions for $\partial\Delta\epsilon_p$ and $\partial\Delta\epsilon_q$ in Eq.(3.60) can be determined by taking the variations of Eqs.(3.22) and (3.23) in terms of $\partial\sigma_{ij}$. By assuming that the model involves 2 internal variables, H^1 and H^2, the variations of Eqs.(3.22) and (3.23) in terms of $\partial\sigma_{ij}$ can be written as :

$$\partial\Delta\epsilon_p\left(\frac{\partial\Phi}{\partial q}\right)+\partial\Delta\epsilon_q\left(\frac{\partial\Phi}{\partial p}\right)$$

$$+\Delta\epsilon_p\left(\frac{\partial^2\Phi}{\partial p\partial q}\frac{\partial p}{\partial\sigma_{ij}}+\frac{\partial^2\Phi}{\partial q^2}\frac{\partial q}{\partial\sigma_{ij}}\right)\partial\sigma_{ij}+\Delta\epsilon_q\left(\frac{\partial^2\Phi}{\partial p^2}\frac{\partial p}{\partial\sigma_{ij}}+\frac{\partial^2\Phi}{\partial p\partial q}\frac{\partial q}{\partial\sigma_{ij}}\right)\partial\sigma_{ij}$$

$$+\left(\Delta\epsilon_p\frac{\partial^2\Phi}{\partial q\partial H^1}+\Delta\epsilon_q\frac{\partial^2\Phi}{\partial p\partial H^1}\right)\partial H^1+\left(\Delta\epsilon_p\frac{\partial^2\Phi}{\partial q\partial H^2}+\Delta\epsilon_q\frac{\partial^2\Phi}{\partial p\partial H^2}\right)\partial H^2=0 \tag{3.62}$$

$$\left(\frac{\partial\Phi}{\partial p}\frac{\partial p}{\partial\sigma_{ij}}+\frac{\partial\Phi}{\partial q}\frac{\partial q}{\partial\sigma_{ij}}\right)\partial\sigma_{ij}+\frac{\partial\Phi}{\partial H^1}\partial H^1+\frac{\partial\Phi}{\partial H^2}\partial H^2=0 \tag{3.63}$$

dH^1 and dH^2 from above equations can be written as functions of $d\sigma_{ij}$ by applying implicit differentiation to Eq.(3.30) as follows :

$$dH^1$$

$$=\frac{-1}{\Omega}\left\{\begin{array}{l}\left(\frac{\partial G^2}{\partial H^2}\frac{\partial G^1}{\partial\Delta\epsilon_p}-\frac{\partial G^1}{\partial H^2}\frac{\partial G^2}{\partial\Delta\epsilon_p}\right)d\Delta\epsilon_p+\left(\frac{\partial G^2}{\partial H^2}\frac{\partial G^1}{\partial\Delta\epsilon_q}-\frac{\partial G^1}{\partial H^2}\frac{\partial G^2}{\partial\Delta\epsilon_q}\right)d\Delta\epsilon_q\\+\left[\left(\frac{\partial G^2}{\partial H^2}\frac{\partial G^1}{\partial p}-\frac{\partial G^1}{\partial H^2}\frac{\partial G^2}{\partial p}\right)\frac{\partial p}{\partial\sigma_{ij}}+\left(\frac{\partial G^2}{\partial H^2}\frac{\partial G^1}{\partial q}-\frac{\partial G^1}{\partial H^2}\frac{\partial G^2}{\partial q}\right)\frac{\partial q}{\partial\sigma_{ij}}\right]d\sigma_{ij}\end{array}\right\} \tag{3.64a}$$

$$dH^2$$

$$=\frac{-1}{\Omega}\left\{\begin{array}{l}\left(-\frac{\partial G^2}{\partial H^1}\frac{\partial G^1}{\partial\Delta\epsilon_p}+\frac{\partial G^1}{\partial H^1}\frac{\partial G^2}{\partial\Delta\epsilon_p}\right)d\Delta\epsilon_p+\left(-\frac{\partial G^2}{\partial H^1}\frac{\partial G^1}{\partial\Delta\epsilon_q}+\frac{\partial G^1}{\partial H^1}\frac{\partial G^2}{\partial\Delta\epsilon_q}\right)d\Delta\epsilon_q\\+\left[\left(-\frac{\partial G^2}{\partial H^1}\frac{\partial G^1}{\partial p}+\frac{\partial G^1}{\partial H^1}\frac{\partial G^2}{\partial p}\right)\frac{\partial p}{\partial\sigma_{ij}}+\left(-\frac{\partial G^2}{\partial H^1}\frac{\partial G^1}{\partial q}+\frac{\partial G^1}{\partial H^1}\frac{\partial G^2}{\partial q}\right)\frac{\partial q}{\partial\sigma_{ij}}\right]d\sigma_{ij}\end{array}\right\} \tag{3.64b}$$

Substituting Eq.(3.64) into Eqs.(3.62) and (3.63) and rearranging,

$$\bar{A}_{11}\partial\Delta\epsilon_p+\bar{A}_{12}\partial\Delta\epsilon_q=\left(B_{11}\delta_{ij}+B_{12}n_{ij}\right)\partial\sigma_{ij} \tag{3.65a}$$

$$\bar{A}_{21}\partial\Delta\epsilon_p+\bar{A}_{22}\partial\Delta\epsilon_q=\left(B_{21}\delta_{ij}+B_{22}n_{ij}\right)\partial\sigma_{ij} \tag{3.65b}$$

where the constants $\bar{A}_{ij}$ and B_{ij} are given in Appendix II.

Substitution of Eq.(3.60) into Eq.(3.65) gives,

$$\partial\Delta\epsilon_p = \left(C_{11}\,\delta_{ij} + C_{12}n_{ij}\right)Z_{ijkl}\,\partial\epsilon_{kl} \tag{3.66a}$$

$$\partial\Delta\epsilon_q = \left(C_{21}\delta_{ij} + C_{22}n_{ij}\right)Z_{ijkl}\,\partial\epsilon_{kl} \tag{3.66b}$$

where the constants C_{ij} are presented in Appendix III.

Substitution of Eq.(3.66) into Eq.(3.60), yields an expression for the tangent moduli consistent with the radial return method for the general pressure-dependent elastoplastic model,

$$\partial\sigma_{ij} = M_{ijmn}\,Z_{mnkl}\,\partial\epsilon_{kl} \quad \rightarrow \quad D_{ijkl} = \frac{\partial\sigma_{ij}}{\partial\epsilon_{kl}} = M_{ijmn}\,Z_{mnkl} \tag{3.67}$$

where

$$M_{ijmn} = J_{ijmn} - M^I_{ijmn} - M^n_{ijmn} \tag{3.68a}$$

$$M^I_{ijmn} = K\left(C_{11}\delta_{ij}\delta_{mn} + C_{12}\delta_{ij}n_{mn}\right) \tag{3.68b}$$

$$M^n_{ijmn} = 2G\left(C_{21}n_{ij}\delta_{mn} + C_{22}n_{ij}n_{mn}\right) \tag{3.68c}$$

Finally, by multiplying M_{ijmn} and Z_{mnkl} and using the relationship between δ_{ij} and n_{ij}, the following explicit expression for the consistent tangent moduli is obtained,

$$D_{ijkl} = d_0\,J_{ijkl} + d_1\,\delta_{ij}\delta_{kl} + d_2\,n_{ij}n_{kl} + d_3\,\delta_{ij}n_{kl} + d_4\,n_{ij}\delta_{kl} \tag{3.69}$$

where the five constants are given as :

$$d_0 = 2G\,\frac{q}{q^{tr}} \tag{3.70a}$$

$$d_1 = K - \frac{2G}{3}\frac{q}{q^{tr}} - 3K^2C_{11} \tag{3.70b}$$

$$d_2 = \frac{4G^2}{q^{tr}}\Delta\epsilon_q - 4G^2C_{22} \tag{3.70c}$$

$$d_3 = -2GKC_{12} \tag{3.70d}$$

$$d_4 = -6GKC_{21} \tag{3.70e}$$

From Eq.(3.69), it should be noted that D_{ijkl} is symmetric if $C_{12} = 3C_{21}$ [111, 112].

3.6 SUMMARY

The basic concept of pressure-dependent elastoplasticity model is that the scalar product of stress and strain rate can be split into deviatoric and spherical parts. This property enables the model to be suitable for porous materials which exhibit a dependence on hydrostatic pressure. The pressure-dependent elastoplasticity model can be implemented into the FE analysis via two solutions methods. The first solution method is static implicit in which the system of non-linear equations has to be solved by an iterative method and a consistent tangent modulus has to be calculated to ensure the quadratic convergence of a global equilibrium step. Another finite element solution method is dynamic explicit, which is designed to solve problems using an explicit time integration algorithm. Since this method does not involve global iterations, the user does not need to define the consistent tangent modulus.

This chapter discusses all the mathematical techniques which involve the construction of the stress updated algorithm for pressure-dependent elastoplasticity model in a finite element code. This includes the details of the numerical integration used to obtain the solutions for pressure-dependent elastoplasticity model which contains 2 internal variables.

CHAPTER 4

IMPLEMENTATION OF THE ROUSSELIER DAMAGE MODEL IN ABAQUS

4.1 INTRODUCTION

The Rousselier damage model is just one model from a particular class of pressure-dependent plasticity models in which the response is dependent on the development of the hydrostatic stress as well as the deviatoric stress tensor. This model defines the softening of material by the accumulation of damage parameter (β) and fracture proceeds from the competition between hardening and damage. Therefore, it is not necessary to introduce a critical value of the damage variable.

In this chapter, a brief introduction of the Rousselier model is given followed by the implementation of this model via ABAQUS user defined subroutines, e.g. UMAT and VUMAT. These subroutines are used to perform FE calculations for a single element model and a notched tensile bar in order to check the correctness of the subroutines.

4.2 REVIEW OF THE ROUSSELIER MODEL

4.2.1 The classical Rousselier damage model [63, 64, 128]

The Rousselier model is based on the thermodynamical concept of generalized standard media. Within the framework of continuum thermodynamics, when the bodies are in thermodynamical equilibrium, any thermodynamical state of a material point can be fully defined by a finite number of state variables which are divided into observable variables and internal variables. Once the state variables have been defined, we can postulate the existence of a thermodynamic potential from which the state laws can be derived. For the case of elastoplasticity, if small strains are considered, the specific free energy, ψ which depends on observable and internal variables can be defined as :

$$\psi\left(\epsilon_{ij}^{e}, p, \beta\right) = \psi_e\left(\epsilon_{ij}^{e}\right) + \psi_p\left(\varepsilon_{eq}\right) + \psi_\beta(\beta)$$

where $\psi_e = \frac{1}{2}\epsilon_{ij}^e C_{ijkl}^e \epsilon_{kl}^e$ is the elastic strain energy. ψ_p and ψ_β are the dissipated energy which relate to the mechanism of hardening and softening (damage) respectively. From thermodynamics of irreversible process, the intrinsic dissipated power for isothermal case is written as :

$$\frac{\sigma_{ij}}{\rho}\dot{\epsilon}_{ij}^p - R\dot{\varepsilon}_{eq} + B\dot{\beta} \geq 0 \tag{4.1}$$

The variables $\frac{\sigma_{ij}}{\rho}$, $-R$, B are the associated forces which correspond to the internal variables ϵ_{ij}^p, ε_{eq}, β respectively in the dissipative mechanism. A more systematic presentation of the internal variables and the associated forces is given in Table 4.1

Table 4.1 Internal variables and the appropriate associated forces.

Dissipative mechanism	Variable, X_i	Associated force, Y_i
Plasticity	ϵ_{ij}^p	σ_{ij}/ρ
Hardening	ε_{eq}	$-R(\varepsilon_{eq})$
Damage	β	$B(\beta)$

Let $X = \left(\dot{\epsilon}_{ij}^p, \dot{\varepsilon}_{eq}, \dot{\beta}\right)$ and $Y = \left(\sigma_{ij}/\rho\,, -R, B\right)$, then the function in Eq.(4.1) can be written in the form of a bilinear function:

$$\dot{\varphi} = \sum X_i Y_i \tag{4.2}$$

The condition that $\dot{\varphi}$ is always positive or zero is automatically satisfied, if a convex function $F\left(\sigma_{ij}/\rho\,, -R, B\right)$ can be defined so that

$$\dot{X}_i = \dot{\lambda}\frac{\partial F}{\partial Y_i} \tag{4.3}$$

where F is the so called plastic potential.

Following Eq.(4.3), Rousellier [64] postulated the breaking function of plastic potential which depended on the first two invariants of the stress tensor.

$$F = F_1\left(\frac{q}{\rho}, R\right) + F_2\left(\frac{\sigma_m}{\rho}, B\right) \tag{4.4}$$

where

$$F_1 = \frac{q}{\rho} - R\left(\epsilon_{eq}\right) \tag{4.5a}$$

$$F_2 = B(\beta) g\left(\frac{\sigma_m}{\rho}\right) \tag{4.5b}$$

In this function, F_1 denotes the hardening part, whereas the softening part of material due to damage is represented by F_2. By considering the mass preservation law and neglecting the variations in volume due to elastic deformations, functions $B(\beta)$ and $g\left(\frac{\sigma_m}{\rho}\right)$ in Eq.(4.5) are finally defined as follows:

$$g\left(\frac{\sigma_m}{\rho}\right) = D\ exp\left(\frac{-p}{\rho\sigma_1}\right) \tag{4.6a}$$

$$B(\beta) = -\frac{\sigma_1}{\rho}\frac{\partial\rho}{\partial\beta} \tag{4.6b}$$

where $-p$ has been substituted for σ_m and σ_1 is a constant. Parameter ρ in Eq.(4.6b) is the dimensionless density. It is obtained by dividing the density of the damaged material by the material density in the initial state. This parameter relates to the value of damage variable β by following equation,

$$\rho(\beta) = \frac{1}{1-f_0+f_0\ exp(\beta)} \tag{4.7}$$

where f_0 is the initial value of the void volume fraction. Substituting Eq.(4.7) into (4.6b) gives,

$$B(\beta) = \frac{\sigma_1\ f_0\ exp(\beta)}{1-f_0+f_0\ exp(\beta)} \tag{4.8}$$

Substituting Eqs.(4.6), (4.7) and (4.8) into Eq.(4.4), the plastic potential proposed by Rousselier is,

$$\mathrm{F} = \frac{q}{\rho} - R\left(\varepsilon_{eq}\right) + B(\beta)\ D\ exp\left(\frac{-p}{\rho\sigma_1}\right) \tag{4.9}$$

where D and σ_1 are material parameters. β denotes an internal variable to describe damage and ε_{eq} is the equivalent plastic strain which is used as the internal variable to describe hardening. The function $R\left(\varepsilon_{eq}\right)$ is the hardening curve of the material which can be determined from the standard tensile test.

Applying the normality rule described in Eq.(4.3) to Eq.(4.9), the evolution equation for the internal variables are :

- Equivalent plastic strain

$$\dot{\varepsilon}_{eq} = \dot{\lambda}\frac{\partial F}{\partial\{-R(\varepsilon_{eq})\}} = \dot{\lambda} \tag{4.10}$$

- Damage variable

$$\dot{\beta} = \dot{\lambda}\frac{\partial F}{\partial B} = \dot{\varepsilon}_{eq} D exp\left(\frac{-p}{\rho\ \sigma_1}\right) \tag{4.11}$$

- Plastic strain tensor

$$\dot{\epsilon}_{ij}^{p} = \dot{\lambda}\frac{\partial F}{\partial(\sigma_{ij}/\rho)} = \dot{\lambda}\left\{\frac{1}{3}\frac{\partial \Phi}{\partial(\sigma_m/\rho)}\delta_{ij} + \frac{\partial \Phi}{\partial(S_{ij}/\rho)}\right\}$$

$$= \dot{\varepsilon}_{eq}\left\{\frac{B(\beta)}{3\sigma_1} D\ exp\left(\frac{-p}{\rho\ \sigma_1}\right)\delta_{ij} + \frac{3S_{ij}}{2q}\right\}$$

Comparing the equation above with Eq. (3.11), we get

$$\frac{1}{3}\dot{\epsilon}_p = \frac{1}{3}\dot{\epsilon}_{kk}^{p} = \dot{\varepsilon}_{eq}\frac{B(\beta)}{3\sigma_1} D\ exp\left(\frac{-p}{\rho\ \sigma_1}\right) \tag{4.12a}$$

$$\dot{\epsilon}_q = \dot{\varepsilon}_{eq} \tag{4.12b}$$

Eq.(4.12b) implies that in the Rousselier damage model, the increment of deviatoric plastic strain is equal to the increment of the equivalent plastic strain $\left(\Delta\epsilon_q = \Delta\varepsilon_{eq}\right)$.

4.2.2 The alternative form of Rousselier damage model

The plastic potential function proposed by Rousselier can be written in another form which relates directly to void volume fraction, f. The details about how to relate this function to f are presented in this section.

By considering a material which contains a void, the relationship between the relative density and f can be written as :

$$\rho = \left(\frac{1-f}{1-f_0}\right) \tag{4.13}$$

Substituting Eq.(4.7) into Eq.(4.13) and rearranging, the volume fraction of cavities can be related to the damage variable by following relation:

$$f = \frac{f_0\, exp(\beta)}{1-f_0+f_0\, exp(\beta)} \tag{4.14}$$

Using the above relation, function $B(\beta)$ in Eq.(4.8) can be written in terms of the void volume fraction as :

$$B(\beta) = \sigma_1 f \tag{4.15}$$

Substituting Eq.(4.15) into Eq.(4.9), the plastic potential takes the form,

$$\mathrm{F} = \frac{q}{\rho} - R\left(\varepsilon_{eq}\right) + Df\sigma_1 exp\left(\frac{-p}{\rho\sigma_1}\right) \tag{4.16}$$

The relative density ρ is related to f by Eq.(4.13). Since the value of f_0 is very small compared to unity, some authors simply take [129]

$$\rho = 1 - f \tag{4.17}$$

Substituting Eq.(4.17) into Eq.(4.16), the Rousselier yield function can be written as,

$$\mathrm{F} = \frac{q}{1-f} - R\left(\varepsilon_{eq}\right) + D\sigma_1 f exp\left(\frac{-p}{(1-f)\sigma_1}\right) \tag{4.18}$$

An evolution equation for f can be determined from mass preservation law. If the volume change due to elastic deformation is neglected, the evolution of f can be defined as :

$$\dot{f} = (1-f)\dot{\epsilon}^p_{kk} = (1-f)\dot{\epsilon}_p \tag{4.19}$$

The equation above shows that in original Rousselier damage model, the evolution of void volume fraction depends only on the plastic volume change or the growth rate of pre-existing voids. However, many studies have shown that void growth is no longer tied to the volumetric plastic strain increment, but it also depends on the deviatoric part of plastic strain tensor. According to this, some authors extend Eq.(4.19) by adding the other rate equation as follows [56, 130] :

$$\dot{f} = (1-f)\dot{\epsilon}_p + A\dot{\epsilon}_q \tag{4.20}$$

4.2.3 Accuracy of the model

The accuracy of the Rousselier model depends on the precision of parameters required in the model. According to the previous section, the following parameters need to be determined [44] :

- The initial void volume fraction (f_0) related to the volume fraction of the inclusions.
- The Rousselier parameters (D and σ_1) which express the fracture resistance of the matrix material.
- The characteristic length (L_c) which expresses the interaction between a crack tip and void, related to interinclusion spacing. This parameter is not included in the equation of the model. However, in FE analysis, this value represents the size of element at the crack tip.

Good estimates of parameters f_0 and L_c are obtained from the metallographic examinations of inclusions [131].

$$f_0 = f_v \frac{(d_x\, d_y)^{1/2}}{d_z} \tag{4.21}$$

$$L_c = \frac{5}{(N_v)^{1/3}} \tag{4.22}$$

where d_x, d_y and d_z are the average dimensions of the inclusions, z is the direction of load, and N_v is the mean number of inclusions per unit volume. f_v is the volume fraction of inclusions. It can be calculated either from metallographic examinations or from the chemical analysis (Franklin's formula [132]). For example, for *MnS* inclusions in ferritic steel, f_v is obtained from chemical analysis as :

$$f_v = 0.054 \left(\%S - \frac{0.001}{\%Mn}\right) \tag{4.23}$$

From the metallographic method, which needs microscopic examination in the three spatial directions of the volume, the value of f_v is :

$$f_v = \frac{\pi}{6} N_v\, dx\, dy\, dz \tag{4.24}$$

The remaining parameters D and σ_1 in the constitutive equation can be determined from a fitting procedure on the experimental data. Procedure on the determination of D and σ_1 for a given material is shown in Figure 2.10. According to this, a first try for σ_1 is suggested to be $2\sigma_f/3$ where σ_f is the equivalent stress when fracture occurs in a smooth round bar tension test [129]. In addition, the parameter D can also be considered as material-independent which can be taken to be equal to 2, at least for a general material containing the value of f_0 equal to or smaller than 0.001 [63, 64, 129]. After all the parameters are obtained, the values of these parameters are used to model the large scale structure.

4.3 IMPLEMENTATION OF ABAQUS USER DEFINED SUBROUTINE

Several FE software packages provide the facility for users to create their own material models. In ABAQUS, UMAT and VUMAT are the two interfaces which allow the users to define any complex, constitutive material models that are not provided in the standard material library of the program.

UMAT is the user defined material for ABAQUS/Standard module which is a general-purpose finite element analyser. This module employs the implicit integration scheme to update the state of the model, so the user must also provide the consistent tangent modulus (CTM) for the mechanical constitutive model.

Another user subroutine VUMAT is used in ABAQUS/Explicit module which was originally developed and primarily used to solve dynamic problems involving deformable bodies. The integration procedure used in this module is based on the implementation of an explicit integration rule together with the use of diagonal or "lumped" element mass matrices [127]. Since no global iterations are involved in the calculation, the user does not need to define a CTM. In addition, ABAQUS/Explicit also provides the element removal feature which is not available in ABAQUS/Standard.

In this research, both user defined subroutines, UMAT and VUMAT, are developed for Rousselier damage model. The numerical algorithms employed in these subroutines use the closest point return mapping method presented in chapter 3.

According to section 4.2, the necessary equations for the application of the closest point return mapping method are summarized as :

$$\mathrm{F} = \frac{q}{\rho} - R\left(\varepsilon_{eq}\right) + Df\sigma_1 exp\left(\frac{-p}{\rho\sigma_1}\right) \tag{4.25}$$

$$\sigma_{ij} = -p\delta_{ij} + \frac{2}{3}qn_{ij} \tag{4.26}$$

$$d\epsilon_{ij}^{p} = \frac{1}{3}d\epsilon_p\delta_{ij} + d\epsilon_q n_{ij} \tag{4.27}$$

$$dH^1 = d\varepsilon_{eq} = d\epsilon_q \tag{4.28}$$

$$dH^2 = df = (1-f)d\epsilon_p = (1-f)d\epsilon_{kk} \tag{4.29}$$

Details of ABAQUS user defined subroutine for Rousselier damage model are given in Appendices IV, V and VI.

4.4 VALIDATION OF UMAT AND VUMAT

UMAT and VUMAT for Rousselier model are used to run tests on FE models of a single element and the necking of notched tensile bars under tension. The results obtained from FE-models are compared with the exact solutions or the benchmark solutions presented in literature in order to verify the correctness of the subroutine codes. The material data used for all FE models is for *22 NiMoCr 3 7* which is given the Tables 4.2, 4.3 and 4.4 [45].

Table 4.2 The stress-strain data for *22 NiMoCr 3 7* material at $220\ ^oC$ [45].

True strain $(\varepsilon_T, \%)$	True stress (σ_T, MPa)	True strain $(\varepsilon_T, \%)$	True stress (σ_T, MPa)
0	0	20	819
1	566	30	860
2	619	40	890
3	647	50	915
4	673	60	935
6	710	70	952
8	734	80	968
10	754	90	982
15	792		

Table 4.3 Chemical composition of *22 NiMoCr 3 7* material (wt %) [45].

C	Si	Mn	P	S	Cr	Mo	Ni	Al	V	Cu
0.25	0.23	0.68	0.009	0.011	0.47	0.75	0.71	0.007	< 0.01	0.18

Table 4.4 Temperature dependent mechanical properties of *22 NiMoCr 3 7* material [133].

Tempearture (^{o}C)	20	160	260	320
Yield stress, $\sigma_{0.2}$ (MPa)	563	549	536	523
Young's modulus, E (GPa)	210	200	190	184
Poisson's ratio, ν	0.3	0.3	0.3	0.3

4.4.1 A single plane strain element under tension

The first test is a uni-axial test on a plane strain element with element size 0.4×0.4 mm^2. The loading and boundary conditions are shown in Figure 4.1. Using the equations given in the previous section and enforcing the consistency condition to determine $d\lambda$, the differential equations for describing this problem are :

$$\frac{d\epsilon_y^p}{d\epsilon_y} = \omega\left\{-\frac{1}{3}\frac{\partial F}{\partial(p/\rho)} + \frac{\partial F}{\partial(S_y/\rho)}\right\} \tag{4.30}$$

$$\frac{d\epsilon_z^p}{d\epsilon_y} = \omega\left\{-\frac{1}{3}\frac{\partial F}{\partial(p/\rho)} + \frac{\partial F}{\partial(S_z/\rho)}\right\} \tag{4.31}$$

$$\frac{d\sigma_y}{d\epsilon_y} = \frac{E}{(1-\nu^2)}\left\{1 - \frac{d\epsilon_y^p}{d\epsilon_y} - \nu\frac{d\epsilon_z^p}{d\epsilon_y}\right\} \tag{4.32}$$

$$\frac{d\sigma_z}{d\epsilon_y} = \nu\frac{d\sigma_y}{d\epsilon_y} - E\frac{d\epsilon_z^p}{d\epsilon_y} \tag{4.33}$$

$$\frac{d\varepsilon_{eq}}{d\epsilon_y} = \omega \tag{4.34}$$

$$\frac{df}{d\epsilon_y} = \omega f(1-f)Dexp\left(\frac{-p}{\rho\sigma_1}\right) \tag{4.35}$$

$$\omega = \frac{\frac{E}{(1-\nu^2)}\left(\frac{\partial F}{\partial \sigma_y} + \nu\frac{\partial F}{\partial \sigma_z}\right)}{\frac{E}{(1-\nu^2)}\left\{\frac{\partial F}{\partial \sigma_y}\frac{\partial F}{\partial\left(\frac{\sigma_y}{\rho}\right)} + \frac{\partial F}{\partial \sigma_z}\frac{\partial F}{\partial\left(\frac{\sigma_z}{\rho}\right)} + \nu\frac{\partial F}{\partial \sigma_z}\frac{\partial F}{\partial\left(\frac{\sigma_y}{\rho}\right)} + \nu\frac{\partial F}{\partial \sigma_y}\frac{\partial F}{\partial\left(\frac{\sigma_z}{\rho}\right)}\right\} - \frac{\partial F}{\partial \varepsilon_{eq}} - \frac{\partial F}{\partial f}\frac{\partial f}{\partial \varepsilon_{eq}}} \tag{4.36}$$

where E and ν are Young's modulus and Poisson ratio respectively. ϵ_y and ϵ_y^p are the total strain and plastic strain in y-direction. ϵ_z^p is the plastic strain in z-direction.

A four-noded linear element with reduced integration (*CPE4R*) in ABAQUS was used for the FE analysis. The Rousselier's parameters, D and σ_1, were assumed to be 2.62 and 5.78×10^8, whereas the value of f_0 was set to be 0.5 percent. The solution of the problem was numerically obtained by integrating the set of Eqs.(4.30-4.35), using a Forward Euler scheme. This method was suggested by Aravas [110] and Zhang [112] and can provide near exact solutions if enough increments are used. Forward Euler integration was performed in order to get the solutions for this problem. This integration was performed from the initial yield strain to a strain of 1.0 using 200,000 increments to ensure high accuracy.

The comparisons between FE results obtained by user defined subroutines and the exact results are shown in Figures 4.2, 4.3 and 4.4. In these figures, the values of stresses, the equivalent plastic strain and void volume fraction are plotted as a function of the logarithmic strain $d\epsilon_y = ln(1 + u/l_0)$, where u is the displacement in y-direction and l_0 is the initial element length. The results of the FE analysis agree very well with the exact solutions.

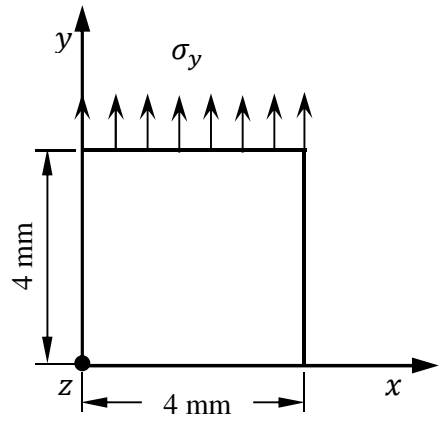

Figure 4.1 Plane strain tension problem.

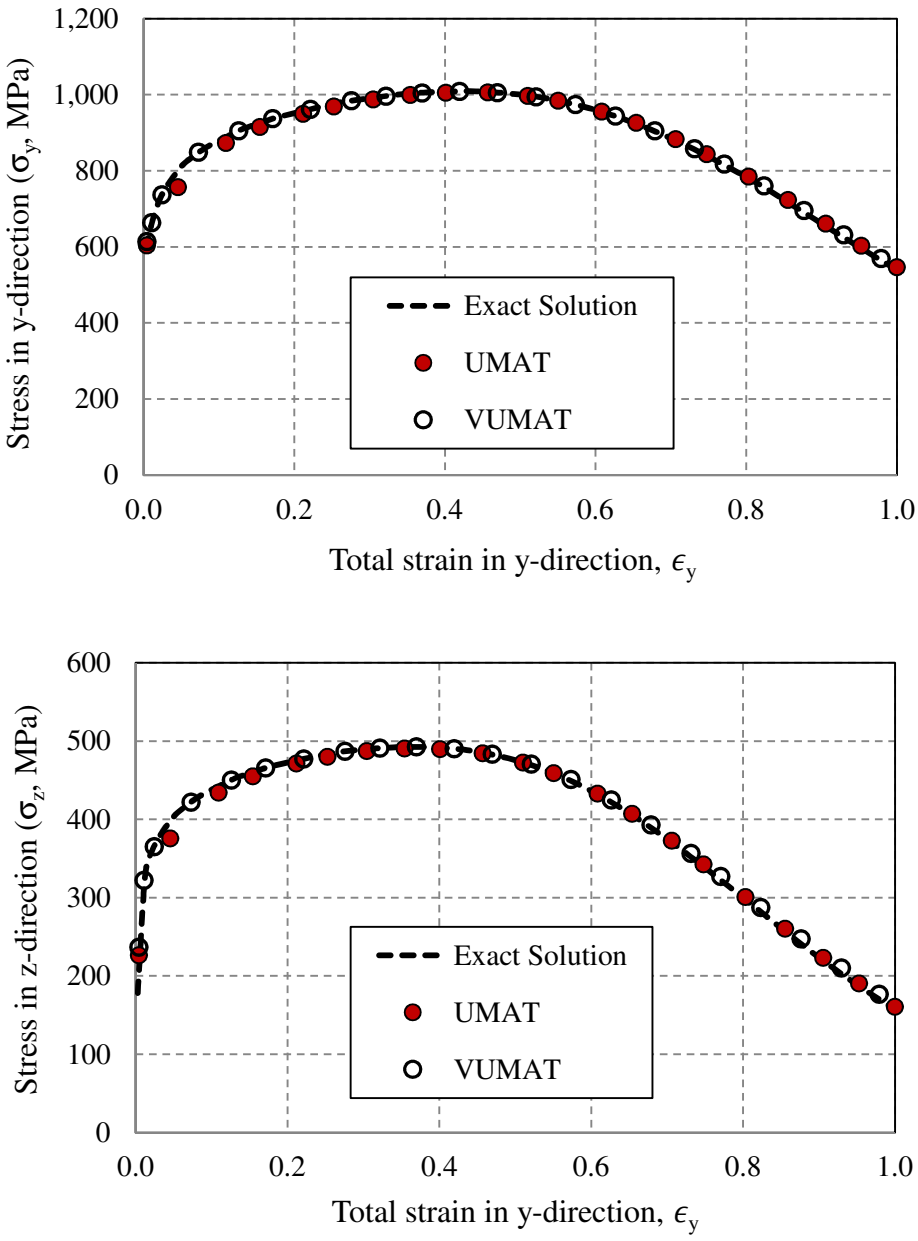

Figure 4.2 The values of stresses in y and z-direction as a function of strain in y-direction.

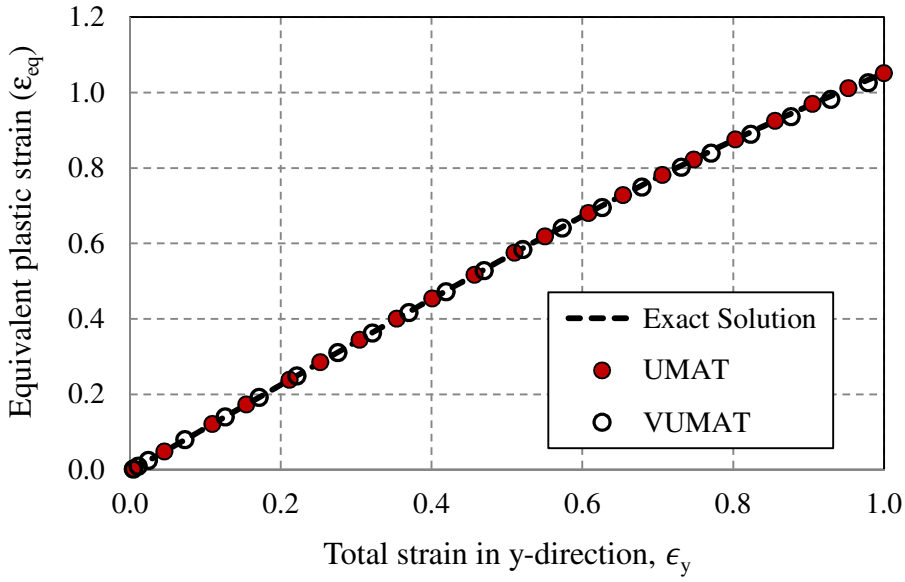

Figure 4.3 The values of equivalent plastic strain as a function of strain in y-direction.

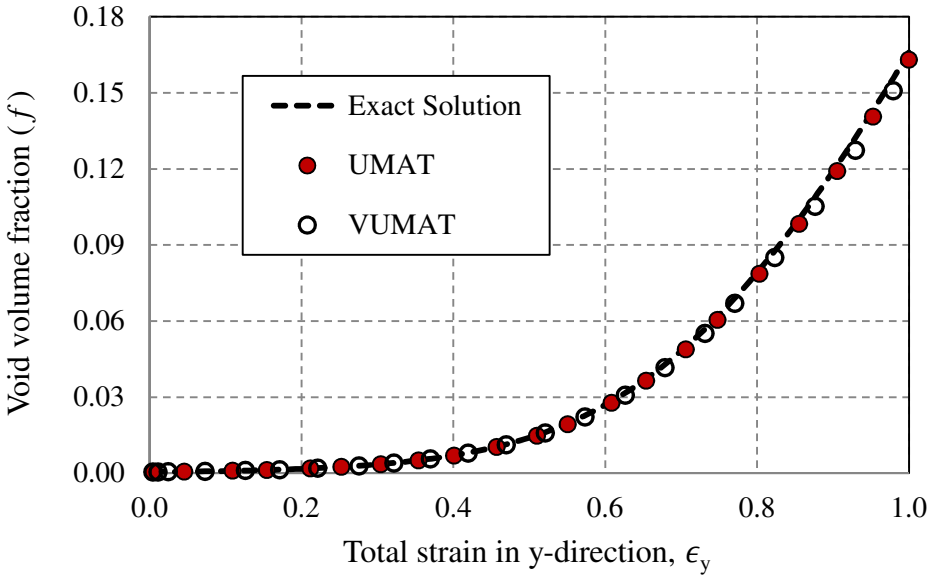

Figure 4.4 The void volume fraction as a function of strain in y-direction.

4.4.2 A single 3D-element under tension

The second test is a tension test on a 0.4×0.4×0.4 mm^3 brick element shown in Figure 4.5. Like the plane strain case, this model was loaded by applying the displacement in y-direction on the top surface of element so that the logarithmic strain reached 100 percent. The equations for describing this problem can be integrated numerically in a way similar to that explained in the previous section and are written as :

$$\frac{d\sigma_y}{d\epsilon_y} = E\left\{1 - \left[-\frac{1}{3}\frac{\partial \Phi}{\partial(p/\rho)} + \frac{\partial \Phi}{\partial(S_y/\rho)}\right]\bar{\omega}\right\} \tag{4.37}$$

$$\frac{d\varepsilon_{eq}^p}{d\epsilon_y} = \bar{\omega} \tag{4.38}$$

$$\frac{df}{d\epsilon_y} = \bar{\omega} f(1-f) D exp\left(\frac{-p}{\rho\sigma_1}\right) \tag{4.39}$$

where

$$\bar{\omega} = \frac{E\frac{\partial F}{\partial \sigma_y}}{E\frac{\partial F}{\partial \sigma_y}\left\{-\frac{1}{3}\frac{\partial F}{\partial(p/\rho)} + \frac{\partial F}{\partial(S_y/\rho)}\right\} - \frac{\partial F}{\partial \varepsilon_{eq}^p} - \frac{\partial F}{\partial f}\frac{\partial f}{\partial \varepsilon_{eq}^p}} \tag{4.40}$$

An eight-noded brick element with reduced integration (*C3D8R*) in ABAQUS was used to model this test. The material properties, the initial void fraction, and the Rousselier parameters were taken to be the same as those used in the previous problem. The FE analysis results and the exact solutions for stress in y-direction, the equivalent plastic strain and void volume fraction are plotted as a function of ϵ_y in Figure 4.6, 4.7 and 4.8 respectively. These results show that the FE results are in good agreement with the exact solution.

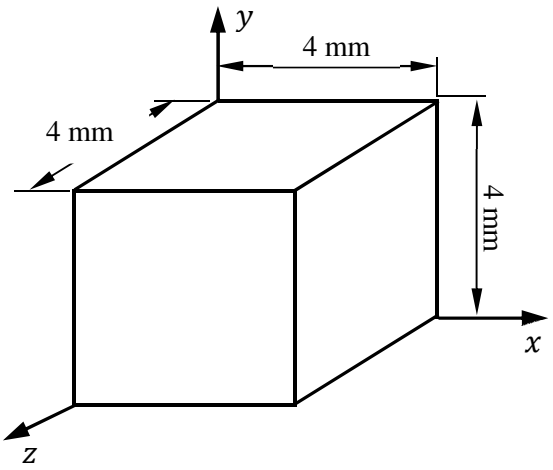

Figure 4.5 Brick element under tension test.

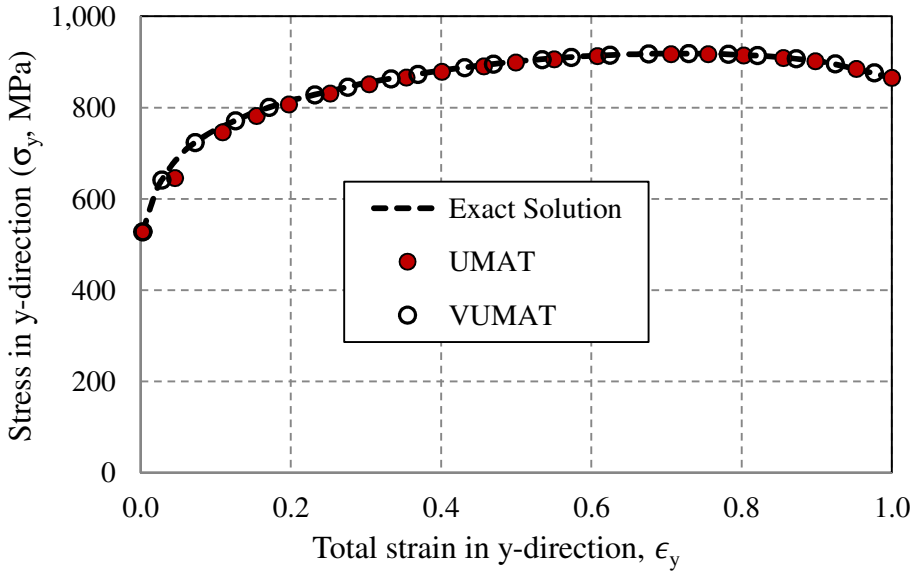

Figure 4.6 The values of stresses in y-direction as a function of strain in y-direction.

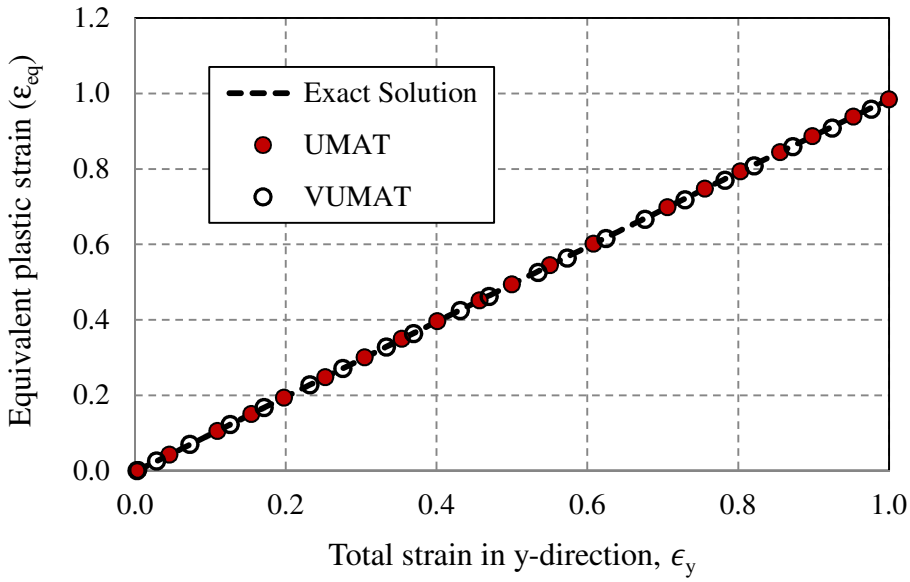

Figure 4.7 The equivalent plastic strain as a function of strain in y-direction.

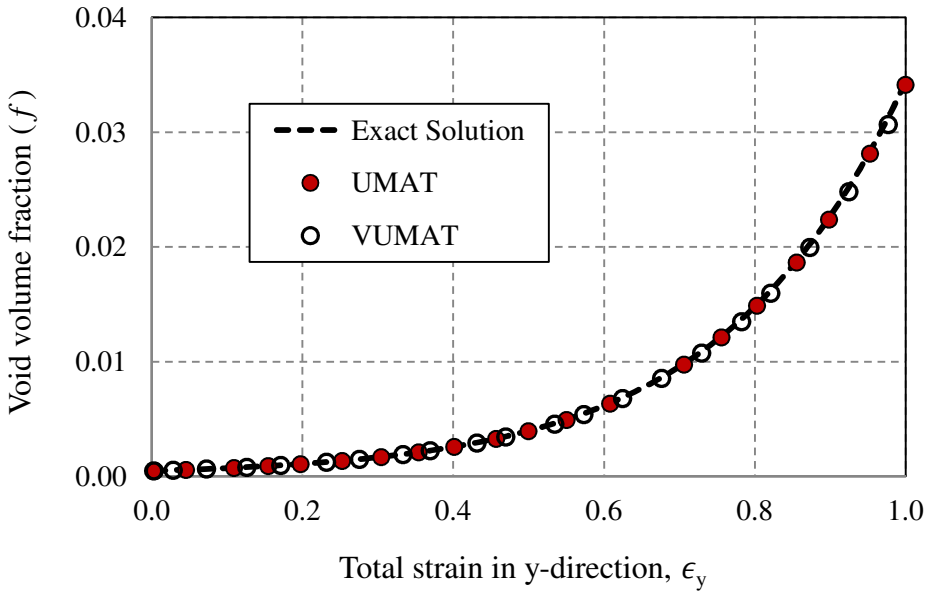

Figure 4.8 The values of void volume fraction as a function of strain in y-direction.

4.4.3 Tensile test of notched tensile specimen

The final test is to demonstrate the implementation of UMAT and VUMAT for real engineering problems with multi-element meshes. It concerns the calibration procedure for estimating the Rousseiler parameters, D and σ_1, for *22 NiMoCr 3 7* material which has been presented in '*Simulation of Nuclear Safety Test* [45]'. FE models of notched tensile bars with different radii under tension are established. The values of D and σ_1 used in running the model are varied until the FE results (load versus diametrical contraction) provide a best fit with the experimental data. Details of modelling and the results are discussed below :

- Experimental testing

The experimental data for tensile testing of *22 NiMoCr 3 7* material has been provided in [45]. This was obtained from 10 mm, 4 mm and 2 mm radius notched tensile specimens (Figure 4.9) tested at 100^{o}C. During testing, the load and the actual diameter at the minimum section were continuously recorded.

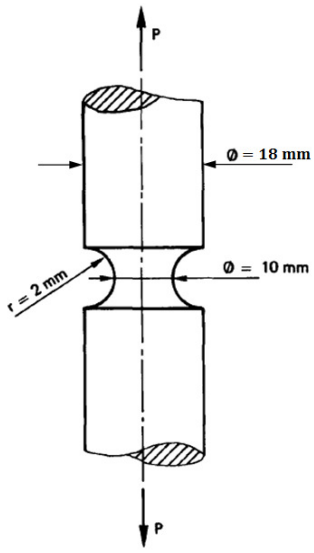

Figure 4.9 Cylindrical notched tensile specimen [45].

- Finite element simulation

The FE models of 3 different radius notched bars (10 mm, 4mm and 2 mm) under tension are employed to calibrate the values of D and σ_1 (Figure 4.10). The element used to mesh each model is *CAX4R* (four-node biquadratic axisymmetric quadrilateral with reduced integration). The size of the element along the minimum section of each model is set to be equal to the value of L_c which relate to the inter-inclusion spacing. From the fractographic examination of *22 NiMoCr 3 7* material, the value of number of inclusions per unit volume is $N_v \approx 2000$ [45], so we can calculate the value of L_c from Eq.(4.21) which is 0.4 mm.

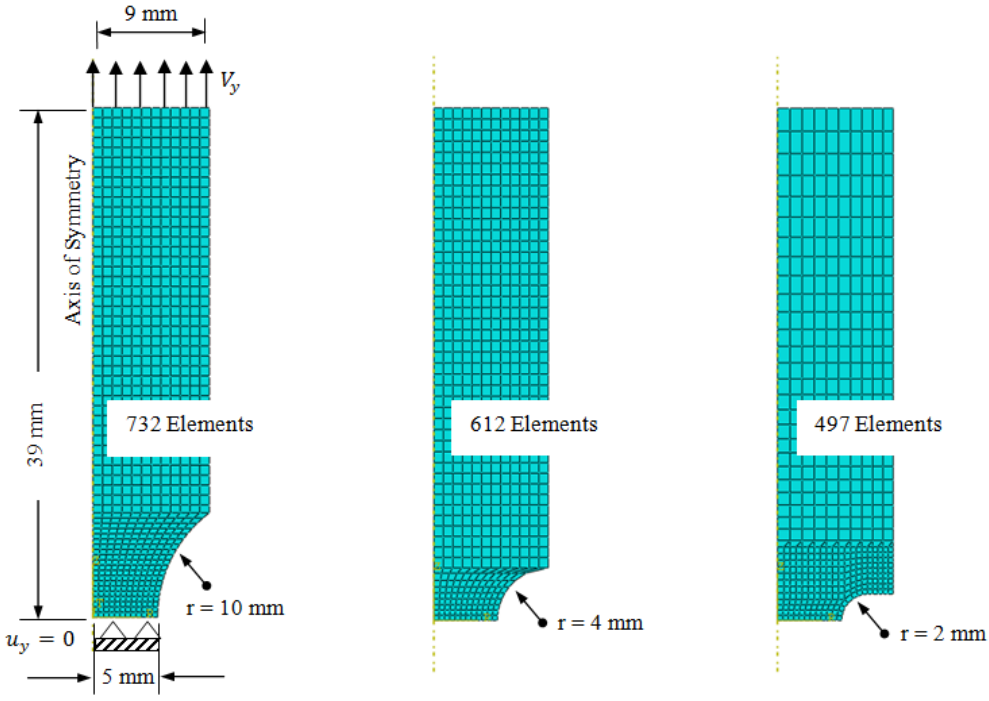

Figure 4.10 The finite element meshes for the notched bars.

- The calibration procedure

The values of D and σ_1 are tuned through the FE-model of 10 mm radius notched tensile bar until the FE results (load versus diametrical contraction) provide the best fit with the experimental data. Figures 4.11 and 4.12 show that the value of D and σ_1 determine the breakpoint of rapid decrease of load corresponding to the initiation of

a macrocrack in the centre of the specimen. The bigger value of D or the smaller value of σ_1 increase the growth rate of the softening part in Rousselier damage model.

After varying the values of σ_1 and D in the FE model, it was found that the curve which provided the best match with experimental curve is obtained with σ_1 = 500 MPa and D = 2.62. These values of σ_1 and D are used again in the FE models of 4 mm and 2 mm notched tensile bars which also provide a good agreement between FE results and the experimental data, as shown in Figures 4.13 and 4.14.

The value of D = 2.62 is the same as calibrated in 'Simulation of Nuclear Safety Test' report [45], whereas the value of σ_1 = 500 MPa obtained from UMAT and VUMAT is only 3.4% different from the one calibrated in the report [45]. Here, it can be concluded that the subroutine provides accurate results for the models analysed here.

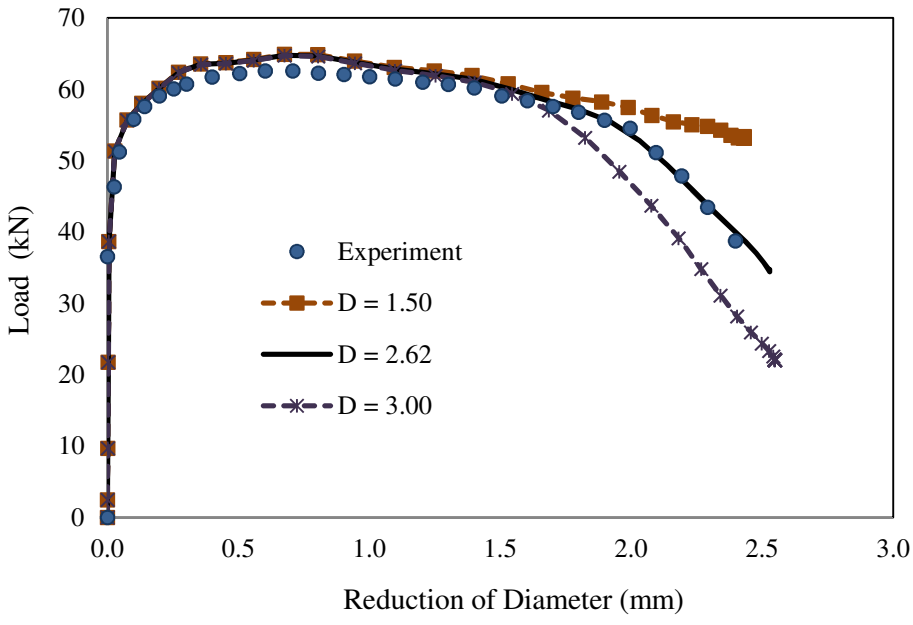

Figure 4.11 Comparison between the experimental data and FE results for 10 mm radius notched tensile bar (fix value of σ_1 = 500 MPa vary value of D).

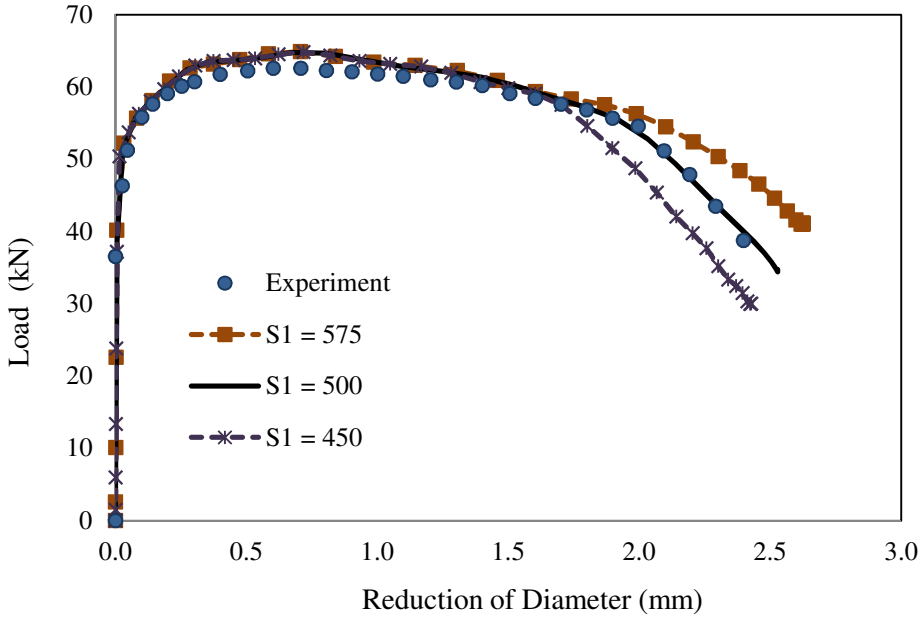

Figure 4.12 Comparison between the experimental data and FE results for 10 mm radius notched tensile bar (fix value of D = 2.62 and vary value of σ_1).

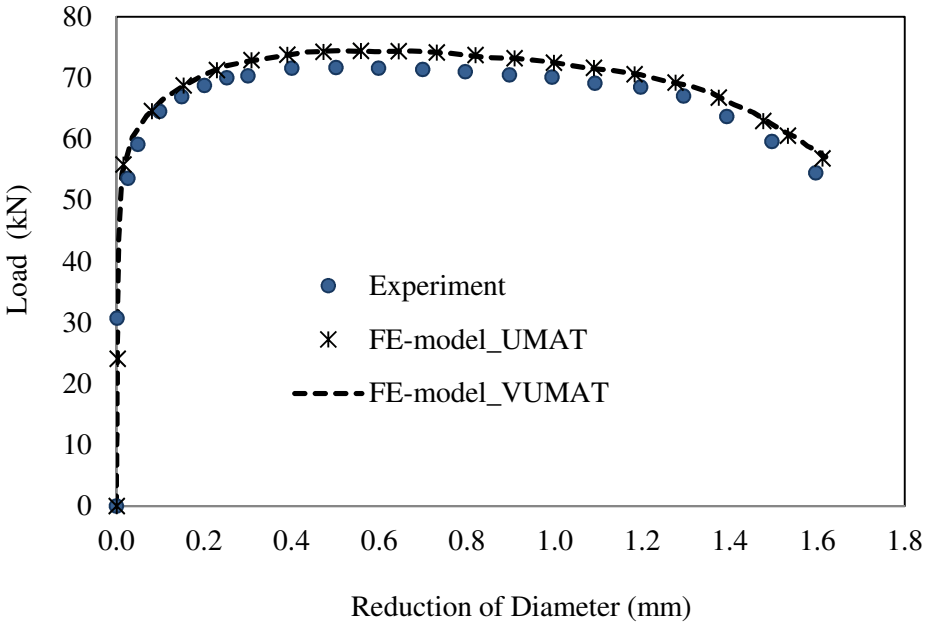

Figure 4.13 Comparison between the experimental data and FE results for 4 mm radius notched tensile bar (σ_1 = 500 MPa and D = 2.62).

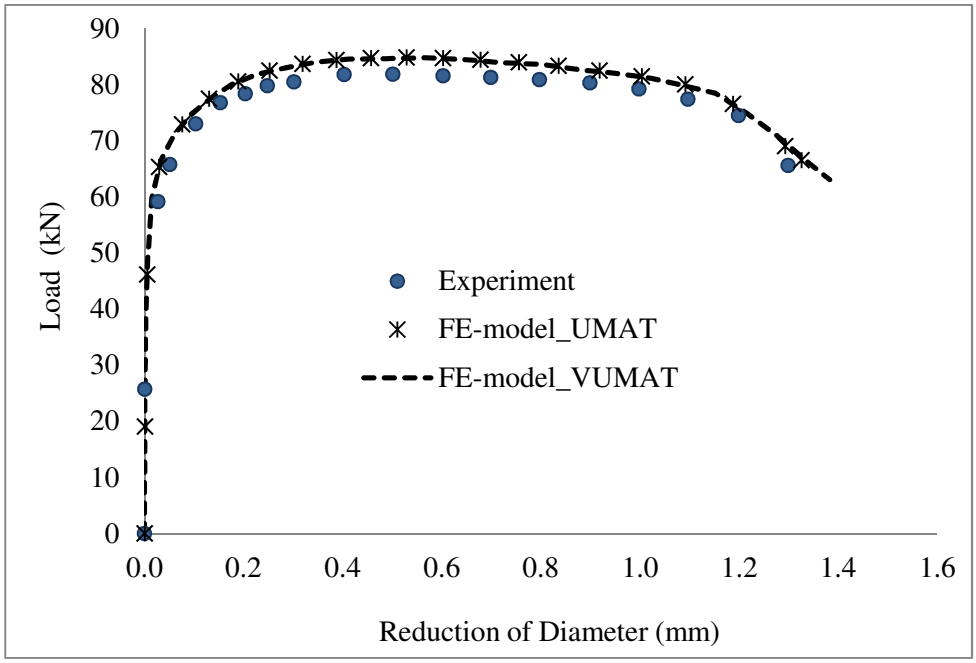

Figure 4.14 Comparison between the experimental data and FE results for 2 mm radius notched tensile bar (σ_1 = 500 MPa and D = 2.62).

- Discussion

As discussed in the preceding sections, the Rousselier damage model can define the softening behaviour of the material without introducing any failure criteria. The weakness of material comes from the development of void volume fraction (f) which depends on the cumulated volumetric plastic strain (Eq.4.19). Figure 4.15 shows the variation of f and the corresponding collapse of stress in y-direction of the 5 elements along the minimum cross section of FE model of 2 mm radius notched tensile bar. It can be seen that the longitudinal stress drops rapidly at the same position where the value of f starts rising sharply.

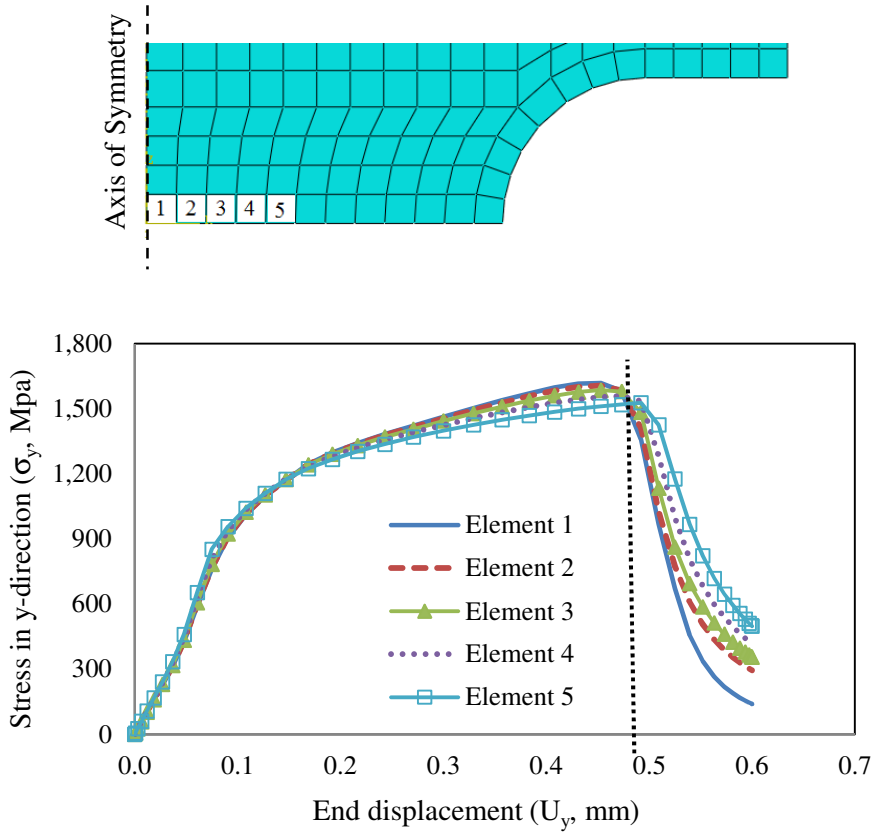

(a)

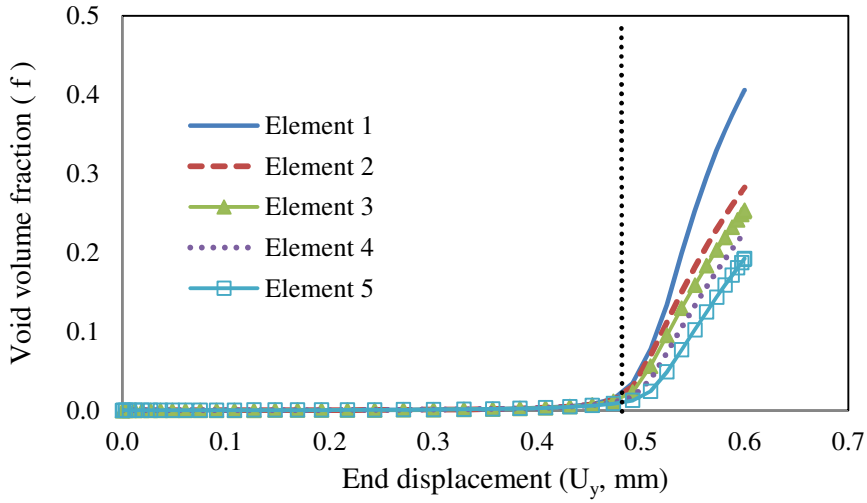

(b)

Figure 4.15 (a) The value of stress in y-direction and (b) void volume fraction of 5 elements in the vicinity of the minimum cross section of FE-model for 2 mm radius notched tensile bar.

4.4.4 Pure shear condition

Another case study which can be used to assess the validity of Rousseleir damage model is the pure shear condition [134]. This is because under pure shear ($\sigma_{kk} = 0$), the relationship between equivalent plastic strain and damage variable takes a simple form which can be proved as follows.

By substituting Eq.(4.12a) into Eq.(4.19), one has

$$df = d\varepsilon_{eq}(1-f)fD\ exp\left(\frac{-p}{\rho\ \sigma_1}\right) \tag{4.41}$$

Since under pure shear condition, σ_{kk} = -p = 0, Eq.(4.41) can be transformed into an ordinary differential equation :

$$\frac{df}{d\varepsilon_{eq}} = (1-f)fD \tag{4.42}$$

Setting $f = f_0$ at $\varepsilon_{eq} = 0$, the analytical solution of Eq.(4.42) can be derived as :

$$f = \frac{f_0 e^{D\varepsilon_{eq}}}{(e^{D\varepsilon_{eq}}-1)\,f_0+1} \tag{4.43}$$

By substituting f_0 = 0.0005 and D = 2.62, into equation above, the evolution of damage variable or void volume fraction with equivalent plastic strain can be obtained as shown in Figure 4.16. However, it is very difficult to define loading and boundary conditions to obtain pure shear condition (or zero hydrostatic pressure) in FE analysis, especially for elastoplastic problem. Therefore, this case study is not used for the validation of UMAT and VUMAT developed in this thesis.

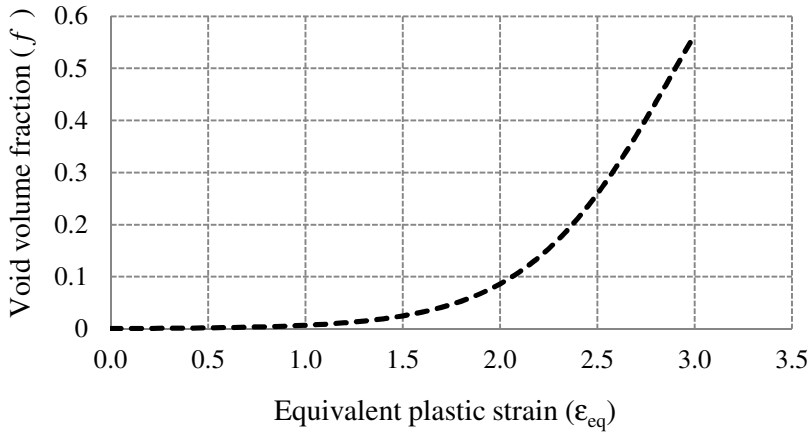

Figure 4.16 The evolution of void volume fraction with the equivalent plastic strain under pure shear condition (f_0 = 0.0005 and D = 2.62).

4.5 THE LIMITATION OF UMAT

Although the user defined subroutine for implicit algorithm, UMAT, provides accurate results, as presented in the previous section, it has convergence problems when dealing with failed elements. This is because when an element loses its load carrying capacity resulting from a progressive degradation of the material stiffness, it provides a singular coefficient in the global stiffness matrix which leads to convergence problems.

In order to avoid these numerical difficulties, two methods were suggested to simulate the material failure. The first method was based on the element removal which allowed the user to remove the failed element out of the model directly. This method was available in ABAQUS/Explicit. The second method was not to allow the material to fail completely by fixing a small amount of load-carrying capacity associated with the material failed. The remaining load-carrying capacity was controlled by a fixed yield function (non-hardening matrix material and constant f) at certain small values, as shown in Figure 4.17 [111]. This method can be used in the implicit FE algorithm.

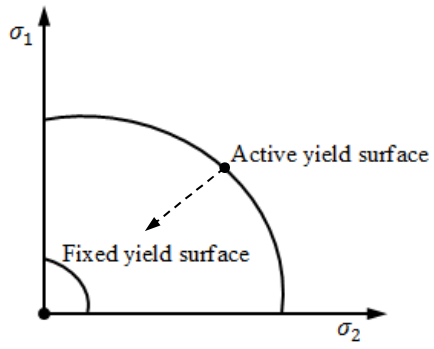

Figure 4.17 Active and fixed yield surface [111].

4.6 SUMMARY

In this chapter, Rousselier damage model is presented. This model is incorporated into the commercial FE code (ABAQUS) via user material subroutines, UMAT and VUMAT, for implicit and explicit finite element algorithms respectively. The correctness of these subroutines has been verified by performing analysis on FE models for single elements and notched tensile bars. Results from these models are in good agreement with the analytical solutions and the benchmark solutions provided in literature. However, UMAT suffers from convergence problems when it is used to simulate models containing failed elements.

CHAPTER 5

GLOBAL APPROACH FOR A LARGE SCALE BENDING TEST

5.1 INTRODUCTION

The purpose of this chapter is to present the results of a structural integrity assessment of a large-scale test undertaken as part of the EU STYLE programme. This test is conducted on a welded pipe containing a circumferential through-thickness crack subjected to a 4-point bending load. The assessment here used a FE model created in ABAQUS, with the weld residual stresses introduced by an iterative technique. Linear elastic fracture mechanics (LEFM) analysis was used to evaluate the mode I stress intensity factor, K_I, for the defect. Elastic-plastic analyses were also performed to characterise the crack driving force, J, along the crack front. The predicted crack mouth opening displacement, *CMOD*, as a function of load was compared with the test results and the derived variation of J was used to predict crack initiation and growth.

5.2 THE LARGE-SCALE MU2 TEST [5]

A large-scale four point bending test was performed by CEA [5] as part of the STYLE project which was completed in June 2013. The test specimen, referred to as MU-2, was a welded pipe consisting of two lengths of Esshete 1250 austenitic stainless steel joined by a girth weld. The weld contained a short, deep weld repair, and a through thickness pre-crack was inserted at the centre of the repair. The main section of MU2 and the pre-crack position are shown schematically in Figure 5.1 and 5.2 respectively.

The MU2 pipe had overall dimensions of 600 mm length, 180 mm outer diameter and 35 mm wall thickness. Both ends of the specimen were welded to extension arms, which were manufactured from 304L stainless steel, to provide a 5 m four point bending span for the four-point bending experiment. The distance between the inner loading points was 1 m and between the outer loading points was 5 m. The

experimental set-up is illustrated in Figure 5.3. From this figure, the maximum value of bending moment applied to MU2 section during the test is equal to the total force applied by the hydraulic system.

The experiment was divided into two main phases; pre-cracking test and ductile tearing test. The pre-cracking test was designed to generate a pre-crack of the dimensions and shape shown in Figure 5.2. To achieve this, a V-shaped slot was introduced into the middle plane of the repair weld by electro-discharge machining (EDM) prior to loading. Due to the high tensile residual stresses present, the specimen was subjected to a sinusoidal fatigue load between a compressive load of -16.7 kN and -58.7 kN, this loading reduced in the final stages of pre-cracking to -37.6 kN, until a sharp, straight-fronted pre-crack was generated from the slot. The ductile tearing test was performed under sequences of loading and unloading to promote the ductile crack growth from the initial fatigue pre-crack and to indicate the stages of ductile tearing through 'beach marks' on the fracture surface. Unfortunately, the high tensile residual stresses precluded crack closure, and no beach marks were observed on the fracture surface following the test. Two clip gauges were attached at the outer surface of the EDM-slotting in order to measure the values of *CMOD*, as shown in Figure 5.4.

Figure 5.5 presents the optical examination of the fracture surface after the test, revealing that the sharp pre-crack generated during Phase I was not completely symmetrical. The crack had a length of about 5 mm on one side of the slot and 8 mm on the other at the outer surface of the pipe. The crack extension generated from ductile tearing test was also not symmetrical as presented in Figure 5.6. The maximum extent of crack growth was about 2.0-2.5 mm in south location and about 3 mm in north location respectively. This happened after the test specimen was subjected to the maximum load of 213.1 kN at the end of the test. In this state, the value of *CMOD* measured from the test was about 2.5 mm.

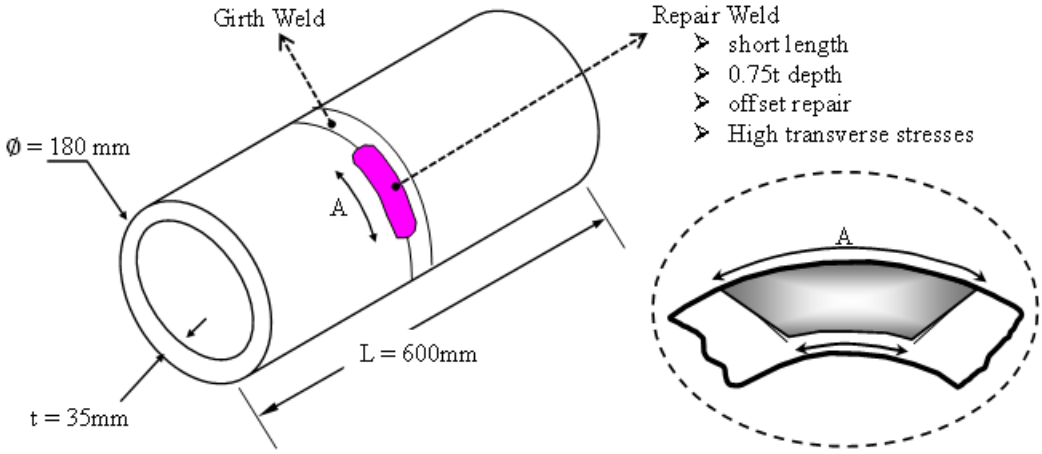

Figure 5.1 Schematic of MU2 pipe.

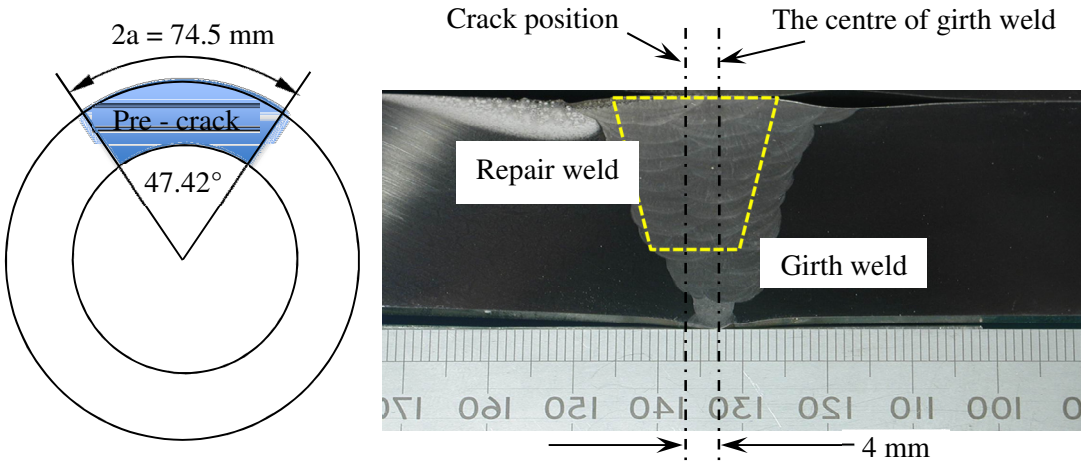

Figure 5.2 Dimensions of the through thickness pre-crack.

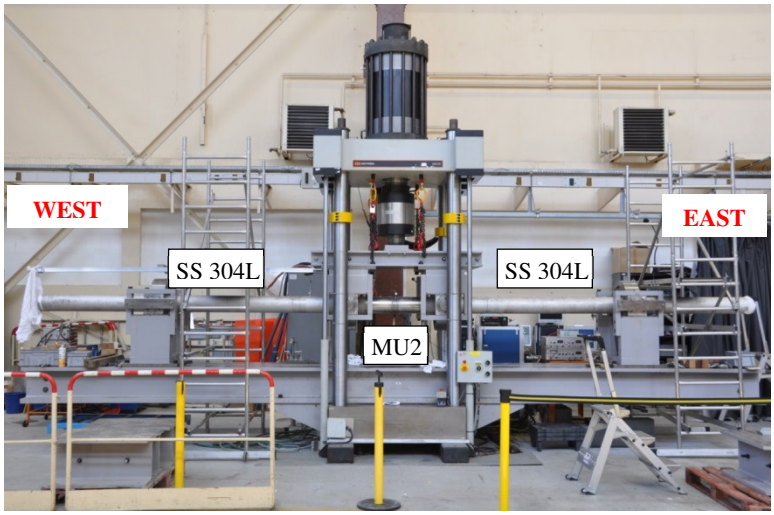

(a)

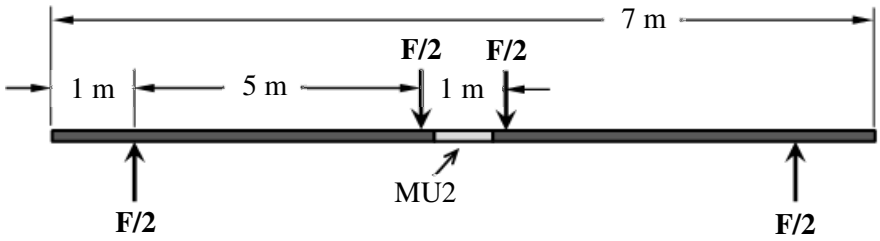

(b)

Figure. 5.3 (a) Set up for the large-scale four point bend experiment (view of south side of the pipe), and (b) loading arrangement for the experiment.

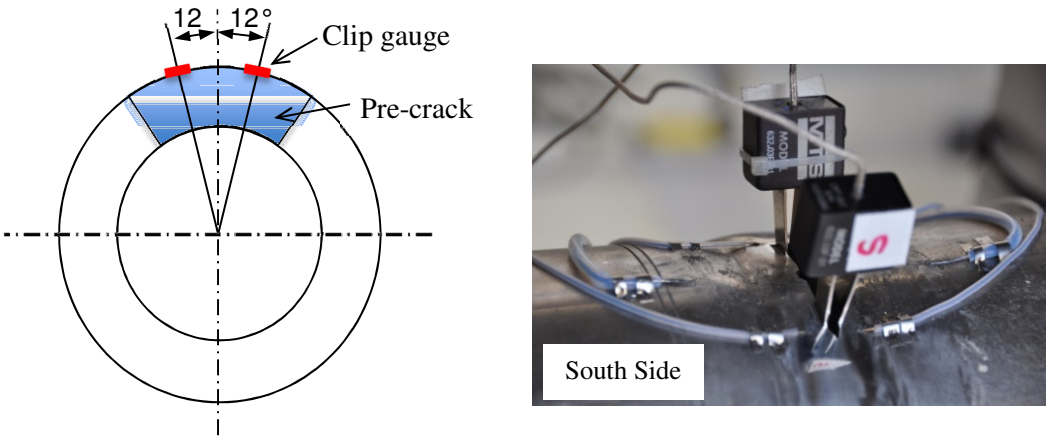

Figure 5.4 Clip gauge position.

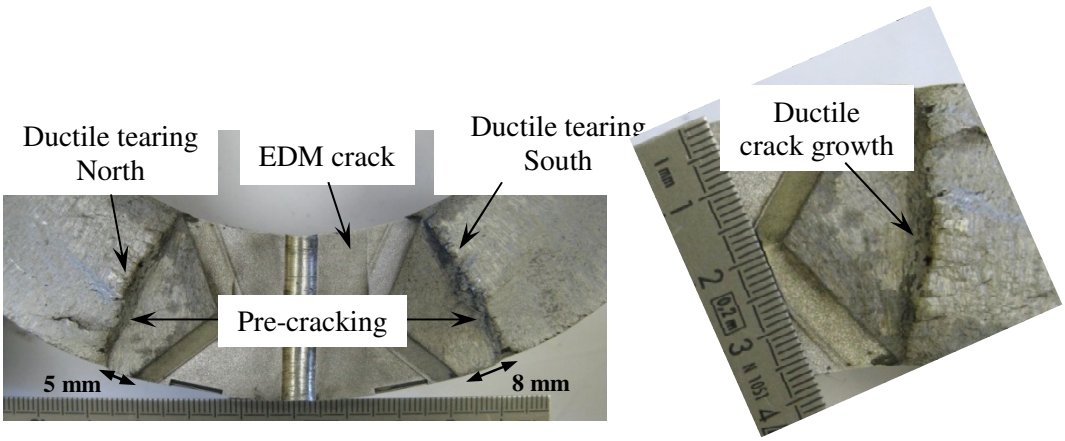

Figure 5.5 Post-test crack surface.

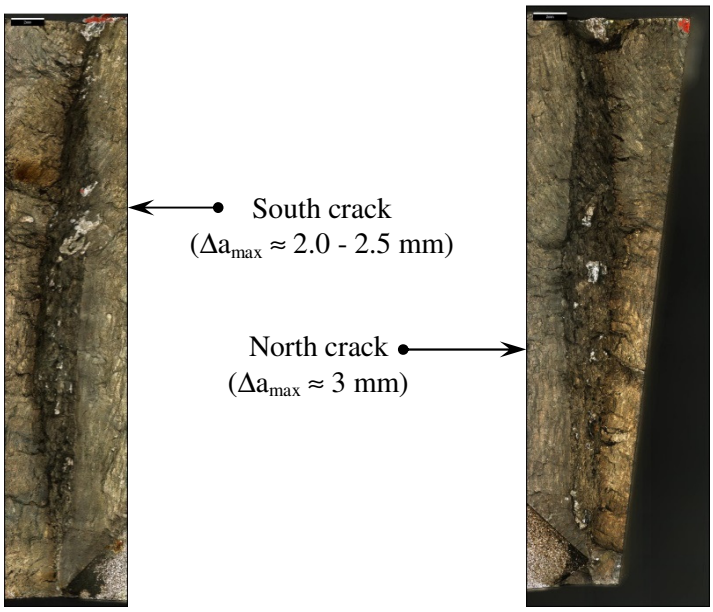

(a) (b)

Figure 5.6 Stable ductile tearing; (a) south crack and (b) north crack.

5.3 FINITE ELEMENT ANALYSES

A FE-model for the large scale four point bend test was established in ABAQUS [127]. Continuum elements with eight nodes and reduced integration (*C3D8R*) were used throughout the model. The total number of elements generated for the model was 463,582. The FE mesh for the specimen is presented in Figure 5.7. Other details of the model are as follows.

- Model construction

A three dimensional FE model was created according to the experimental set-up shown in Figure 5.3. In this model, the full test specimen including the MU2 test section, the two 304L extension pieces and the welding zones was taken as a single part. Due to the symmetry, one half of the full test specimen was modelled, with the symmetry conditions applied to nodes on the symmetry surface. The mounting rings were created as 3D discrete rigid shells of revolution with inner diameter exactly the same as the outer diameter of the cylinder. The positions of the mounting rings on the test specimen were set to be the same as the loading points and the support points in the experiment, Figure 5.8.

- Introduction of cracks

A through thickness symmetric circumferentially oriented pre-crack presented in Figure 5.2 was introduced into the FE model. This was achieved by using the interactive seam crack command. In this approach, a partition was created in the MU-2 test section in the crack plane. After this step had been completed, crack front and the direction of crack extension were defined in order to perform a contour integral analysis.

- Contact conditions

The contact between the test specimen and the mounting rings was defined by using the finite sliding surface-to-surface contact with frictionless tangential behaviour and hard contact normal behaviour. The master surface was defined both on the inner surface of the mounting ring and on its end faces as some overlap might have occurred during the simulation.

- Boundary and loading conditions

The mounting rings were positioned at a distance between the supporting points of 5.0 m and between loading points of 1.0 m. For the supporting point rings, all translations and rotations were prevented, with the exception of rotation about the z-axis. The same constraints were applied to the loading point rings but with an applied downward vertical displacement. The latter constraint was applied at a single point on the outside surface of MU-2 section, opposite to the crack location to prevent movement in axial direction of the test specimen. All boundary conditions applied to the model are presented in Figure 5.9.

- Material properties

Two sets of tensile test data for unaged parent metal and unaged weld metal were used for the Esshete stainless steel. The data for parent metal was documented in Serco Assurance report, 'A Constitutive Model for Parent Esshete 1250 and Associated Single Bead Weld Metal'[84]. The true stress/strain data for unaged weld metal were obtained from the tensile tests performed by EDF-energy [135]. The information about the tests is given in chapter 6. Young's modulus values for parent and weld metals were 204.5 GPa and 157.85 GPa respectively.

As the data for the 304L extension piece and the extension weld material for the test were not available, the material properties for 316L were used instead. A report published by Idaho National Laboratory [136] suggests that the tensile properties for 316L and 304L are very close at room temperature. Young's modulus for 316L parent and weld were taken as 195.6 GPa and 171.0 GPa respectively, with Poisson's ratio of 0.294. The tensile data for both Esshete 1250 and 304L is shown in Figure 5.10.

- Validation of the model

In order to verify the loading and boundary conditions for the FE model, it was run using elastic material property of unaged weld metal only. The result of interest here was the value of stress intensity factor, K_I, along the crack front with respect to the distance from the pipe inner surface. This relationship was compared with a standard solution of K_I for circumferential through-thickness crack in cylinder which can be calculated as follows [40] :

$$K_I = \{\sigma_a G_1 + \sigma_b (G_1 - 2G_2) + \sigma_{gb} G_3\}\sqrt{\pi a} \quad (5.1)$$

where σ_{gb} is the maximum bending stress in the uncracked cylinder. σ_a and σ_b are uniform stress and through wall bending stress respectively, which were assumed to be zero for this case. G_1, G_2 and G_3 are the influence coefficients depending on crack size and pipe geometry. These parameters are listed in Table IV.3.4.10.1 of R6 standard [40].

Figure 5.11 shows the values of K_I along the crack front which obtained from three elastic FE models. These models have different mesh size along the crack front. These are 0.5 mm, 1.0 mm and 2.0 mm respectively (Figure 5.12). The results show that the values of K_I obtained each model agrees well to within 6% of Eq.(5.1) except near the outer surface of the cylinder where the FE models predict a decrease in K_I. This implies that for elastic FE analysis, the values of K_I are independent of the mesh size between 0.5-2.0 mm.

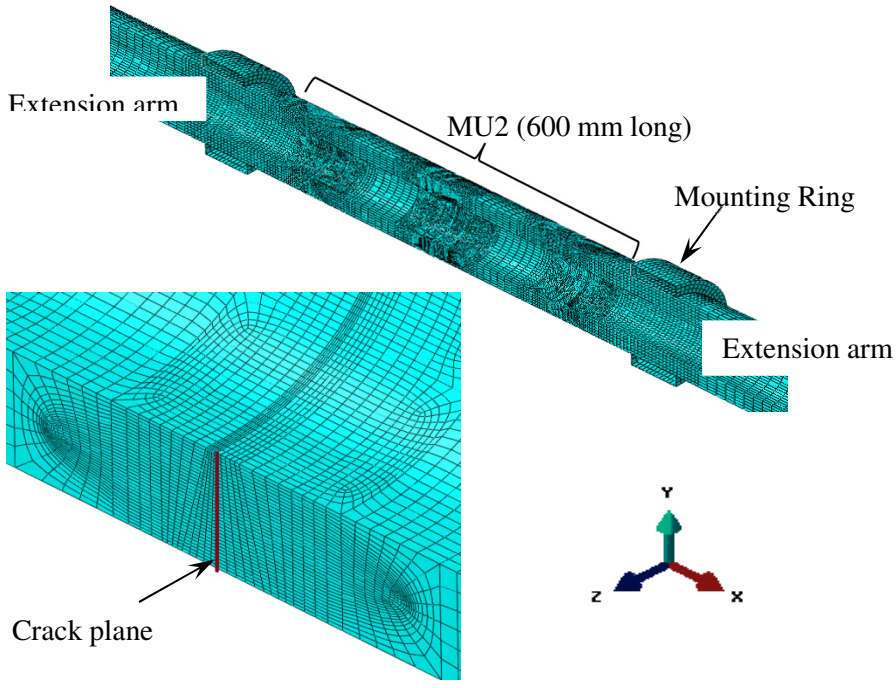

Figure 5.7 FE mesh for the specimen.

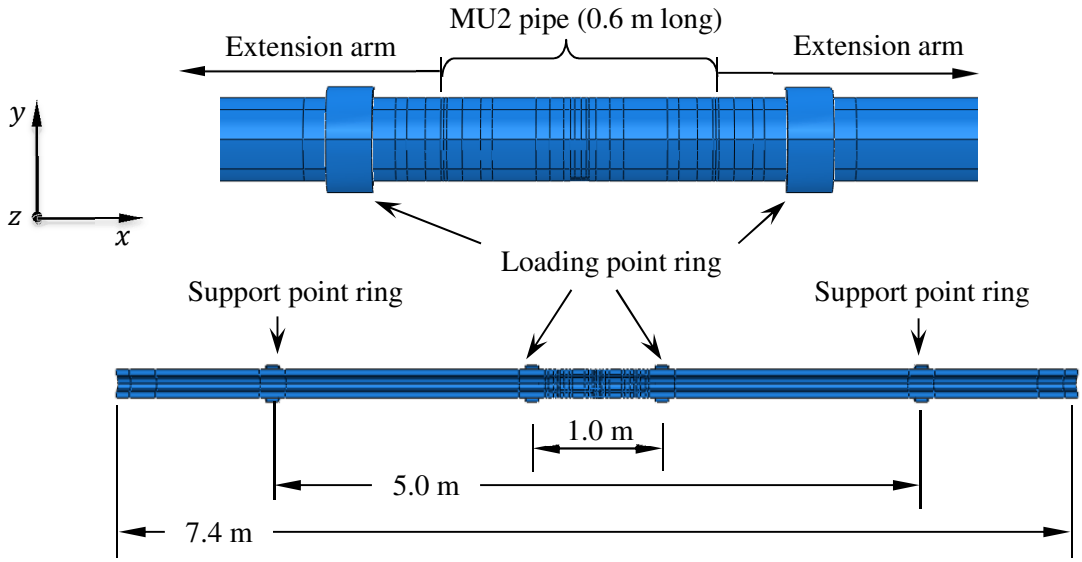

Figure 5.8 Assembly of the full test specimen and mounting rings.

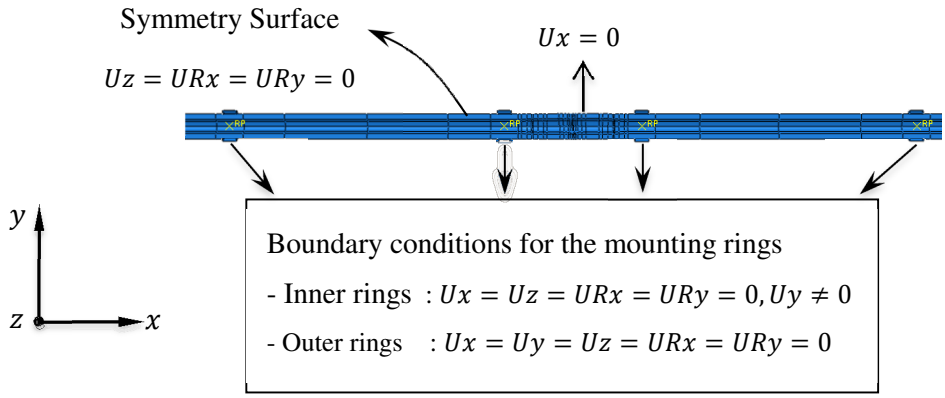

Figure 5.9 Boundary conditions applied to the full model.

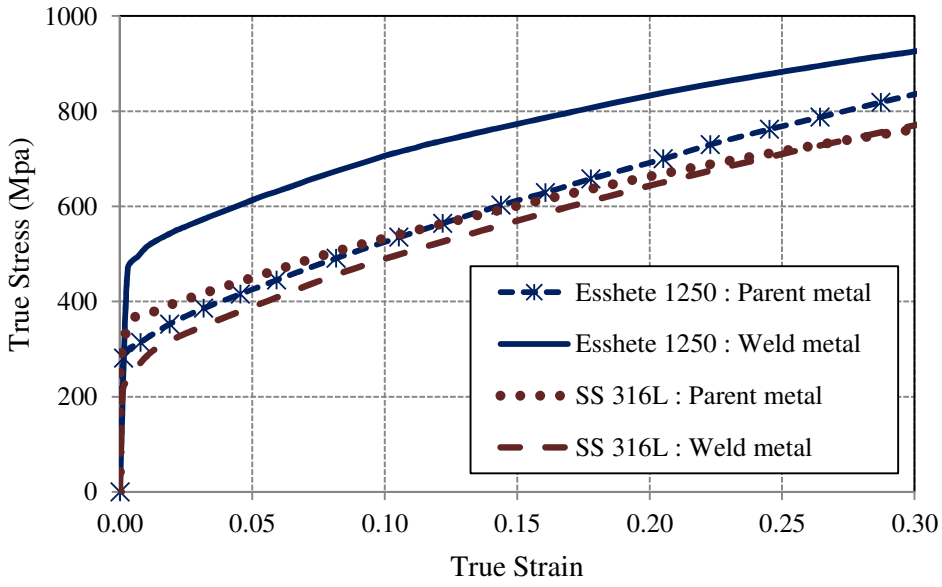

Figure 5.10 Stress-Strain data for Esshete 1250 and SS316L materials.

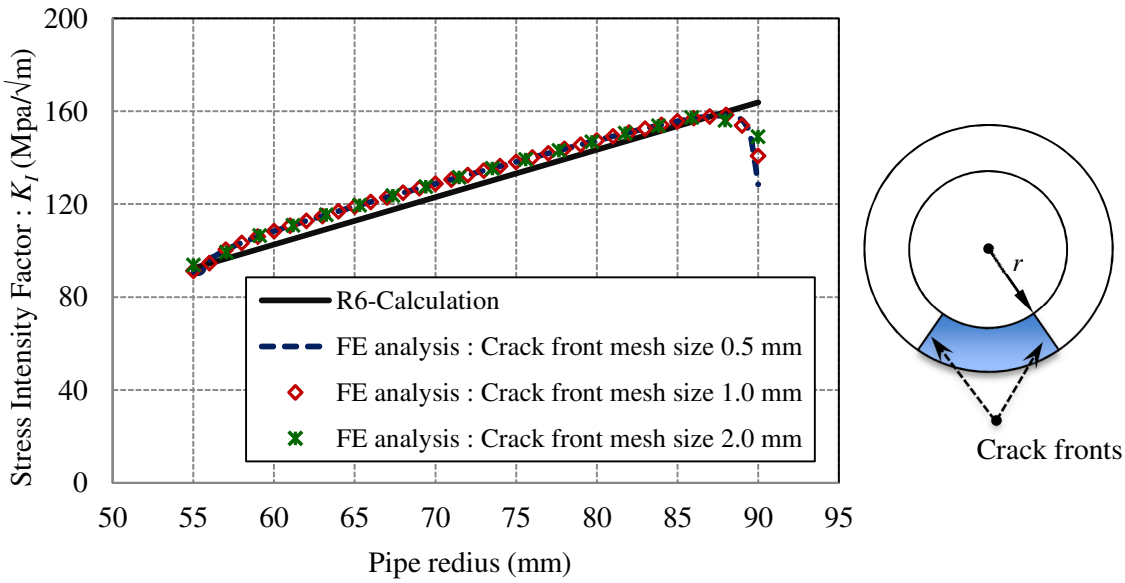

Figure 5.11 Comparison between R6-Calculation and elastic FE-results for K_I along the crack front at a bending moment of 230 kN-m.

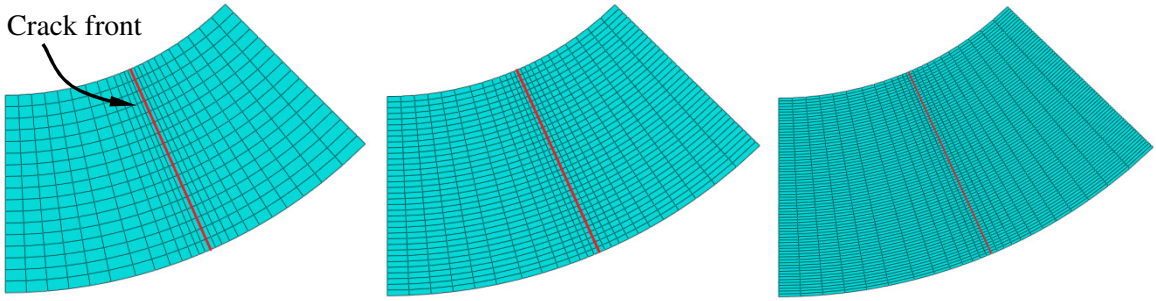

(a) (b) (c)

Figure 5.12 The variation in mesh size along the crack front of FE models of MU2 test : (a) 2.0 mm, (b) 1.0 mm and (c) 0.5 mm.

5.4 RESIDUAL STRESS MAPPING

- Measured residual stress

The measured residual stress data for weld Esshete pipe were given in large scale bending test simulation report [137, 138]. These values were obtained from the application of the deep-hole technique described by Son Do et al. [139]. Figure 5.13 illustrates two lines of residual stress measurement, one along the centre line of the repair weld and through the pipe wall thickness, and a second directly opposite to the centre repair weld. In both cases, only the in-plane (i.e. hoop and axial) residual stresses were measured using incremental deep hole drilling, described by Son Do et al. [139].

- Mapping technique

The residual stresses were introduced into the FE-model of the full test specimen, but without the presence of a crack. Two mapping zones for the repair weld and the remainder of original weld were defined according to the recommendation of Son Do and Smith [137, 138]. These are shown in Figure 5.13. The residual stress distribution was input into 2 mapping zones of the FE model directly as an initial condition by ABAQUS user-defined subroutine named *SIGINI*. Mapping zone 1 was used to map the residual stresses obtained from the repair path, whereas the stresses measured from opposite repair path were transferred to mapping zone 2. This process was done by assuming that the stresses along the measuring line were the same everywhere within the mapping zones.

Since the residual stress field introduced directly into the FE-model is always in non-equilibrium state, an equilibrium step (static step with no additional load applied) was performed in order to obtain a self-equilibrated distribution of residual stress before applying loads or displacement to the model. This step resulted in a difference between the initial stress input and the equilibrium residual stress obtained. To minimise this error, an iterative method [140] was used to modify the input values of initial stress to reproduce a desired residual stress distribution in the FE model. The adjustment equation used was as follows:

$$[\sigma]_{Input}^{i+1} = [\sigma]_{Input}^{i} + \alpha\{[\sigma]_{Measured} - [\sigma]_{Output}^{i}\} \quad (5.2)$$

where $[\sigma]_{Input}$ is the initial stress input into the FE-model, $[\sigma]_{Measured}$ is the measured residual stress and $[\sigma]_{Output}$ is the resultant residual stress obtained after an equilibrium step. The superscript, *i*, in Eq.(5.2) represents the *i*th adjustment and α is an adjustment factor, taken to be 1 here. The procedure starts with i = 0 and $[\sigma]_{Input} = [\sigma]_{Measured}$. After $[\sigma]_{Output}$ is obtained from the FE analysis, $[\sigma]_{Input}$ for the next iteration is calculated by using Eq. (5.2). This procedure was repeated until an agreement between $[\sigma]_{Output}$ and $[\sigma]_{Measured}$ was obtained.

- Mapped stress

Figure 5.14 shows the converged residual stress profiles after applying the iterative technique. This was achieved after 16 iterations. The output stresses in both hoop and axial direction along the repair path agree to within 9% of the measured values. The output hoop stresses also agree with the measured values opposite the weld repair except in the region between the inner pipe surface and 17 mm (r = 70 mm) from the inner pipe surface. The maximum difference between mapped and measured hoop stress in this region was ~ 25 MPa.

The overall agreement between mapped and measured axial stress along the opposite repair path was not as good. The difference between mapped and measured values was about 54 MPa at the inner surface, increased to 68 MPa near the mid pipe thickness, and then decreased to about 34 MPa at the outer pipe surface.

The converged residual stresses were then mapped onto the cracked models for subsequent simulations with loading. With the introduction of the crack, the residual

stresses redistributed again and showed high stress values ahead the crack tip, as shown in Figure 5.15. Since the values of redistributed stress in the vicinity of the crack are higher than the yield strength of weld material, it generates the plastic strain around the crack front before the external load is applied.

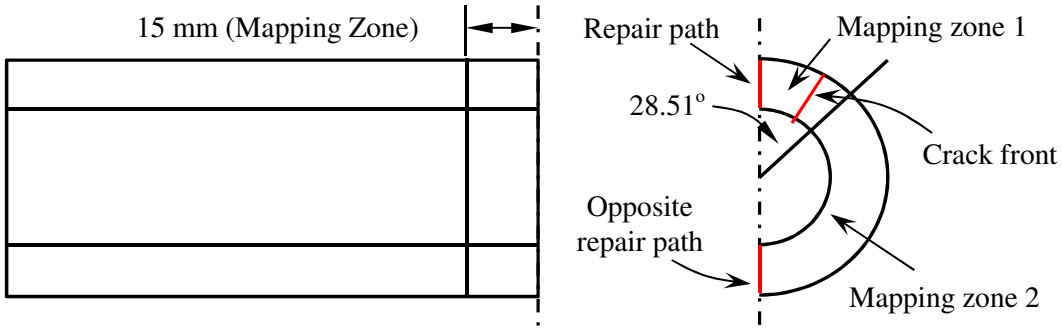

Figure 5.13 The location of two lines of residual stress measurement and mapping zones for the FE model.

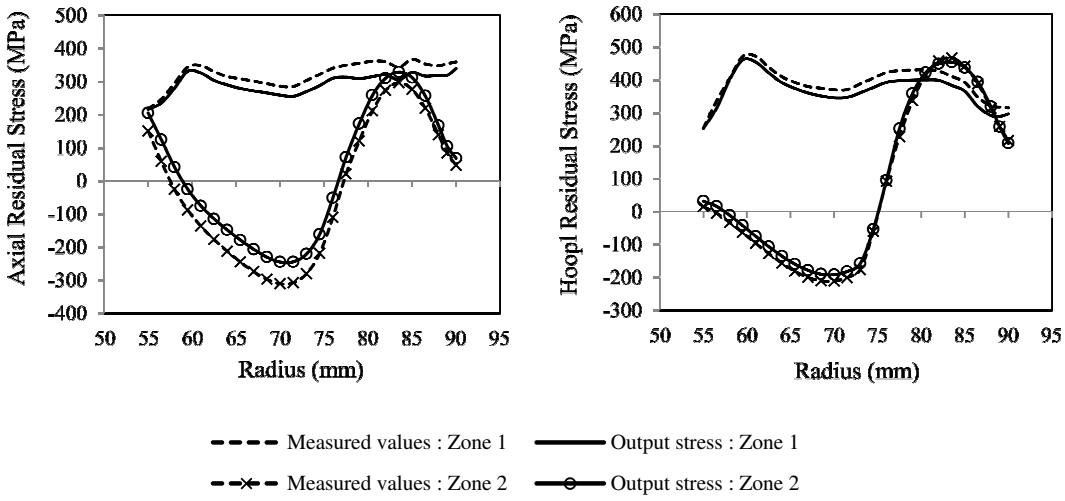

Figure 5.14 The measured stress and their corresponding iterated values from the FE model after an equilibrium step.

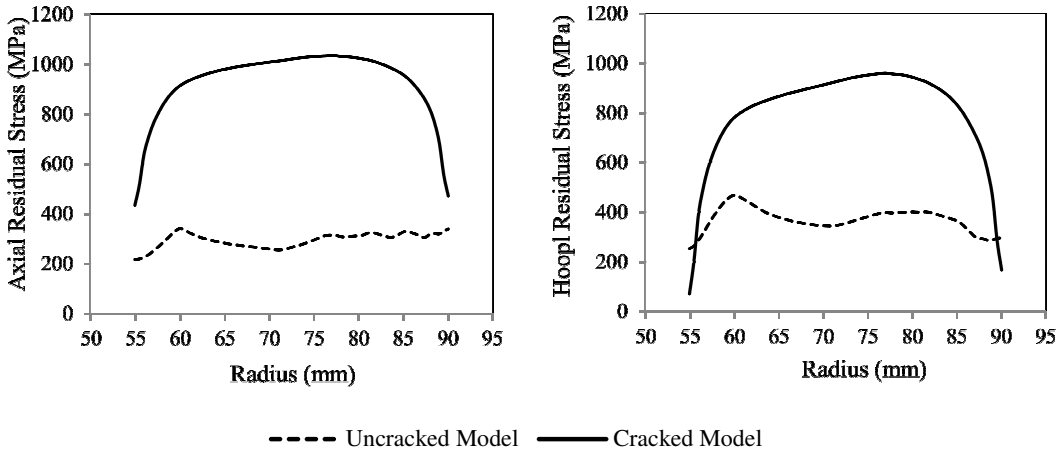

Figure 5.15 The elevated stress with the introduction of the crack along the crack front.

5.5 RESULTS AND DISSCUSSION

The FE model was first loaded by assuming that the materials behaved elastically. The model was run with and without residual stresses. In all cases, the model was run with the crack present. Load versus CMOD behaviour was plotted together with the data from the experiment, as shown in Figure 5.16. The effect of residual stresses on the elastic response was not significant and the compliance computed from load vs. CMOD curve was approximately 1.42×10^{-3} mm/kN.

The FE model was then run with elastic-plastic material properties. The relationship between load and CMOD is plotted in Figures 5.16 and 5.17 respectively. When the residual stresses were not present, the non-linear behaviour initiated at about 85 kN, whereas with the residual stresses, the non-linear behaviour occurred as soon as the pipe was subjected to external loading. The reason for this behaviour is that the residual stress had already produced plastic tensile strain around the crack front prior to any primary load being applied.

The relationship between load and CMOD with the residual stress present is in close agreement with the experiment up to the value of CMOD 0.4 mm. Within this region, CMOD $\leq$ 0.4 mm, the difference of reaction force obtained from FE-results and experiment is lower than 9% as shown in Figure 5.17.

At CMOD > 0.4 mm, the reaction force obtained from FE analysis are higher than the experimentally measured load by approximately 14 kN. This is likely to result from a number of limitations in the analysis. Firstly, the influence of crack extension on the global load versus CMOD has not been reflected in the analysis, which was only influenced by the initial crack length. Crack growth will reduce the applied load at a given value of CMOD, bringing the FEA and experimental data closer together. Secondly, the material properties in the heat affected zone were not taken into account in this simulation. Thirdly, the model did not consider any influence of residual stresses at the welds joining the MU-test section to the extension arms.

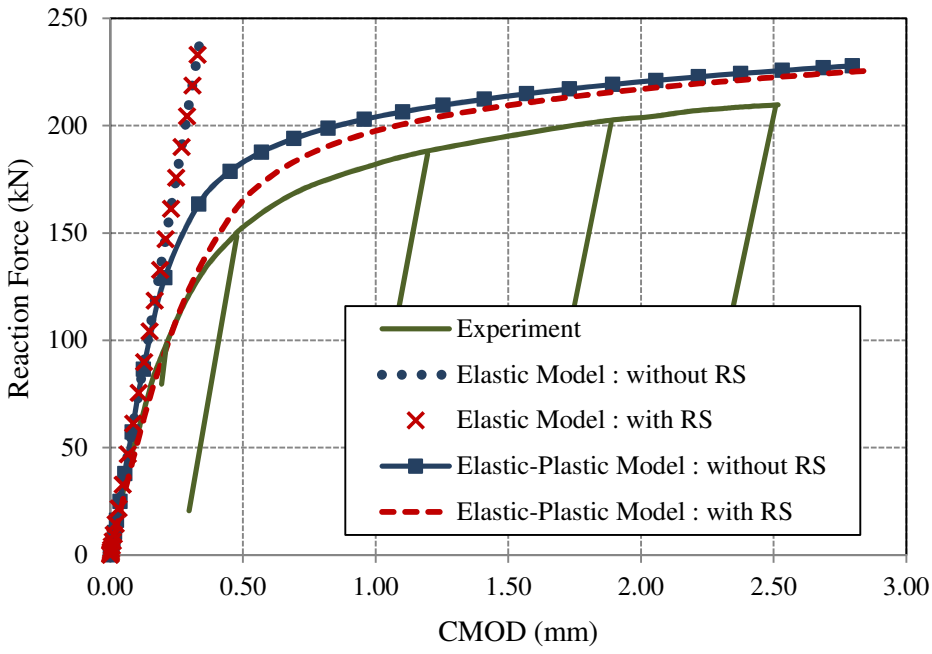

Figure 5.16 A comparison of CMOD versus reaction force between experiment and FE models at full scale CMOD.

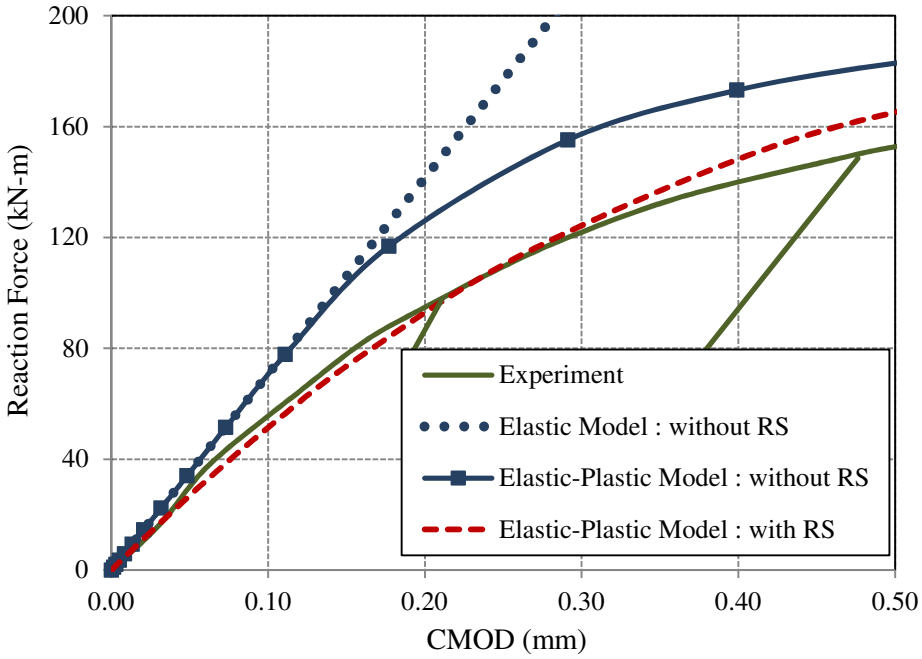

Figure 5.17 A comparison of CMOD versus reaction force between experiment and FE models at the values of CMOD < 0.5 mm.

- *J*-integral and crack extension

Figure 5.18 presents the variation of the *J*-integral along the crack front (or pipe radius) at a bending moment of 213 kN-m taken from the FE models. For the elastic loading case, the value of *J* increases linearly from the inner surface to 34 mm from the inner surface or at r = 89 mm. This linear variation agrees with the R6-Calculation [40] which is presented in Figure 5.11. However, the values of *J* drop rapidly at the outer surface of the pipe because of the effect of plane stress condition.

As expected, the *J*-integral values along the crack front are higher after running the model with elastic-plastic material properties due to the development of plasticity at the crack-tip. In this case, the location of the maximum value of *J* changes from being close to the outer surface in the elastic loading case to be at 27 mm from the inner wall (r = 82 mm). After introducing the residual stress, *J*-integral values along the crack front are higher by over 35%. This is because of the combined primary and secondary loading at the crack front. The maximum value of J-integral, however, is still at the same location along the crack front as in case without the introduction of residual stress.

The variation of *J* with applied moment at 82 mm from the inner pipe surface is shown in Figure 5.19. This clearly illustrates the influence of the residual stress on the value of *J*. With the introduction of residual stresses, the value of *J* is higher at the start of loading in comparison with the case where residual stresses were not present. Then, the difference in the value of *J* between these 2 cases, with and without residual stress, increases slightly with the increase of load. This supports the hypothesis that residual stresses increase the potential of crack initiation and the rate of crack propagation in the starting period of loading. However, as the load rises to approximately 160 kN-m, *J* starts to rise sharply and the difference in the values of *J* for the two cases reduces rapidly and then remains constant. This is because as plasticity develops in ahead the crack tip, the residual stress is relaxed and its contribution to the crack driving force progressively reduces.

The value of applied moment at any state of crack growth can be determined by using the information from the *J*-R curve for unaged material [141], which is represented by a power law equation as follows:

$$J = 0.429\ \Delta a^{0.696} \tag{5.3}$$

For example, if crack initiation was defined at 0.2 mm of tearing, the value of *J* corresponding to the initiation of crack can be calculated from Eq.(5.3) which is equal to 140 kJ/m^2. By using the relation in Figure 5.19, an initiation moment in MU-2 test is predicted to be 81 kN.m. Given the loading arrangements for the test, this corresponds to an applied load of 81 kN.

The *J*-integral distribution across the crack front has subsequently been used to estimate the amount of stable crack extension in the final state of the test. This was done by using Eq.(5.3). The results are shown in Figure 5.20. The predicted level of stable crack growth was estimated from the analysis (including residual stresses), both at an applied load of 213 kN and at CMOD of 2.5 mm, i.e. the final conditions in the MU-2 test. For the applied load of 213 kN, the maximum value of stable crack growth is predicted to be 1.6 mm. This value is about 2.6 mm at a final CMOD of 2.5 mm. The maximum value of ductile crack growth estimated is close to the test result (in south direction) which is 2.0-2.5 mm as shown in Figure 5.6a.

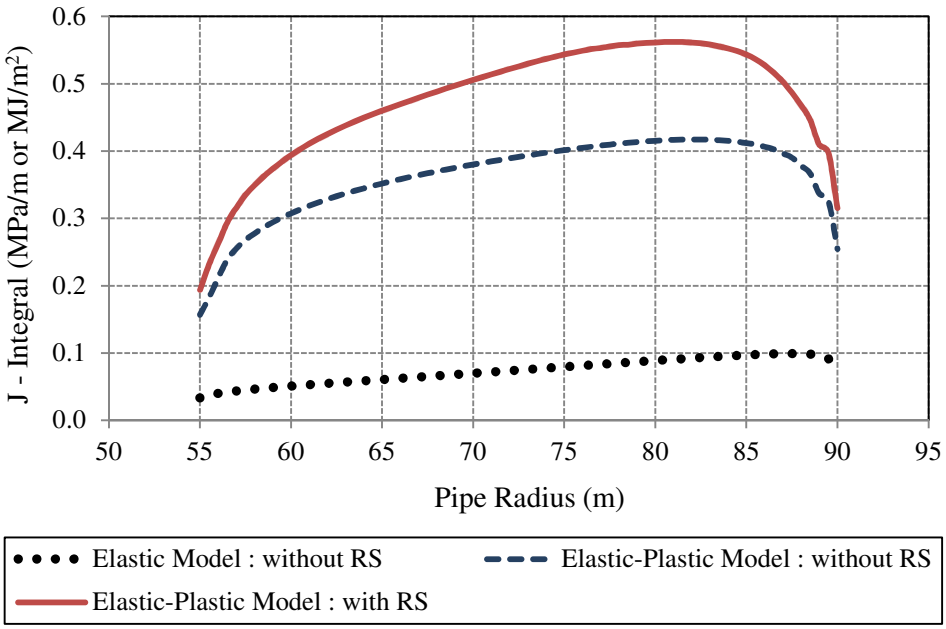

Figure 5.18 Comparison of J-integral along the crack front (pipe radius) at a bending moment of 213 kN.

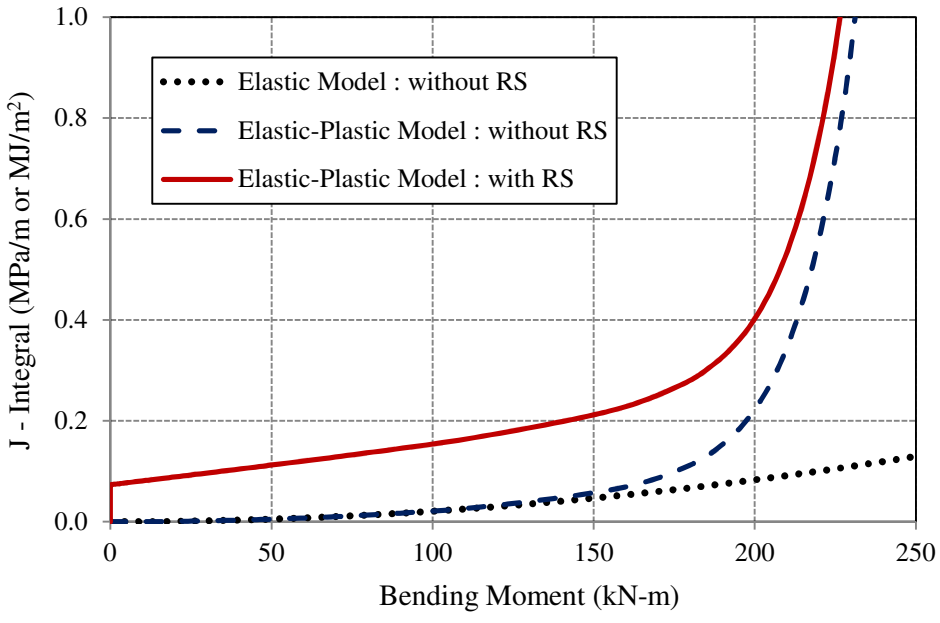

Figure 5.19 The variation of J-integral as a function of applied moment at 82 mm from the inner pipe surface.

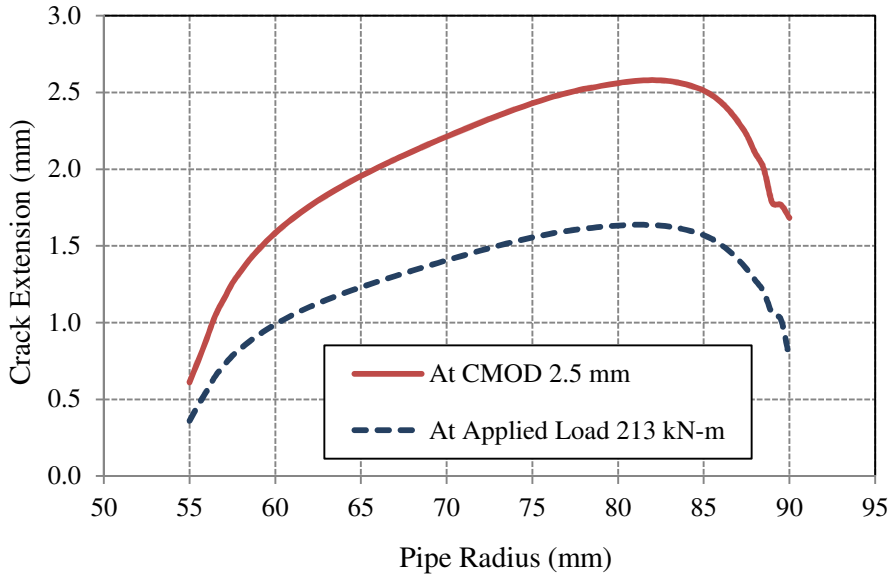

Figure 5.20 Estimation of stable crack growth along the crack front (pipe radius) in the final state of the test.

5.6 SUMMARY

This chapter has presented a detailed three-dimensional finite element assessment of the MU2 welded pipe test undertaken within the STYLE project. In this assessment, fracture mechanics parameters have been used to predict the crack initiation load in the test and the extent of crack initiation along the crack front. The analyses have taken into account the weld residual stress present in the test as characterised by deep hole drilling. The details of FE analysis of MU2 test are summarised in Figure 5.21. The following conclusions can be drawn from the analysis.

- Residual stresses are shown to influence the load versus crack mouth opening displacement behaviour during the test. An earlier onset of non-linear behaviour and a greater crack opening is predicted at a given load when residual stresses are included.
- The model predicts the location of crack initiation at 27 mm from the pipe inner surface which is close to the position observed in the actual test in south direction (about 24 mm). By assuming that the initiation of crack occured at 0.2 mm of ductile tearing, the initiation load was predicted to be 81 kN.

- The maximum extent of crack growth was predicted to be between 1.6 mm and 2.6 mm, whereas the actual crack growth observed in the test was around 2.5 mm in south direction and 3 mm in north direction.

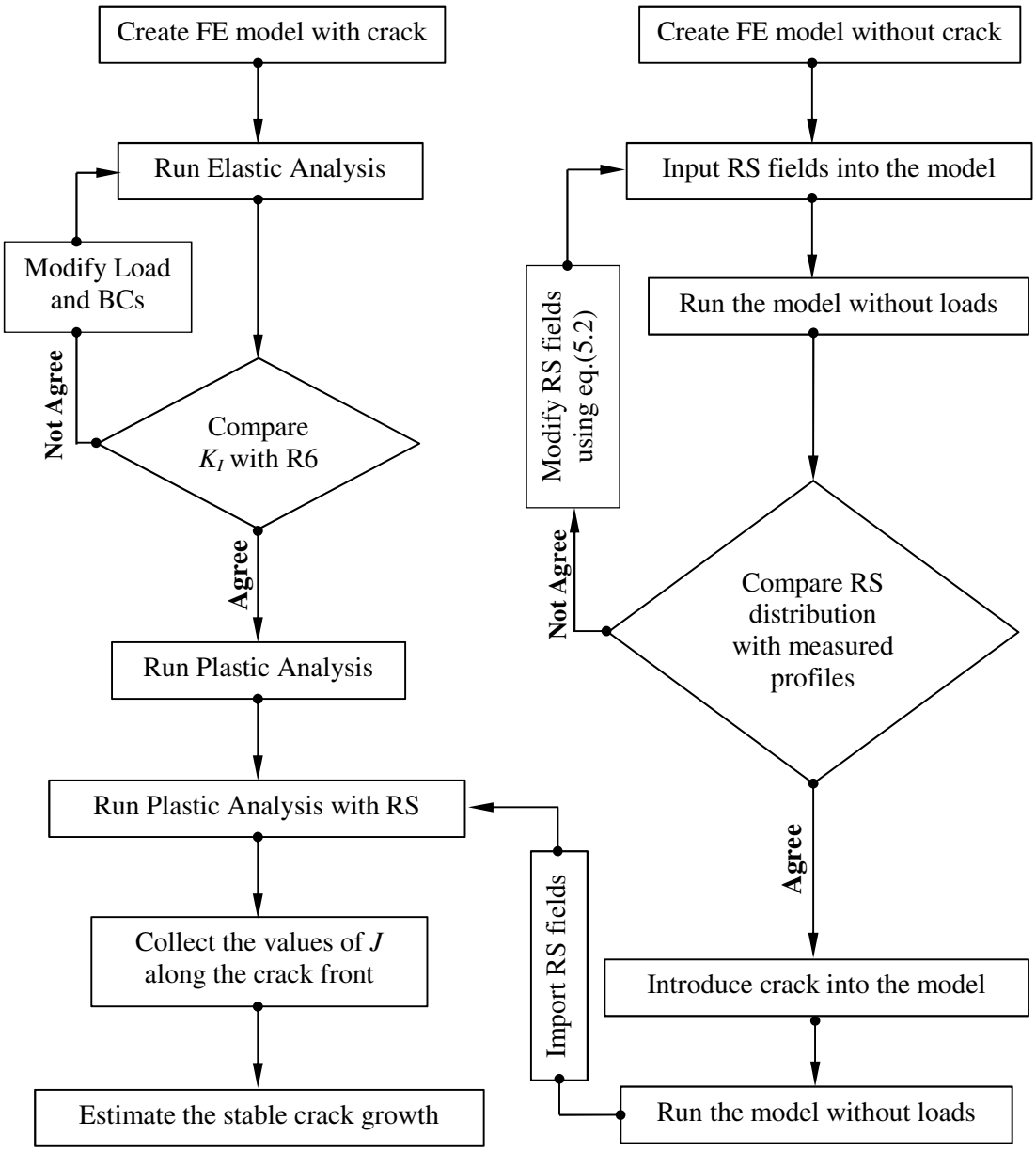

Figure 5.21 The steps of FE analysis of MU2 test.

CHAPTER 6

DETERMINATION OF ROUSSELIER MODEL PARAMETERS FOR ESSHETE WELD MATERIAL

6.1 INTRODUCTION

In order to develop a mechanistic model for MU-2, a series of tensile tests and ductile fracture toughness tests on Compact-Tension specimens were performed within the STYLE EU programme. These tests are referred to 'MU-5 tests' and the resulting experimental data was used as the basis for calibration of parameters for Rousselier ductile damage model.

This chapter focuses on the determination of Rousselier model parameters for Esshete weld material based on the results from tensile and compact-tension tests. Details of the FE-model used for this determination are presented. This includes the ABAQUS user defined subroutine for Rousselier damage model (presented in the previous chapter) and its implementation in the FE models. The main conclusions from this work are drawn in the last chapter.

6.2 EXPERIMENTAL TESTS

6.2.1 Smooth tensile test specimens

The tensile tests for the Esshete weld material was performed by EDF energy [40, 135] at ambient temperature. The data were obtained from tests on two smooth round bars extracted from the weld material in a second pipe of Esshete material. This pipe, called MU-5, was welded under identical conditions as that used for MU2 but without the repair weld. The extracted specimens were oriented in the axial direction with respect to the pipe. The geometry and the cutting profile of the specimens as extracted from the pipe are shown in Figure 6.1.

Figure 6.2 shows the relationship between load and the actual gauge length displacement recorded from the tensile tests of the two smooth round bars, designated here as specimen 8 and specimen 9. These specimens had an original

diameter of 3.83 mm and 3.88 mm and failed at approximately 5.1 mm and 5.8 mm displacement respectively, soon after they reached the maximum applied load of about 8 kN.

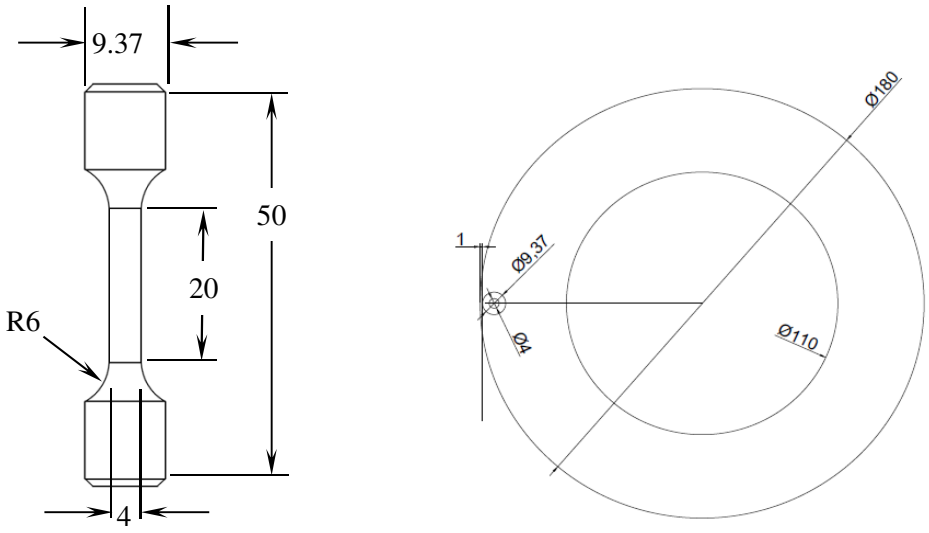

Figure 6.1 (a) Geometry and dimensions of tensile test specimen, and (b) cutting profile for obtaining a specimen blank from the MU-5 pipe (dimensions are in millimetres).

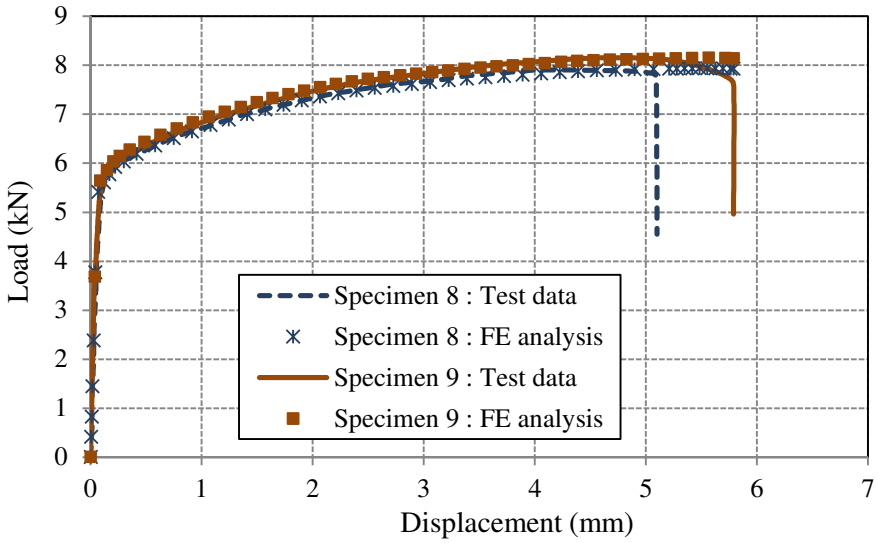

Figure 6.2 Load-displacement curves for smooth round tensile bars.

6.2.2 Side-grooved compact tension (CT) specimens

Deep cracked CT specimens, with 20% side grooves (10% on either side), were made from the same weld pipe as the tensile specimens. The specimens were extracted with the crack plane located at the weld centre-line. Specimens were oriented with the loading direction parallel to the axial direction and crack growth direction in the circumferential direction of the pipe. The specimens had standard size, i.e. 25 mm thick, with the length of fatigue pre-crack chosen to provide high constraint conditions. It is recommended [28] that the length of fatigue pre-crack from the machined notch must not be less than 5% of the total crack size, a_0 or 1.5 mm. The schematic of CT specimen and the cutting diagrams from the MU-5 pipe are presented in Figure 6.3.

The tests were carried out on two CT specimens by EDF Energy at room temperature [142], which provided the upper and lower bounds of crack growth resistance curve. However, the specimen which provided the lower bound value has been considered here for comparison and calibration to ensure that the calibrated model was appropriate to predict structural behaviour in a conservative manner. This specimen contained an initial crack length of 23.77 mm.

During testing, using the unloading compliance method [28, 143], the applied load reached a maximum value of approximately 81 kN at a Crack Mouth Opening Displacement (CMOD) of 1.75 mm before reducing to 64 kN at a CMOD of 3.5 mm (with ductile crack growth and the associated change in compliance). This can be seen in Figure 6.4. The level of crack growth seen in this Figure is approximately 4.5 mm.

Figure 6.5 showed the crack resistance curve with measured data points and an associated power-law regression curve of the test data. The equation of the regression curve was presented in Eq.(5.3). From this Figure, the value of toughness defined by a 0.2 mm offset line and a 1.5 mm Exclusion line were 0.245 and 0.726 MPa-m respectively.

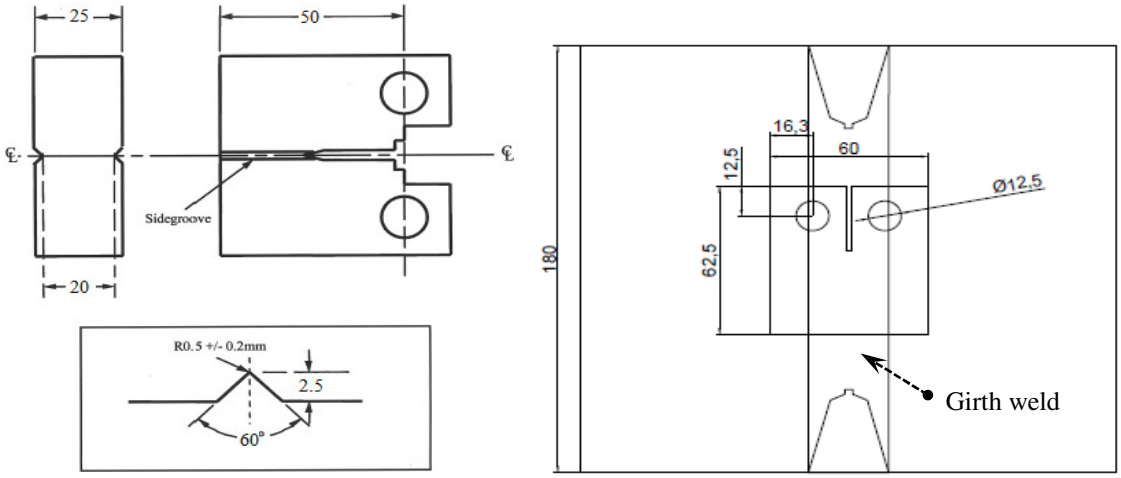

(a) (b)

Figure 6.3 (a) Geometry and dimensions of side-grooved CT specimen and (b) cutting profile for extracting the side-grooved CT specimen blank from MU-5 pipe (dimensions are in millimetres).

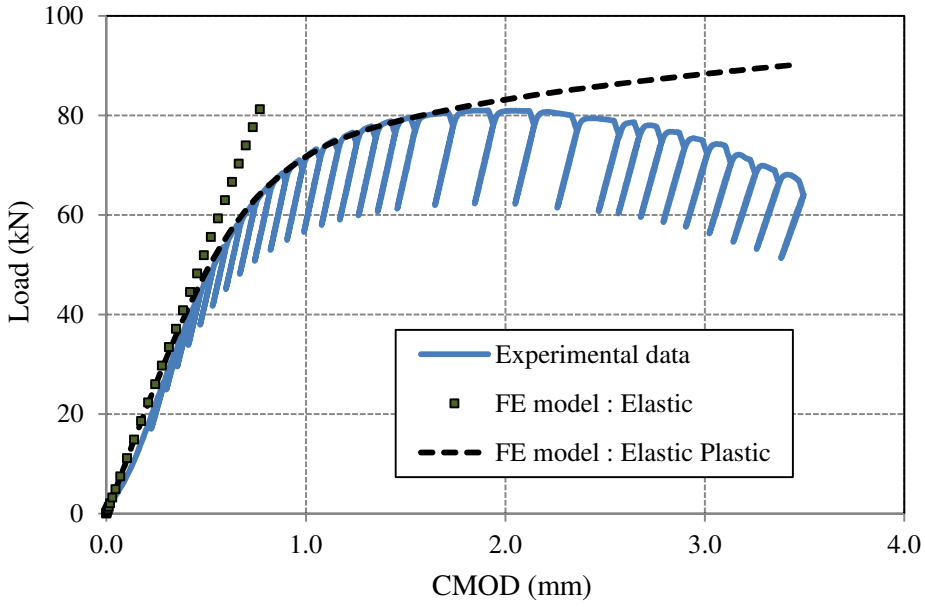

Figure 6.4 Load-CMOD curve for the side grooved CT specimen.

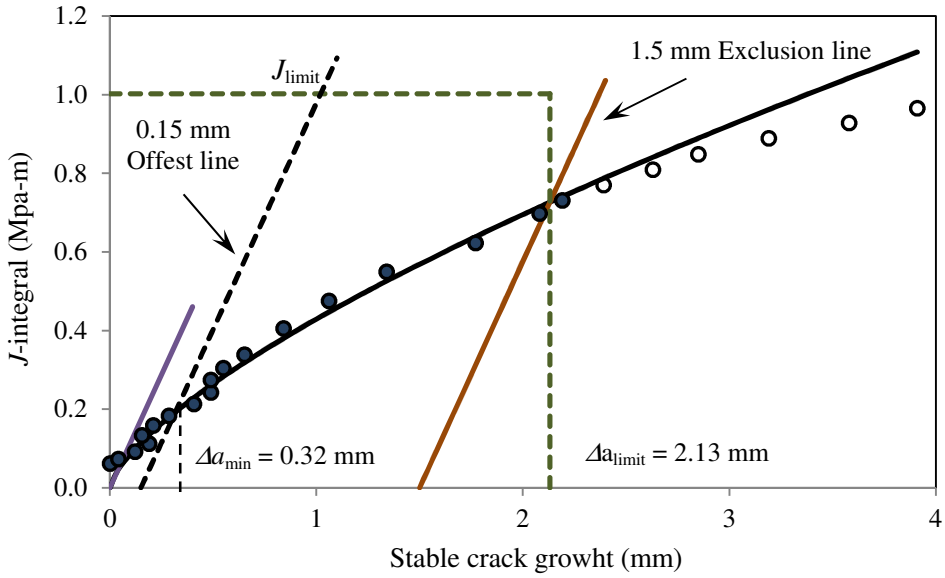

Figure 6.5 Crack resistance curve for the Esshete 1250 weld metal.

6.3 MATERIAL PROPERTIES

A true stress true strain curve for the Esshete weld material was derived from the load-displacement curves presented in Figure 6.2. As the test specimens failed at true strain values of approximately 0.22 and 0.25, the relationship between true stress and true strain beyond this point was extrapolated by using the Ramberg-Osgood equation:

$$\varepsilon = \frac{\sigma}{E} + \frac{\alpha\sigma_0}{E}\left(\frac{\sigma}{\sigma_0}\right)^n \tag{6.1}$$

The value $\frac{\alpha\sigma_0}{E}$ was set to be 0.002 in order to have the yield offset equal to the accepted value of strain of 0.2%. The data was fitted with a normalising stress (σ_0) of 267 MPa and a strain hardening coefficient (n) of 4. The true stress-strain data from this extrapolation is given in Table 6.1.

The values of elastic modulus and yield stress were estimated from true stress strain curve plotted using data in Table 6.1. The elastic modulus was estimated from the linear section of the curve whereas the yield stress value was determined using 0.2

percent offset method. This process was performed in a spreadsheet and provided the values of elastic modulus and yield stress of 157.85 GPa and 468 MPa respectively.

Table 6.2 illustrated the tensile properties for Esshete 1250 weld metals provided in literatures. This Table showed that the values of elastic modulus and yield stress determined in this study were similar to the tensile data for ESAB OK 69.86 electrodes presented in the Serco Assurance report [84]. The value of elastic modulus obtained in this study was close to the elastic value for Single pass groove weld, whereas the yield stress value was in the middle between the values of yield stress for single pass grooved weld and Multi-pass Butt weld.

As no estimate of Poisson's ratio was provided, a value of 0.3 was assumed. In addition, the material density was assumed to be constant for all materials at 7,850 kg/mm^3 [142].

Table 6.1 The stress-strain data for Esshete weld metal.

True strain ($\varepsilon_T, \%$)	True stress (σ_T, MPa)	True strain ($\varepsilon_T, \%$)	True stress (σ_T, MPa)
0.0	0	15.6	780
0.2	468	20.7	840
1.9	544	30.6	930
2.4	556	41.4	1,005
3.4	578	51.0	1,060
4.4	599	61.2	1,110
6.3	638	71.5	1,155
8.3	676	81.2	1,193
10.2	710	91.0	1,228

Table 6.2 The Tensile data for Esshete 1250 weld metals at room temperature.

Reference	Weld metal	Elastic modulus (GPa)	0.2% Proof stress (MPa)	Weld Type
[84]	ESAB OK 69.86	159.09 - 183.33	320-351	Single pass Groove
	ESAB OK 69.86	201.59 - 208.78	553.9-565.9	Multi-pass Butt
[144]	ESAB OK 69.86	167.7	534.4	Multi-pass Butt
[145]	ESAB OK 69.86		522-531	Multi-pass Butt
[146]	Nicrex UE-1		530	Multi-pass Butt
[147]	Nicrex UE-1		629.5	Weld Pad
Estimation from Table 6.1	Esshete weld metal	157.8	468	

6.4 FINITE ELEMENT MODELS FOR THE CALIBRATION OF ROUSSELIER MODEL

The FE models for smooth round tensile bar and side-grooved CT specimen were generated in ABAQUS. These models were used in the determination of Rousselier model parameters for Esshete weld material. Details of the models are given as follows :

6.4.1 FE model of tensile specimen

- Geometry, loading, and boundary conditions

Two FE models to simulate the tensile tests for specimens 8 and 9 were created in ABAQUS/Explicit. These models had a diameter of 3.8 mm and 3.88 mm respectively. Only a quarter of the specimen was modelled due to axial and planar symmetry. The normal displacements in the minimum section and the axis of symmetry were constrained. To reproduce the test, a displacement of velocity (v_y) was applied in y-direction on the top edge of the model. The details of this model are presented in Figure 6.6.

- Meshing

The FE model to describe the tensile specimen was composed of 520 axisymmetric elements, ABAQUS type *CAX4R*. There were 10 elements through the radius and an element width/height at the center of the specimen was set to be equal to 0.1 mm (Figure 6.6).

- Validation of the model

The FE-model was analysed as an elastic-plastic problem in order to check the accuracy of the boundary conditions, loading, and the finite element mesh. A large deformation FE analysis was performed to account for geometric none-linearity. The relationship between load and the applied displacement in axial direction obtained from FE-analysis is in good agreement with the experimental data, Figure 6.2.

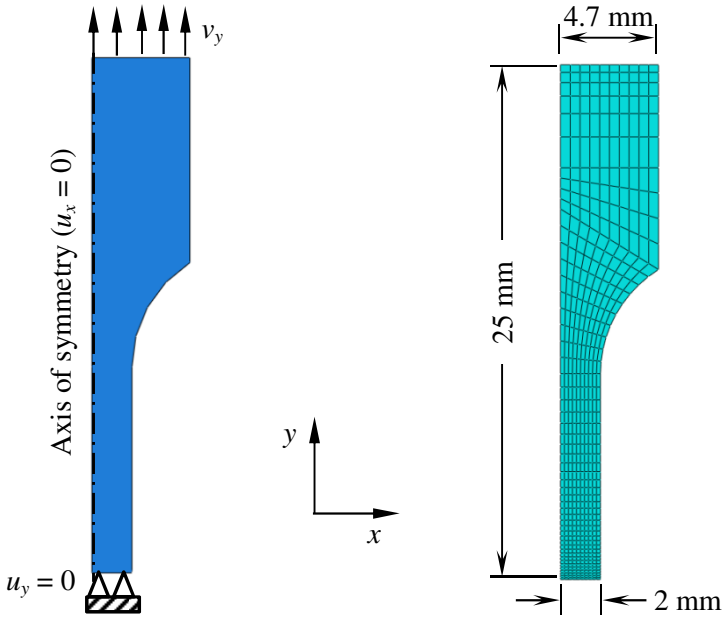

Figure 6.6 FE model of the tensile specimen:
(a) loading and boundary conditions and (b) the finite element mesh (520 elements).

6.4.2 FE model of side-grooved CT specimens

- Geometry, loading, and boundary conditions

Figure 6.7 shows a 3-dimensional FE element model constructed to simulate the side-grooved CT specimen. Reflective symmetry about crack plane and the longitudinal mid-plane enable the use of one quarter model as shown. This model was created by assuming that the model has straight a crack front with 23.77 mm initial crack length.

In this analysis, the loading pin was modelled as a rigid body and was assembled to the CT model by surface-to-surface contact with frictionless tangential behaviour and hard contact normal behaviour. The CT model was loaded by applying a displacement to the centre of the pin in the vertical (y) direction, whereas all other motions of the pin were restrained.

- Meshing

A continuum element with 8 nodes and reduced integration (C3D8R in ABAQUS) was employed for the CT specimen FE model. As the element size around the crack area needs to be varied between 50-200 μm [148, 149], partitions were created on the crack plane in order to form a dense mesh along the crack front, as shown in Figure 6.7b. The transition of element size between the dense mesh area and the rest of specimen was controlled by "the Advancing front technique" available in Mesh controls module in ABAQUS/CAE.

- Validation of the model

The validity of the FE model of the CT specimen was confirmed by comparing FE results with standard solutions and the experimental data. For this purpose, the model was run as both elastic and elastic-plastic problems. The validation of FE results is discussed below:

Elastic model

A linear elastic FE model of the CT specimen was run in ABAQUS/Standard. The displacement applied to the pin was 0.385 mm. This value corresponded to the value of CMOD of 0.77 mm and the applied load 81.3 kN respectively. Values of the Mode I stress intensity factor, K_I, along the crack front at a given load were examined. These values was compared with the standard solution of K_I for a side-grooved CT specimen, calculated as follows [29].

$$K_I = \frac{P}{\sqrt{BB_N W}} f\left(\frac{a_i}{W}\right) \tag{6.2}$$

where P is the load applied to the specimen, a_i is an initial (or current) crack length, W is the specimen width, B is the specimen thickness and B_N is the specimen thickness measured at the side grooves. $f\left(\frac{a_i}{W}\right)$ is the compliance function given by :

$$f\left(\frac{a_i}{W}\right) = \frac{(2+a/W)}{(1-a/W)^{3/2}}\left\{0.866 + 4.64\left(\frac{a}{W}\right) - 13.32\left(\frac{a}{W}\right)^2 + 14.72\left(\frac{a}{W}\right)^3 - 5.6\left(\frac{a}{W}\right)^4\right\}$$

Figure 6.8 presents the values of K_I along the crack front obtained from FE analysis. These values agree very well with the standard solution with the difference less than 5% except in the area adjacent to the side grooved surface. This is because the area near the outer surface of specimen is influenced by the stress concentrating effect of the side-groove.

Elastic-plastic model

An elastic-plastic FE model was also analysed in ABAQUS/Explicit. The result of interest in this case is the relationship between load and CMOD. This result was compared with the experimental data obtained from the test as presented in Figure 6.4. It can be seen that the FE results agree well with the experimental data up to about 2.0 mm of CMOD. It should be noted here that there was crack propagation during the test, whereas the FE models were run with a single crack size.

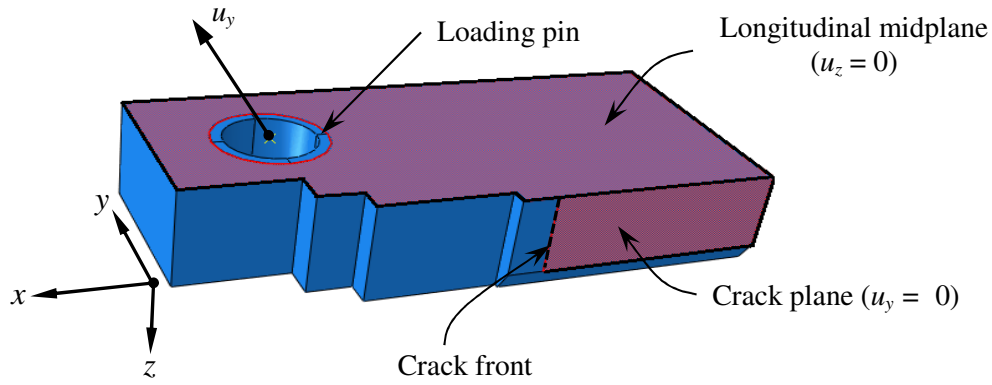

(a)

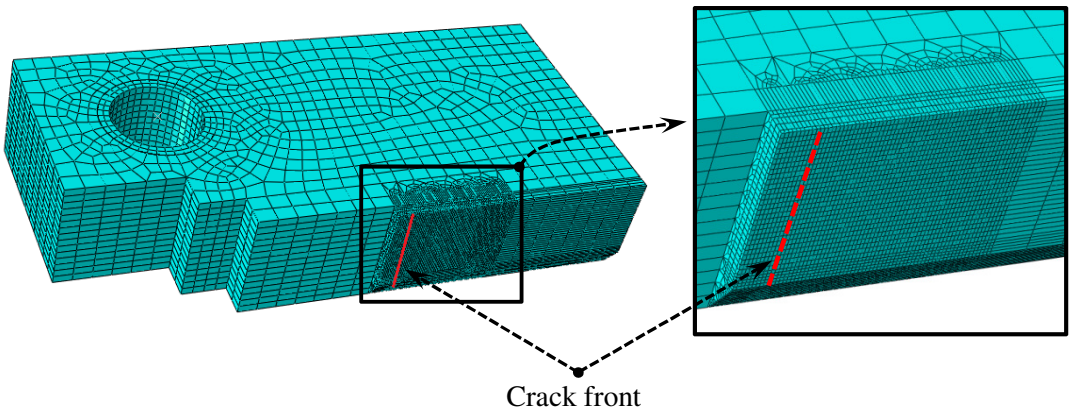

(b)

Figure 6.7 FE model of the CT specimen:

(a) loading and boundary conditions and (b) the finite element mesh.

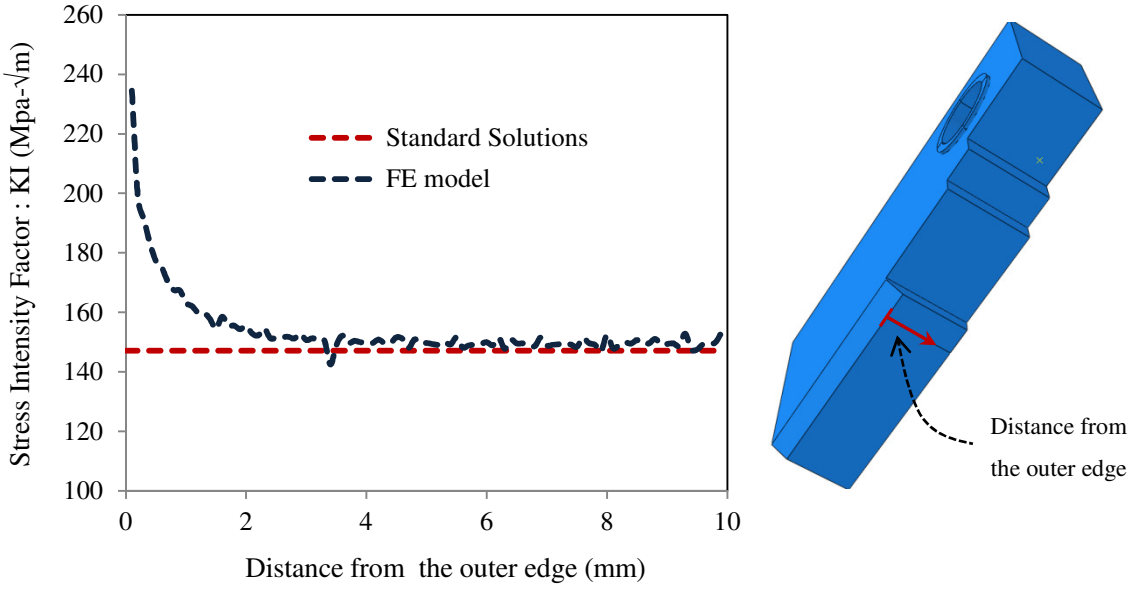

Figure 6.8 The comparison of FE solutions for K_I along the crack front at load 81.3 kN.

6.5 RESULTS AND DISCUSSION

6.5.1 The initial void volume fraction, f_0

Table 6.3 presents the chemical composition of the parent Esshete 1250 and its associated weld. These values were taken from the Serco Assurance Report [84] and were used to estimate the values of f_0 by Franklin's formula, Eq.(4.23). The results of this calculation are given Table 6.4. It gives the average value of f_0 for Esshete weld material as 0.0004. This value was in the middle range of the values of f_0 for austenitic stainless steels and its filler metals, as given in Table 6.5.

6.5.2 The critical void volume fraction at fracture, f_c

In these FE simulations, f_c is defined as the void volume fraction at fracture. This value is used as the criterion for deleting the failed elements. According to the discussion presented in [58], the value of f_c can be chosen as 0.15 for general metals.

Table 6.3 Chemical compositions of the Parent Esshete and associated welds [84].

Material	C	Si	Mn	P	S	Cr	Ni	Mo	V	Cu	Al	Sn	Nb
Esshette 1250 tube	0.097	0.45	6.23	0.025	0.004	14.71	9.38	0.95	0.28	0.13	0.004	0.005	0.92
MMA electrode	0.100	0.40	5.5	≤0.03	≤0.01	16.50	9.00	1.00	0.30	-	-	-	0.80
5mm MMA electrode	0.100	0.32	6.8	0.023	0.007	16.50	8.60	1.06	0.26	0.05	<0.01	<0.01	1.01
4mm MMA electrode	0.099	0.31	6.9	0.024	0.008	16.30	8.70	1.06	0.25	0.08	<0.01	<0.01	0.98
3.25mm MMA electrode	0.100	0.32	7.0	0.025	0.007	16.10	8.60	1.06	0.27	0.05	<0.01	<0.01	1.02
2.5mm TIG electrode	0.100	0.48	4.67	0.015	0.008	17.50	8.31	1.02	0.25	0.12	0.001	0.001	1.08

Table 6.4 The initial void volume fraction, f_0, for Parent Esshete and associated Welds (Estimated by using Franklin's formula).

Material	f_0
Esshette 1250 tube	0.0002
MMA electrode	0.0005
5mm MMA electrode	0.0004
4mm MMA electrode	0.0004
3.25mm MMA electrode	0.0004
2.5mm TIG electrode	0.0004

Table 6.5 The values of f_0 and L_c from the literature and from the Rousselier calibration.

Reference	Material	f_0	L_c (μm)	Specimen
[148]	316L(N)	0.00072	125	CT
[149]	Austenitic cladding layer	0	50	SENB
[150]	20MnMoNi 5 5 steel with an austenitic stainless steel cladding	0.00021	120	Tensile bar and CT
[64]	Austenitic weld	0.0001	400	Notched tensile bar
[151]	E308L (filler metal)	0.001	100	SENB
Rousselier parameter calibration	Esshete weld metal	0.0004	50	Side-grooved CT

6.5.3 Rousselier parameters (D and σ_1) and crack tip mesh size (L_c)

As described in [64, 129], the parameter D can be set as 2.0 for materials containing the value of f_0 equal or less than 0.001, so that only σ_1 and L_c need to be determined. The value of σ_1 was first calibrated via the FE model of the tensile specimen test. This specimen has high ductility with no major stress or strain gradients and the effect of L_c on the results of this model is very small. Once the value of σ_1 was obtained for the material of interest, L_c was then determined from a calibration using the FE model of side-grooved CT specimen and the *JR*-curve data shown in Figure 6.5. In this case, the strain gradient is very high at the crack tip and the predicted crack resistance strongly depends on the mesh size.

First calibration

The FE model for a smooth tensile test specimen, discussed in section 6.4.1, was simulated in ABAQUS/Explicit with the implementation of VUMAT. The value of σ_1 was chosen by trial and error using different values until a close agreement was

reached between the analytical and experimental data. From this, a values of σ_1 = 170 MPa was obtained which provided the best match with the displacement at failure, as shown in Figure 6.9. This value was considerably lower than the first trial value (σ_1 = 538 MPa) computed from the equivalent stress at fracture, as suggested in [129].

The value of σ_1 = 170 MPa was then used in the FE model of the side-grooved CT specimen, outlined in section 6.4.2, in order to determine the value of L_c. The process of calibration was performed by fitting the relationship between the values of *J*-integral and crack growth (Δa) obtained from FE analysis with crack resistance curve shown in Figure 6.5. From this FE analysis, the *J*-integral value at any loading point was determined from the increment of area under load versus CMOD. If *U* represents the area under the curve up to a point at constant displacement corresponding to fracture, the *J*-integral at this point is then determined in the same manner as in the test [28]:

$$J = \frac{\eta\, U}{B_n b_0}\left\{1 - \frac{(0.75\eta - 1)\Delta a}{b_0}\right\} \tag{6.3}$$

where B_n = net specimen thickness, b_0 = length of initial uncracked ligament, η = 2 + 0.522(b_0/W),and W = specimen width.

The corresponding value of Δa was derived from the number of failed elements ahead of the crack front in the FE model. However, as the number of failed elements along the crack front was not uniform, a nine-point average measurement technique was used to average the value of Δa [28, 29]:

$$\Delta a = \frac{1}{8}\left(\frac{\Delta a_1 + \Delta a_9}{2} + \sum_{i=2}^{8} \Delta a_i\right) \tag{6.4}$$

where Δa_i, i = 1-9, are the values of crack growth between the measurement positions 1 to 9, as shown in Figure 6.10.

It was found that the value of σ_1 = 170 MPa, which was very low compared with the suggested value (σ_1 = 538 MPa), provided a very high growth rate of the softening part of Rousselier yield function. This value made the elements in the area ahead of the crack front fail rapidly at the early stage of loading. From this, the FE model of

side-grooved CT specimen could not provide a close agreement between the analysis and the experiments.

The reason of this problem may be explained by the work published by Taylor and Sherry [152] who studied the mechanism of ductile fracture in the aluminum alloy AL2024-T315 using combination of synchrotron X-ray and focused ion beam tomography. They found that the distribution of f below the fracture surface of CT specimen was considerably different from that observed in notched specimens although these specimens were extracted from the same virgin material. They also showed that the void volume fraction in CT specimen was far more localized toward the fracture surface than that observed in the notched tensile specimens. In addition, the maximum value of f just under the fracture surface of the CT specimen was almost two times higher than that in the notched specimen. These indicate the difference in the rupture mechanism between notched tensile and CT specimens. According to this it may be not possible to define a single set of ductile damage parameters for all test specimen geometries in ductile failure simulation, because, for some materials, their failure mechanism may be not only dependent on the microstructure but also the test specimen geometry which influences the local stress and strain state in the fracture process zone.

Based on above, the values of σ_1 and L_c were, therefore, recalibrated using only the FE model of the side-grooved CT specimen which has a level of constraint closer to that experienced by with the MU2 test specimen.

Second calibration

The FE model of side-grooved CT specimen was run in ABAQUS/Explicit, and VUMAT for the Rousselier damage model was incorporated into the model for the analysis. The calibration started by fixing the element dimension ahead the crack tip to be equal to 100×100×100 μm^3 and varying the value of σ_1 between 468 MPa and 535 MPa. The results of this calibration are presented in Figure 6.11. It can be seen that the value of σ_1 affects the slope of the *J*-R curve. This is because σ_1 controls the softening part of the Rousselier yield function which affects the initiation load for the microcrack along the crack front of the model. For the same load conditions, a higher value of σ_1 increases the crack initiation load which results in an increase in

the slope of the *J*-R curve. From Figure 6.11, value of σ_1 = 506 MPa provided the slope of the *J-R* curve close to the one obtained from the fracture test.

σ_1 = 506 MPa was then used in the FE analysis of the smooth tensile bar. As expected, this model predicted a greater displacement at fracture of approximately 6.4 mm which is 0.8 mm greater than the value in the test, as shown Figure 6.9.

The FE model of the side-grooved CT specimen was rerun again in order to calibrate the value of L_c. For this, different crack front mesh sizes, ranging from L_c = 50-100 μm^3 were considered with the other parameters fixed (D = 2 and σ_1 = 506 MPa). The minimum distance containing the array of these fine elements was set to be at least $5J_{max}/\sigma_y$ where J_{max} is the maximum value of the *J*-integral at failure of a pre-cracked specimen [40]. The results of this analysis are presented in Figure 6.12. It shows that an increase in the mesh size elevates the crack growth resistance. The best material behaviour is obtained by using a value of L_c = 50 μm. This mesh size, 50 μm, is consistent with the metallography of Esshete 1250, presented in [153], which illustrates that the average grain size of Esshete 1250 is less than 100 μm, Figure 6.13.

The global effect of crack front mesh size is presented in Figure 6.14 which shows that the size of crack front elements affects the change of slope of load versus CMOD curve. The curve obtained from the FE model with L_c = 50×50×50 μm^3 provides a good fit to the experimental data up the value of CMOD 0.9 mm. After this point, the load gradually decreases below the experimental curve.

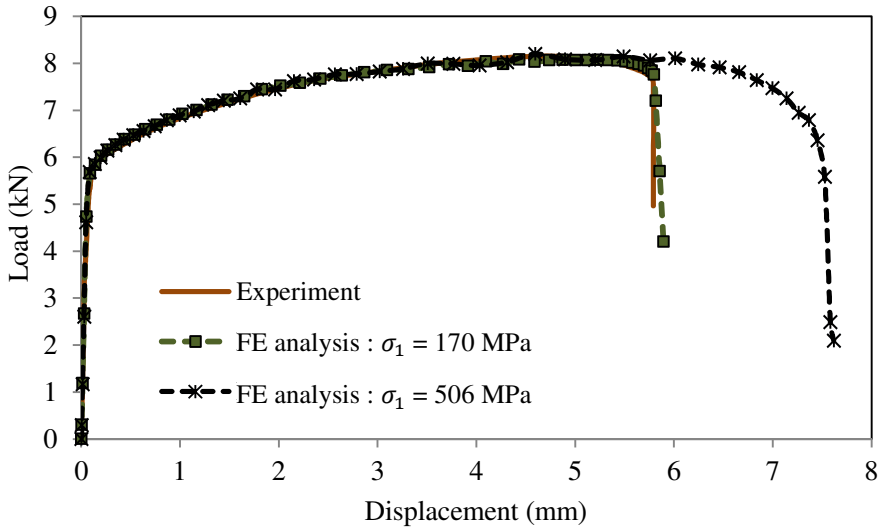

Figure 6.9 Predicted (FE) and experimental load vs. displacement curves for the smooth round bar (specimen 9).

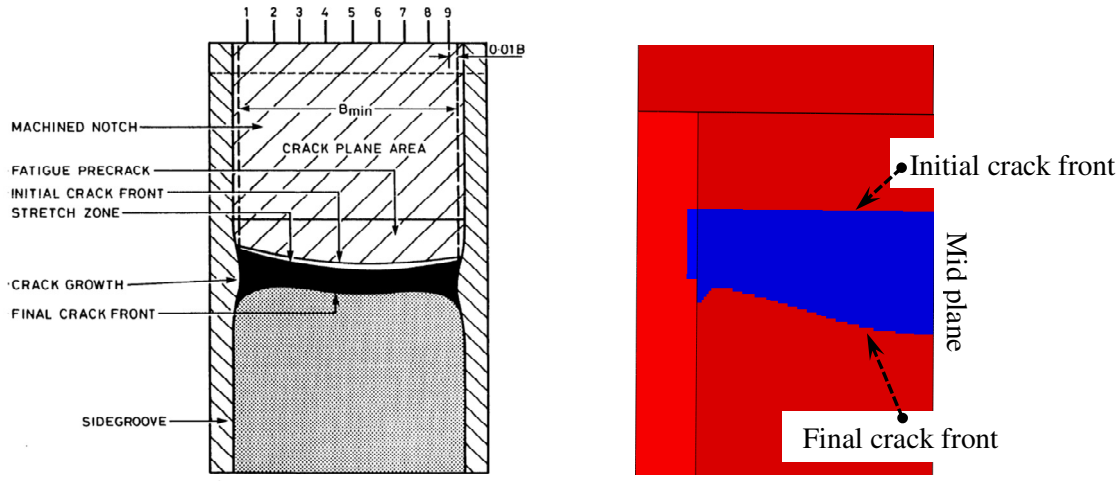

(a) (b)

Figure 6.10 (a) Locations for crack length increment (Δa) measurement [28] and (b) the final crack surface from FE analysis of side-grooved CT specimen.

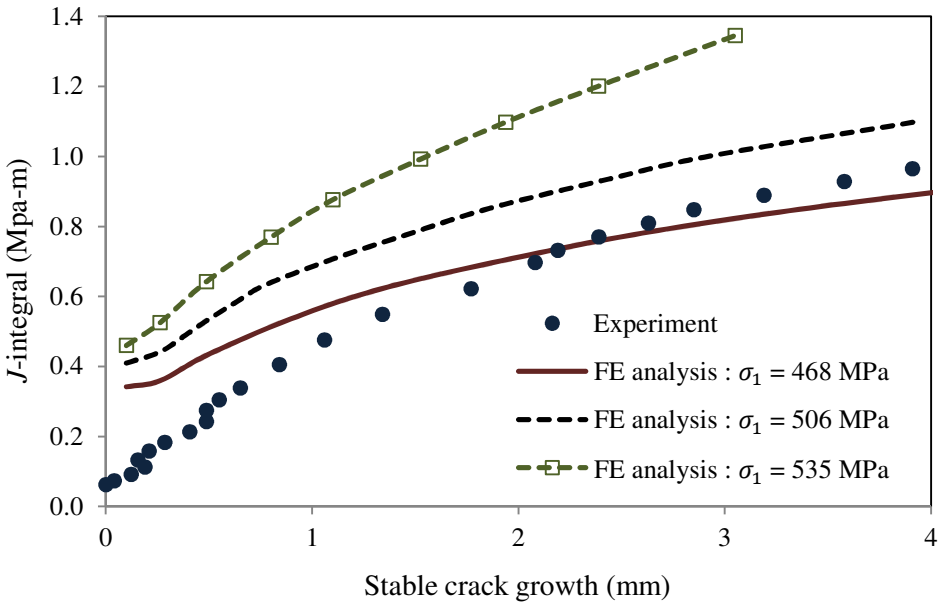

Figure 6.11 Predicted (FE) and experimental crack resistance (J-Δa) curves for side-grooved CT specimen (L_c = 100×100×100 μm^3).

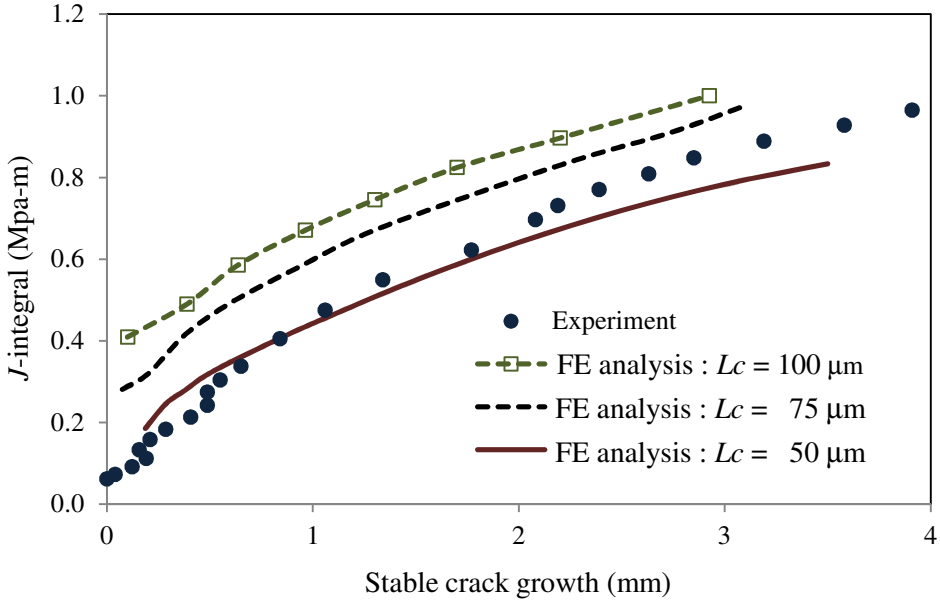

Figure 6.12 Predicted (FE) and experimental crack resistance (J-Δa) curves for side-grooved CT specimen (σ_1= 506 MPa, D = 2.0).

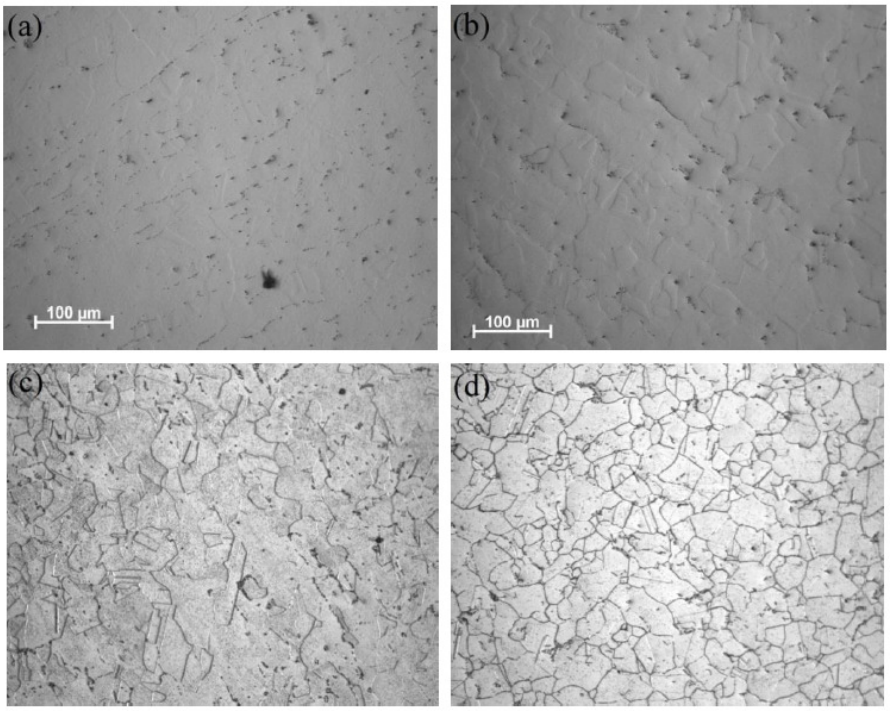

Figure 6.13 Optical micrographs (magnification × 20) of Esshete 1250 with different preparations: (a) unaged before etching; (b) aged before etching; (c) unaged after etching; (d) aged after etching [153].

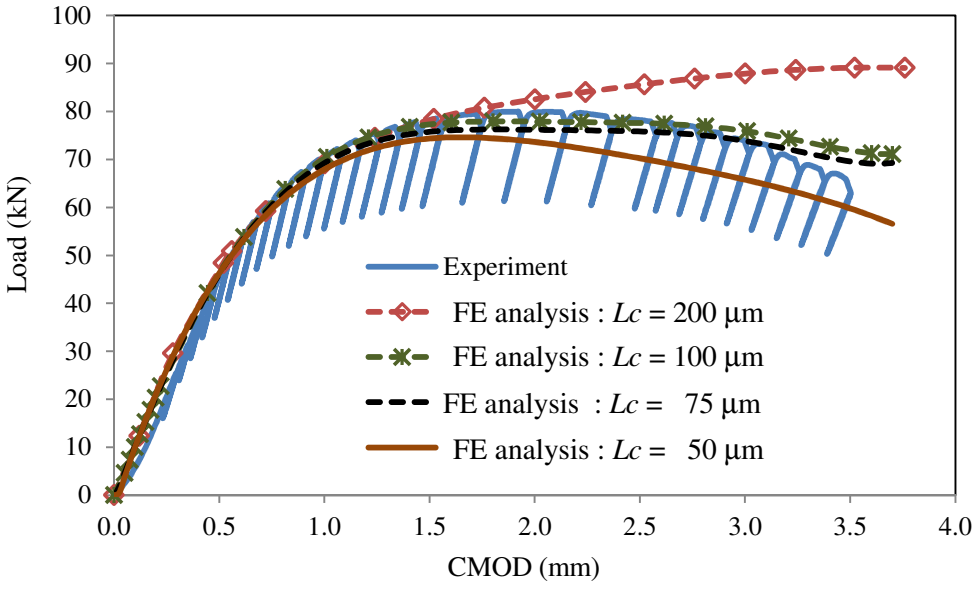

Figure 6.14 Predicted (FE) and experimental load-CMOD curves for a side-grooved CT specimen.

6.6 SUMMARY

The main aim for the work presented in this chapter was to determine Rousselier model parameters, f_0, f_c, D, σ_1 and L_c, for Esshete weld material. In this work, D and f_c were defined as material constants as discussed in [58, 129], and f_0 was estimated from the manganese sulphide (MnS) inclusions using Franklin formula. The remaining parameters, σ_1 and L_c, were chosen by trial and error using different values until close agreement was reached between FE predictions and experimental results.

It was not impossible to define a set of σ_1 and L_c which provided reasonable agreement between FE predictions and experimental data for both smooth tensile bars and CT specimens due to the difference in the failure mechanism of these specimens. *J*-R curve for Esshete weld material, therefore, was the only available test result used to determine the values of σ_1 and L_c.

The Rousselier model parameters for Esshete weld material obtained from this work are summarized in Table 6.6. These parameters are subsequently used to predict crack initiation and growth in MU-2 test. This is presented in chapter 7.

Table 6.6 Values of Rousselier parameters calibrated for the Esshete weld material.

Rousselier parameter	Calibrated Value
The initial void volume fraction, f_0	0.0004
The critical void volume fraction, f_c	0.15
Material parameter D	2.0
Material parameter σ_1	506 MPa
Crack tip element size, L_c	50 μm

CHAPTER 7

PREDICTION OF DAMAGE IN A LARGE SCALE BENDING TEST USING ROUSSELIER MODEL

7.1 INTRODUCTION

In this chapter, the Rousselier damage model, incorporated in the FE analysis of the MU2 test, is presented. The model is used to predict crack initiation and crack extension in the MU2 specimen. The analysis was performed by employing the Rousselier model parameters for Esshete weld material calibrated in the manner discussed in chapter 6. The results obtained from this analysis were compared with the results obtained by fracture mechanics approach presented in chapter 5 in order to assess the validation of the analysis and to gain new insights into the influence of residual stresses on ductile tearing and the capability of the Rousselier model to simulate the behaviour observed. Details of FE analysis and the conclusions drawn from this work are also presented in this chapter.

7.2 TRUNCATED FINITE ELEMENT MODEL OF MU2 TEST

The Rousselier damage model was developed to simulate the behaviour of cracked structures and components directly, without the need to use the usual fracture mechanics parameters to interpret the local crack tip behaviour. This model has been used in FE simulations to predict ductile failure in many cracked components. However, the difficulty arises when Rousselier model is employed to analyse ductile failure in large-scale components. This is because Rousselier model is a mesh-size-dependent damage model in which the element size in a high stress and strain gradient region must be small enough to represent the average interparticle spacing. The FE model consequently contains a very large number of elements, e.g. in excess of more than a million elements, resulting in high computational costs.

The number of elements in the model can be reduced by using submodelling technique. This technique enables the user to study the area of interest in detail by modelling only the important section of the model, i.e. a submodel or truncated

model. Using submodelling technique in ABAQUS involves two main steps. The first step is to create and analyse the FE model of the full structure which is called global model. This model can be created using a relatively coarse mesh and possibly a simplified geometry. Once the global model is analysed, the truncated FE model containing only the important or critical section of the structure is created and analysed by prescribing the boundary conditions obtained from the global model.

Based on above procedure, the submodelling technique was employed for the simulation of MU2 test using Rousselier damage model. Details of the model are as follows :

- Model construction

This analysis involves two FE models; a global model and a truncated model. As the full FE model of the MU2 test detailed in Figures 5.7-5.9 of chapter 5 was used as the global model, only the truncated FE model of the MU2 test was established in ABAQUS. This model focuses on the middle section of MU2 test specimen which contains both Esshete parent and weld materials. Due to symmetry, only one half of the test specimen was modelled with symmetry boundary conditions applied on the symmetry surface. The model was generated using the eight-node reduced integration elements (C3D8R). As the mesh size in the region ahead of the crack front must be controlled, partitions were created on the crack plane in order to generate a dense mesh around the crack front. The geometry of the truncated FE model and the partitions on the crack plane are shown in Figure 7.1

- Mesh generation

From the calibration of the Rousselier parameters described in chapter 6, a uniform square-section mesh size of 50 μm was required in the region ahead of the crack front to represent the average critical interparticle spacing. This element size was very small compared to the thickness of the MU2 pipe (35 mm) and hence affects the overall number of elements generated for the model. With this element size, 700 elements were needed to be generated through the pipe thickness with more than 3,000,000 elements for the entire truncated model.

In order to reduce the number of elements in the vicinity of the crack tip, the dimension of elements parallel to the crack front, and within the plane strain region of the specimen, was increased form 50 μm to 200 μm. The dimension of elements towards the plane stress region, the inner and outer edge of the pipe, and in the crack growth direction was maintained as 50 μm. Following this, 70 elements were generated through pipe thickness in the crack plane with 608,000 elements for the model in total. The specimen mesh is shown in Figures 7.2 and 7.3 respectively.

- Boundary and loading conditions

In this analysis, the displacement fields obtained from the FE analysis of the global model of MU2 test, described in chapter 5, were prescribed to both end surfaces of the truncated model. This process was followed by using the submodelling technique available in boundary condition module in ABAQUS. The other constraint applied was to prevent the movement in the axial direction by fixing a single point on the outside surface of model, opposite the crack location. All the boundary conditions applied to the model are shown in Figure 7.4.

- Validation of the truncated FE model

The truncated FE model was run with reference to elastic and elastic-plastic material properties in ABAQUS/Standard. The results of interest here are the relationship between load and Crack Mouth Opening Displacement (CMOD) and the variation in the *J*-integral along the crack front. These results are compared with those obtained from the global FE model of the MU2 test, presented in chapter 5, to validate the truncated FE model and to provide confidence that the truncated FE model can be used to represent the full FE model of the MU2 test.

Figure 7.5 shows a comparison between the global load versus CMOD behaviour of the MU2 test obtained from both global and truncated FE models. It can be seen that the truncated model gives results of load versus CMOD which are very close to the global model results. At the same value of CMOD, the difference of reaction force obtained from the global and the truncated FE models is less than 1%. This confirms that the truncated FE model can be used to represent the global FE model in terms of the global load-displacement behaviour.

Figure 7.6 presents the variation of the *J*-integral along the crack front. It shows that the *J* values obtained from the global and truncated FE models are not significantly different for the elastic case. For elastic-plastic analysis the values of *J*-integral obtained from the truncated FE model agree well with the global FE model results only in the regions adjacent to the inner and outer surfaces; between the inner surface and 5 mm from the inner pipe surface (r = 55-60 mm), and between 8 mm from the outer pipe surface and the outer surface (r = 82-90 mm). Within this region, the values of the *J*-integral analysed from both models are different by less than 4%. Outside these regions, the values of *J*-integral obtained from the truncated model were lower than those obtained from the global model by approximately 5.5%. The maximum difference in the *J*-integral value between global and truncated models was 6.1% and occurred at 27 mm (r = 82 mm) from the inner pipe surface. This is likely to be due to the increased mesh refinement in the vicinity of the crack tip within the truncated model.

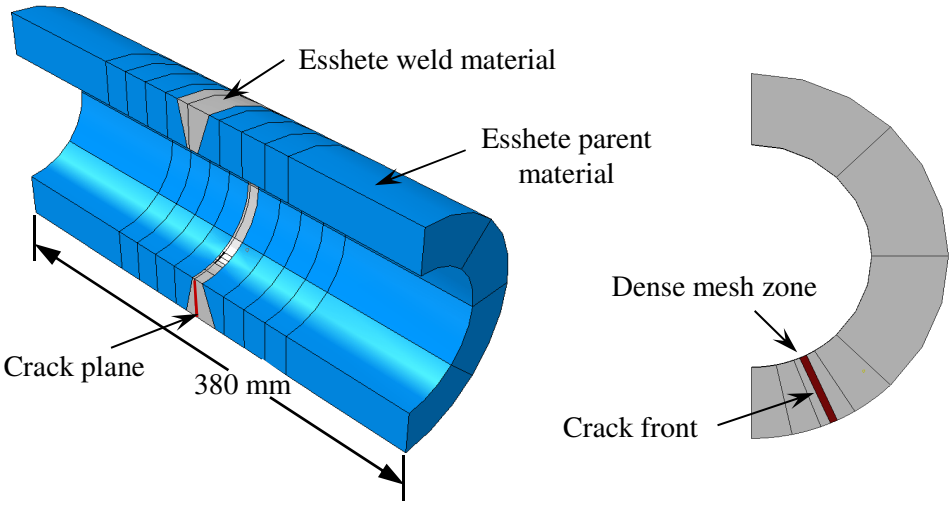

Figure 7.1 (a) Truncated FE model of the MU2 test and (b) partitions on the crack plane.

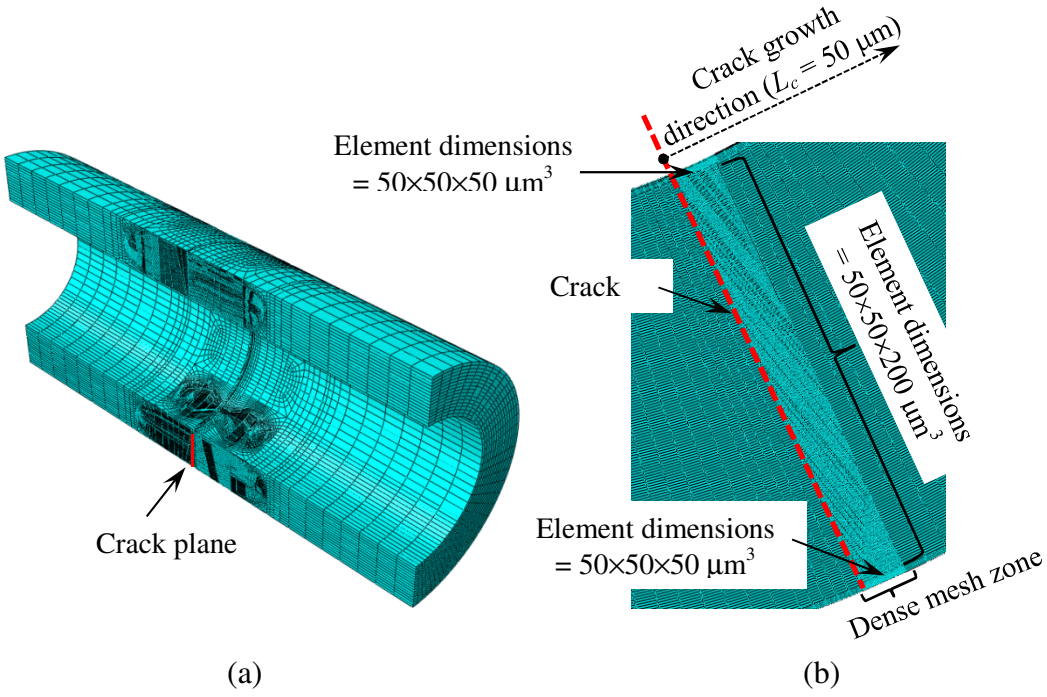

Figure 7.2 (a) FE mesh overview and (b) FE mesh generated on the crack plane for the truncated model of MU2 specimen.

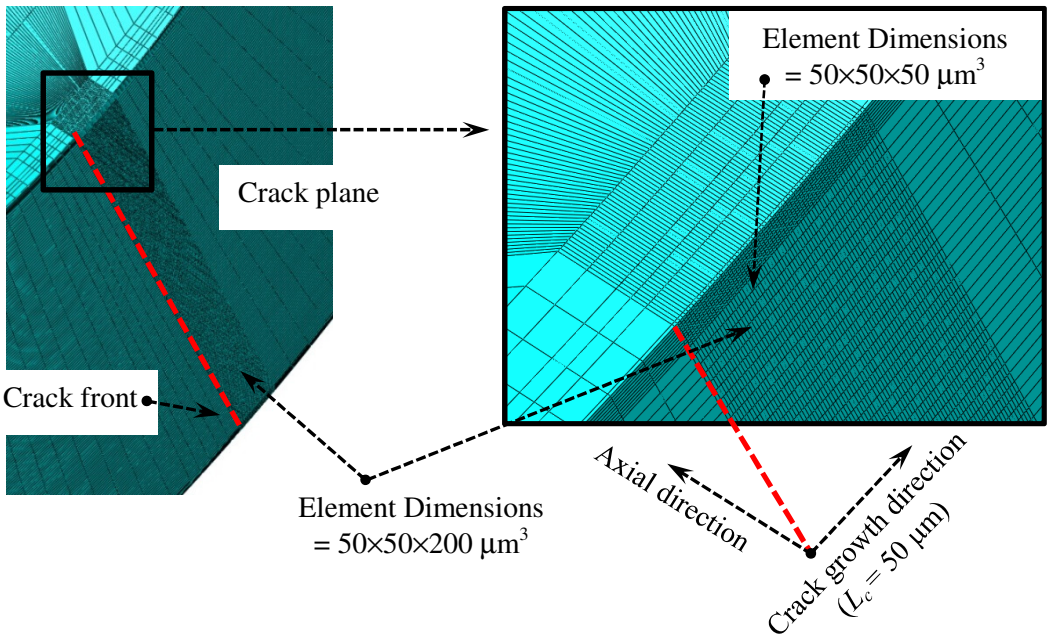

Figure 7.3 Close-up of crack front region and the FE mesh for the truncated model of MU2 specimen.

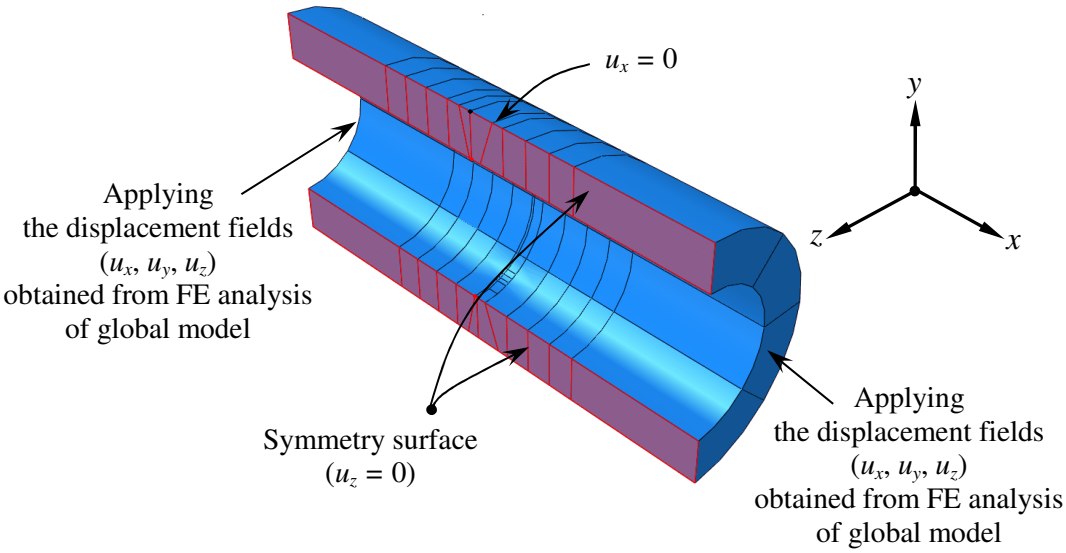

Figure 7.4 Boundary conditions applied to the truncated FE model of MU2 specimen.

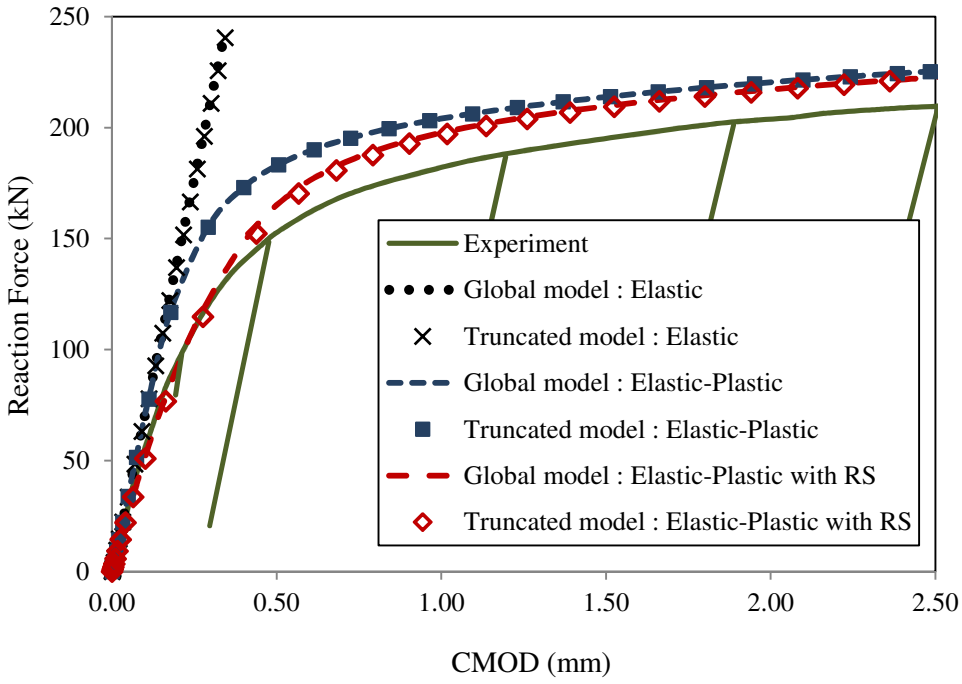

Figure 7.5 A comparison of CMOD versus reaction force between global and truncated FE models.

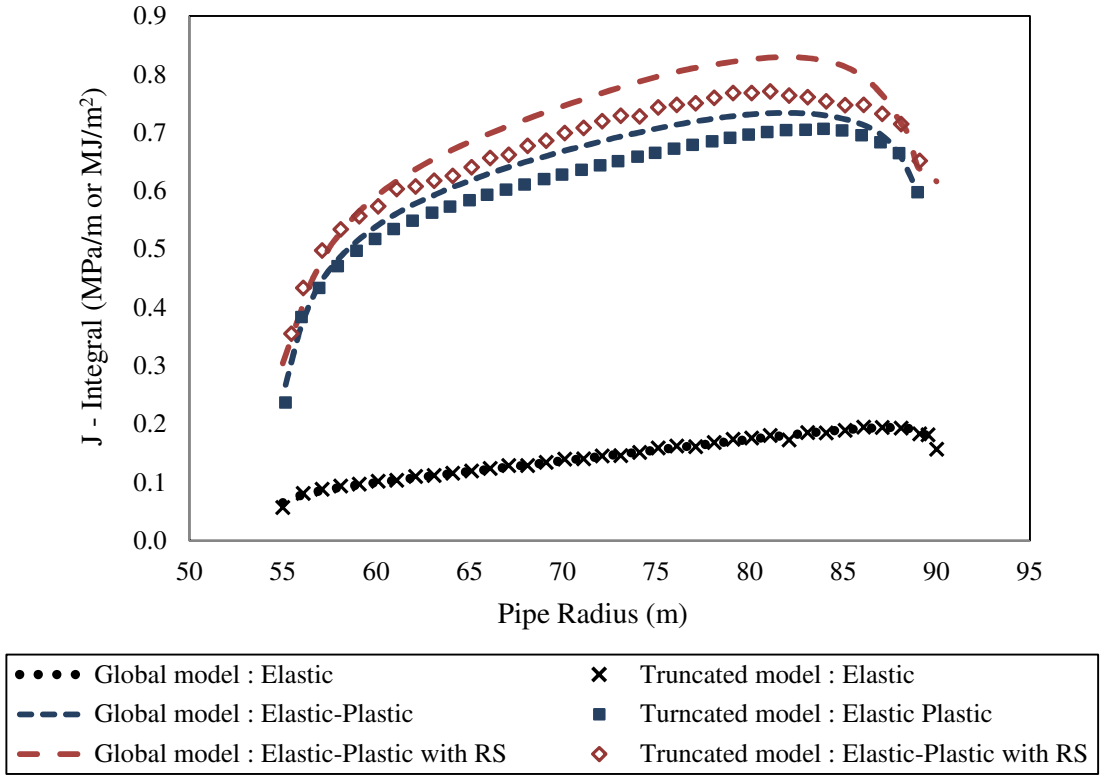

Figure 7.6 Comparison of J-integral along the crack front (pipe radius) between global and truncated FE models.

7.3 RESIDUAL STRESS MAPPING FOR TRUNCATED FE MODEL

Similar to the global FE model simulation of the MU2 test described in chapter 5, the measured residual stress profiles for the weld in the Esshete pipe, given in [137, 138], were introduced into the truncated FE model but without the presence of the crack. From this, two mapping zones for the input of the residual stress profiles were defined, as shown in Figure 5.12. These residual stress fields were imported into the truncated FE model by using the iterative technique described in section 5.4.

Figure 7.7 shows the comparison of the converged residual stress profiles in global and truncated FE models after applying the iterative technique. This is achieved after 21 iterations for the truncated model. It can be seen that the converged residual stress profiles generated within the truncated model are very close to that generated within the global FE model. For mapping zone 1, the converged values of axial and hoop residual stresses generated in the truncated model are different from the global model

by less than 6%. For mapping zone 2, the maximum difference of converged residual stresses in axial and hoop directions between the two FE models are 30.2 MPa and 20.2 MPa respectively. As described in section 5.4, these converged residual stresses were mapped onto the cracked truncated model for subsequent simulation of the MU2 test.

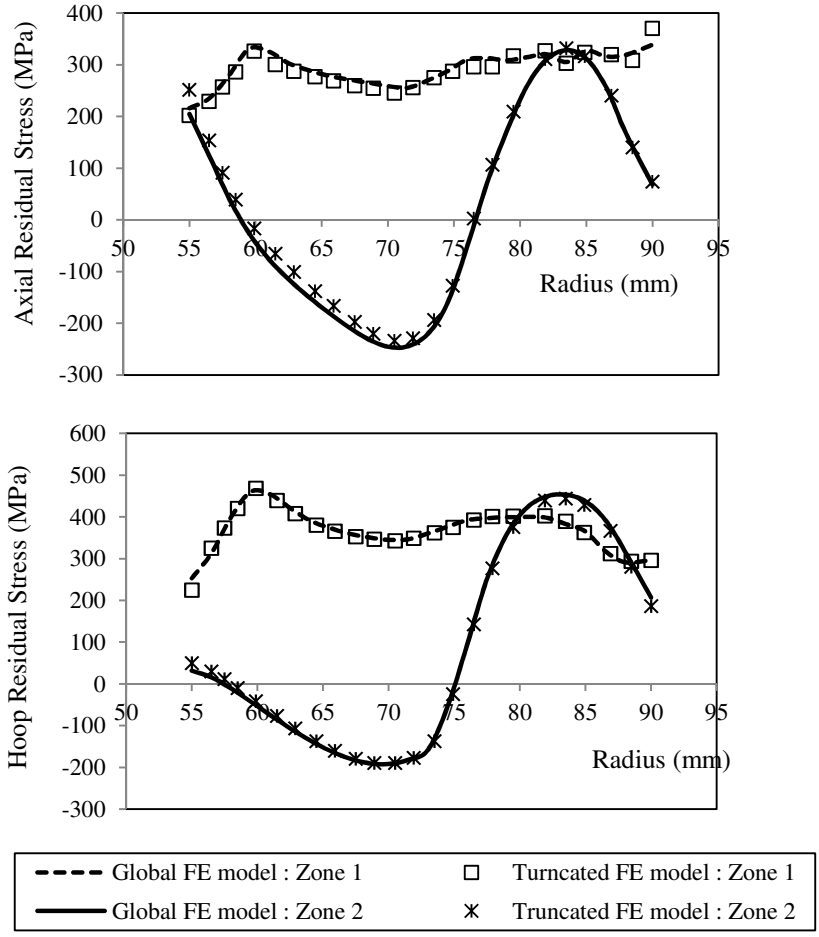

Figure 7.7 The converged stress profiles generated for full and truncated FE models.

Figure 7.8 shows the contours of stress triaxiality defined as the ratio of mean stress to von Mises equivalent stress (σ_m/q) on the cracked plane after the redistribution of residual stresses due to the introduction of crack. It shows that in the area ahead of the crack front, the level of stress triaxiality is predicated to be very high in the

central region of the crack plane. This is because the stress state in this region is under plane strain. On the other hand, in the area near the free surfaces, the stress triaxiality is predicted to be lower because a state of plane stress exists in this region. As the crack growth is highly influenced by the level of stress triaxiality ahead of the crack front, the initiation of crack growth and the maximum extent of crack growth can be predicted to occur in the central area of the crack plane.

Figure 7.8 also shows that in the central region of crack plane, the level of stress triaxiality is reasonably uniform in a direction parallel to crack front, except the areas adjacent to the inner and outer surfaces. This information supports the assumption that in the simulation of MU2 test using Rousselier damage model, the dimension of the elements ahead of the crack front can be extended from 50 to be 200 μm in the direction parallel to the crack front without any significant effect on the results.

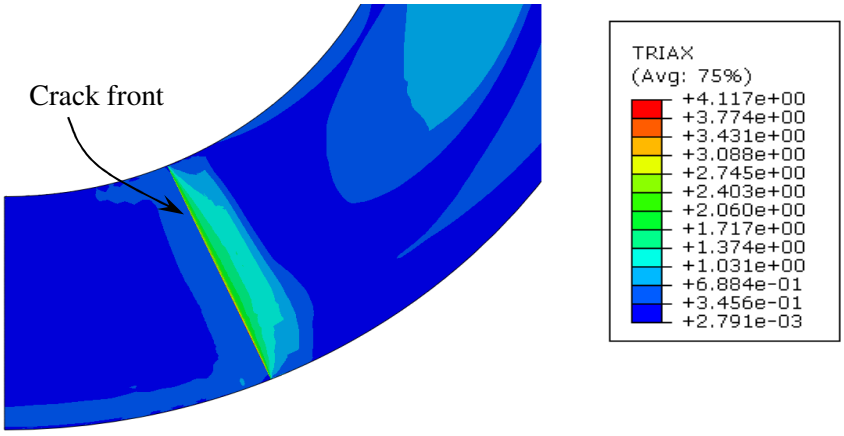

Figure 7.8 The contour plot of stress triaxiality on the crack plane after the redistribution of residual stresses due to the introduction of crack.

7.4 RESULTS AND DISSCUSSION

7.4.1 Fracture mechanics approach

The truncated FE model of the MU2 test including residual stresses was run using ABAQUS/Standard. The results of interest here are the relationship between the applied load and CMOD, and the value of *J*-integral along the crack front with

respect to distance from the pipe's inner surface. Figure 7.5 shows that the truncated FE model in the presence of residual stress provides the relationship between CMOD and applied load within 2% of results obtained from global FE model analysis.

Similar to the case without the residual stress, the truncated FE model in the presence of residual stress produced the variation of *J*-integral along a crack front which agreed well with the global FE model results only in the regions adjacent to the free surfaces. Within the region between the inner surface and 5 mm from the inner pipe surface (r = 55-60 mm) and the region between 3 mm from the outer pipe surface and the outer surface (r = 87-90 mm), the values of the *J*-integral obtained from both global and truncated models are different by less than 4%. Outside these regions, the values of *J*-integral obtained from the truncated model were lower than those obtained from the global model by approximately 6.5%, as shown in Figure 7.6. The maximum difference in the *J*-integral value between the two FE models was 8.2% and occurred at 29 mm (r = 84 mm) from the inner pipe surface. However, both truncated and global FE models provide the same position of the maximum value of *J*-integral which was at 27 mm from the inner pipe surface (r = 82 mm). In addition, at CMOD of 2.5 mm, *J*-integral values along the crack front are higher by about 11% in average after introducing the residual stress to both FE models.

These values of *J*-integral along the crack front were used to estimate the amount of stable crack extension along the crack front in the final state of the test (CMOD = 2.5 mm) with reference to Eq.(5.3). This provided a lower prediction of crack extension than the case using the global FE analysis by about 8.1%, as illustrated in Figure 7.9. However, the positions of maximum crack growth predicted by truncated FE model was consistent with that predicted by the global FE model to be between 25-30 mm from the inner pipe surface (i.e. r ~ 80-85 mm).

7.4.2 Rousselier damage model

The truncated FE model for MU2 test with the introduction of residual stress was rerun in ABAQUS/Explicit with VUMAT for the Rousselier damage model incorporated in the model for the analysis. This analysis was performed using the Roussleir parameters presented in Table 6.6. The results from this analysis are as described below :

- Crack initiation

The crack initiation and propagation in the MU2 specimen were estimated from the failure of elements occurring on the crack plane of the truncated FE model. A part of the FE model ahead of the crack front, where the crack was expected to initiate, was examined in greater detail. Figure 7.10 shows the dimensions of this part of the model. It indicates that crack initiation position, defined by the failure of the first element ahead the crack front, is predicted to be located between 21 mm to 28 mm from the inner pipe surface (i.e. r = 76-83 mm). This crack initiation position corresponds to a value of CMOD of 0.073 mm and bending moment of approximately 37 kN-m.

- Crack propagation

The crack propagation profile is presented in Figure 7.11. It can be seen that the crack extended from the crack initiation position in a direction normal to the crack front. As the high stress triaxiality existed in the region between 21 – 28 mm (Figure 7.8) from the inner pipe surface, the crack extended more rapidly in this region. In the regions adjacent to the inner and outer surfaces, the crack extended more slowly because these were within the low stress triaxiality zone.

The estimation of stable crack growth along the crack front in the final state of the test, CMOD = 2.5 mm, is shown in Figure 7.9. It can be seen that Rousselier damage model provides a lowest estimation of the maximum crack growth when compared with the results obtained from the fracture mechanics approach. The maximum crack extension estimated by Rousselier model is about 2.1 mm and occurs at between 20.3-25.3 mm from the inner pipe surface (r ~ 75-80 mm), whereas the prediction from fracture mechanics approach provide the maximum values of crack extension of between 2.3 and 2.6 mm at 27 mm (r = 82 mm) from the inner pipe surface. However, both approaches give similar final crack shapes which correspond well to the test results in south direction, Figure 5.6a.

- Bending moment and crack extension

Figure 7.12 shows the relationship between maximum crack extension and the applied bending moment, predicted by fracture mechanics approach and Rousselier damage model. A significant difference between the two approaches is that fracture

mechanics approach predicts a stable crack growth of 0.08 mm at the beginning of loading due to the effect of residual stresses, whereas the Rousselier model predicts the same value of stable crack growth at a bending moment of 160 kN-m. However, both fracture mechanics approach and the Rousselier model predict a slow crack growth between the starting period of loading and the bending moment of 160 kN-m. After this point, the crack is predicted to extend rapidly with the increase of applied bending moment.

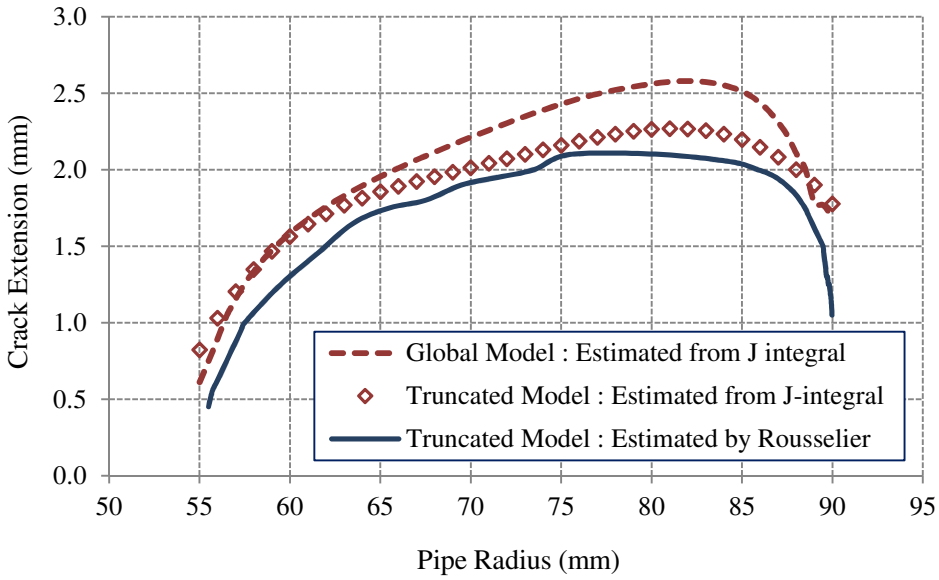

Figure 7.9 Estimation of stable crack growth along the crack front (pipe radius) in the final state of the test (CMOD = 2.5 mm).

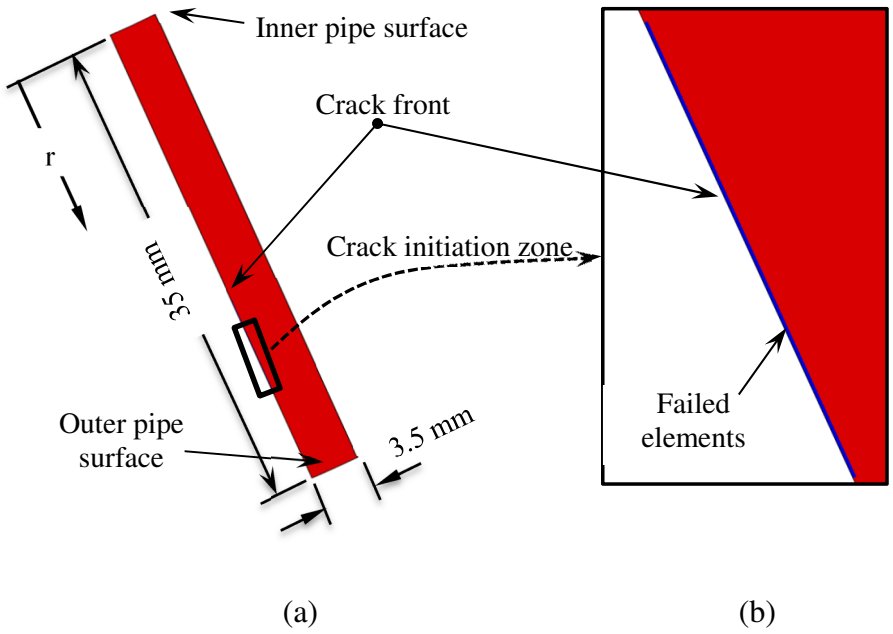

Figure 7.10 (a) A part of FE truncated model ahead the crack front and (b) the crack initiation zone.

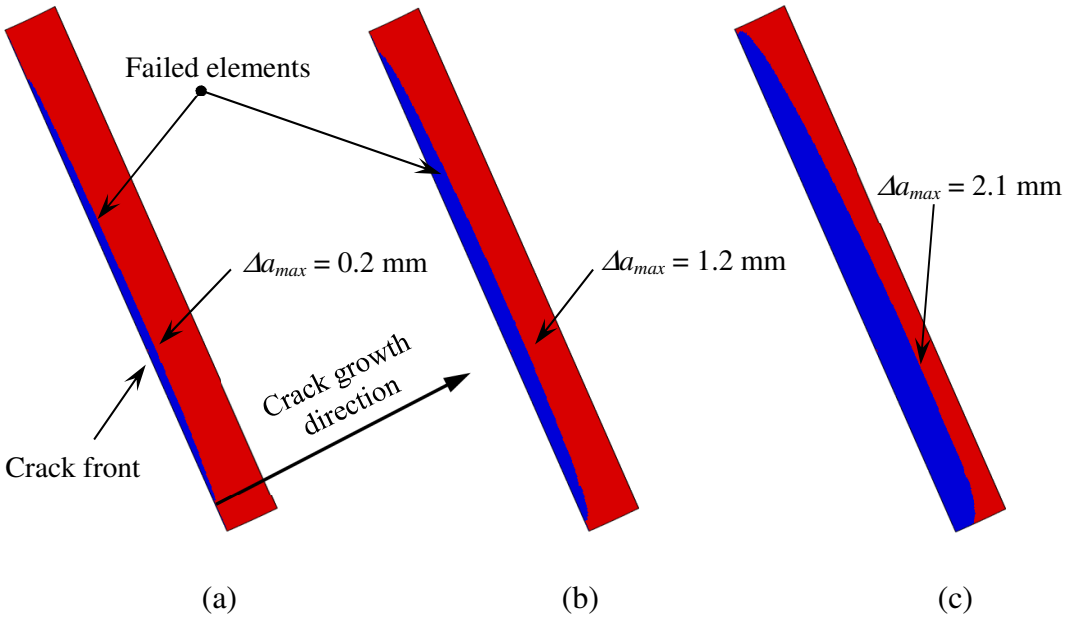

Figure 7.11 The crack propagation profiles : (a) at CMOD of 1.2 mm, (b) at CMOD of 2.0 mm and (c) at CMOD of 2.5 mm (final stage of the test).

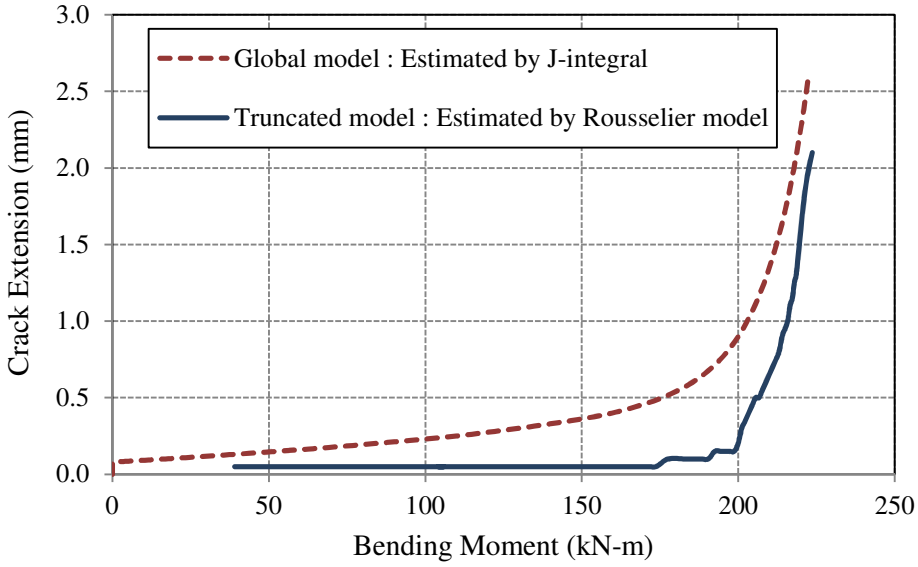

Figure 7.12 Relationship between the maximum crack extension and the applied bending moment predicted by fracture mechanics approach and Rousselier damage model.

7.5 SUMMARY

This chapter presents the Rousselier damage model as applied to the FE simulation of ductile tearing of the MU2 test. The simulation used the Rosselier model parameters which were calibrated in chapter 6. In this analysis, a submodelling technique was employed in the model construction in order to reduce the number of elements required for the model. The results obtained from this analysis are compared with the results obtained from fracture mechanics approach. The following conclusion are drawn :

- Crack initiation and propagation as predicted by Rousselier model is highly influenced by the level of stress triaxiality ahead the crack front.
- For the MU2 test, the Rousselier model has predicted the location of crack initiation in the region between 21 mm and 28 mm from the inner pipe surface. By assuming that the initiation of crack occurred at 0.05 mm of ductile tearing, the initiation load was predicted to be 36.6 kN-m.
- The maximum extension of crack as predicted by the Rousselier model was 2.1 mm and occurred between ~20 mm and 25 mm from the inner pipe

surface. The fracture mechanics approach predicted the maximum value of crack extension to be about 2.3 mm for the truncated FE model and about 2.6 mm for the global model at 27 mm from the inner pipe surface.

- The Rousselier damage model provided a lower estimation of crack extension between 9-19% along the crack front compared with that derived from the fracture mechanics approach.
- Both fracture mechanics and Rousselier damage model predicted a similar final crack shape which correspond closely to the test results in south direction (Figure 5.6a). These results represent a positive step towards to achieve the goal to use the micro-mechanical model, i.e. Rousselier model, to analyses the failure behaviour of welded structures and components.

CHAPTER 8

CONCLUSIONS AND RECOMMENDATIONS FOR FUTURE WORK

Structural integrity assessment of components and structures in safety driven environments, such as nuclear power plants, is extremely important. New techniques have been continually developed over the last four decades for such assessments. These include numerical techniques, such as the Finite Element Method (FEM), which have been developed for various thermo-mechanical analyses required for the assessment. FEM can now be used with many commercially available software codes such as ABAQUS, which is available on many high-end computational platforms. This software has the capability of modelling linear, non-linear, time-dependent, temperature dependent material behaviour under complex loading conditions. It incorporates many 'global' parameters, such as J-integral, for the characterisation of cracked components and structures. It also allows the development of sophisticated micro-mechanical models based on 'local' approach of fracture assessment which usually employs a damage parameter for such characterisations. The main task for the users in these cases is to first implement these models via 'user routines'. This requires the development of a compatible computer code based on the mathematical formulation of the model and its rigorous testing and validation against the established benchmarks. This was the first major task of this research programme. Once successfully completed, the next challenge was to use the model for simulating a complex but real life case study. This was provided by the European (STYLE) project. A part of this project required the assessment of a weld pipe repair in the presence of a residual stress field. This was achieved by using both global and local approaches and comparing these assessments with the experimental data.

8.1 CONCLUSIONS

Welded structures in a power station endure operational loads together with residual stresses introduced during manufacture and repair. It is, therefore, necessary to understand the combined effect of mechanical loading and residual stresses on the ductile fracture behaviour of these structures in order to provide an accurate structural integrity assessment. Recently, STYLE (Structural integrity for lifetime management-non-RPV component) performed a large scale bending test on a welded steel pipe containing a circumferential through-thickness crack (the MU2 test). The data obtained from the tests was used to support the FE models developed in this research to study the impact of high magnitude repair-weld residual stresses on ductile crack initiation and growth.

In this research, a three-dimensional FE model of MU2 test was developed using ABAQUS. The weld residual stress field was introduced into the FE model as initial stresses using an iterative method. The parameters of conventional fracture mechanics (global approach) and Rousselier damage model (local approach) were employed to study the combined influence of primary and residual stresses on ductile fracture behaviour including crack initiation and growth. The main contributions from this research can be summarized as follows :

8.1.1 The implementation of Rousselier damage model in ABAQUS

The Rousselier model was chosen as the micro-mechanical model for implementation in ABAQUS and subsequent FE simulation of MU2 test. This model defines the softening of the material by a single damage parameter and the fracture proceeds from the competition between hardening and damage. It is not necessary to introduce a critical value of the damage variable. In addition, the number of parameters in the model which need to be defined is less than other micro-mechanical models, such as the well known Gurson model.

In this research, the Rousselier model was implemented into ABAQUS via the user defined subroutines for ABAQUS/Standard and ABAQUS/Explicit modules, i.e. UMAT and VUMAT. The subroutines were developed based on the integration algorithm proposed by Aravas and Zhang as discussed in sections 3.3 and 3.6. The

validation of these subroutines was checked by comparing the FE results obtained from the implementation of these subroutines with the analytical and other benchmark solutions. This process was presented in section 4.4 and showed that UMAT and VUMAT provide accurate results. However, the UMAT developed in this work shows convergence problems when the elements start to fail. The suggestion for further development of UMAT to overcome this limitation is given in section 4.5.

8.1.2 The simulation of a challenging case study (MU2 test)

One of the main challenges in this research was to establish a three-dimensional FE model of the MU2 test which is a complex case study relevant to residual stresses in weld components in nuclear industry. To achieve this, novel modelling techniques of meshing and submodelling, were used in the construction of the model. This included an iterative method used for generating the input residual stress fields. This technique enables to obtain the redistribution of residual stresses in the component after the introduction of crack (crack initiation). Details of this technique are discussed in section 5.4.

Details of various procedures used to establish the FE model for MU2 test are given in chapters 5, 6 and 7. Together with the process of the implementation of fracture mechanics and Rousselier models, this case study provides a sound basis for structural integrity assessment of welded engineering components used in nuclear power plant.

8.1.3 The new understanding of the influence of residual stress on ductile fracture

As mentioned before, the influence of residual stress on ductile fracture was studied via the FE simulation of MU2 test. The results of this simulation show that Rousselier damage model provides a lower estimate of crack extension along the crack front than the global fracture mechanics approach. However, both fracture mechanics approach and the Rousselier model predict similar crack shapes which correspond closely to the test results in south direction, c.f. Figure 5.6(a). The main conclusions of this research are as follows :

- When the crack initiates in the residual stress zone of welded components, the residual stresses in this zone redistribute in order to obtain self-equilibrium. This process results in higher residual stress values ahead of the crack front which are in excess of the yield strength of the weld material.
- After the initiation of crack, the effect of redistributed residual stresses on the global behaviour was not significant in the calculation based on elastic behaviour. However, for elastic-plastic behaviour, these stresses generate plastic strain around the crack front which affects the global behaviour of the component. For example, the non-linear behaviour of global load versus CMOD was clearly shown in the very early part of loading, Figure 5.15.
- The numerical results indicated that the presence of the residual stress led to a reduction in the load carrying capacity of the STYLE test specimen geometry under four-point bending.
- Residual stresses reduce the load carrying capacity of the cracked components which results in the reduction of crack initiation load and increases of the maximum crack extension.
- Residual stresses increase the rate of crack propagation in the early period of loading. However, this effect decreases with the increase of crack growth and converge to the case without residual stresses. This is because of the relaxation of residual stresses in the materials.
- The Rousselier model results indicate that crack initiation and propagation is highly influenced by the level of stress triaxiality ahead the crack front, i.e. the crack initiates and extends more rapidly in high stress triaxiality zone.

8.2 RECOMMENDATION FOR IMPROVING THE ACCURACY OF THE FE MODEL

In this research, there are differences found between the results obtained from FE simulations and the experiments. These pertain to the global load vs CMOD and the crack extension at the end of the test. This may be because of certain limitations of the analysis. Additional work is suggested in order to improve the accuracy of the FE simulations.

Recommendations for improving the relationship between global load and CMOD

- The material properties of the heat affected zone and the influence of residual stresses in the weld joint between the MU2 specimen and the extension arm need to be taken into account in the FE analysis.
- A different residual stress defining technique which includes the knowledge of the history of prior deformation in the structure, such as the Eigenstrain method [154], may be used to define the initial residual stresses in the model.

Recommendations for improving the final crack extension

- The evolution of void volume fraction in the Rousselier damage model needs to include the effect of deviatoric plastic strain or the contribution of new voids that are nucleated with plastic strain.
- In the calibration of Rousselier model parameters, the effects of residual stress field need to be included in the analysis.

8.3 RECOMMENDATIONS FOR FURTHER RESEARCH

The simulation work carried out and presented in this thesis can be extended in several ways as described below :

User defined subroutine for Rousselier damage model

- Including the effect of deviatoric plastic strain or the contribution of voids nucleation into the evolution equation for void volume fraction.
- Improving the solution method used for solving the set of non-linear equations in the Rousseleir model [Eqs.(3.22)-(3.26)]. This can be achieved by using a trust region method [121] in the early stage of calculation to avoid convergence problems and reduce the number of iterations in the computation.
- Modifying the user defined subroutine for ABAQUS/Standard, UMAT, to run the model under failure condition by fixing a small amount of load-carrying capacity in the failed material.

Application of the developed methodology

- Applying the methodology developed here to study the effects of residual stresses on other problems, such as the pipe with different crack shapes and orientations.
- Using the methodology with other finite element software packages, such as the open source Code Aster, to benchmark the computational results.
- Developing the user defined subroutine which itself performs automatic calculations to obtain self-equilibrium of the residual stress fields.

REFERENCES

1. R.A.Ainsworth, J.K.Sharples, and S.Smith, "*Effects of residual stresses on fracture behaviour–experimental results and assessment methods*," The Journal of Strain Analysis for Engineering Design, vol.35(4), pp.307-316, 2000.
2. J.Liu, Z.L.Zhang, and B.Nyhus, "*Residual stress induced crack tip constraint,*" Engineering Fracture Mechanics, vol.75(14), pp.4151-4166, 2008.
3. X.B.Ren, Z.L.Zhang, and B.Nyhus, "*Effect of residual stresses on the crack-tip constraint in a modified boundary layer mode,*" International Journal of Solids and Structures, vol.46(13), pp.2629-2641, 2009.
4. X.B.Ren, Z.L.Zhang, and B.Nyhus, "*Effect of residual stresses on ductile crack growth resistance,*" Engineering Fracture Mechanics, vol.77(8), pp.1325-1337, 2010.
5. M.Bourgeois, "*Mock-Up 2 Test,*" STYLE report D-1.15, CEA, France, 2014.
6. M.C.Smith, M.Bourgeois, S.Arun, S.D.Cao, Y.Kayser, D.Smith and A.Sherry, "*Understanding the impact of high-magnitude repair-weld residual stresses on ductile crack initiation and growth-the STYLE mock up 2 large scale test*," in Proceedings of the ASME 2014 Pressure Vessels & Piping Conference, California, USA, 2014.
7. G.R.Irwin, "*Analysis of stresses and strains near the end of a crack traversing a plate*," Journal of Applied Mechanics, vol.24, pp.361-364, 1957.
8. H.M.Westergaard, "*Bearing pressure and cracks*," Journal of applied mechanics, vol.6, pp.49-53, 1939.
9. M.L.Williams, "*On the stress distribution at the base of a stationary crack,*" Journal of applied mechanics, vol.24, pp.109-114, 1957.
10. J.R.Rice, "*Limitations to the small scale yielding approximation for crack tip plasticity*," Journal of the Mechanics and Physics of Solids, vol.22(1), pp.17-26, 1974.
11. Andrew Abu-Muharib, A.P.Jivkov, P.James, and J.R.Yates "*Cleavage fracture modelling for RPV steels: Discrete model for collective behaviour of micro-cracks*," in Proceedings of the ASME 2013 Pressure Vessels & Piping Conference, California, USA, 2013.
12. A.H.Sherry, C.C.France, and M.R.Goldthorpe, "*Compendium of T-stress solutions for two and three dimentional cracked geometries*," Fatigue & Fracture of Engineering Materials & Structures, vol.18(1), pp.141-155, 1995.
13. V.Tvergaard and J.W.Hutchinson, "*Effect of T-stress on mode I crack growth resistance in a ductile solid*," International Journal of Solids and Structures, vol.31(6), pp.823-833, 1994.
14. S.Suresh, *Fatigue of materials*, Cambridge: Cambridge University Press, 1991.
15. Y.Murakami, *Stress intensity factors handbook*, vol.1-2, Oxford: Pergamon, 1987.
16. H.Tada, *The stress analysis of cracks handbook*, 3rd ed. New York: ASME Press, 2000.
17. BS 7910:2005, *Guide to methods for assessing the acceptability of flaws in metallic structures*, British Standard Institution, UK, 2005.

18. BS 7448-2:1997, *Fracture mechanics toughness tests. Method for determination of KIc, critical CTOD and critical J values of welds in metallic materials, British Standard Institution*, UK, 1997.
19. N.P.Andrianopoulos and V.C.Boulougouris, "*On an intrinsic relationship between plane stress and plane strain critical stress intensity factors*," International Journal of Fracture, vol.67(1), pp.R9-R12, 1994.
20. J.R.Rice, "*A path independent integral and the approximate analysis of strain concentration by notches and cracks*," Journal of Applied Mechanics, vol.35(2), pp.379-386, 1968.
21. *Ramberg-Osgood relationship*, Retrieved from http://en.wikipedia.org/wiki/Ramberg%E2%80%93Osgood_relationship [Accessed October 14, 2014].
22. J.W.Hutchinson, "*Singular behaviour at the end of a tensile crack in a hardening material*," Journal of the Mechanics and Physics of Solids, vol.16(1), pp.13-31, 1968.
23. J.R.Rice and G.F.Rosengren, *Plane strain deformation near a crack tip in a power-law hardening material.* Journal of the Mechanics and Physics of Solids, vol.16(1), pp.1-12, 1968.
24. M.Janssen, J.Zuidema and R.J.H.Wanhill, *Fracture mechanics*, 2nd ed. New York: Spon Press, 2004.
25. G.A.Webster and R.A.Ainsworth, *High temperature component life assessment*, London: Chapman & Hall, 1994.
26. ASTM E813-81*, Standard test method for J_{IC},* A Measure of Fracture Toughness*,* Annual book of ASTM standards, part.10, pp.822-840, Philadelphia, 1981.
27. T.L.Anderson, *Fracture mechanics: fundamentals and applications*, 3rd ed, London: Taylor & Francis/CRC, 2005.
28. ESIS P2-92, *ESIS procedure for determining the fracture behaviour of materials*, European Structural Integrity Society, 1992.
29. ASTM E1820-01, *Standard test method for measurement of fracture toughness*, American Society for Testing of Material, Philadelphia, 2002.
30. J.W.Hancock, W.G.Reuter and D.Parks, "*Constraint and toughness parameterized by T*," Constraint effects in fracture, pp. 21–40, ASTM STP 1171, American society for Testing and Materials, Philadelphia, 1993.
31. J.A.Joyce and R.E.Link, "*Effects of constraint on upper shelf fracture toughness*," Fracture Mechanics, vol.26, pp.142-77, ASTM STP 1256, American Society for Testing and Materials, Philadelphia, 1995.
32. X.K.Zhu and S.K.Jang, "*J–R curves corrected by load-independent constraint parameter in ductile crack growth*," Engineering Fracture Mechanics, vol.68(3), pp.285-301, 2001.
33. C.Betegon and J.W.Hancock, "*Two-parameter characterization of elastic-plastic crack-tip fields*," Journal of Applied Mechanics, Transactions ASME, vol.58(1), pp.104-110, 1991.
34. N.P.O'Dowd and C.F.Shih, "*Family of crack-tip fields characterized by a triaxiality parameter-I. Structure of fields*," Journal of the Mechanics and Physics of Solids, vol.39(8), pp.989-1015, 1991.
35. N.P.O'Dowd and C.F.Shih, "*Family of crack-tip fields characterized by a triaxiality parameter-II. Fracture applications*," Journal of the Mechanics and Physics of Solids, vol.40(5), pp.939-963, 1992.

36. Y.J.Chao, S.Yang and M.A.Sutton, "*On the fracture of solids characterized by one or two parameters: Theory and practice*," Journal of the Mechanics and Physics of Solids, vol.42(4), pp.629-647, 1994.
37. T.Pardoen, Y.Marchal and F.Delannay, "*Thickness dependence of cracking resistance in thin aluminium plates*," Journal of the Mechanics and Physics of Solids, vol.47(10), pp.2093-2123, 1999.
38. A.R.Dowling and C.H.A.Townley, "*The effect of defects on structural failure. A two-criteria approach*," International Journal of Pressure Vessels and Piping, vol.3(2), pp.77-107, 1975.
39. P.J.Budden, J.K.Sharples and A.R.Dowling, "*The R6 procedure: recent developments and comparison with alternative approaches*," International Journal of Pressure Vessels and Piping, vol.77(14-15), pp.895-903, 2000.
40. *R6: assessment of the integrity of structures containing defects,* Revision 4, British Energy Generation Limited, 2005.
41. S.Cravero and C.Ruggieri, "*Structural integrity analysis of axially cracked pipelines using conventional and constraint-modified failure assessment diagrams*," International Journal of Pressure Vessels and Piping, vol.83(8), pp.607-617, 2006.
42. D.P.G.Lidbury, A.H.Sherry, B.A.Bilby, I.C.Howard, Z.H.Li and C.Eripret, "*Prediction of the first spinning cylinder test using continuum damage mechanics*," Nuclear Engineering and Design, vol.152(1-3), pp.1-10, 1994.
43. B.A.Bilby, I.C.Howard, Z.H.Li and M.A.Sheikh, "*Some experience in the use of damage mechanics to simulate crack behaviour in specimens and structures*," International Journal of Pressure Vessels and Piping, vol.64(3), pp.213-223, 1995.
44. M.Bethmont, G.Rousselier, K.Kussmaul, A.Sauter and A.Jovanovic, "*The method of local approach of fracture and its application to a thermal shock experiment*," Nuclear Engineering and Design, vol.119(2-3), pp.249-261, 1990.
45. I.C.Howard and M.A.Sheikh, "*Simulation of nuclear safety tests*," Final Report, Department of Mechanical and Process Engineering, The University of Sheffield, UK, 1994.
46. C.Eripret, D.P.G.Lidbury, A.H.Sherry and I.C.Howard, "*Prediction of fracture in the transition regime: Application to an A533B pressure vessel steel*," Advances in Fracture Research, pp.197-205, Pergamon: Oxford, 1997.
47. A.Pineau, "*Development of the local approach to fracture over the past 25 years: Theory and applications*," Interanational Journal of Fracture, vol.138, pp.139-166.
48. J.R.Rice and D.M.Tracey, "*On the ductile enlargement of voids in triaxial stress fields*," Journal of the Mechanics and Physics of Solids, vol.17(3), pp.201-217, 1969.
49. A.Imad, J.Wilsius, M.Naït Abdelaziz and G.Mesmacque, "*Experiments and numerical approaches to ductile tearing in an 2024-T351 aluminium alloy*," International Journal of Mechanical Sciences, vol.45(11), pp.1849-1861, 2003.
50. R.Taktak, N.Benseddiq and A.Imad, "*Analysis of ductile tearing using a local approach to fracture*," Fatigue & Fracture of Engineering Materials & Structures, vol.32(6), pp.525-530, 2009.
51. F.Murdy and M.Di Fant, "*A Round Robin on the Measurement of Local Criteria*," RE 93.319, IRSID, 1993.

52. F.M.Beremin, "*Three-Dimensional Constitutive Relations and Ductile Fracture*," Experimental and Numerical Study of the Different Stages in Ductile Rupture: Application to Crack Initiation and Stable Crack Growth, pp.157-172, North Holland Publishing Company, 1981.
53. A.L.Gurson, "*Continuum Theory of Ductile Rupture by Void Nucleation and Growth: Part I---Yield Criteria and Flow Rules for Porous Ductile Media*," Journal of Engineering Materials and Technology, vol.99(1), pp.2-15, 1977.
54. V.Tvergaard, "*On localization in ductile materials containing spherical voids*," International Journal of Fracture, vol.18(4), pp.237-252, 1982.
55. V.Tvergaard, "*Material Failure by Void Growth to Coalescence*," Advances in Applied Mechanics, pp.83-151, Elsevier, 1989.
56. C.C.Chu and A.Needleman, "*Void Nucleation Effects in Biaxially Stretched Sheets*," Journal of Engineering Materials and Technology, vol.102(3), pp.249-256, 1980.
57. V.Tvergaard and A.Needleman, "*Analysis of the cup-cone fracture in a round tensile bar*," Acta Metallurgica, vol.32(1), pp.157-169, 1984.
58. Z.L.Zhang, C.Thaulow and J.Ødegård, "*A complete Gurson model approach for ductile fracture*," Engineering Fracture Mechanics, vol.67(2), pp.155-168, 2000.
59. Z.L.Zhang, "*A Complete Gurson Model*," Nonlinear fracture and damage mechanics, UK: WIT Press, Southampton, 2001.
60. P.Thomason, *Ductile fracture of metals*, Pergamon Press, Oxford, 1990.
61. P.F.Thomason, "*A three-dimensional model for ductile fracture by the growth and coalescence of microvoids*," Acta Metallurgica, vol.33(6), pp.1087-1095, 1985.
62. P.F.Thomason, "*A view on ductile-fracture modelling*," Fatigue & Fracture of Engineering Materials & Structures, vol.21(9), pp.1105-1122, 1998.
63. G.Rousselier, *Ductile fracture models and their potential in local approach of fracture.* Nuclear Engineering and Design, vol.105(1), pp.97-111, 1987.
64. G.Rousselier, J.C.Devaux, G.Mottet and G.Devesa, "*A Methodology for Ductile Fracture Analysis Based on Damage Mechanics: An Illustration of A Local Approach of Fracture*," Nonlinear Fracture Mechanics Volume II: Elastic-plastic Fracture, pp.332-354, ASTM STP 995, 1989.
65. F.Dotta and C.Ruggieri, "*Structural integrity assessments of high pressure pipelines with axial flaws using a micromechanics model*," International Journal of Pressure Vessels and Piping, vol.81(9), pp.761-770, 2004.
66. C.Ruggieri and F. Dotta, "*Numerical modeling of ductile crack extension in high pressure pipelines with longitudinal flaws*," Engineering Structures, vol.33(5), pp.1423-1438, 2011.
67. C.F.Shih, B.Moran and T.Nakamura, "*Energy release rate along a three-dimensional crack front in a thermally stressed body,*" International Journal of Fracture, vol.30(2), pp.79-102, 1986.
68. T.Belytschko and T.Black, "*Elastic crack growth in finite elements with minimal remeshing,*" International Journal for Numerical Methods in Engineering, vol.45(5), pp.601-620, 1999.
69. J.Dolbow, N.Moës and T.Belytschko, "*Discontinuous enrichment in finite elements with a partition of unity method,*" Finite Elements in Analysis and Design, vol.36(3), pp.235-260, 2000.

70. T.Belytschko, Y.Krongauz, D.Organ, M.Fleming and P.Krysl, "*Meshless methods: An overview and recent developments,*" Computer Methods in Applied Mechanics and Engineering, vol.139(1-4), pp.3-47, 1996.
71. M.Ortiz and A.Pandolfi, "*Finite-deformation irreversible cohesive elements for three-dimensional crack-propagation analysis,*" International Journal for Numerical Methods in Engineering, vol.44(9), pp.1267-1282, 1999.
72. M.Elices, G.V.Guinea, J.Gómez and J.Planas, "*The cohesive zone model: advantages, limitations and challenges,*" Engineering Fracture Mechanics, vol.69(2), pp.137-163, 2002.
73. N.Chandra, H.Li, C.Shet and H.Ghonem, "*Some issues in the application of cohesive zone models for metal–ceramic interfaces,*" International Journal of Solids and Structures, vol.39(10), pp. 2827-2855, 2002.
74. R.Kregting, "*Cohesive zone models towards a robust implementation of irreversible behaviour,*" 2005.
75. P.J.Holt and R.A.W.Bradford, "*Application of probabilistic modelling to the lifetime management of nuclear boilers in the creep regime: Part 1*," International Journal of Pressure Vessels and Piping, vol.95(0), pp.48-55, 2012.
76. D.B.Park, S.M.Hong, K.H.Lee, M.Y.Huh, J.Y.Suh, S.C.Lee and W.S.Jung, "*High-temperature creep behavior and microstructural evolution of an 18Cr9Ni3CuNbVN austenitic stainless steel*," Materials Characterization, vol.93(0), pp.52-61, 2014.
77. P.Yvon and F.Carré, "*Structural materials challenges for advanced reactor systems*," Journal of Nuclear Materials, vol.385(2), pp.217-222, 2009.
78. J.R.Davis, *Stainless steels*, Ohio : ASM International, 1994.
79. J.C.Lippold and D.J.Kotecki, *Welding metallurgy and weldability of stainless steels*, New Jersey: John Wiley, 2005.
80. W.Hoffelner, *Materials for Nuclear Plants from Safe Design to Residual Life Assessments*. Germany: Springer Verlag, 2013.
81. J.C.M.Farrar, "*Group E Standard austenitic stainless steels*," The Alloy Tree: A Guide to Low-Alloy Steels, Stainless Steels and Nickel-base Alloys, pp.65-77, Woodhead Publishing, 2004.
82. A.Shibli, "*7-Boiler steels, damage mechanisms, inspection and life assessment*," Power Plant Life Management and Performance Improvement, pp. 272-303, Woodhead Publishing, 2011.
83. D.T.Llewellyn, *Steels: Metallurgy and Applications*, 3rd ed. Burlington: Elsevier Science, 1998.
84. C.Austin and J.P.Hayes, "*A Constitutive Model for Parent Esshete 1250 and Associated Single Bead Weld Metal*," Serco Assurance Report SA/SIA/17261/R01, SERCO, UK, 2005.
85. M.W.Spindler, and S.L.Spindler, "*Creep deformation, rupture and ductility of Esshete 1250*," International Journal of Pressure Vessels and Piping, vol.85(1-2), pp.89-98, 2008.
86. F.Faure and R.H.Leggatt, "*Residual stresses in austenitic stainless steel primary coolant pipes and welds of pressurized water reactors*," International Journal of Pressure Vessels and Piping, vol.65(3), pp.265-275, 1996.

87. D.George and D.J.Smith, "*Through thickness measurement of residual stresses in a stainless steel cylinder containing shallow and deep weld repairs*," International Journal of Pressure Vessels and Piping, vol.82(4), pp.279-287, 2005.
88. P.J.Bouchard, D.George, J.R.Santisteban, G.Bruno, M.Dutta, L.Edwards, E.Kingston and D.J.Smith, "*Measurement of the residual stresses in a stainless steel pipe girth weld containing long and short repairs*," International Journal of Pressure Vessels and Piping, vol.82(4), pp.299-310, 2005.
89. P.J.Bouchard, *Validated residual stress profiles for fracture assessments of stainless steel pipe girth welds.* International Journal of Pressure Vessels and Piping, vol.84(4), pp.195-222, 2007.
90. W.Zinn and B.Scholtes, "*Residual stress formation processes during welding and joining*," Handbook of residual stress and deformation of steel, pp.391-396, Ohio: ASM International, 2002.
91. R.W.Messler, "*Principles of welding: processes, physics, chemistry, and metallurgy*," New York: John Wiley, 1999.
92. D.Deng, "*FEM prediction of welding residual stress and distortion in carbon steel considering phase transformation effects*," Materials & Design, vol.30(2), pp.359-366, 2009.
93. T.Kannengiesser and A.Kromm, "*Formation of welding residual stresses in low transformation temperature (LTT) materials*," Soldagem & Inspeção, vol.14, pp.74-81, 2009.
94. N.S.Rossini, M.Dassisti, K.Y.Benyounis and A.G.Olabi, "*Methods of measuring residual stresses in components*," Materials & Design, vol.35(0), pp.572-588, 2012.
95. R.H.Leggatt, D.J.Smith, S.D.Smith and F.Faure, "*Development and experimental validation of the deep hold method for residual stress measurement*," Journal of Strain Analysis for Engineering Design, vol.31(3), pp.177-186, 1996.
96. E.M.Beaney, "*Measurement of sub-surface stress*," Report RD/B/N4325, Central Electricity Generating Board, UK, 1978.
97. I.M.Zhdanov and A.K.Gonchar, "*Determination of welding residual stresses at depth in metals*," Automatic Welding, vol.31, pp.22-24, 1978.
98. X.Ficquet, C.E.Truman, D.J.Smith, B.Brown and T.Dauda, "*Measurement of residual stresses in large industrial components using the deep hole drilling technique*," in Proceedings of the ASME 2005 Pressure Vessels & Piping Conference, Denver, Colorado, 2005.
99. D.George, D.J.Smith and P. Bouchard, "*Evaluation of Through Wall Residual Stresses in Stainless Steel Weld Repairs*," Materials Science Forum, vol.347-349, pp.646-651, 2000.

100. D.J.SMITH, P.J.Bouchard and D.George, "*Measurement and prediction of residual stresses in thick section steel welds*," Journal of Strain Analysis, vol.35(4), pp.287-305.
101. E.Kingston and D.J.Smith, "*Residual stress measurements in rolling mill rolls using deep hole drilling technique*," Ironmaking & Steelmaking, vol.32(5), pp. 379-380, 2005.
102. H.Kitano, S.Okano, and M.Mochizuki, "*A study for high accuracy measurement of residual stress by deep hole drilling technique*," Journal of Physics: Conference Series, vol.379(1), 2012.
103. M.G.Bateman, O.H.Miller, T.J.Palmer, C.E.P.Breen, E.J.Kingston, D. J.Smith and M.J.Pavier, "*Measurement of residual stress in thick section composite laminates using the deep-hole method*," International Journal of Mechanical Sciences, vol.47(11), pp.1718-1739, 2005.
104. P.V.Marcal and I.P.King, "*Elastic-plastic analysis of two-dimensional stress systems by the finite element method*," International Journal of Mechanical Sciences, vol.9(3), pp.143-155, 1967.
105. Y.Yamada, N.Yoshimura and T.Sakurai, "*Plastic stress-strain matrix and its application for the solution of elastic-plastic problems by the finite element method*," International Journal of Mechanical Sciences, vol.10(5), pp.343-354, 1968.
106. O.C.Zienkiewicz, S.Valliappan and I.P.King, "*Elasto-plastic solutions of engineering problems 'initial stress', finite element approach*," International Journal for Numerical Methods in Engineering, vol.1(1), pp.75-100, 1969.
107. G.C.Nayak and O.C.Zienkiewicz, "*Elasto-plastic stress analysis. A generalization for various contitutive relations including strain softening*," International Journal for Numerical Methods in Engineering, vol.5(1), pp.113-135, 1972.
108. M.L.Wilkins, "Calculation of elastic-plastic flow," Methods of Computational Physics 3, Academic Press, New York, 1964.
109. M.Ortiz and E.P.Popov, "*Accuracy and stability of integration algorithms for elastoplastic constitutive relations*," International Journal for Numerical Methods in Engineering, vol.21(9), pp.1561-1576, 1985.
110. N.Aravas, "*On the numerical integration of a class of pressure-dependent plasticity models*," International Journal for Numerical Methods in Engineering, vol.24(7), pp.1395-1416, 1987.
111. Z.L.Zhang, "*Explicit consistent tangent moduli with a return mapping algorithm for pressure-dependent elastoplasticity models*," Computer Methods in Applied Mechanics and Engineering, vol.121(1-4), pp.29-44, 1995.
112. Z.L.Zhang, "*A Practical Micro Mechanical Model Based Local Approach Methodology for the Analysis of Ductile Fracture of Welded T-Joints*," PhD Thesis, Lappeenranta University of Technology, Finland, 1994.
113. Z.L.Zhang, "*On the accuracies of numerical integration algorithms for Gurson-based pressure-dependent elastoplastic constitutive models*," Computer Methods in Applied Mechanics and Engineering, vol.121(1-4), pp.15-28, 1995.
114. Z.L.Zhang and E.NIEMl, "*A class of generalized mid-point algorithms for the Gurson-Tvergaard material model*," International Journal for Numerical Methods in Engineering, vol.38, pp.2033-2053, 1995.

115. M.A.Keavey, "*A canonical form return mapping algorithm for rate independent plasticity*," International Journal for Numerical Methods in Engineering, vol.53(6), pp.1491-1510, 2002.
116. M.A.Keavey, "*A simplified canonical form algorithm with application to porous metal plasticity*," International Journal for Numerical Methods in Engineering, vol.65(5), pp.679-700, 2006.
117. E.A.de Souza Neto, D.Peric and D.R.J.Owen, *Computational methods for plasticity: theory and applications*, Oxford: Wiley-Blackwell, 2008.
118. W.F.Chen and D.J.Han, *Plasticity for Structural Engineers*, New York: Springer-Verlag, 1988.
119. F.Dunne and N.Petrinic, *Introduction to computational plasticity*, Oxford: Oxford University Press, 2005.
120. J.C.Simo and R.L.Taylor, "*Consistent tangent operators for rate-independent elastoplasticity*," Computer Methods in Applied Mechanics and Engineering, vol.48(1), pp.101-118, 1985.
121. D.W.Beardsmore, M.A.Wilkes and A.Shterenlikht, "*An implementation of the gurson-tvergaard-needleman plasticity model for abaqus standard using a trust region method*," in Proceedings of the ASME 2006 Pressure Vessels & Piping Conference, Vancouver, Canada, 2006.
122. N.Rebelo, J.C.Nagtegaal and L.M.Taylor, "*Comparison of Implicit and Explicit Finite Element Methods in the Simulation of Metal Forming Processes*," in NUMIFORM 82: Numerical Methods in Industrial Forming Processes, pp.99-108, Rotterdam, Balkema, 1992.
123. J.S.Sun, K.H.Lee and H.P.Lee, "*Comparison of implicit and explicit finite element methods for dynamic problems*," Journal of Materials Processing Technology, vol.105(1–2), pp.110-118, 2000.
124. F.J.Harewood and P.E.McHugh, "*Comparison of the implicit and explicit finite element methods using crystal plasticity*," Computational Materials Science, vol.39(2), pp.481-494, 2007.
125. C.V.Nielsen, W.Zhang, L.M.Alves, N.Bay and P.A.F.Martins, *Modeling of Thermo-Electro-Mechanical Manufacturing Processes: Applications in Metal Forming and Resistance Welding*, Springer, 2013.
126. W.J.Chung, J.W.Cho and T.Belytschko, "*On the dynamic effects of explicit FEM in sheet metal forming analysis*," Engineering Computations (Swansea, Wales), vol.15(6-7), pp.750-776, 1998.
127. *ABAQUS verson 6.12 documentation*, Dassault Systemes Simulia Crop., Rhode Island, 2012.
128. J.Lemaitre and J.L. Chaboche, *Mechanics of solid materials*, Cambridge: Cambridge University Press, 1990.
129. G.Rousselier, "*The Rousselier Model for Porous Metal Plasticity and Ductile Fracture*," Handbook of Materials Behavior Models Volume II: Failure of Materials, pp.436-445, CA: Academic Press, 2001.
130. K.Nahshon and J.W.Hutchinson, "*Modification of the Gurson Model for shear failure*," European Journal of Mechanics A/Solids, vol.27(1), pp.1-17, 2008.
131. R.Batisse, M.Bethmont, G.Devesa and G.Rousselier, "*Ductile fracture of A 508 Cl 3 steel in relation with inclusion content: The benefit of the local approach of fracture and continuum damage mechanics*," Nuclear Engineering and Design, vol.105(1), pp.113-120, 1987.

132. A.G.Franklin, "*Comparison between a quantitative microscope and chemical methods for assessment of nonmetallic inclusions*," Journal of the Iron and Steel Institute (London), vol.207, pp.181-186, 1969.
133. J. Sievers, H.Schulz, B.R.Bass, C.E.Pugh and J.Keeney, *CSNI Project For Fracture Analyses of Large- Scale International Reference Experiments (Phase I)*, Comparison Report (GRS-108), Gesellschaft für Anlagenund Reaktorsicherheit, Köln, Germany, 1994.
134. J.Guo, S.Zhao, R.Murakami and S.Zang, "*Experimental and numerical investigation for ductile fracture of Al-alloy 5052 using modified Rousselier model*," Computational Materials Science, vol.71(0), pp.115-123, 2013.
135. *EDF Energy tensile test report: specimen ID 10049-8*, 2013.
136. R.K.Blandford,D.K.Morton, S.D.Snow and T.E.Rahl, "*Tensile stress-strain results for 304L and 316L stainless steel plate at temperature*," in Proceedings of the ASME 2007 Pressure Vessels & Piping Conference, Texas, USA, 2007.
137. S.Do and D.J.Smith, "*Simulations of the large scale four-point bending experiment*," STYLE report, University of Bristol, UK, 2013.
138. S.Do and D.J.Smith, "*Simulations of a Large-scale Four Point Bending Experiment; Influence of Residual Stresses from a Repair Weld*," Procedia Materials Science, vol.3(0), pp.1599-1605, 2014.
139. S.Do, D.J.Smith and M.C.Smith, "*Effect of ageing on residual stresses in welded stainless steel cylinders*," in Proceedings of the ASME 2012 Pressure Vessels & Piping Conference, Toronto, Canada, 2012.
140. Y.Lei, N.P.O'Dowd and G.A.Webster, "*Fracture mechanics analysis of a crack in a residual stress field*," International Journal of Fracture, vol.106(3), pp.195-216, 2000.
141. M.C.Smith, "*Materials characterisation to support the MU2 large scale test*," STYLE report, 2014.
142. P.M.James and M.Ford, "*Post Test Finite Element Analysis of MU-2*," STYLE report, AMEC, Warrington, UK, 2014.
143. B.K.Neale and R.H.Priest, "*The Unloading Compliance Method for Crack Length Measurement Using Compact Tension and Precracked Charpy Specimens*," Elastic-Plastic Fracture Test Methods: The User's Experience, ASTM STP 856, American Society for Testing and Materials, Philadelphia, 1985.
144. M.W.Spindler and S.L.Spindler, "*Creep deformation, rupture and ductility of Esshete 1250 weld metal*," Materials Science and Technology, vol.30(1), pp.17-23, 2014.
145. P.Wilkins, "*OK 69.86 and SP146/11*," *Private Faxed Communication from ESAB Group (UK) Ltd to Wilkins P*, 1997.
146. J.N.Clark and J.Myers, *Stress Relaxation and Tensile Tests on Esshete 1250 Type Weld Metal*, Central Electricity Generating Board Technology Planning and Research Division, 1985.
147. R.D.Nicholson and R.G.Thomas, "*The Effect of Heat Treatment on the Structure and Mechanical Properties of a Complex Austenitic Weld Metal*," Microstructural Science, vol.9, pp.203-214, 1981.
148. A.H.Sherry and M.A.Wilkes, "*Numerical simulation of tearing–fatigue interactions in 316l(N) austenitic stainless steel*," International Journal of Pressure Vessels and Piping, vol.82(12), pp.905-916, 2005.

149. W.Schmitt, D.Z.Sun and J.G.Blauel, "*Damage mechanics analysis (Gurson model) and experimental verification of the behaviour of a crack in a weld-cladded component*," Nuclear Engineering and Design, vol.174(3), pp.237-246, 1997.
150. P.L.Delliou, D.Moinereau, E.Keim and T.Nicak, "*STYLE project: Assessment of transferbility of fracture material properties from specimen to large components by local approach to fracture*," in Proceedings of the ASME 2014 Pressure Vessels & Piping Conference, California, USA, 2014.
151. M.K.Samal, M.Seidenfuss, E.Ross and K.Balani, "*Investigation of failure behavior of ferritic-austenitic type of dissimilar steel welded joints*, " Engineering Failure Analysis, vol.18(3), pp.999-1008, 2011.
152. K.L.Taylor and A.H.Sherry, "*The characterization and interpretation of ductile fracture mechanisms in AL2024-T351 using X-ray and focused ion beam tomography,*" Acta Materialia, vol.60(3), pp. 1300-1310, 2012.
153. X.Feng, "*Effect of Materials Ageing on the Ductile Fracture of Stainless Steel*," MENG 4th year project report, School of materials, The University of Manchester, UK, 2014.
154. T.S.Jun, and A.M.Korsunsky, "*Evaluation of residual stresses and strains using the Eigenstrain Reconstruction Method*," International Journal of Solids and Structures, vol.47(13), pp.1678-1686, 2010.

APPENDIX I

COEFFICIENTS IN EQUATION 3.31

$$A_{11} = P + \Delta\epsilon_p\left(K\frac{\partial P}{\partial p} + \frac{\partial P}{\partial H^1}\frac{\partial H^1}{\partial \Delta\epsilon_p} + \frac{\partial P}{\partial H^2}\frac{\partial H^2}{\partial \Delta\epsilon_p}\right) + \Delta\epsilon_q\left(K\frac{\partial Q}{\partial p} + \frac{\partial Q}{\partial H^1}\frac{\partial H^1}{\partial \Delta\epsilon_p} + \frac{\partial Q}{\partial H^2}\frac{\partial H^2}{\partial \Delta\epsilon_p}\right)$$

$$A_{12} = Q + \Delta\epsilon_p\left(-3G\frac{\partial P}{\partial q} + \frac{\partial P}{\partial H^1}\frac{\partial H^1}{\partial \Delta\epsilon_q} + \frac{\partial P}{\partial H^2}\frac{\partial H^2}{\partial \Delta\epsilon_q}\right) + \Delta\epsilon_q\left(-3G\frac{\partial Q}{\partial q} + \frac{\partial Q}{\partial H^1}\frac{\partial H^1}{\partial \Delta\epsilon_q} + \frac{\partial Q}{\partial H^2}\frac{\partial H^2}{\partial \Delta\epsilon_q}\right)$$

$$A_{21} = K\frac{\partial \Phi}{\partial p} + \frac{\partial \Phi}{\partial H^1}\frac{\partial H^1}{\partial \Delta\epsilon_p} + \frac{\partial \Phi}{\partial H^2}\frac{\partial H^2}{\partial \Delta\epsilon_p}$$

$$A_{22} = -3G\frac{\partial \Phi}{\partial q} + \frac{\partial \Phi}{\partial H^1}\frac{\partial H^1}{\partial \Delta\epsilon_q} + \frac{\partial \Phi}{\partial H^2}\frac{\partial H^2}{\partial \Delta\epsilon_q}$$

$$b_1 = -\Delta\epsilon_p P - \Delta\epsilon_q Q$$

$$b_2 = -\Phi$$

where

$$\frac{\partial H^1}{\partial \Delta\epsilon_p} = w_{11}\left[\left(\frac{\partial h^1}{\partial \Delta\epsilon_p}\right) + K\left(\frac{\partial h^1}{\partial p}\right)\right] + w_{12}\left[\left(\frac{\partial h^2}{\partial \Delta\epsilon_p}\right) + K\left(\frac{\partial h^2}{\partial p}\right)\right]$$

$$\frac{\partial H^2}{\partial \Delta\epsilon_p} = w_{21}\left[\left(\frac{\partial h^1}{\partial \Delta\epsilon_p}\right) + K\left(\frac{\partial h^1}{\partial p}\right)\right] + w_{22}\left[\left(\frac{\partial h^2}{\partial \Delta\epsilon_p}\right) + K\left(\frac{\partial h^2}{\partial p}\right)\right]$$

$$\frac{\partial H^1}{\partial \Delta\epsilon_q} = w_{11}\left[\left(\frac{\partial h^1}{\partial \Delta\epsilon_q}\right) - 3G\left(\frac{\partial h^1}{\partial q}\right)\right] + w_{12}\left[\left(\frac{\partial h^2}{\partial \Delta\epsilon_q}\right) - 3G\left(\frac{\partial h^2}{\partial q}\right)\right]$$

$$\frac{\partial H^2}{\partial \Delta\epsilon_q} = w_{21}\left[\left(\frac{\partial h^1}{\partial \Delta\epsilon_q}\right) - 3G\left(\frac{\partial h^1}{\partial q}\right)\right] + w_{22}\left[\left(\frac{\partial h^2}{\partial \Delta\epsilon_q}\right) - 3G\left(\frac{\partial h^2}{\partial q}\right)\right]$$

$$w_{11} = \left(\delta_{22} - \frac{\partial h^2}{\partial H^2}\right)/\Omega\,, \qquad w_{12} = \left(\frac{\partial h^1}{\partial H^2}\right)/\Omega$$

$$w_{21} = \left(\frac{\partial h^2}{\partial H^1}\right)/\Omega \qquad w_{22} = \left(\delta_{11} - \frac{\partial h^1}{\partial H^1}\right)/\Omega$$

$$\Omega = \left(\delta_{11} - \frac{\partial h^1}{\partial H^1}\right)\left(\delta_{22} - \frac{\partial h^2}{\partial H^2}\right) - \left(\delta_{21} - \frac{\partial h^2}{\partial H^1}\right)\left(\delta_{12} - \frac{\partial h^1}{\partial H^2}\right)$$

APPENDIX II

COEFFICIENTS IN EQUATION 3.65

$$\overline{A}_{11} = P + \Delta\epsilon_p\left(\frac{\partial P}{\partial H^1}\frac{\partial H^1}{\partial \Delta\epsilon_p} + \frac{\partial P}{\partial H^2}\frac{\partial H^2}{\partial \Delta\epsilon_p}\right) + \Delta\epsilon_q\left(\frac{\partial Q}{\partial H^1}\frac{\partial H^1}{\partial \Delta\epsilon_p} + \frac{\partial Q}{\partial H^2}\frac{\partial H^2}{\partial \Delta\epsilon_p}\right)$$

$$\overline{A}_{12} = Q + \Delta\epsilon_p\left(\frac{\partial P}{\partial H^1}\frac{\partial H^1}{\partial \Delta\epsilon_q} + \frac{\partial P}{\partial H^2}\frac{\partial H^2}{\partial \Delta\epsilon_q}\right) + \Delta\epsilon_q\left(\frac{\partial Q}{\partial H^1}\frac{\partial H^1}{\partial \Delta\epsilon_q} + \frac{\partial Q}{\partial H^2}\frac{\partial H^2}{\partial \Delta\epsilon_q}\right)$$

$$\overline{A}_{21} = \frac{\partial \Phi}{\partial H^1}\frac{\partial H^1}{\partial \Delta\epsilon_p} + \frac{\partial \Phi}{\partial H^2}\frac{\partial H^2}{\partial \Delta\epsilon_p}$$

$$\overline{A}_{22} = \frac{\partial \Phi}{\partial H^1}\frac{\partial H^1}{\partial \Delta\epsilon_q} + \frac{\partial \Phi}{\partial H^2}\frac{\partial H^2}{\partial \Delta\epsilon_q}$$

$$B_{11} = \frac{\Delta\epsilon_p}{3}\left(\frac{\partial P}{\partial p} + \frac{\partial P}{\partial H^1}\frac{\partial H^1}{\partial p} + \frac{\partial P}{\partial H^2}\frac{\partial H^2}{\partial p}\right) + \frac{\Delta\epsilon_q}{3}\left(\frac{\partial Q}{\partial p} + \frac{\partial Q}{\partial H^1}\frac{\partial H^1}{\partial p} + \frac{\partial Q}{\partial H^2}\frac{\partial H^2}{\partial p}\right)$$

$$B_{12} = -\Delta\epsilon_p\left(\frac{\partial P}{\partial q} + \frac{\partial P}{\partial H^1}\frac{\partial H^1}{\partial q} + \frac{\partial P}{\partial H^2}\frac{\partial H^2}{\partial q}\right) - \Delta\epsilon_q\left(\frac{\partial Q}{\partial q} + \frac{\partial Q}{\partial H^1}\frac{\partial H^1}{\partial q} + \frac{\partial Q}{\partial H^2}\frac{\partial H^2}{\partial q}\right)$$

$$B_{21} = \frac{1}{3}\left(Q + \frac{\partial \Phi}{\partial H^1}\frac{\partial H^1}{\partial p} + \frac{\partial \Phi}{\partial H^2}\frac{\partial H^2}{\partial p}\right)$$

$$B_{22} = -\left(P + \frac{\partial \Phi}{\partial H^1}\frac{\partial H^1}{\partial q} + \frac{\partial \Phi}{\partial H^2}\frac{\partial H^2}{\partial q}\right)$$

where

$$\frac{\partial H^1}{\partial \Delta\epsilon_p} = w_{11}\left(\frac{\partial h^1}{\partial \Delta\epsilon_p}\right) + w_{12}\left(\frac{\partial h^2}{\partial \Delta\epsilon_p}\right), \qquad \frac{\partial H^2}{\partial \Delta\epsilon_p} = w_{21}\left(\frac{\partial h^1}{\partial \Delta\epsilon_p}\right) + w_{22}\left(\frac{\partial h^2}{\partial \Delta\epsilon_p}\right)$$

$$\frac{\partial H^1}{\partial \Delta\epsilon_q} = w_{11}\left(\frac{\partial h^1}{\partial \Delta\epsilon_q}\right) + w_{12}\left(\frac{\partial h^2}{\partial \Delta\epsilon_q}\right), \qquad \frac{\partial H^2}{\partial \Delta\epsilon_q} = w_{21}\left(\frac{\partial h^1}{\partial \Delta\epsilon_q}\right) + w_{22}\left(\frac{\partial h^2}{\partial \Delta\epsilon_q}\right)$$

$$\frac{\partial H^1}{\partial p} = w_{11}\left(\frac{\partial h^1}{\partial p}\right) + w_{12}\left(\frac{\partial h^2}{\partial p}\right), \qquad \frac{\partial H^2}{\partial p} = w_{21}\left(\frac{\partial h^1}{\partial p}\right) + w_{22}\left(\frac{\partial h^2}{\partial p}\right)$$

$$\frac{\partial H^1}{\partial q} = w_{11}\left(\frac{\partial h^1}{\partial q}\right) + w_{12}\left(\frac{\partial h^2}{\partial q}\right), \qquad \frac{\partial H^2}{\partial q} = w_{21}\left(\frac{\partial h^1}{\partial q}\right) + w_{22}\left(\frac{\partial h^2}{\partial q}\right)$$

Here, w_{ij} $(i = j = 1,2)$ have been already defined in Appendix I.

APPENDIX III

COEFFICIENTS IN EQUATION 3.66

$$C_{11} = [(\overline{A}_{22} + 3GB_{22})B_{11} - (\overline{A}_{12} + 3GB_{12})B_{21}]/\Delta$$

$$C_{12} = [(\overline{A}_{22} + 3GB_{22})B_{12} - (\overline{A}_{12} + 3GB_{12})B_{22}]/\Delta$$

$$C_{21} = [(\overline{A}_{11} + 3KB_{11})B_{21} - (\overline{A}_{21} + 3KB_{21})B_{11}]/\Delta$$

$$C_{22} = [(\overline{A}_{11} + 3KB_{11})B_{22} - (\overline{A}_{21} + 3KB_{21})B_{12}]/\Delta$$

where

$$\Delta = (\overline{A}_{11} + 3KB_{11})(\overline{A}_{22} + 3GB_{22}) - (\overline{A}_{12} + 3GB_{12})(\overline{A}_{21} + 3KB_{21})$$

APPENDIX IV

THE SCHEMATIC FLOW DIAGRAM OF UMAT

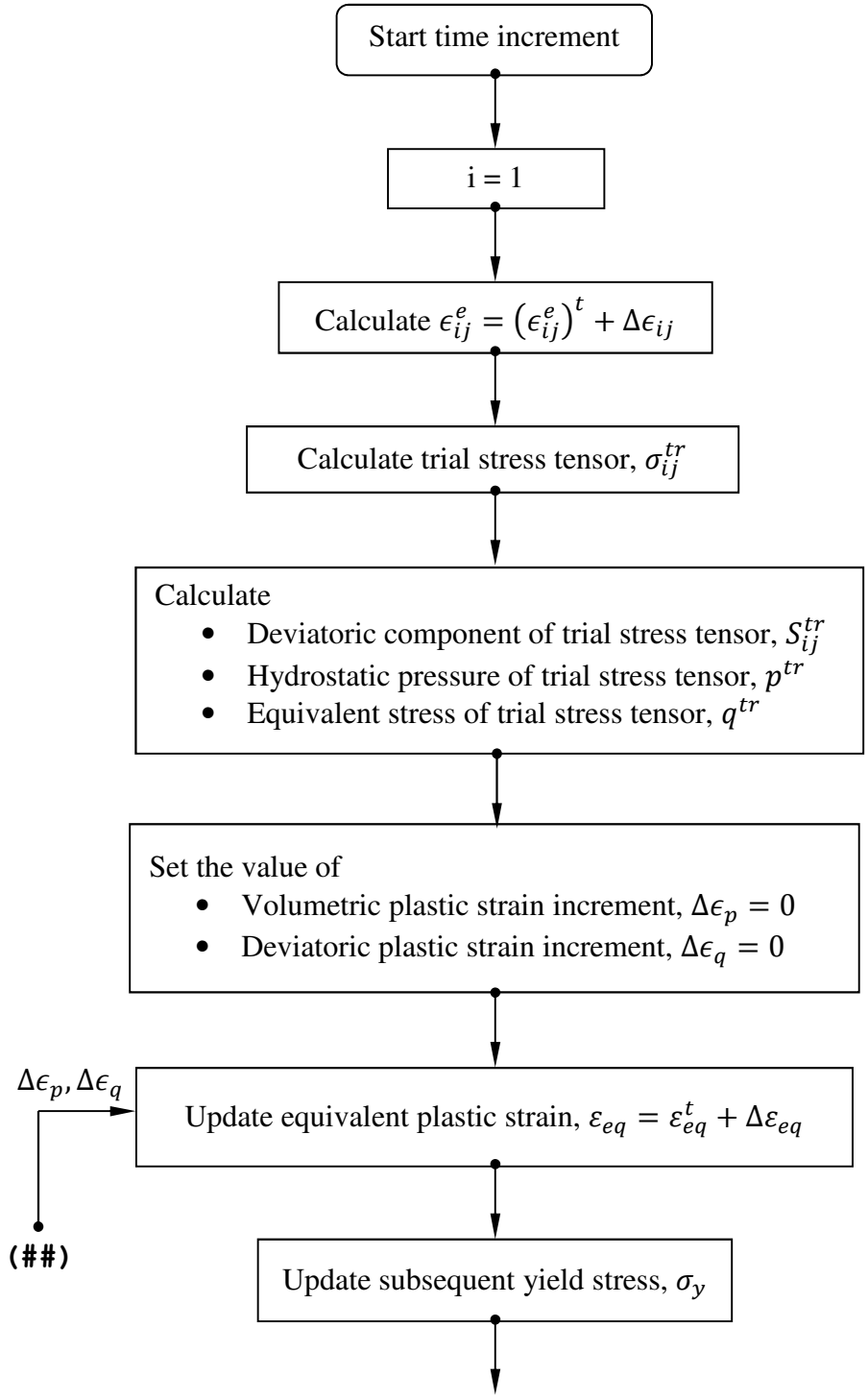

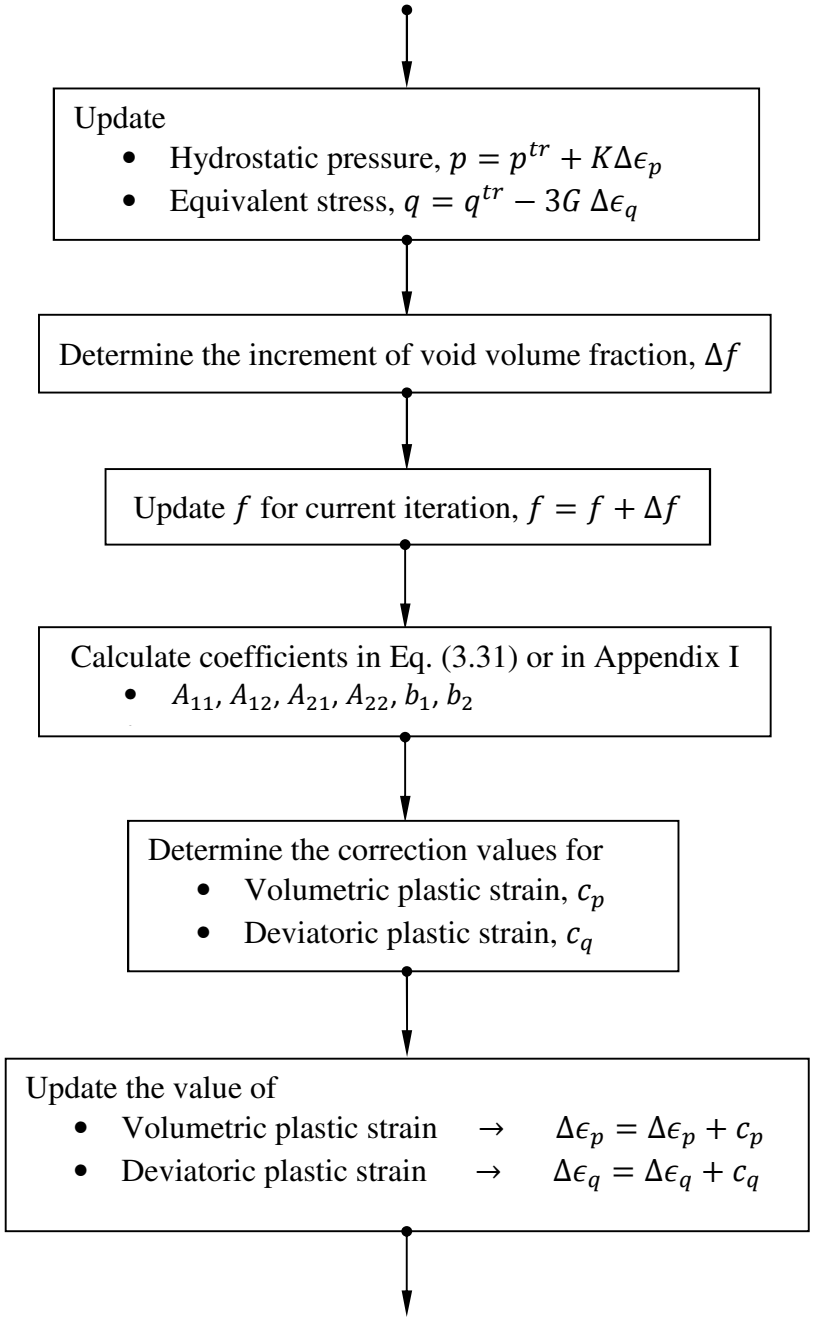
Update
• Hydrostatic pressure, $p = p^{tr} + K\Delta\epsilon_p$
• Equivalent stress, $q = q^{tr} - 3G\ \Delta\epsilon_q$
Determine the increment of void volume fraction, Δf
Update f for current iteration, $f = f + \Delta f$
Calculate coefficients in Eq. (3.31) or in Appendix I
• $A_{11}, A_{12}, A_{21}, A_{22}, b_1, b_2$
Determine the correction values for
• Volumetric plastic strain, c_p
• Deviatoric plastic strain, c_q
Update the value of
• Volumetric plastic strain → $\Delta\epsilon_p = \Delta\epsilon_p + c_p$
• Deviatoric plastic strain → $\Delta\epsilon_q = \Delta\epsilon_q + c_q$

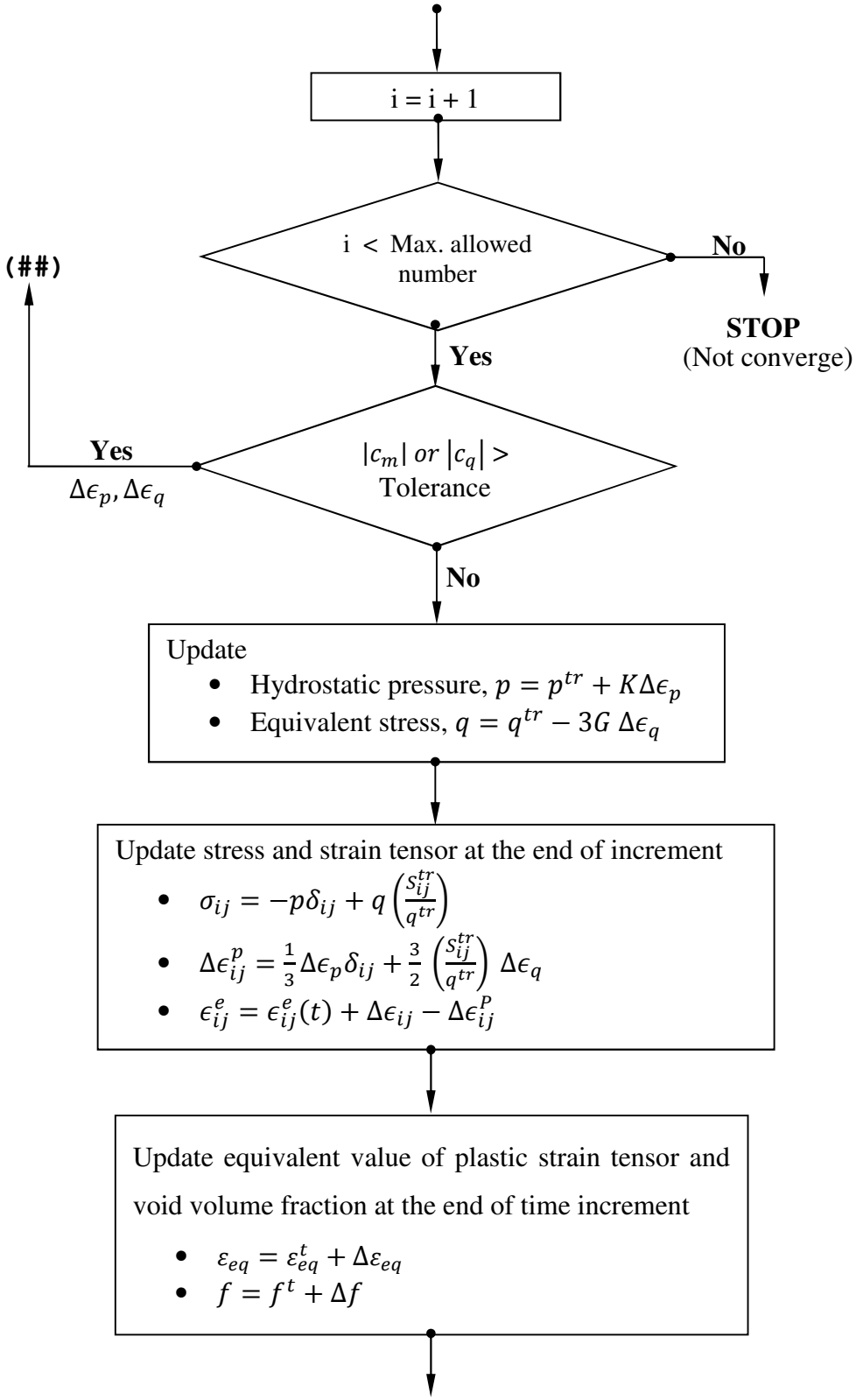
i = i + 1
i < Max. allowed number
No
STOP
(Not converge)
Yes
(##)
Yes
$\Delta\epsilon_p, \Delta\epsilon_q$
$|c_m|$ or $|c_q|$ > Tolerance
No
Update
Hydrostatic pressure, $p = p^{tr} + K\Delta\epsilon_p$
Equivalent stress, $q = q^{tr} - 3G\ \Delta\epsilon_q$
Update stress and strain tensor at the end of increment
$\sigma_{ij} = -p\delta_{ij} + q\left(\frac{S_{ij}^{tr}}{q^{tr}}\right)$
$\Delta\epsilon_{ij}^{p} = \frac{1}{3}\Delta\epsilon_p\delta_{ij} + \frac{3}{2}\left(\frac{S_{ij}^{tr}}{q^{tr}}\right)\Delta\epsilon_q$
$\epsilon_{ij}^{e} = \epsilon_{ij}^{e}(t) + \Delta\epsilon_{ij} - \Delta\epsilon_{ij}^{P}$
Update equivalent value of plastic strain tensor and void volume fraction at the end of time increment
$\varepsilon_{eq} = \varepsilon_{eq}^{t} + \Delta\varepsilon_{eq}$
$f = f^{t} + \Delta f$

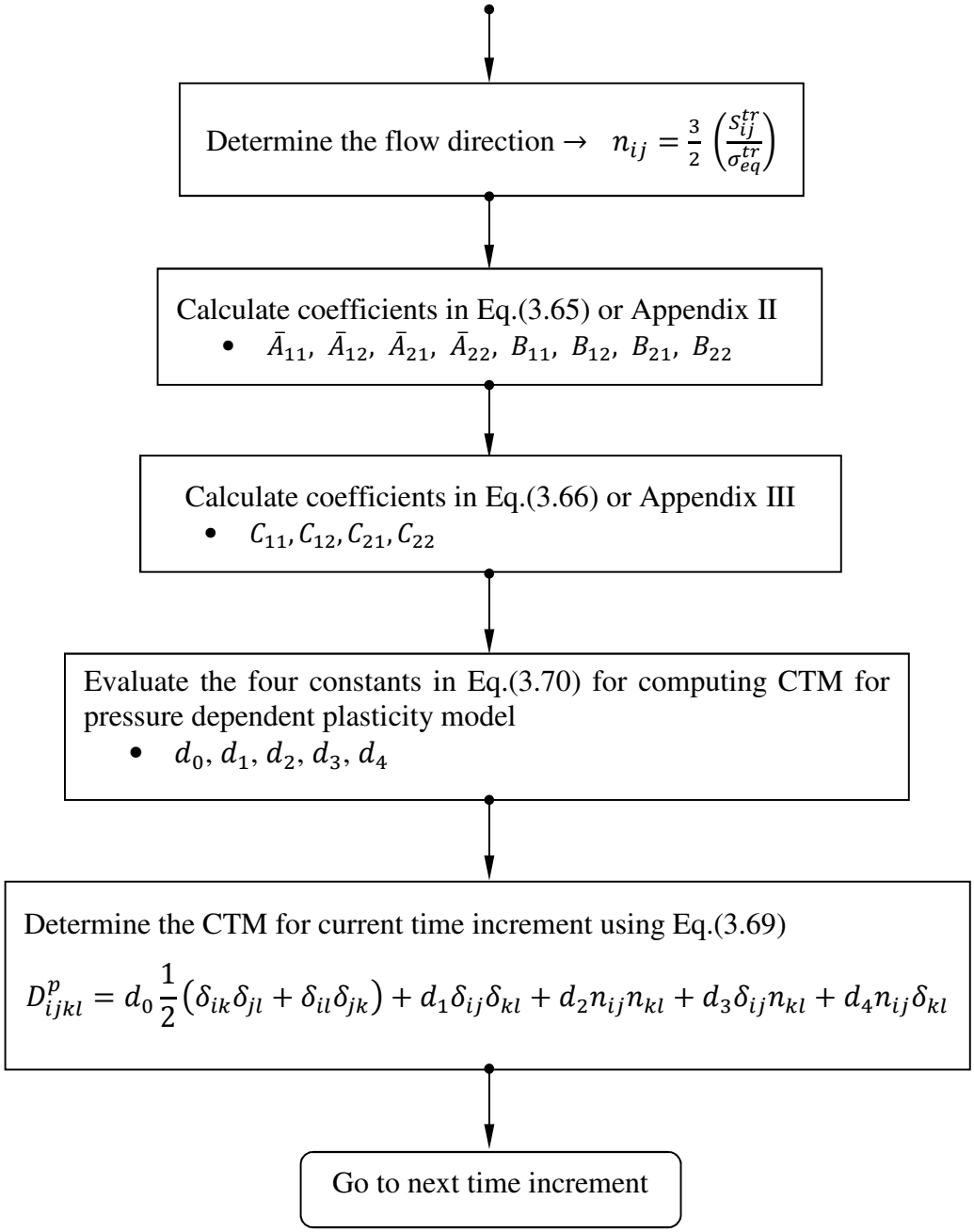
Determine the flow direction → $n_{ij} = \frac{3}{2}\left(\frac{S_{ij}^{tr}}{\sigma_{eq}^{tr}}\right)$
Calculate coefficients in Eq.(3.65) or Appendix II
• $\bar{A}_{11},\ \bar{A}_{12},\ \bar{A}_{21},\ \bar{A}_{22},\ B_{11},\ B_{12},\ B_{21},\ B_{22}$
Calculate coefficients in Eq.(3.66) or Appendix III
• $C_{11}, C_{12}, C_{21}, C_{22}$
Evaluate the four constants in Eq.(3.70) for computing CTM for pressure dependent plasticity model
• d_0, d_1, d_2, d_3, d_4
Determine the CTM for current time increment using Eq.(3.69)
$D_{ijkl}^{p} = d_0 \frac{1}{2}\left(\delta_{ik}\delta_{jl} + \delta_{il}\delta_{jk}\right) + d_1\delta_{ij}\delta_{kl} + d_2 n_{ij}n_{kl} + d_3\delta_{ij}n_{kl} + d_4 n_{ij}\delta_{kl}$
Go to next time increment

APPENDIX V

EXTRACTED VARIABLES DEFINED IN UMAT

- For stress update

No.	Variable in UMAT	Meaning	Remark
1	FF0	$\emptyset$	$\frac{q}{\rho} - R(\epsilon_{eq}) + f\sigma_1 Dexp\left(\frac{-p}{\rho\sigma_1}\right)$
2	FQ0OLD	$\frac{\partial\emptyset}{\partial q}$	$\frac{1}{\rho}$
3	FP0OLD	$\frac{\partial\emptyset}{\partial p}$	$-\frac{f}{\rho} Dexp\left(\frac{-p}{\rho\sigma_1}\right)$
4	FEM	$\frac{\partial\emptyset}{\partial H^1} = \frac{\partial\emptyset}{\partial\varepsilon_{eq}}$	$-\frac{\partial R(\epsilon_{eq})}{\partial\varepsilon_{eq}} = -h$ = Slope on hardening curve
5	FF	$\frac{\partial\emptyset}{\partial H^2} = \frac{\partial\emptyset}{\partial f}$	$q\frac{\partial\frac{1}{\rho}}{\partial f} + Dexp\left(\frac{-p}{\rho\sigma_1}\right)\left\{\sigma_1 - fp\ \frac{\partial\frac{1}{\rho}}{\partial f}\right\}$
6	HEF(1,1)	$\frac{\partial h^1}{\partial\Delta\epsilon_p}$	0
7	HEF(1,2)	$\frac{\partial h^1}{\partial\Delta\epsilon_q}$	1
8	HEF(1,3)	$\frac{\partial h^1}{\partial p}$	0
9	HEF(1,4)	$\frac{\partial h^1}{\partial q}$	0
10	HEF(2,1)	$\frac{\partial h^2}{\partial\Delta\epsilon_p}$	$1 - f$
11	HEF(2,2)	$\frac{\partial h^2}{\partial\Delta\epsilon_q}$	0

No.	Variable in UMAT	Meaning	Remark
12	HEF(2,3)	$\frac{\partial h^2}{\partial p}$	0
13	HEF(2,4)	$\frac{\partial h^2}{\partial q}$	0
14	EMH1	$\frac{\partial h^1}{\partial H^1} = \frac{\partial h^1}{\partial \varepsilon_{eq}}$	0
15	EMH2	$\frac{\partial h^1}{\partial H^2} = \frac{\partial h^1}{\partial f}$	0
16	FH1	$\frac{\partial h^2}{\partial H^1} = \frac{\partial h^2}{\partial \varepsilon_{eq}}$	0
17	FH2	$\frac{\partial h^2}{\partial H^2} = \frac{\partial h^2}{\partial f}$	$-\Delta\epsilon_p$
18	FP0	$Q = \frac{\partial \emptyset}{\partial p}$	$-\frac{f}{\rho} Dexp\left(\frac{-p}{\rho\sigma_1}\right)$
19	FP(1)	$\frac{\partial Q}{\partial p}$	$\frac{f}{\sigma_1\rho^2} Dexp\left(\frac{-p}{\rho\sigma_1}\right)$
20	FP(2)	$\frac{\partial Q}{\partial q}$	0
21	FP(3)	$\frac{\partial Q}{\partial H^1} = \frac{\partial Q}{\partial \varepsilon_{eq}}$	0
22	FP(4)	$\frac{\partial Q}{\partial H^2} = \frac{\partial Q}{\partial f}$	$-\frac{1}{\sigma_1\rho^2} Dexp\left(\frac{-p}{\rho\sigma_1}\right)\left\{\sigma_1\left(\rho + \frac{f}{1-f_0}\right) - \rho\, f\, p \frac{\partial \frac{1}{\rho}}{\partial f}\right\}$
23	FQ0	$P = \frac{\partial \emptyset}{\partial q}$	$\frac{1}{\rho}$
24	FQ(1)	$\frac{\partial P}{\partial p}$	0
25	FQ(2)	$\frac{\partial P}{\partial q}$	0

No.	Variable in UMAT	Meaning	Remark
26	FQ(3)	$\frac{\partial P}{\partial H^1} = \frac{\partial P}{\partial \varepsilon_{eq}}$	0
27	FQ(4)	$\frac{\partial P}{\partial H^2} = \frac{\partial P}{\partial f}$	$\frac{\partial \frac{1}{\rho}}{\partial f}$
28	DIVID	Ω	$1 + \Delta\epsilon_p$
29	CC(1,1)	w_{11}	1
30	CC(1,2)	w_{12}	0
31	CC(2,1)	w_{21}	0
32	CC(2,2)	w_{22}	$\frac{1}{1+\Delta\epsilon_p}$
33	H1EP	$\frac{\partial H^1}{\partial \Delta\epsilon_p}$	0
34	H2EP	$\frac{\partial H^2}{\partial \Delta\epsilon_p}$	$\frac{1-f}{1+\Delta\epsilon_p}$
35	H1EQ	$\frac{\partial H^1}{\partial \Delta\epsilon_q}$	1
36	H2EQ	$\frac{\partial H^2}{\partial \Delta\epsilon_q}$	0
37	RHO	ρ	$\frac{1-f}{1-f_0}$
38	FZEB	$\frac{\partial \frac{1}{\rho}}{\partial f}$	$\frac{1-f_0}{(1-f)^2}$
39	EPR		$\exp\left[\frac{-p}{\rho\sigma_1}\right]$

No.	Variable in UMAT	Meaning	Remark
40	DEPR		$\mathrm{Dexp}\left[\frac{-\mathrm{p}}{\rho\sigma_1}\right]$
41		H^1	$\varepsilon_{\mathrm{eq}}$
42		H^2	f
43		h^1	$\Delta\epsilon_{\mathrm{q}}$
44		h^2	$(1-\mathrm{f})\Delta\epsilon_{\mathrm{p}}$

- For the consistent tangent modulus (CTM)

No.	Variable in UMAT	Meaning	Remark
45	H1EP	$\frac{\partial \mathrm{H}^1}{\partial \Delta\epsilon_{\mathrm{p}}} = \frac{\partial \varepsilon_{\mathrm{eq}}}{\partial \Delta\epsilon_{\mathrm{p}}}$	0
46	H1EQ	$\frac{\partial \mathrm{H}^1}{\partial \Delta\epsilon_{\mathrm{q}}} = \frac{\partial \varepsilon_{\mathrm{eq}}}{\partial \Delta\epsilon_{\mathrm{q}}}$	1
47	H1P	$\frac{\partial \mathrm{H}^1}{\partial \mathrm{p}} = \frac{\partial \varepsilon_{\mathrm{eq}}}{\partial \mathrm{p}}$	0
48	H1Q	$\frac{\partial \mathrm{H}^1}{\partial \mathrm{q}} = \frac{\partial \varepsilon_{\mathrm{eq}}}{\partial \mathrm{q}}$	0
49	H2EP	$\frac{\partial \mathrm{H}^2}{\partial \Delta\epsilon_{\mathrm{p}}} = \frac{\partial \mathrm{f}}{\partial \Delta\epsilon_{\mathrm{p}}}$	$\frac{1-\mathrm{f}}{1+\Delta\epsilon_{\mathrm{p}}}$
50	H2EQ	$\frac{\partial \mathrm{H}^2}{\partial \Delta\epsilon_{\mathrm{q}}} = \frac{\partial \mathrm{f}}{\partial \Delta\epsilon_{\mathrm{q}}}$	0
51	H2P	$\frac{\partial \mathrm{H}^2}{\partial \mathrm{p}} = \frac{\partial \mathrm{f}}{\partial \mathrm{p}}$	0
52	H2Q	$\frac{\partial \mathrm{H}^2}{\partial \mathrm{q}} = \frac{\partial \mathrm{f}}{\partial \mathrm{q}}$	0

APPENDIX VI

UMAT FOR ROUSSELIER MODEL

```
C=============================================================
C     A USER MATERIAL SUBROUTINE FOR ROUSSELIER MODEL
C                       DEVELOPED BY
C                       SUTHAM ARUN
C              THE UNIVERSITY OF MANCHESTER
C           CONTACT:sutham.arun@manchester.ac.uk
C This subroutine based on the algorithm proposed by
C                 N.Aravas and Z.L.Zhang
C=============================================================
C
  SUBROUTINE UMAT(STRESS,STATEV,DDSDDE,SSE,SPD,SCD,
  1 RPL,DDSDDT,DRPLDE,DRPLDT,STRAN,DSTRAN,
  2 TIME,DTIME,TEMP,DTEMP,PREDEF,DPRED,MATERL,NDI,NSHR,NTENS,
  3 NSTATV,PROPS,NPROPS,COORDS,DROT,PNEWDT,CELENT,
  4 DFGRD0,DFGRD1,NOEL,NPT,KSLAY,KSPT,KSTEP,KINC)
C
  INCLUDE 'ABA_PARAM.INC'
C
  CHARACTER*80 MATERL
  DIMENSION STRESS(NTENS),STATEV(NSTATV),
  1 DDSDDE(NTENS,NTENS),DDSDDT(NTENS),DRPLDE(NTENS),
  2 STRAN(NTENS),DSTRAN(NTENS),TIME(2),PREDEF(1),DPRED(1),
  3 PROPS(NPROPS),COORDS(3),DROT(3,3),
  4 DFGRD0(3,3),DFGRD1(3,3)
C
  DIMENSION  EPLAS(6), SE(NTENS),  SDE(NTENS),
  1          S(NTENS), DEP(NTENS), EET(NTENS),
  2          DDE(NTENS,NTENS),     DDP(NTENS,NTENS),
  3          SA(NTENS),HEF(2,4),   CC(2,2),
  4          FQ(4),    FP(4),      DW(6),    DJ(6)
C
```

```
      PARAMETER (ZERO = 0.D0,OP5 = 1.5D0,ONE = 1.0D0,TWO = 2.0D0,
     1           THREE = 3.0D0,FOUR = 4.0D0,SIX = 6.0D0,
     2           TOL = 1.D-14,MNI   = 100)
C
      DATA DW/1.0,1.0,1.0,0.5,0.5,0.5/
      DATA DJ/1.0,1.0,1.0,0.0,0.0,0.0/
C-----------------------------------------------------------------
C
C The variables and parameters in UMAT :
C     CLAME      =     Lame's constant
C     C1K        =     Bulk modulus, K
C     C2G        =     Material constant, 2G
C     C3G        =     MaterIAl constant, 3G
C     C3K        =     Material constant, 3K
C     D          =     Rousselier Parameter
C     DDE        =     CTM of elastic part, D^e_ijkl
C     DDP        =     CTM of plastic part, D^p_ijkl
C     DH         =     The slope on the hardening curve
C     DEP        =     The increment of plastic strain, Δε^p_ij
C     DEMP       =     Volumetric plastic strain increment, Δε_p
C     DEEQP      =     Deviatoric plastic strain increment.Δε_q
C     DF         =     Void volume fraction increment, Δf
C     E          =     Young's modulus
C     EEQPT      =     Equivalent plastic strain, ε_eq
C     EET        =     Elastic strain tensor, ε^e_ij
C     EPLAS      =     Plastic strain tensor, ε^p_ij
C     F0         =     Initial void volume fraction, f_0
C     FT         =     Void volume fraction, f
C     G          =     Shear modulus, G
C     H          =     Subsequent yield criteria for each
C                      increment
C     NVALUE     =     Number of ordered pair of hardening data
C     POISSON    =     Poisson's ratio, ν
C     P          =     Hydrostatic pressure, p
```

```
C     PE          =     Hydrostatic pressure, p^tr
C     RHOT        =     Relative density, ρ
C     S1          =     Rousselier Parameter, σ1
C     SA          =     Flow direction, nij
C     SDE         =     Deviatoric component of trial stress
C                       tensor, Sij^tr
C     SE          =     Trial stress tensor, σij^tr
C     SEQ         =     Equivalent values of stress tensor, q
C     sigdif      =     Parameter for checking if material has
C                       already yield
C     SM          =     Mean values of stress tensor, σm
C     YS          =     First Yield Stress, σy
C-------------------------------------------------------------
C The state variable is stored as:
C     STATEV(1,2,..,NTENS) = Elastic strain tensor
C     STATEV(NTENS+1,NTENS+2,..,2*NTENS) = Plastic strain tensor
C     STATEV(2*NTENS+1) =  Equivalent plastic strain
C     STATEV(2*NTENS+2) =  Void volume fraction
C     STATEV(2*NTENS+3) =  Relative density
C-------------------------------------------------------------
C User needs to input:
C     props(1)    =     Young's modulus, E
C     props(2)    =     Poisson's ratio, POISSON
C     props(3)    =     First Yield Stress, YS
C     props(4)    =     Rousselier Parameter, S1
C     props(5)    =     Rousselier Parameter, D
C     props(6)    =     Initial void volume fraction, F0
C     props(7..)  =     Set of hardening data
C-------------------------------------------------------------
C Subroutine used in UMAT:
C     KFI   → Determine the increment of void volume fraction
C     KHARD → Determine the current yield stress
C-------------------------------------------------------------
C
```

```
C Import material properties and parameters
      E          =     props(1)
      POISSON    =     props(2)
      YS         =     props(3)
      S1         =     props(4)
      D          =     props(5)
      F0         =     props(6)
C
C Compute the values of elastic properties for UMAT
      C3K        =     E/(ONE-TWO*POISSON)
      C2G        =     E/(ONE+POISSON)
      G          =     C2G/TWO
      C3G        =     THREE*G
      CLAME =     (C3K-C2G)/THREE
      C1K        =     C3K/THREE
C
C Calculate a number of ordered pair of hardening data
      NVALUE     =     (NPROPS/2)-3
C
C Recover the value of elastic(EET)and plastic(EPLAS) strain
C tensor at the begining of increment
      CALL ROTSIG(STATEV(1),      DROT,EET,  2,NDI,NSHR)
      CALL ROTSIG(STATEV(1+NTENS),DROT,EPLAS,2,NDI,NSHR)
C
C Recover the value of equivalent plastic strain (EEQPT),
C void volume fraction (FT) and relative density (RHO)
C at the begining of increment
     EEQPT   =   STATEV(1 + 2*NTENS)
     FT      =   STATEV(2 + 2*NTENS)
     RHOT    =   STATEV(3 + 2*NTENS)
C
      IF(EEQPT.EQ.0.0) THEN
            FT         = F0
            RHOT       = ONE
      END IF
C
```

```
C Define stiffness matrix,[K] or Jacobian matrix
C for elastic case(DDE)
      DO    200   K1 = 1, NTENS
            DO    100 K2 = 1, NTENS
                  DDE(K2,K1)    =  0.0
                  DDP(K2,K1)    =  0.0
                  DDSDDE(K2,K1) =  0.0
 100        CONTINUE
 200  CONTINUE
C
       DO   400   K1 = 1, NDI
            DO    300 K2 = 1, NDI
                  DDE(K2,K1) = CLAME
 300        CONTINUE
            DDE(K1,K1) = C2G + CLAME
 400  CONTINUE
      DO    500   K1 = NDI + 1, NTENS
            DDE(K1,K1) = G
 500  CONTINUE
C
C Compute trial stress tensor from elastic strains
C increment(DSTRAN)
C
       DO   700   K1 = 1, NTENS
            DO    600 K2 = 1, NTENS
                  STRESS(K2)= STRESS(K2)+ DDE(K2,K1)*DSTRAN(K1)
 600        CONTINUE
 700  CONTINUE
C
C Calculate equivalent values(SEQ) and mean value(SM) of trial
C stress tensor(STRESS)
      CALL SINV(STRESS,SM,SEQ,NDI,NSHR)
C
C Determine subsequent yield stress(SEQO)
      CALL KHARD(H,DH,EEQPT,PROPS(7),NVALUE)
C
```

```
C Check if the stress value is beyond the yield surface
      sigdif = (SEQ/RHOT) - H + FT*S1*D*EXP(SM/(S1*RHOT))
C
      IF ( sigdif .le. zero ) THEN
C
C           In Case of elastic (Not Yielding)
C Store elastic(EET), plastic(EPLAS) strain tensor
C in state variable array
            DO 800  K1  = 1, NTENS
                  STATEV(K1)       =     EET(K1)
                  STATEV(K1+NTENS) =     EPLAS(K1)
800         CONTINUE
C
C Store value of equivalent plastic strain (EEQPT),
C void volume fraction (FT) and relative density (RHO)
C in state variable array
            STATEV(1 + 2*NTENS) = EEQPT
            STATEV(2 + 2*NTENS) = FT
            STATEV(3 + 2*NTENS) = RHOT
C
C Set Jacobain matrix(DDSDDE) of current increment
C = Jacobian matrix of elastic part(DDE)
            DDSDDE = DDE
C
      ELSE
C
C           In Case of plastic (Yielding)
   IF(TIME(1).EQ.0.0.AND.(SEQ.NE.0.0.AND.sigdif.GT.10000.0))THEN
      PNEWDT = 0.5
      GO TO 5000
   ENDIF
C
C Define new parameters to store the trial stress tensor(SE)
            SE = STRESS
C
```

```
C Determine mean value(SME)and equivalent value(SEQE) of
C trial stress tensor(SE)
          CALL SINV(SE,SME,SEQE,NDI,NSHR)
C
C Determine hydrostatic pressure(PE)
          PE    = - SME
C
C Calculate deviatoric component(SDE) of SE
C
          SDE     =   SE
          DO 1000  I = 1, NDI
               SDE(I) = SDE(I) - SME
1000      CONTINUE
C
C Set the initial value of equivalent(DEEQP) and
C mean value(DEMP) of plastic strain increment tensor
          DEMP  =     0.D0
          DEEQP =     0.D0
C Set the initial value of void volume fraction(DF)
          DF    =     0.D0
C Set the initial value of iteration number(ITER)
          ITER  =     0
C
C-----------------------------------------------------------------
C Starting iterative Process for computing the increment values
C of Mean Value(CM) and Equivalent Value(CEQ) of Plastic strain
C increment tensor
C-----------------------------------------------------------------
C
C Update iteration number
1500      ITER  =     ITER + 1
C
C Update equivalent value of plastic strain(EEQP) for
C current iteration
          EEQP  =     EEQPT + DEEQP
C
```

```
C Calculate subsequent yield stress(H) and slop on the hardening
C curve(DH) for current iteration
          CALL KHARD(H,DH,EEQP,PROPS(7),NVALUE)
C
C Compute mean(SM) and equivalent values(SEQ) of stress tensor
C for current iteration using Eq.(3.21)
          P          =     PE     + C1K*DEMP
          SEQ   =     SEQE - C3G*DEEQP
          IF(SEQ.LE.0.0) SEQ = 0.D0
C
C Determine the increment of void volume fraction(DF)
C for current iteration using Newton-Raphson method
          CALL KFI(FT, DEMP, DF)
C
C Update the values of void volume fraction(F)
C for current iteration
          F     =     FT + DF
C
C Compute variable no.37-40 defined in Appendix V
          RHO   =     (ONE - F)/(ONE-F0)
          FZEB  =     (ONE - F0)/((ONE - F)*(ONE - F))
          EPR   =     EXP(-P/(RHO*S1))
          DEPR  =     D*EPR
C
C Compute variable no.1-5 defined in Appendix V
     FF0        =     (SEQ/RHO) - H + F*S1*DEPR
     FQ0OLD     =     one/RHO
     FP0OLD     =     -(F/RHO)*DEPR
     FEM        =     - DH
     FF         =     SEQ*FZEB + DEPR*(S1 - F*P*FZEB)
C
C Compute variable no.6-9 defined in Appendix V
     HEF(1,1)   =     ZERO
     HEF(1,2)   =     ONE
     HEF(1,3)   =     ZERO
     HEF(1,4)   =     ZERO
```

```
C Compute variable no.10-13 defined in Appendix V
      HEF(2,1)   =     ONE - F
      HEF(2,2)   =     ZERO
      HEF(2,3)   =     ZERO
      HEF(2,4)   =     ZERO
C
C Compute variable no.14-17 defined in Appendix V
      EMH1       =     zero
      EMH2       =     zero
      FH1        =     zero
      FH2        =     -DEMP
C
C Compute variable no.28-32 defined in Appendix V
      DIVID      =     (ONE-EMH1)*(ONE-FH2)-(EMH2*FH1)
      CC(1,1)    =     (one-FH2)/DIVID
      CC(2,2)    =     (one-EMH1)/DIVID
      CC(1,2)    =     EMH2/DIVID
      CC(2,1)    =     FH1/DIVID
C
C Compute variable no.33-36 defined in Appendix V
      H1EP  = 0.D0
      H2EP  = 0.D0
      H1EQ  = 0.D0
      H2EQ  = 0.D0
C
      DO 1600 I = 1,2
           H1EP = H1EP + CC(1,I)*(HEF(I,1) + C1K*HEF(I,3))
           H2EP = H2EP + CC(2,I)*(HEF(I,1) + C1K*HEF(I,3))
           H1EQ = H1EQ + CC(1,I)*(HEF(I,2) - C3G*HEF(I,4))
1600       H2EQ = H2EQ + CC(2,I)*(HEF(I,2) - C3G*HEF(I,4))
C
C Compute variable no.18-22 defined in Appendix V
      FP0   = -(F/RHO)*DEPR
      FP(1) = (F/(S1*RHO*RHO))*DEPR
      FP(2) = zero
      FP(3) = zero
```

```
      FP(4) = -(one/(S1*RHO*RHO))*DEPR
     1       *(S1*(RHO +(F/(one-F0)))-RHO*F*P*FZEB)
C
C Compute variable no.23-27 defined in Appendix V
      FQ0        =    ONE/RHO
      FQ(1) =     zero
      FQ(2) =     zero
      FQ(3) =     zero
      FQ(4) =     FZEB
C
C Define the Aravas's coefficients in Eq.(3.31)
C using formula given in Appendix I
      A11   =     FQ0+DEMP*(C1K*FQ(1)+FQ(3)*H1EP+FQ(4)*H2EP)
  1           + DEEQP*(C1K*FP(1)+FP(3)*H1EP+FP(4)*H2EP)
      A12   =     FP0+DEMP*(-C3G*FQ(2)+FQ(3)*H1EQ+FQ(4)*H2EQ)
  1           + DEEQP*(-C3G*FP(2) + FP(3)*H1EQ + FP(4)*H2EQ)
      B1    =  - DEMP*FQ0 - DEEQP*FP0
C
      A21   =     C1K*FP0OLD + FEM*H1EP + FF*H2EP
      A22   =    -C3G*FQ0OLD + FEM*H1EQ + FF*H2EQ
      B2    =    -FF0
C
C Determine the correction values for volumetric(CM) and
C deviatoric(CEQ) component of plastic strain increment tensor
C for current iteration
      DET   =     A11*A22 - A12*A21
      CM    =     (A22*B1 - A12*B2)/DET
      CEQ   =     (A11*B2 - A21*B1)/DET
C
C Update mean value(DEMP) and equivalent value(DEEQP) of
C plastic strain increment tensor for current iteration
      DEMP  =     DEMP  + CM
      DEEQP =     DEEQP + CEQ
C
```

```
C Checking whether the number of current iteration exceed the
C maximum allowed number
          IF (ITER.LT.MNI) GOTO 1700
          WRITE(102,*)'THE ITERATION CANNOT CONVERGE'
          STOP
C
C Start new iteration, if the increment values of volumetric or
C deviatoric part of plastic strain tensor is not less than
C the tolerance
1700      IF((ABS(CM).GT.TOL).OR.(ABS(CEQ).GT.TOL)) GOTO 1500
C
C-----------------------------------------------------------------
C                    ENDING ITERATIVE PROCESS
C-----------------------------------------------------------------
C
C Update final values of hydrostatic pressure(P)and equivalent
C value(SEQ) of stress tensor(S) for current increment
     P    =    PE + C1K*DEMP
     SEQ  =    SEQE - C3G*DEEQP
C
C Update the final values of stress tensor(S) and
C plastic strain increment(DEP) for current increment
C using Eqs.(3.33) and (3.34)
          S    =    0.D0
          DEP  =    0.D0
          S    =    SEQ*(SDE/SEQE)
          DEP  =    1.5*(SDE/SEQE)*DEEQP
          DO 1900 I= 1, NDI
               S(I)   =   S(I)   - P
               DEP(I) =   DEP(I) + DEMP/THREE
1900      CONTINUE
C Store the stress tensor of current increment to variable
C 'STRESS'
          STRESS = S
C
```

```
C Update plastic strain tensor(EPLAS) at the end of increment
          DO 2000 K1 = 1, NTENS
               if (K1.le.NDI) then
                    EPLAS(K1)  = EPLAS(K1) + DEP(K1)
               else
                    EPLAS(K1)  = EPLAS(K1) + two*DEP(K1)
               end if
2000      CONTINUE
C
C Update elastic strain tensor(EET) at the end of time step
C using Eq.(3.35)
          EET   = EET  - DEP
C
C Update the final values of equivalent plastic strain(EEQPT)
C and void volume fraction (FT) for current increment
          EEQPT =   EEQPT  + DEEQP
          FT    =   FT + DF
C
C-----------------------------------------------------------------
C          Consistent Tangent Modulus for Plastic Part
C-----------------------------------------------------------------
C
C Determine the flow direction(SA) using Eq.(3.20)
          DO 2200 I = 1, NTENS
          SA(I) =  OP5*(SDE(I)/SEQE)
2200      CONTINUE
C
C Set the initail vaules of variable no.45-52 defined in
C Appendix V
          H1EP = ZERO
          H1EQ = ZERO
          H1P  = ZERO
          H1Q  = ZERO
C
          H2EP = ZERO
          H2EQ = ZERO
```

```
           H2P  = ZERO
           H2Q  = ZERO
C
C Compute variable no.45-52 defined in Appendix V using formula
C given in Appendix II
           DO 2300 I = 1,2
                H1EP =     H1EP + CC(1,I)*HEF(I,1)
                H1EQ =     H1EQ + CC(1,I)*HEF(I,2)
                H1P  =     H1P  + CC(1,I)*HEF(I,3)
                H1Q  =     H1Q  + CC(1,I)*HEF(I,4)
C
                H2EP =     H2EP + CC(2,I)*HEF(I,1)
                H2EQ =     H2EQ + CC(2,I)*HEF(I,2)
                H2P  =     H2P  + CC(2,I)*HEF(I,3)
                H2Q  =     H2Q  + CC(2,I)*HEF(I,4)
2300       CONTINUE
C
C Determine coefficients in Eq.(3.65) using formula given
C in Appendix II
      AA11 = FQ0 + (DEMP*FQ(3) + DEEQP*FP(3))*H1EP
     1           + (DEMP*FQ(4) + DEEQP*FP(4))*H2EP
      AA12 = FP0 + (DEMP*FQ(3) + DEEQP*FP(3))*H1EQ
     1           + (DEMP*FQ(4) + DEEQP*FP(4))*H2EQ
      AA21 = FEM*H1EP + FF*H2EP
      AA22 = FEM*H1EQ + FF*H2EQ
C
      BB11 =  (DEMP/three)*(FQ(1)+ FQ(3)*H1P + FQ(4)*H2P) +
     1        (DEEQP/three)*(FP(1)+ FP(3)*H1P + FP(4)*H2P)
      BB12 = -(DEMP)* (FQ(2) + FQ(3)*H1Q + FQ(4)*H2Q) -
     1        (DEEQP)*(FP(2) + FP(3)*H1Q + FP(4)*H2Q)
      BB21 =  (FP0 + FEM*H1P + FF*H2P)/three
      BB22 = -(FQ0 + FEM*H1Q + FF*H2Q)
C
```

```
C Determine coefficients in Eq.(3.66) using formula given
C in Appendix III
C
      DIV   =     (AA11 + C3K*BB11)*(AA22 + C3G*BB22) -
     1            (AA12 + C3G*BB12)*(AA21 + C3K*BB21)
C
     C11 =  ((AA22 + C3G*BB22)*BB11 - (AA12 + C3G*BB12)*BB21)/DIV
     C21 =  ((AA11 + C3K*BB11)*BB21 - (AA21 + C3K*BB21)*BB11)/DIV
     C12  = ((AA22 + C3G*BB22)*BB12 - (AA12 + C3G*BB12)*BB22)/DIV
     C22  = ((AA11 + C3K*BB11)*BB22 - (AA21 + C3K*BB21)*BB12)/DIV
C
C Evaluate the four coefficients given by Zhange using Eq.(3.70)
      D0    =   C2G*(SEQ/SEQE)
      D1    =   C1K-(C2G/THREE)*(SEQ/SEQE)-THREE*C1K*C1K*C11
      D2    =   ((FOUR*G*G*DEEQP)/SEQE)-FOUR*G*G*C22
      D3    =  -(C2G)*C1K*C12
      D4    =  -(SIX*G)*C1K*C21
C
C Determine the consistent tangent modulus(CTM) for
C presure-dependent plasticity model using Eq.(3.69)
       DO 2600    I = 1, NTENS
            DO 2500    J = 1, NTENS
                 DIJ = 0.0
                 IF(I.EQ.J) DIJ = 1.0
                 DDP(I,J) = DIJ*DW(I)*D0   + D1*DJ(I)*DJ(J) +
     1                      D2*SA(I)*SA(J) +  D3*DJ(I)*SA(J) +
     2                      D4*SA(I)*DJ(J)
2500        CONTINUE
2600  CONTINUE
C Set Jacobain matrix(DDSDDE) of current increment =
C Jacobian matrix of plastic part(DDP)
            DDSDDE = DDP
C
```

```
C Store elastic(EET), plastic(EPLAS) and equivalent value of
C plastic strain(EEQPT)in state variable array
          DO 2800 K1  = 1, NTENS
               STATEV(K1)            = EET(K1)
               STATEV(K1 + NTENS)    = EPLAS(K1)
2800      CONTINUE
               STATEV(1  + 2*NTENS)  = EEQPT
               STATEV(2 + 2*NTENS)   = FT
               STATEV(3 + 2*NTENS)   = RHOT
C
     ENDIF
5000 RETURN
     END
C
C=================================================================
C
  SUBROUTINE KHARD(SYIELD,HARD,EQPLAS,TABLE,NVALUE)
  INCLUDE 'ABA_PARAM.INC'
  DIMENSION TABLE(2,NVALUE)
C
C SET YIELD STRESS TO LAST VALUE OF TABLE, HARDENING TO ZERO
     SYIELD=TABLE(1,NVALUE)
     HARD=0.0
C
C IF MORE THAN ONE ENTRY, SEARCH TABLE
     IF(NVALUE.GT.1) THEN
       DO 10 K1=1,NVALUE-1
       EQPL1=TABLE(2,K1+1)
          IF(EQPLAS.LT.EQPL1) THEN
          EQPL0=TABLE(2,K1)
               IF(EQPL1.LE.EQPL0) THEN
          WRITE(6,1)
 1        FORMAT(//,30X,'***ERROR - PLASTIC STRAIN MUST BE ',
 1               'ENTERED IN ASCENDING ORDER')
                CALL XIT
               ENDIF
```

```
C CURRENT YIELD STRESS AND HARDENING
            DEQPL=EQPL1-EQPL0
            SYIEL0=TABLE(1,K1)
            SYIEL1=TABLE(1,K1+1)
            DSYIEL=SYIEL1-SYIEL0
            HARD=DSYIEL/DEQPL
            SYIELD=SYIEL0+(EQPLAS-EQPL0)*HARD
            GOTO 20
            ENDIF
 10   CONTINUE
 20   CONTINUE
      ENDIF
      RETURN
  END SUBROUTINE KHARD
C
C=============================================================
C
  SUBROUTINE KFI(FT, DEMP, DF)
  INCLUDE 'ABA_PARAM.INC'
  PARAMETER (one = 1.d0, TOL = 1.D-14, MNI = 500)
C
C Set the initial value of iteration number (I) and
C the increment of void volume fraction(DF)
      I     = 0
      DF    = 0.D0
C-------------------------------------------------------------
C          Starting iterative process for finding DF
C                     by Newton-Raphson Method
C-------------------------------------------------------------
C Update void volume fraction(F) for current iteration
1000       F  = FT + DF
C
C Determine the correction values(CF) of void volume fraction
C increment using Newton-Raphson method based on Eq.(4.20)
           F1 = DF  - (one - F)*DEMP
           F2 = one +  DEMP
```

```
           CF = -F1/F2
C
C Update the value of void volume fraction increment(DF) for
C current iteration
           DF = DF + CF
C
C Update the iteration number
           I = I + 1
C
C Checking whether the number of current iteration exceed
C the maximum allowed number or not
           IF (I .LT. MNI) GOTO 1100
           WRITE(102,*)'KBI CANNOT CONVERGE'
           STOP
C
C Checking whether the correction value(CF) is greater than
C the tolerance
           TCF = CF*1000.
1100       IF (ABS(TCF) .GT. TOL) GOTO 1000
C
C-------------------------------------------------------------
C                     ENDING ITERATIVE PROCESS
C-------------------------------------------------------------
C
  END SUBROUTINE KFI
C
```

PPENDIX VII

LIST OF PUBLICATIONS

- S.Arun, A.H.Sherry, M.A.Sheikh and M.C.Smith, "*Rousselier parameter calibration for Esshete weld metal*," in Proceedings of the ASME 2014 Pressure Vessels & Piping Conference, Massachusetts, USA, 2015.
- S.Arun, A.H.Sherry, M.C.Smith and M.A.Sheikh, "*Finite element simulation of a circumferential through-thickness crack in a cylinder*," in Proceedings of the ASME 2014 Pressure Vessels & Piping Conference, California, USA, 2014.